

Electronic Thesis and Dissertation Repository

9-23-2013 12:00 AM

Image quality of energy-dependent approaches for x-ray angiography

Jesse Evan Tanguay
The University of Western Ontario

Supervisor
Ian Cunningham
The University of Western Ontario

Graduate Program in Medical Biophysics
A thesis submitted in partial fulfillment of the requirements for the degree in Doctor of Philosophy
© Jesse Evan Tanguay 2013

Follow this and additional works at: <https://ir.lib.uwo.ca/etd>



Part of the [Applied Statistics Commons](#), [Cardiovascular Diseases Commons](#), [Diagnosis Commons](#), and the [Probability Commons](#)

Recommended Citation

Tanguay, Jesse Evan, "Image quality of energy-dependent approaches for x-ray angiography" (2013). *Electronic Thesis and Dissertation Repository*. 1658.
<https://ir.lib.uwo.ca/etd/1658>

This Dissertation/Thesis is brought to you for free and open access by Scholarship@Western. It has been accepted for inclusion in Electronic Thesis and Dissertation Repository by an authorized administrator of Scholarship@Western. For more information, please contact wlsadmin@uwo.ca.

Image quality of energy-dependent approaches for x-ray angiography

(Thesis format: Integrated Article)

by

Jesse Tanguay

Graduate Program
in
Medical Biophysics

Submitted in partial fulfillment
of the requirements of the degree of
Doctor of Philosophy

The School of Graduate and Postdoctoral Studies
Western University
London, Ontario, Canada

© Jesse Tanguay 2013

ABSTRACT

Digital subtraction angiography (DSA) is an x-ray-based imaging method widely used for diagnosis and treatment of patients with vascular disease. This technique uses subtraction of images acquired before and after injection of an iodinated contrast agent to generate iodine-specific images. While it is extremely successful at imaging structures that are near-stationary over a period of several seconds, motion artifacts can result in poor image quality with uncooperative patients and DSA is rarely used for coronary applications.

Alternative methods of generating iodine-specific images with reduced motion artifacts might exploit the energy-dependence of x-ray attenuation in a patient. This could be performed either by acquiring two or more post-injection images at different x-ray energies or from an analysis of the spectral shape of the transmitted spectrum. The first method, which we call energy-subtraction angiography (ESA), was introduced as a dual-energy alternative to DSA over two decades ago but technological limitations of the time resulted in poor image quality. The second potential method, energy-resolved angiography (ERA), requires energy-resolving photon-counting (EPC) x-ray detectors that are under development in a number of laboratories.

The goals of this thesis were to: 1) develop a method of comparing image quality in terms of signal-to-noise ratio (SNR) obtained using ESA and ERA with DSA assuming ideal instrumentation for each; 2) develop a method of describing performance and image quality that can be obtained in practice with photon-counting detectors, and; 3) assess the potential of ESA and ERA by comparing the available iodine SNR with that of DSA including the effects of non-ideal detector performance.

It is shown that using ideal instrumentation both ESA and ERA can provide iodine-specific images with SNR equal to that of DSA. However, stochastic x-ray interaction and detection processes will degrade SNR obtained with ERA and ESA to a larger extent than DSA. Energy-resolved angiography will achieve near-ideal performance only with low detector electronic noise levels, high collection efficiency of secondary quanta liberated in the detector, and low Compton cross sections. It is concluded that, when these conditions are satisfied, ESA and ERA can provide iodine SNR within 25% of that of DSA for the same patient entrance exposure, and therefore may provide alternatives to DSA in situations where motion artifacts are expected to result in compromised DSA procedures, such as in coronary applications. This could have important applications for subtraction imaging of the coronary arteries in the near future.

Keywords: x-ray angiography, dual energy imaging, energy-resolved imaging, photon counting detectors, x-ray image quality, x-ray detector performance

CO-AUTHORSHIP

The following thesis contains material from manuscripts either published or submitted for publication. Permission to reproduce manuscripts published in Medical Physics (American Institute of Physics) is included in Appendix G.

Chapter 2 has been published in Medical Physics as “A theoretical comparison of angiographic image quality using energy-dependent and conventional subtraction approaches,” by J. Tanguay, H. K. Kim, and I. A. Cunningham. I was responsible for study concept, mathematical developments, data simulation, data analysis and interpretation, and manuscript preparation, all of which was performed under the supervision of I.A. Cunningham. All of the co-authors edited the manuscript.

Chapter 3 has been published in Medical Physics as “The detective quantum efficiency of photon-counting x-ray detectors using cascaded-systems analyses,” by J. Tanguay, S. Yun, H. K. Kim, and I. A. Cunningham. I was responsible for study concept, mathematical developments, data simulation, data analysis and interpretation, and preparation of the manuscript, all under the supervision of I. A. Cunningham. All of the co-authors assisted in editing the manuscript.

Chapter 4 will be submitted for publication to Medical Physics as “Energy precision and detective quantum efficiency of photon-counting x-ray detectors using a cascaded-systems approach: Large elements with x-ray reabsorption,” by J. Tanguay, S. Yun, H. K. Kim, and I. A. Cunningham. I was responsible for mathematical developments, data simulation, data analysis and interpretation, and manuscript preparation, all of which was performed under the supervision of I. A. Cunningham. All of the co-authors participated in editing the manuscript.

Chapter 5 will be submitted for publication to Medical Physics as “Cascaded-systems analysis of angiographic image quality obtained using energy-dependent and conventional subtraction approaches,” by J. Tanguay, S. Yun, H. K. Kim, and I. A. Cunningham. I was responsible for mathematical developments, data simulation, data analysis and interpretation, and manuscript preparation, all of which was performed under the supervision of I. A. Cunningham.

Appendix E has been published in Medical Physics as “The role of x-ray Swank factor in energy-resolving photon-counting imaging,” by J. Tanguay, H. K. Kim, and I. A. Cunningham. I was responsible for study concept, mathematical development, data analysis and interpretation, and preparation of the manuscript, all under the supervision of I. A. Cunningham. Dr. H. K. Kim was responsible for data simulation and all of the co-authors assisted in editing the manuscript.

ACKNOWLEDGMENTS

I would first like to acknowledge my supervisor Dr. Ian Cunningham who patiently instilled in me skills required to be a critical and forward-thinking scientist/researcher. I thank him for providing freedom and support to explore my own ideas while at the same time challenging me to always stay focused on research problems at hand. Dr. Cunningham's continued enthusiasm for asking and answering important scientific questions in the field of medical imaging is inspiring and has made my graduate studies an enjoyable and rewarding experience.

My advisory committee, Dr. Ting Lee, Dr. Maria Drangova, and Dr. James White, provided invaluable advice and insight during my committee meetings. I thank them for their time and for providing alternative perspectives on the important scientific questions that should be addressed in my thesis.

I would like to thank the administrative support of Wendy Hough from the Department of Medical Biophysics, and Jan Challice from the Imaging Laboratories at Robarts Research Institute. Wendy provided invaluable guidance regarding submission procedures for graduate scholarship applications and Jan was especially helpful when booking flights and hotels for conferences, and determining how many alcoholic beverages I was allowed to claim on an expense report, which, more often than not, was zero.

I would like to acknowledge the Cunningham group's laboratory assistant Mike McDonald. Mike was very helpful in the design of experimental methods and tools and, during our lab meetings, always provided valuable insight on my research. I would also like to acknowledge the scientific discussions I have had with PhD candidate Christiane Burton, the most recent addition to Dr. Cunningham's research team who will be further developing some of the ideas presented in this thesis.

The research presented in this thesis would be impossible without financial support. I wish to acknowledge the financial support of the Natural Sciences and Engineering Research Council of Canada (Grant No. 386330-2010), the Canadian Institute of Health Research, the NSERC Canadian Graduate Scholarship program (CGS-D3-409690-2011), and the Ontario Graduate Scholarship Program.

While graduate studies in the field of science is a time to develop skills required to ask and answer important scientific questions, it is also a time to develop new friendships both within and outside the research lab. I would like to thank the following people (in no particular order) for providing an intoxicatingly good time outside of the lab: Kathleen Lynch, Roy Haldenby, Jon Lavers, Denis

Lenane, Jeremy Cepek, Travis Down, Ken Gray, Matt Nemeth, Steve Cable, Tom “Cool Guy” Hrinivich, Nate Hayward, Damien Pike, and Jon Snir.

Finally, I would like to thank the two most important women in my life, my mother and Dr. Miranda Kirby, for teaching me that with enough ambition, passion, and hard work, it is possible to achieve goals that can initially seem overwhelming; my sisters Stevie and Bailey for their endless supply of love and support; and my fathers Rob and Steve for teaching me the value of hard work. Your love and support has been invaluable and will not be forgotten.

Contents

ABSTRACT	ii
CO-AUTHORSHIP	iii
ACKNOWLEDGMENTS	iv
CONTENTS	vi
LIST OF TABLES	xiii
LIST OF FIGURES	xiv
LIST OF SYMBOLS	xxii
1 Burden of coronary artery disease, limitations of conventional angiographic approaches, and research problem	1
1.1 Burden of coronary artery disease	1
1.2 Role of x-ray angiography in diagnosis and assessment of coronary artery disease . .	3
1.2.1 Stable angina	3
1.2.2 Unstable angina and myocardial infarction	4
1.3 Conventional coronary angiography	4
1.3.1 Visualizing arteries requires contrast-enhancing agents	5
1.3.2 Contrast-material injection requires cardiac catheterization	6
1.3.3 The need for subtraction approaches	7
1.4 Digital subtraction angiography	8
1.4.1 Increased contrast-sensitivity compared to non-subtraction angiography . . .	9
1.4.2 Motion compromises DSA studies of coronary arteries	11
1.5 Energy-dependent angiography	11

1.5.1	Energy-subtraction angiography (ESA)	12
1.5.1.1	K-edge subtraction angiography	12
	Limitations of early K-edge subtraction approaches	12
1.5.1.2	Triple-energy approaches	14
	Limitations of early triple-energy approaches.	15
1.5.1.3	Dual-energy approaches	15
	Limitations of early dual-energy approaches.	16
1.5.1.4	Current state of energy-subtraction angiography	16
1.5.2	Energy-resolved angiography	17
1.5.2.1	State-of-the-art energy-resolving photon-counting x-ray detectors . .	17
1.5.2.2	Potential advantages of energy-resolved angiography	18
1.6	Research problem	19
1.7	Research goal	19
1.8	Research objectives	20
1.9	Thesis outline	20
	Chapter 2: A theoretical comparison of x-ray angiographic image quality obtained with energy-dependent and conventional subtraction methods	20
	Chapter 3: Fundamental signal and noise limits of photon counting x-ray detectors .	21
	Chapter 4: Modeling signal and noise propagation in energy-resolving photon-counting x-ray detectors	22
	Chapter 5: Cascaded-systems analysis of angiographic image quality obtained using energy-dependent and conventional subtraction approaches	23
2	A theoretical comparison of x-ray angiographic image quality obtained with energy-dependent and conventional subtraction methods	24
2.1	Introduction	24
2.2	Theory	26
2.2.1	Angiographic image signal	27
2.2.2	Angiographic image noise	29
	2.2.2.1 General case: Cross-correlated measurements	30
	2.2.2.2 Special case: Independent measurements	31
2.2.3	Iodine Detectability	31
2.3	Methods and materials	31

2.3.1	Theoretical comparison of energy-resolved, energy-subtraction and digital-subtraction angiography	31
2.3.1.1	Digital subtraction angiography, DSA	32
2.3.1.2	Energy-subtraction angiography, ESA	32
2.3.1.3	Energy-resolved angiography, ERA	33
2.3.2	Monte Carlo Validation	33
2.3.3	Visual comparison of ESA with DSA	34
2.4	Results	35
2.4.1	Dependence on imaging parameters	35
2.4.1.1	Exposure technique	35
2.4.1.2	Taylor-expansion point	36
2.4.1.3	Iodine concentration	37
2.4.1.4	Water thickness	37
2.4.2	Background suppression	39
2.4.3	Visual comparison of ESA with DSA	40
2.5	Discussion	40
2.6	Conclusions	41
3	Fundamental signal and noise limits of photon counting x-ray detectors	42
3.1	Introduction	42
3.2	Theory	44
3.2.1	Signal and noise in SPC detectors	44
3.2.1.1	Incident x-ray quanta, \tilde{q}_o	45
3.2.1.2	Conversion to secondary image-forming quanta, \tilde{q}_{sec}	45
3.2.1.3	Collection of secondary quanta by sensor elements	45
3.2.1.4	Detector-element signals, \tilde{d}^\dagger	46
3.2.1.5	Thresholded signal, \tilde{s}^\dagger	46
3.2.1.6	Mean SPC signal, \bar{c}	47
3.2.1.7	SPC autocovariance and Wiener noise power spectrum:	48
3.2.2	Special Case: Low count rates and no charge sharing	50
3.2.2.1	Mean signal, \bar{c}	50
3.2.2.2	Wiener noise power spectrum	50
3.2.3	PDF transfer through elementary processes	51

3.2.3.1	Quantum selection	52
3.2.3.2	Quantum gain	52
3.2.3.3	Quantum relocation	53
3.2.4	Application to simple SPC detector model	54
3.2.4.1	Mean signal, \bar{c}	56
3.2.4.2	Noise power spectrum and individual element noise	57
3.2.4.3	Photon-counting $DQE(0)$	57
3.3	Monte Carlo Validation	58
3.4	Results	58
3.4.1	Optimal threshold t	58
3.4.2	DQE(0) dependence on additive noise, collection efficiency, and mean gain	62
3.5	Discussion	62
3.6	Conclusions	63
4	Modeling signal and noise transfer in photon-counting and energy-resolving photon-counting x-ray detectors	64
4.1	Introduction	64
4.2	Theory	66
4.2.1	SPC noise factor and energy response function	66
4.2.2	EPC energy imprecision and energy response function	67
4.2.3	Determining the energy response function from the PDF of image quanta	67
4.2.3.1	PDF of image quanta following a cascade of quantum processes	67
4.2.3.2	PDF of image quanta from parallel cascades	69
4.2.4	Liberation of secondary quanta in x-ray convertor	74
4.2.4.1	Generalized interaction process	75
4.2.4.2	Photoelectric interactions	79
4.2.4.3	Incoherent interactions	80
4.2.4.4	PDF of detector element signal \tilde{d}	81
4.2.5	Mean number of photon counts	81
4.3	Results	82
4.3.1	PDF of detector element signals, $p_d(d E)$	82
4.3.2	Relative energy imprecision of EPC detectors	83
4.3.3	Optimal SPC threshold	84

4.3.4	Zero-frequency DQE of SPC detectors	85
4.4	Discussion and Conclusions	85
5	Cascaded-systems analysis of angiographic image quality obtained using energy-	
	dependent and conventional subtraction approaches	88
5.1	Introduction	88
5.2	Theory	90
5.2.1	Angiographic image signal	90
5.2.2	Angiographic image noise	91
5.2.2.1	Energy-integrating systems	91
5.2.2.2	Energy-resolving systems	92
5.2.3	Cascaded model of mean gain, variance, and PDF of \tilde{d}	93
5.2.3.1	Mean gain	93
5.2.3.2	Energy-integrating pixel variance	95
5.2.3.3	PDF of prethresholding detector element signals	97
5.2.4	Iodine Detectability	98
5.3	Methods	98
5.3.1	Monte Carlo simulation of upper-limit of side-escape fraction	98
5.3.2	Theoretical comparison of angiographic image quality	99
5.3.2.1	Energy-resolved angiography, ERA	101
5.3.2.2	Digital subtraction angiography, DSA	101
5.3.2.3	Energy subtraction angiography, ESA	102
5.4	Results	102
5.4.1	Performance characteristics of CdZnTe detectors	102
5.4.1.1	Mean gain and zero-frequency NPS of collected secondaries	102
5.4.1.2	Fraction of fluorescent x rays reabsorbed in neighboring elements	102
5.4.1.3	Response function	103
5.4.2	Comparison of iodine SNR obtained with ERA, ESA, and DSA assuming CdZnTe x-ray detectors for each	104
5.4.2.1	Influence of depth-dependent collection efficiency	104
5.4.2.2	Dependence on exposure and electronic noise levels	105
5.5	Discussion	107
5.6	Conclusions	108

6	Conclusions	110
7	Future work I: Comparison of energy-dependent angiography with conventional non-subtraction angiography	113
7.1	Introduction	113
7.2	Theoretical framework for comparing subtraction and non-subtraction angiography	115
7.2.1	Modeling anatomic fluctuations	115
7.2.2	Angiographic image signal	116
7.2.2.1	Non-subtraction angiography	116
7.2.2.2	Subtraction angiography	117
7.2.3	Image noise power spectrum including both quantum and anatomic fluctuations	118
7.2.3.1	Non-subtraction angiography	119
7.2.3.2	Subtraction angiography	121
7.2.4	Task-based iodine detectability	122
7.3	Monte Carlo simulation of quantum and anatomic noise	123
7.3.1	Simulating variations in soft-tissue density	123
7.3.2	Imaging simulation	123
7.4	Preliminary results: Soft-tissue suppression capabilities of energy-dependent angiography	123
7.4.1	Dependence on magnitude of soft-tissue variability	124
7.4.2	Dependence of iodine detectability on exposure level	126
7.5	Discussion of preliminary comparisons	127
8	Future work II: Theoretical analysis of charge sharing in photon-counting x-ray detectors using a cascaded-systems approach	129
8.1	Introduction	129
8.2	Cascaded-systems analysis of charge sharing in photon-counting detectors	130
8.2.1	PDF of the number of image quanta collected in detector elements	131
8.2.2	Mean signal	132
8.2.3	Spatial resolution of photon-counting systems	133
8.2.3.1	Photon-counting point spread function	133
8.2.3.2	Photon-counting modulation transfer function	134
8.3	Methods and Materials	135

8.3.1	Theoretical comparison of charge sharing effects in SPC and energy-integrating x-ray detectors	135
8.3.2	Monte Carlo validation	135
8.4	Preliminary results	135
8.4.1	Influence of charge sharing on recorded count rates	135
8.4.2	Influence of charge sharing on spatial resolution	136
8.4.3	Optimal SPC threshold	138
8.5	Discussion of preliminary results	138
A	Supplemental material for Chapter 2	139
A.1	Linearization of the log signals	139
A.2	Log-signal covariance	140
B	Supplemental material for Chapter 3	141
B.1	PDF of readout signal, $p_d(d(\mathbf{r}))$	141
B.2	Joint PDF of readout signal, $p_d(d(\mathbf{r}), d(\mathbf{r} + \boldsymbol{\tau}))$	143
B.3	Presampling NPS of SPC image $\tilde{c}(\mathbf{r})$	146
B.4	Calculation of $\xi_T(t)$ and $\xi_F(t)$	147
C	Supplemental material for Chapter 4	148
C.1	Joint PDF of parallel processes	148
C.1.1	Joint PDF and branch points	148
C.1.1.1	Joint PDF of parallel cascades	149
C.1.1.2	Joint PDF of quantum-labelled parallel cascades	151
C.2	PDF of number of quanta for a generalized interaction model	152
C.2.1	PDF of \tilde{N}_A	153
C.2.1.1	Conversion to secondary quanta	153
C.2.1.2	Depth-dependent collection of secondary quanta	154
C.2.2	PDF of $\tilde{N}_B + \tilde{N}_C$	154
C.2.2.1	PDF of \tilde{N}_B for fixed \tilde{z}_1 and $\tilde{\theta}$	155
C.2.2.2	PDF of \tilde{N}_C for fixed \tilde{z}_1 and $\tilde{\theta}$	156
C.2.2.3	PDF of $\tilde{N}_B + \tilde{N}_C$	158
C.2.3	PDF of $\tilde{N}_t = \tilde{N}_A + \tilde{N}_B + \tilde{N}_C$	158
C.3	PDF of reabsorption depth \tilde{z}_2	158

D Supplemental material for Chapter 5	160
D.1 Energy-binned image signal for energy-resolving photon-counting x-ray detectors . . .	160
D.2 Mean energy-binned signals	161
D.3 Covariance bewteen EPC energy bins	162
E Monte Carlo simulation of fundamental energy-resolution limits in energy-resolving photon-counting x-ray detectors	164
E.1 Introduction	164
E.2 Theory: Energy imprecision of EPC x-ray detectors	166
E.3 Application to Common Detector Materials	168
E.4 Results	169
E.4.1 Relative energy accuracy	170
E.4.2 Swank factor and relative energy imprecision	172
E.5 Discussion	172
E.6 Conclusions	174
F Bibliography	175
G Permission to reproduce copyrighted material	198
G.1 Permission to reproduce figures 1.3, 1.4, 1.5b, 1.6, 1.7, and 1.8	199
G.2 Permission to reproduce Chapters 2, 3, and Appendix E	217
Curriculum Vitae	219

List of Tables

2.1	Exposure parameters used for the Monte Carlo study.	33
2.2	Exposure parameters used for the experimental study.	34
4.1	Physical and electrical properties including mass density, electron and hole mobility-lifetime products, effective ionization energy, K-fluorescent energy, K-shell participation fraction, and K-fluorescence yield for <i>a</i> -Se. Mobility-lifetime products for Se are taken from Ref. 94 and effective ionization energies are taken from Ref. 157.	79
4.2	Random variables and PDFs defining the type of x-ray interaction used in the generic model shown in Fig. 4.2.5.	79
5.1	Mean gain values for photoelectric and incoherent interactions. The variables E_K and E' represent fluorescent and Compton-scatter photon energy, respectively.	93
5.2	Physical and electrical properties used for CdZnTe calculations. Atomic number, mass density, fractional atom No, fractional atomic weight, Average K-fluorescent energy [keV], K-shell participation fraction, and K-fluorescence yield are take from Ref. 106. Electron and hole mobility-lifetime products are taken from Ref. 158.	98
E.1	Material properties used for the Monte Carlo calculations.	169

List of Figures

1.1.1 Percentage of hospitalizations due to all diagnoses (left) and due to cardiovascular diseases (right). (Data taken from Ref. 14.)	2
1.3.1 A plot of the linear attenuation coefficients of bone, water, and calcium carbonate. Also plotted is the mass attenuation coefficient of iodine, the most commonly used contrast material for x-ray angiography.	6
1.3.2 An x-ray angiogram of an amputated hand acquired in 1896 using a contrast agent composed primarily of calcium carbonate. (Image taken from Ref. 3. Permission to reproduce is in Appendix G.)	6
1.3.3 A frame from the first coronary angiogram acquired in 1958 using selective injection of iodine-based contrast agents into the coronary arteries. (Image taken from Ref. 40. Permission to reproduce is in Appendix G.)	7
1.3.4 a) An illustration of a conventional coronary angiography procedure showing a catheter extending from the femoral artery to the heart by way of the aorta and x-ray projection onto a two-dimensional x-ray detector. b) A coronary angiogram acquired in 2011 showing luminal narrowing of the left anterior descending artery (arrow). (Image taken from Ref. 160. Permission to reproduce is in Appendix G.)	8
1.4.1 An example of mask (a), contrasted (b), and subtracted (c) images from a DSA examination of the popliteal artery acquired using intra-arterial injection of an iodine-based contrast material. Non-iodinated structures are removed from the subtracted image. (Image taken from Ref. 23. Permission to reproduce is in Appendix G.)	9
1.4.2 An example of motion artifacts encountered in cerebral angiography. Improper registration of the mask image (a) and contrasted image (b) results in motion artifacts in the subtracted image (c). Motion artifacts appear as streaks at the edges of high-contrast structures. (Image taken from Ref. 23. Permission to reproduce is in Appendix G.)	10

1.4.3 An example of mask (a), contrasted (b), and subtracted (c) images from a DSA examination of the left coronary arteries. Attempt to subtract mask and contrasted images results in severe motion artifacts. (Image taken from Ref. 23. Permission to reproduce is in Appendix G.)	10
1.5.1 Examples of x-ray spectra used in early K-edge subtraction (top), triple-energy subtraction, and dual-energy subtraction (bottom) studies, respectively.	13
2.2.1 Schematic showing x-ray paths through iodinated and background regions of a patient for the incident spectrum $\bar{q}_0(E)$	27
2.2.2 Plots of the mass-attenuation coefficients for potential basis materials for angiographic applications.	27
2.4.1 Dependence of iodine SNR on exposure parameters. The top row illustrates the dependence of DSA and ERA on the applied tube voltage. The bottom row illustrates the dependence of ESA on both the high-energy applied tube voltage and the low-to-high-energy mAs ratio.	35
2.4.2 X-ray spectra for DSA, ERA, and ESA. The pre-injection DSA spectrum has been transmitted through 20 cm of water and all post-injection spectra have been transmitted through 20 cm of water and 40 mg cm ⁻² of iodine. The total entrance exposure for each spectral combination is 40 mR.	36
2.4.3 Dependence of iodine signal (left) and performance index P _I (right) on the Taylor-expansion point $\mathbf{A}_0 = [A_{I0}, A_{W0}]$ for 20 cm of water and iodine area densities of 20 mg cm ⁻² and 50 mg cm ⁻² . For each technique we have expanded about zero iodine area density, ie. $A_{I0} = 0$	37
2.4.4 Simulated iodine-specific images of various iodine concentrations in 20 cm of water generated by Monte Carlo calculations.	38
2.4.5 Illustration of iodine signal and P _I for 20 cm of water and various iodine concentrations. Solid lines represent theoretical calculations and symbols represent Monte Carlo calculations.	38
2.4.6 Illustration of the dependence of iodine signal and P _I on water thickness for 20 g cm ⁻² of iodine. Solid lines represent theoretical calculations and symbols represent Monte Carlo calculations.	38

2.4.7 Comparison of simulated iodine-specific images containing 20 cm of water with two horizontal vessels having diameters of 0.2 and 0.5 cm filled with 0.1 g cm ⁻³ of iodine and two circular vessels with diameters of 0.2 and 0.5 cm. A 2-cm thick layer of water is overlaid on the right half of the image to provide background contrast.	39
2.4.8 Visual comparison of ESA with DSA using a vascular phantom consisting of two tubes of variable inner diameter (steps of 0.15, 0.4 and 0.8 cm) containing 0.1 g cm ⁻³ of iodine in 20 cm of water. An extra 2.5 cm of PMMA was placed over the left tube to provide background (non-iodinated) contrast. a) Iodinated image (63 kV, 9 mR). b) DSA image (63 kV, 18 mR). c) ESA image (50/130 kV, 15 mR).	40
3.2.1 One-dimensional schematic representation of the process of converting a distribution of incident x-ray quanta (\tilde{q}_o) to secondary quanta such as liberated charges in a photoconductor (\tilde{q}_{sec}) incident on the sensors, to the detector presampling signal \tilde{d} , and then to the thresholded signal \tilde{s}^\dagger from one detector readout. The superscript \dagger indicates a function consisting of a uniform sequence of delta functions scaled by discrete detector values and superscript j has been omitted for simplicity.	44
3.2.2 Schematic illustration of transfer of the PDF describing the total number of image quanta through a quantum selection stage. The PDF for \tilde{N}_{out} is shifted to the left relative of that for \tilde{N}_{in} and approaches a Poisson distribution for small α	52
3.2.3 Schematic illustration of PDF transfer through a quantum gain stage. The PDF for \tilde{N}_{out} is shifted to the right relative to that for \tilde{N}_{in} and the shape of $p_{out}(N_{out})$ depends in part on the PDF describing \tilde{g}	53
3.2.4 Schematic illustration of PDF transfer through a quantum relocation stage where the PDFs for \tilde{N}_{out} and \tilde{N}_{in} are always the same.	53
3.2.5 Schematic representation of the CSA model used to describe transfer of signal, noise and PDF of image quanta through an SPC x-ray detector. Letters a) to e) correspond to labels in Fig. 3.2.1. Figures in bottom row represent PDFs at output of each stage.	54
3.3.1 Graphical illustration of the dependence of normalized pixel value \bar{c}_o (counts per incident photon) on threshold t for selected values of $\beta\gamma\bar{g}$, σ_e , and $\lambda = \bar{q}_o a_t a$. The detector quantum efficiency has been set to unity for all calculations. Lines and symbols represent theoretical and MC calculations, respectively.	59

3.3.2 Graphical illustration of the dependence of σ_c^2 normalized by $\bar{q}_o a$ (number of incident quanta) on threshold t for selected values of $\beta\gamma\bar{g}$, σ_e , and $\lambda = \bar{q}_o a_t a$. The detector quantum efficiency has been set to unity for all calculations. Lines and symbols represent theoretical and MC calculations, respectively.	60
3.3.3 Graphical illustration of the PDF of \tilde{d} for $\beta\gamma\bar{g} = 10^3$, $\lambda = \bar{q}_o a_t a = 1/8$ and various values of σ_e	61
3.3.4 DQE(0) as a function of coupling and collection efficiency $\beta\gamma$ for selected values of σ_e/\bar{g} . The detector quantum efficiency has been set to unity for all calculations. Lines and symbols represent theoretical and MC calculations, respectively.	61
4.2.1 Schematic representation of PDF transfer (describing total number of image quanta) through a cascade of quantum gain or loss processes. Each PDF consists of a series of δ -functions describing the probability of integer-only number of quanta.	68
4.2.2 Schematic representation PDF transfer where \tilde{N}_o is separated into two different cascaded (A and B) and then combined.	69
4.2.3 Schematic representation of PDF transfer through parallel cascades of quantum gain and loss processes. $\tilde{N}_{A,0}$ and $\tilde{N}_{B,0}$ represent the number of quanta in each subset of the input process.	70
4.2.4 Schematic illustration of the CSA model describing PDF transfer of the total number of secondary quanta through photoelectric and incoherent interactions using parallel cascades. The RV \tilde{N}_o is the total number of incident x-ray quanta in one readout and is chosen to be unity. The RVs \tilde{N}_{pe} and \tilde{N}_{inc} describe the total number of secondary quanta collected from photoelectric and incoherent interactions.	74
4.2.5 Schematic illustration of the interaction model used in this work showing: (a) an incident x-ray photon interacting in the x-ray convertor and subsequent production of a scatter photon at polar θ and azimuthal angle ϕ ; and (b) CSA model. The three paths in (b) represent events that liberate charges from: (path A) primary interaction site when no scatter/emission photon is generated; (path B) primary interaction site when a scatter/emission photon is generated; and (path C) remote reabsorption of scatter/emission photon.	76
4.2.6 Collection efficiency β as a function of interaction depth z for a Se x-ray convertor material with material properties listed in Tab. 4.1.	77

4.3.1	Probability density functions of the total number of quanta collected by detector elements for 20-keV (left) and 80-keV (right) photons incident on Se-based convertor materials for selected thicknesses and applied electric fields.	82
4.3.2	Graphical illustration of the dependence of relative imprecision σ_{rel} on incident photon energy for selected convertor thicknesses, applied electric fields, and additive noise levels.	83
4.3.3	Illustration of the dependence of normalized SPC pixel value \bar{c}_o (counts per incident photon) on threshold t for selected convertor thicknesses, incident photon energies, and applied electric fields. Curves are calculated for $\sigma_e = 100$ e-h pairs and $\lambda = 1/10$.	84
4.3.4	Illustration of the dependence of DQE(0) on incident photon energy for selected convertor thicknesses, applied electric fields, and additive noise levels. The gray curve indicates the quantum efficiency.	85
5.2.1	Schematic illustration of the CSA model used to describe energy deposition and conversion to secondaries in CdZnTe detectors. Transfer of the mean, NPS, and PDF of the number of quanta through each path is described using the generic interaction model described in Chapter 5.	95
5.3.1	Schematic illustration of the Monte Carlo simulation used to determine the upper limit of the fraction of x-ray interactions that result in lateral escape of characteristic photons from an adaptively-binned CdZnTe element. A) Illustration of emission of characteristic x ray at a polar angle of $\pi/2$ radians. B) Illustration of reabsorption of a Cd characteristic x ray. C) Illustration of reabsorption of a Te characteristic x-ray and subsequent production of a Cd characteristic x ray. D) Flow-chart representation of the Monte Carlo simulation.	100
5.4.1	Dependence of mean gain $G(E)$ and normalized zero-frequency NPS of secondaries $\bar{q}_o \text{NPS}(0,0) / \bar{q}_{\text{sec}}^2$ on incident photon energy.	103
5.4.2	Upper limit of the fraction of interactions that result in lateral escape of characteristic photons from an adaptively-binned element. All values were obtained using the Monte Carlo simulation illustrated in Fig. 5.3.1 with material properties listed in Tab. 5.2. .	104
5.4.3	Dependent of mean number of photons incident per element per readout λ on element width for selected detector exposure levels. Numbers are calculated assuming a total exposure time of 1/30 sec and readout time of 100 ns and a 100 kV spectrum transmitted through 30 cm of water.	104

5.4.4	Probability density functions of prethresholding detector element signals for 50 keV photons incident on a 0.5-mm thick CdZnTe-based x-ray detector for selected applied electric fields and additive noise levels.	105
5.4.5	Dependence of SNR_1/\sqrt{X} on iodine density [mg cm^{-2}] for 30 cm of water and selected additive noise levels, exposure levels, and applied electric fields. Exposure levels indicated are those at the x-ray detector.	106
6.0.1	A plot of the applied tube power required to generate ESA images at angiographic exposure levels (~ 0.5 mR at the detector) as a function of total exposure time. Calculations are based on the imaging geometry, exposure parameters, and patient thickness described in Chapter 5. The horizontal line indicates 80 kW.	111
7.2.1	Examples of anatomic backgrounds simulated using Eq. (7.2.3) for selected values of $\kappa = \bar{K}/A$ and ρ for $\sigma_W = 5$	117
7.4.1	An illustration of the dependence of iodine detectability per unit exposure d/X on object size for subtraction and non-subtraction angiography for uniform background consisting of 30 g cm^{-2} of water. Calculations are based on 0.01 g cm^{-2} of iodine.	124
7.4.2	An illustration of the dependence of iodine detectability per unit exposure d/X on object size for subtraction and non-subtraction angiography for selected levels of background variability σ_W and correlation length ρ . Calculations are based on 0.01 g cm^{-2} of iodine, a mean background level of 30 g cm^{-2} of water, and 20 mR entrance exposure. Also, plotted is the detectability index for non-subtraction angiography at 80 mR entrance exposure.	125
7.4.3	Comparison of simulated images of a large iodinated object (area density of 0.01 g cm^{-2}) in inhomogeneous backgrounds with increasing variability σ_W for conventional non-subtraction angiography, DSA, ESA, and ERA. Images were generated using a total entrance exposure of 20 mR assuming parallel beam x-ray geometry.	126
7.4.4	Comparison of simulated images containing 30 cm of water with background variance $\sigma_W = 1 \text{ g cm}^{-2}$ with vertical vessels having radii of 0.08 – 0.3 mm filled with 0.1 g cm^{-3} of iodine at 20-160 mR entrance exposures.	127
8.2.1	Cascaded model used to describe the influence of charge sharing in photon-counting x-ray detectors.	130

8.2.2	A 1-D schematic illustration of the relationship between PSF (\mathbf{r}) and PSF _{pix} (\mathbf{r}) for Gaussian-distributed secondary quanta with variance σ^2 . The PSF represents the probability density that a secondary quantum is detected at position \mathbf{r} where the pixel PSF represents the probability that a secondary quantum is detected in a pixel centered at \mathbf{r}	132
8.4.1	Plots of normalized SPC pixel value c_o as a function of threshold value (expressed as a fraction of the mean prethesholding signal \bar{d}) for selected charge-sharing levels. All calculations have been performed for $\lambda = 1/8$, $\sigma_e = k\bar{g}/10$, and $\alpha = 1$. Lines and symbols represent theoretical and Monte Carlo calculations, respectively.	136
8.4.2	Plots of the PSF and MTF of photon counting systems for selected thresholds and levels of charge sharing. All calculations have been performed assuming $\sigma_e = k\bar{g}/10$. Lines and symbols represent theoretical and Monte Carlo calculations, respectively. .	137
E.3.1	Detector geometry modeled in the Monte Carlo calculations. The geometry simulates the large-area limit of a detector element. In this case, variability in deposited energy is a result of Compton scatter and characteristic x rays that escape through the top and bottom surfaces.	168
E.4.1	The response functions $R(\varepsilon, E)$ for 0.5-mm thick <i>a</i> -Se, Si, CdZnTe, and HgI ₂ detectors for 100-keV photons incident on the detector center as determined by Monte Carlo show the photo-peak at energy E , escape peaks and a Compton edge ($\alpha = E/m_o c^2$). A non-zero Fano factor would result in broadening of peaks in the response functions.	170
E.4.2	Results of the Monte Carlo simulation. In the left, center and right columns are plots of the accuracy, Swank factor, and relative imprecision, respectively, as a function of incident photon energy for each detector material and thicknesses of 0.2 mm, 0.5 mm, and 1.0 mm.	171
E.5.1	A plot of the relationship between relative imprecision and the Swank factor given by Eq. (E.2.8) and compared with Monte Carlo results for 0.2-mm detector thickness. The multiple data points for each material correspond to the energies evaluated. . .	173

List of Symbols

In the following, overhead $\tilde{\cdot}$ indicates a random variable, superscript \dagger indicates a sampled detector signal consisting of a uniformly spaced distribution of δ -functions scaled by element signals, and RPP indicates a random point process consisting of a spatial distribution of randomly positioned δ -functions in the image plane.

Symbol	Definition
$\mu_b(E)$	Linear-attenuation coefficient of material b and photon energy E .
$\frac{\mu}{\rho^b}(E)$	Mass-attenuation coefficient of material b and photon energy E .
A_b	Area density of material b and photon energy E .
\tilde{M}	Mean pixel value for unsubtracted “raw” images used for subtraction angiography.
\bar{q}_o	Mean number of x-ray quanta per unit area [mm^{-2}].
\tilde{N}_o^j	Total number of x-ray photons incident on detector during j th readout interval.
$\tilde{q}_o^j(\mathbf{r})$	Distribution of δ functions describing positions of x-ray quanta incident on detector during j th readout interval [RPP, mm^{-2}].
\bar{q}_o	Mean fluence of x-ray quanta [$\text{mm}^{-2}\text{s}^{-1}$].
$\tilde{q}_{\text{sec}}^j(\mathbf{r})$	Distribution of secondary image quanta incident on digital sensor during j th readout interval [RPP, mm^{-2}].
$\tilde{d}^j(\mathbf{r})$	Presampling detector signal for j th readout describing signal from hypothetical element centered at any position \mathbf{r} .
\tilde{d}_{nm}^j	Signal for j th readout from detector element at position nm .
$\tilde{e}(\mathbf{r})$	Zero-mean RV describing additive readout noise from hypothetical element at any position \mathbf{r} .
$\tilde{d}^{\dagger j}(\mathbf{r})$	Sampled signals for j th readout from detector as sequence of scaled δ -functions [mm^{-2}].
$\tilde{d} _1$	Element signal given one incident photon.
$\tilde{d} _0$	Element signal given no incident photons.

$\xi_1(t)$	Probability that $\tilde{d} _1$ is greater than threshold t .
$\xi_0(t)$	Probability that $\tilde{d} _0$ is greater than threshold t .
$\tilde{s}^j(\mathbf{r})$	Presampling thresholded signal for j th readout.
\tilde{s}_{nm}^j	Thresholded signal for j th readout from element at position nm .
$\tilde{c}(\mathbf{r})$	Presampling photon-counting image signal.
$\tilde{c}^\dagger(\mathbf{r})$	Sampled photon-counting image signal as scaled δ -functions.
σ_c^2	Pixel variance in photon-counting image.
\bar{c}_o	Mean normalized photon-counting pixel value [counts per incident photon].
σ_o^2	Normalized photon-counting pixel variance.
$R_s^j(\boldsymbol{\tau})$	Autocorrelation of $\tilde{s}^j(\mathbf{r})$.
$R_c(\boldsymbol{\tau})$	Autocorrelation of $\tilde{c}(\mathbf{r})$.
$K_c(\boldsymbol{\tau})$	Autocovariance of $\tilde{c}(\mathbf{r})$.
$K_{c^\dagger}(\boldsymbol{\tau})$	Autocovariance of $\tilde{c}^\dagger(\mathbf{r})$.
Δ_x, Δ_y	Center-to-center detector element spacings in x and y directions [mm].
a_x, a_y	Widths of sensitive region of each element (aperture) in x and y directions [mm].
a	Detector element aperture area $a = a_x a_y$ [mm ²].
\mathbf{r}_{nm}	Location of element nm in image.
$P(X)$	Probability of observing an event X .
$p_x(x)$	Probability density function for RV x .
$p_x(x y)$	Probability density function for RV x given y .
$\text{pr}_x(x)$	Probability mass function for RV x .
$\text{pr}_x(x y)$	Probability mass function for RV x given y .
$p(x, y)$	Joint probability density function of x and y .
u, v	Spatial frequencies in x, y directions [mm ⁻¹].
\mathbf{k}	Two-dimensional frequency vector with components u and v [mm ⁻¹].
\tilde{g}_i	Number of secondary quanta liberated by i th interacting x-ray photon.
α	Detector quantum efficiency equal to probability that x-ray photon incident on converter material liberates secondaries.
γ	Sensor quantum efficiency equal to probability that a secondary coupled to sensor element contributes to element signal.

β Coupling efficiency equal to probability that a liberated secondary is coupled to sensor.

Chapter 1

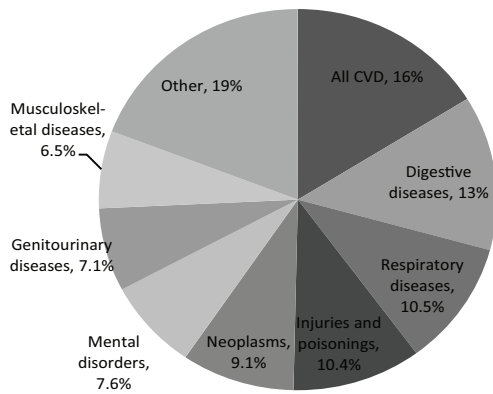
Burden of coronary artery disease, limitations of conventional angiographic approaches, and research problem

1.1 Burden of coronary artery disease

Cardiovascular diseases (CVDs) are leading causes of hospitalization in Canada (Fig. 1.1.1) and, while rates of CVD have been decreasing over the past three decades, the number of hospitalizations continues to increase because of an aging population. ^[14,140] Coronary artery disease (CAD), caused by arterial wall thickening and formation of blood clots on walls of the coronary arteries, is the most common CVD, accounting for approximately 9% of all 2.5-3 million hospitalizations each year (Fig. 1.1.1). ^[140]

Arterial wall thickening, known as atherosclerosis, is the end result of a process that starts with irregular and excessive uptake of lipids, such as cholesterol, by white blood cells in arterial walls. Through a cascade of other processes, including recruitment of more white blood cells into arterial walls where they engulf more lipid to form a lipid pool, migration of smooth muscle cells to the intima of the arterial wall where they combine with connective tissue to form a fibrous cap, an atherosclerotic plaque is formed. ^[65] In some cases the arterial wall calcifies, hardens, and protrudes into the arterial

Percentage of hospitalizations in Canada due to all diagnoses, 2005/06



Percentage of hospitalizations in Canada due to cardiovascular disease, 2005/06

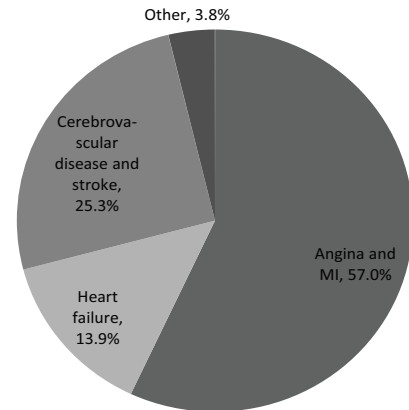


Figure 1.1.1: Percentage of hospitalizations due to all diagnoses (left) and due to cardiovascular diseases (right). (Data taken from Ref. 14.)

lumen resulting in an obstruction of blood flow. Depending on the degree of obstruction, ^[73,74] this may result in a restriction of blood supply to cardiac muscles, known as myocardial ischaemia, most often presented as chest pain, known as angina. Angina may be chronic and stable with chest pain elicited during physical exertion or emotional stress and relieved at rest. ^[2,66,71,82] In contrast, angina symptoms may occur at rest indicating a potentially life-threatening cardiac event. When angina occurs at rest, it is usually the end result of arterial wall damage caused by an unstable atherosclerotic plaque. Arterial wall damage triggers formation of a blood clot, known as a thrombus, that can dislodge and partially block the flow of blood to the myocardium. Depending on the degree and duration of myocardial ischaemia, this may lead to death of cardiac muscles, known as a myocardial infarction. In more severe cases, a coronary artery may be completely occluded leading to an acute myocardial infarction, more commonly known as a heart attack.

Depending on clinical presentation and disease progression, many patients hospitalized for CAD will undergo vascular imaging procedures for visualization of diseased arteries. ^[66,71,140,150] The most common vascular imaging procedure used in diagnosis and assessment of patients suspected of CAD is x-ray angiography. With this approach, a two-dimensional x-ray projection image is acquired following injection of contrast agents directly into one or more coronary arteries, as described in detail in Sec. 1.3.

1.2 Role of x-ray angiography in diagnosis and assessment of coronary artery disease

In most cases, initial diagnoses of stable angina, unstable angina, and myocardial infarction are made on the basis of symptom type and severity, patient history, physical examination, and laboratory investigations, including tests for glucose and cholesterol levels in the case of stable angina, and tests for bio-markers of cardiac cell death in the case of unstable angina and myocardial infarction. The role of x-ray angiography and other cardiac-specific investigations is to confirm diagnosis, assess risk of cardiac death and myocardial infarction, and evaluate treatment options. As described below, these goals are usually accomplished simultaneously using a number of diagnostic and prognostic procedures, with x-ray angiography being particularly important in determining those patients that may benefit from revascularization procedures. ^[66,71,150]

1.2.1 Stable angina

Following an initial clinical investigation, assessment of left-ventricular function using ultrasound approaches is suggested for all patients suspected of stable angina in Canada, the United States, and Europe, ^[66,71,150] for the purpose of ruling out non-CAD causes of chest pain and stratification of patients into low, medium, and high risk of myocardial infarction. ^[42,66] In addition, follow-up myocardial perfusion imaging with single-photon-emission computed tomography may be required for determining the likelihood and extent of myocardial ischaemia. ^[66,71,150] While an initial investigation and non-invasive imaging tests are useful in establishing the presence of CAD, they do not allow for determination of the anatomic location of flow-obstructing atherosclerotic lesions.

Determining lesion location and severity is important for predicting risk of myocardial infarction and, therefore, identifying patients that may benefit from revascularization procedures. ^[42,66,71,150,207] In Canada, the United States, and Europe, with the exception of low-risk groups, the majority of patients suspected of having stable angina will therefore undergo x-ray angiography. ^[66,71,150] For this reason, x-ray angiography has been described as “filter and funnel” for access to revascularization procedures, where *“the decision to perform myocardial revascularization [is] clear only after coronary angiography [has] been performed.”*^[8] This is also true for patients suspected of unstable angina and myocardial infarction.

1.2.2 Unstable angina and myocardial infarction

As described above, unstable angina is characterized by the onset of angina symptoms at rest, most often as a result of myocardial ischaemia caused by partial occlusion of a coronary artery by a thrombus. Patients with unstable angina may be at risk of developing an acute myocardial infarction (heart attack) and require urgent hospitalization for medical treatment and/or assessment of suitability for revascularization procedures.

Conservative approaches to assessment of unstable angina and myocardial infarction use non-invasive diagnostic and prognostic tests, such as those described above, to avoid the risk of dislodging a thrombus during arterial catheterization. The goal of non-invasive procedures is to detect left-ventricular dysfunction and severe ischaemia that occurs spontaneously or at a low stress threshold. Patients with these symptoms are immediately referred to coronary angiography for risk stratification and assessment of suitability of revascularization procedures.^[13] Alternatively, an early invasive approach may be implemented where patients undergo immediate or deferred coronary angiography with the goal of identifying patients without CAD and those with CAD that may benefit from either percutaneous coronary intervention (PCI) or coronary artery bypass grafting (CABG). In a summary of recent meta-analyses, Anderson *et al.*^[13] conclude that, while conservative approaches are associated with lower in-hospital mortality rates, early invasive approaches are associated with lower mortality rates between patient discharge and end of patient follow up. Therefore, while there are risks and benefits associated with conservative and early invasive approaches, similar to stable angina, x-ray coronary angiography acts as “filter and funnel” for access to revascularization procedures for patients suffering from unstable angina or myocardial infarction.

1.3 Conventional coronary angiography

As described above, the goal of conventional coronary angiography is to visualize diseased coronary arteries. Like all x-ray-based medical-imaging procedures, the principle behind angiography is that x rays are differentially attenuated by different tissues in the body.^[151] At diagnostic x-ray energies (10-150 keV), the primary methods of attenuation are photoelectric absorption and Compton scattering. The probability of an absorption or scattering event per unit length is described by the linear attenuation coefficient, often denoted μ , and depends on x-ray energy and material properties of the object, including mass density and atomic number. Spatial differences in object attenuation properties and thickness result in differences in x-ray transmission factors. A conventional angiographic

image is generated from measurements of the intensity of a transmitted x-ray spectrum using x-ray detectors that record the total energy deposited by all photons interacting in each detector element. Spatial variations in deposited energy provide contrast in x-ray images.

Visualization of coronary arteries is complicated by the fact that the linear attenuation coefficient of blood-filled arteries is similar to that of cardiac muscles and other surrounding soft tissues, making it difficult or impossible to distinguish arteries from surrounding anatomy. Coupled with the complicated motion of coronary anatomy, this constitutes a unique imaging challenge that requires x-ray detectors with high spatial and temporal resolution, use of contrast-enhancing agents, and cardiac catheterization.

1.3.1 Visualizing arteries requires contrast-enhancing agents

In the same year that Wilhelm Roentgen^[151] discovered x rays, images showing veins and arteries of cadavers were obtained by acquiring x-ray images after injection of materials with higher atomic number than those of surrounding soft-tissue and bone structures.^[3] Contrast agents used in these studies were composed primarily of calcium carbonate. Figure 1.3.1 is a plot of the mass attenuation coefficients (equal to the linear attenuation coefficient divided by density) of calcium carbonate, water, and bone, and Fig. 1.3.2 is an image showing the vasculature of an amputated hand acquired in 1896 by E. Haschek and O. T. Lindenthal^[80] using a calcium-carbonate contrast agent. While calcium carbonate is useful in visualizing vascular beds of cadavers, it is not suitable for living humans.

The decades following publication of Haschek and Lindenthal's image (Fig. 1.3.2) saw the introduction of iodine-based contrast agents.^[3] Iodine-based contrast agents are well suited for angiography because of distinct differences between the mass attenuation coefficient of iodine and soft-tissue and bone structures, shown in Fig. 1.3.1. Angiographic images showing passage of an iodine-based contrast agent from the antecubital vein (a vein in the upper arm) to the pulmonary vessels were published by J.A. Sicard and G. Forestier^[179] in 1923. While risks associated with early ionic contrast materials have been greatly reduced with modern non-ionic contrast materials, high doses of iodine-based contrast materials may impair kidney and left ventricular function.^[63,84,85,119,120] Despite this, iodine-based materials remain the most commonly used contrast agents in x-ray angiography.

Development of iodine-based contrast agents enabled angiographic studies of peripheral vascular beds but visualization of coronary arteries remained elusive until the development of sophisticated cardiac catheterization techniques that enabled selective injection of contrast material into coronary

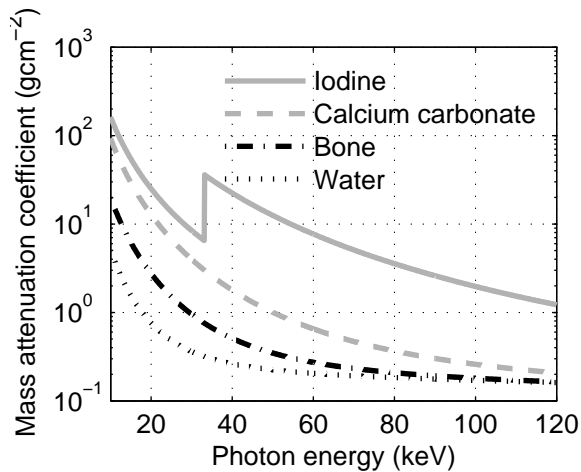


Figure 1.3.1: A plot of the linear attenuation coefficients of bone, water, and calcium carbonate. Also plotted is the mass attenuation coefficient of iodine, the most commonly used contrast material for x-ray angiography.



Figure 1.3.2: An x-ray angiogram of an amputated hand acquired in 1896 using a contrast agent composed primarily of calcium carbonate. (Image taken from Ref. 3. Permission to reproduce is in Appendix G.)

arteries.

1.3.2 Contrast-material injection requires cardiac catheterization

In 1929, Dr. Werner Forssmann^[64] published an x-ray image of a catheter extending from the antecubital vein of his right arm to his right atrium. However, later attempts at contrast-material injection to coronary arteries by way of venous catheterization resulted in insufficient contrast between coronary arteries and surrounding anatomy. Catheterization of the aorta through peripheral arteries was developed in the 1940s and, combined with the development of specially-designed catheters, enabled selective opacification of coronary arteries.^[3,40] In 1958, Sones and Shirey^[183] obtained the first coronary angiogram (Fig. 1.3.3) using selective intra-arterial catheterization. Catheterization techniques have evolved since the early work of Sones and Shirey and there are now a variety of catheters specifically designed for imaging the coronary arteries. Common cardiac catheterization approaches now involve puncturing the femoral artery, inserting a sheath, guiding a catheter through the sheath into the femoral artery, and then guiding the tip of the catheter to a coronary artery by way of the aorta. Figure 1.3.4b is an example of a modern intra-arterial coronary angiogram showing coronary artery stenosis of the left anterior descending artery. Conventional coronary angiography, illustrated in Fig. 1.3.4a, is generally defined as a procedure where an x-ray image of the cardiac anatomy is acquired after selective injection of a contrast agent, usually iodine-based, into one or more coronary

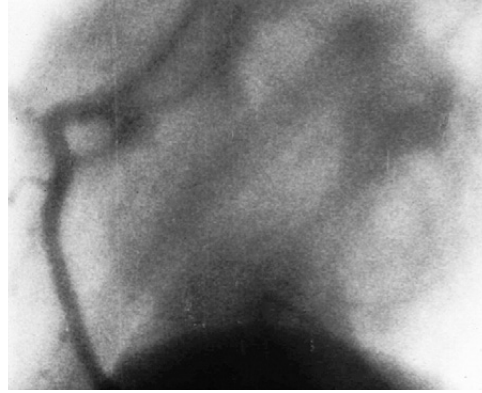


Figure 1.3.3: A frame from the first coronary angiogram acquired in 1958 using selective injection of iodine-based contrast agents into the coronary arteries. (Image taken from Ref. 40. Permission to reproduce is in Appendix G.)

arteries using a specially-designed catheter. While there is risk of dislodging a thrombus during arterial catheterization, overall it is generally accepted that the benefits of intra-arterial angiography outweigh acute risks. Intra-arterial contrast injection enables opacification of coronary arteries but projection of over and under-lying anatomical structures causes image intensity variations that can obscure arterial visualization.

1.3.3 The need for subtraction approaches

Image intensity variation caused by projection of soft-tissue and bone structures (with different densities and thicknesses) onto a two-dimensional image plane is commonly referred to as anatomic noise.^[19,27,162,163] Effects of anatomic noise on disease detection in radiography were recognized as early 1974 by Revesz *et al.*^[147] who showed that increased complexity of anatomic backgrounds in radiographic images results in decreased probability of detecting, for example, lung nodules in thoracic imaging. Samei *et al.*^[163] arrived at a similar conclusion when they showed that projection of the ribs and pulmonary vessels impairs lung-nodule detection using chest radiography. A similar problem is encountered in coronary angiography where coronary arteries, cardiac muscles, lungs, and ribs are superimposed on a two-dimensional image plane. O'hara *et al.*^[141] demonstrated that detection of stenoses in the presence of anatomic noise requires higher contrast between vasculature and surrounding tissues than in the case of a uniform background. Adequate visualization of diseased vasculature with conventional angiography therefore requires high doses of iodine-based contrast material that, when used in excess, can impair kidney and left ventricular function.^[63,84,85,119,120]

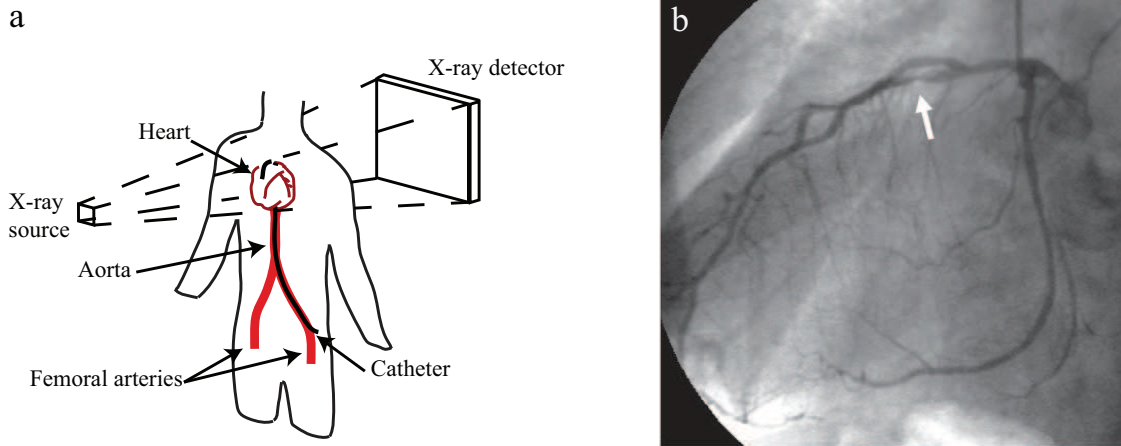


Figure 1.3.4: a) An illustration of a conventional coronary angiography procedure showing a catheter extending from the femoral artery to the heart by way of the aorta and x-ray projection onto a two-dimensional x-ray detector. b) A coronary angiogram acquired in 2011 showing luminal narrowing of the left anterior descending artery (arrow). (Image taken from Ref. 160. Permission to reproduce is in Appendix G.)

Temporal subtraction techniques^[34,35,38,50,51,56,132,133,149] that suppress soft-tissue and bone structures in angiographic images were introduced in the 1970s with the goal of improving visualization of diseased vasculature and reducing contrast-material doses. Because this approach was made possible by the introduction of digital imaging technology, it is most commonly referred to as digital subtraction angiography (DSA).

1.4 Digital subtraction angiography

Digital subtraction angiography requires subtraction of an x-ray image acquired prior to contrast injection, known as a mask image, from a post-injection image.^[96,132,133] Assuming there is no motion between mask and contrasted images, all non-iodinated anatomic features are removed from subtracted images, as illustrated in Fig. 1.4.1. During a DSA procedure it is common to acquire a sequence of both mask and contrasted images and choose the pair that better suppresses non-iodinated structures. When background structures are adequately suppressed, DSA images are free of anatomic noise sources resulting in improved contrast sensitivity.

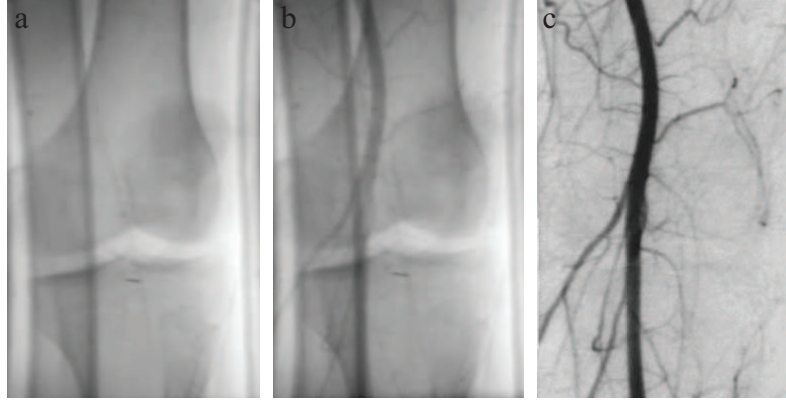


Figure 1.4.1: An example of mask (a), contrasted (b), and subtracted (c) images from a DSA examination of the popliteal artery acquired using intra-arterial injection of an iodine-based contrast material. Non-iodinated structures are removed from the subtracted image. (Image taken from Ref. 23. Permission to reproduce is in Appendix G.)

1.4.1 Increased contrast-sensitivity compared to non-subtraction angiography

Because of its high contrast sensitivity, DSA was initially introduced with the goal of replacing intra-arterial angiography with less-invasive intra-venous approaches.^[32,34,35,37,38,93,96] Early attempts at intra-venous DSA of the coronary arteries included the use of 5-cm long catheters placed in the antecubital vein and 55-cm long catheters placed at the superior vena cava.^[133] However, intra-venous approaches often result in contrast enhancement of non-cardiac vessels, such as the pulmonary vessels, that obscure visualization of coronary anatomy.^[119] In addition, because contrast materials dilute as they travel through the circulatory system, contrast-enhancement levels achieved in early intra-venous DSA studies were 10-20 times lower than intra-arterial injections and only reduced iodine doses by one half.^[96,119,133] Because of this inefficient use of contrast material, DSA procedures are almost always performed using intra-arterial injections. While DSA has not eliminated the need for intra-arterial injections, intra-arterial DSA procedures can be performed using up to 40% less iodine than conventional non-subtraction approaches.^[96]

Digital subtraction angiography is very successful at providing high-contrast images of vasculature that is stationary over a period of several seconds, such as the cerebral arteries, and arteries in the arms and legs (Fig. 1.4.1). However, because of the need to subtract a mask image acquired many seconds before or after contrasted images, DSA procedures are often compromised by motion artifacts.^[37,47,96,119]

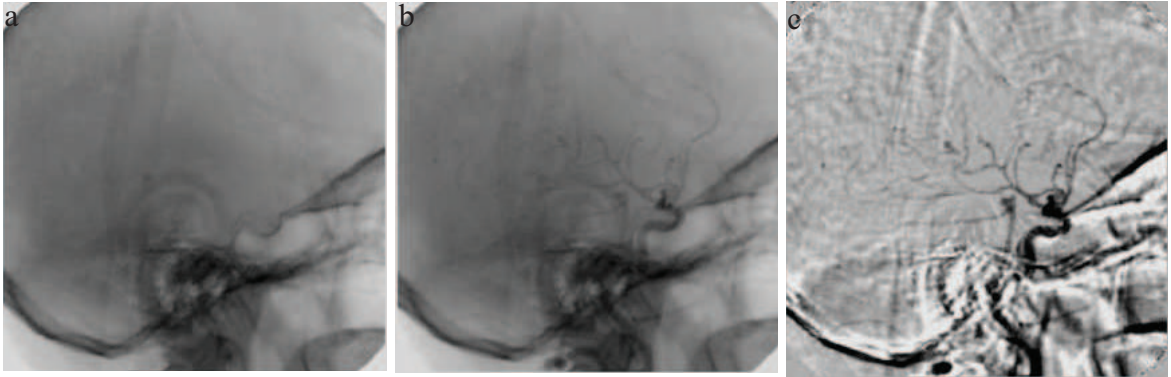


Figure 1.4.2: An example of motion artifacts encountered in cerebral angiography. Improper registration of the mask image (a) and contrasted image (b) results in motion artifacts in the subtracted image (c). Motion artifacts appear as streaks at the edges of high-contrast structures. (Image taken from Ref. 23. Permission to reproduce is in Appendix G.)

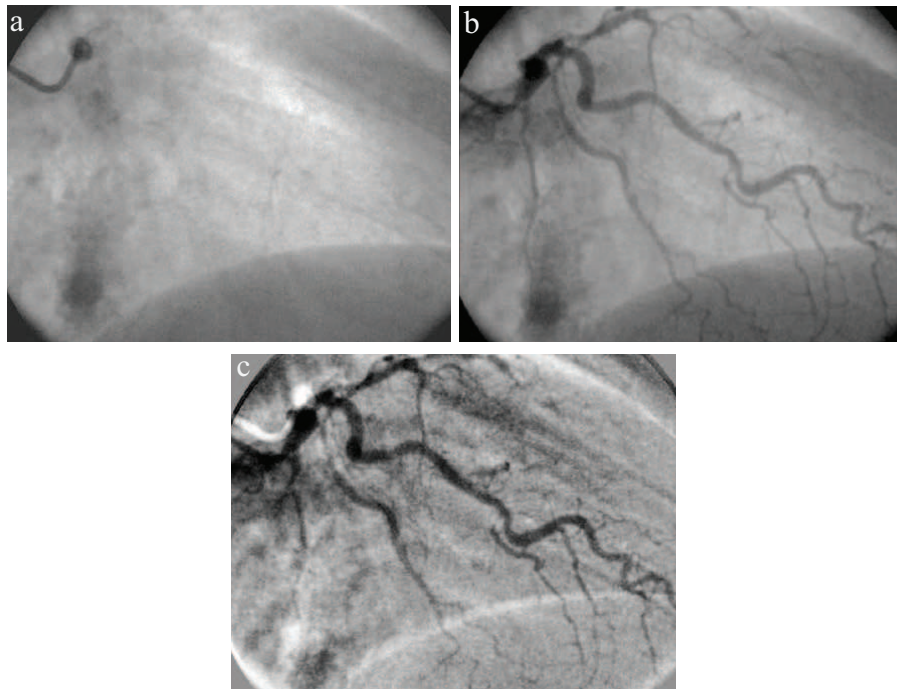


Figure 1.4.3: An example of mask (a), contrasted (b), and subtracted (c) images from a DSA examination of the left coronary arteries. Attempt to subtract mask and contrasted images results in severe motion artifacts. (Image taken from Ref. 23. Permission to reproduce is in Appendix G.)

1.4.2 Motion compromises DSA studies of coronary arteries

Motion artifacts often appear as light and dark streaks at the edges of high contrast structures that are not properly registered in pre and post-injection images, such as in Fig. 1.4.2, and may be produced in a number of different ways. Involuntary motions such as swallowing after injection into the carotid artery and movement of extremities degrade visualization of peripheral arteries, [37,75,188,200] and respiratory and bowel motions degrade DSA studies of the aorta. [32] While there are no large studies on the frequency of motion artifacts, smaller studies by Chilcote *et al.* [47] suggest that *motion artifacts can compromise up to 30% of peripheral DSA procedures.*

Motion artifacts constitute a major problem for coronary imaging. A number of techniques for minimizing motion artifacts in coronary studies were proposed in the 1980s, [95,119,149] most of which involved weighted averages of series of mask and contrasted images, but none adequately removed motion artifacts and therefore never gained widespread use. Post-processing approaches have been helpful for retrospective registration, particularly for simpler motion of peripheral arteries, [23,122,123] but have been unsuccessful in coronary imaging (Fig. 1.4.3). Instead, as described above, high quality images of coronary arteries require relatively high contrast-material doses to ensure that arteries are clearly distinguished over background structures.

Alternative methods of generating iodine-specific images with reduced motion artifacts might exploit the energy-dependence of x-ray attenuation in a patient. This could be performed either by acquiring two or more post-injection images at different x-ray energies or from an analysis of the spectral shape of the transmitted spectrum. We call these methods energy-subtraction angiography (ESA) and energy-resolved angiography (ERA), respectively, and both would eliminate the need for a pre-injection mask image.

1.5 Energy-dependent angiography

Energy-dependent approaches were introduced in the late 1970s as an alternative approach to DSA. Early efforts implemented an ESA approach using subtraction of two or three post-injection images acquired with x-ray spectra having different average energies. [36,39,75,88,149] When images are acquired in rapid succession after contrast-material injection, it is possible to obtain “DSA-like” images that are less susceptible to motion artifacts than DSA.

1.5.1 Energy-subtraction angiography (ESA)

Energy subtraction for enhancement of iodinated vasculature was attempted as early as 1953 by Jacobson^[92] and was further developed in the 1970s and 1980s by researchers at the University of Wisconsin, including Mistretta *et al.*,^[88,130,131] Kelcz *et al.*,^[97,98] and Van Lysel *et al.*^[112,113,115,116] Early ESA researchers used dual-energy methods that exploit the K-edge discontinuity of the iodine attenuation coefficient (Fig. 1.3.1).

1.5.1.1 K-edge subtraction angiography

Because the attenuation coefficients of soft tissue and bone are smoothly varying functions of photon energy, subtraction of two images acquired using energies directly above and below the K-edge energy of iodine (≈ 33 keV) has the potential to suppress soft-tissue and bone structures. Jacobson^[92] isolated characteristic emissions from target materials with absorption edges above and below 33 keV to generate monoenergetic exposures. This approach was revisited by Zhong *et al.*^[222] using emissions from barium and cerium targets and is successful at imaging stationary objects but is not suitable for imaging coronary arteries because of the time required to generate sufficient x-ray exposure levels. Building on the work of Jacobson,^[92] Mistretta *et al.*^[88,130,131] developed a “quasi-monoenergetic” approach using narrow x-ray spectra with average energies above and below 33 keV, such as those illustrated in Fig. 1.5.1. These approaches used a fixed applied tube voltage, usually between 50 and 70 kilovolts (kV), in combination with rapid switching of iodine and cerium filters to generate low and high-energy x-ray spectra, respectively.^[37,88,130] Because low and high-energy images can be acquired within a few milliseconds, this approach is less susceptible to motion artifacts than DSA. In 1979, Houk *et al.*^[88] acquired K-edge-subtraction images of the left and right ventricles of a dog with minimal motion artifacts. However, despite initial enthusiasm, K-edge subtraction approaches are rarely used in modern peripheral or coronary angiography because of a number of practical limitations.

Limitations of early K-edge subtraction studies

Suppression of soft-tissue and bone structures is optimal when using mono-energetic exposures with energies directly above and below 33 keV. In this case, soft tissue and bone can be completely removed from subtracted images. However, generation of mono-energetic x-ray spectra is impracticable in a clinical setting. Quasi-monoenergetic K-edge subtraction is an alternative approach but requires heavy filtration of low-kV x-ray spectra. With this approach, suppression of soft-tissue and

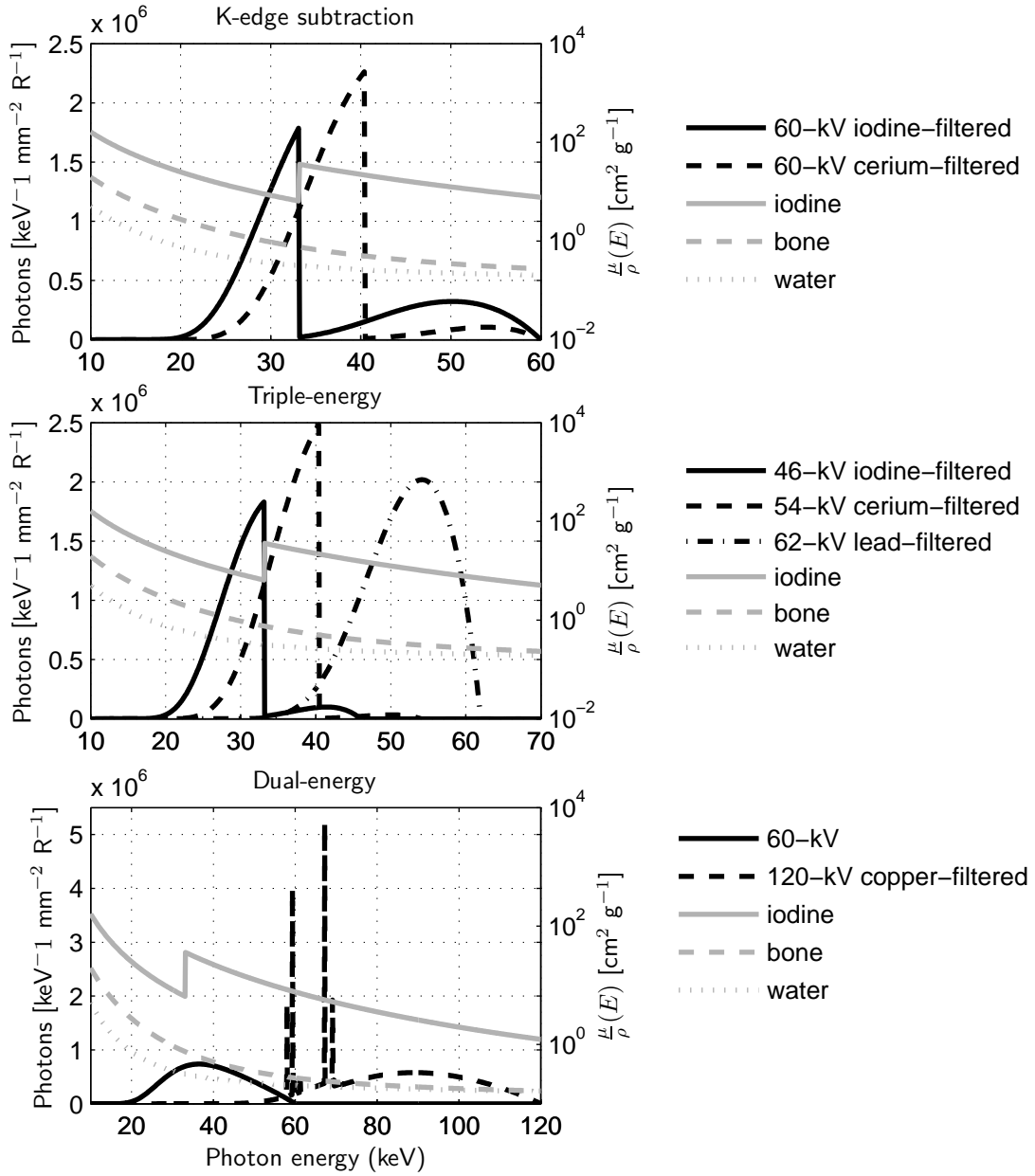


Figure 1.5.1: Examples of x-ray spectra used in early K-edge subtraction (top), triple-energy subtraction, and dual-energy subtraction (bottom) studies, respectively.

bone structures improves with decreasing spectral width.^[130,131] However, because x-ray tubes are limited in the number of photons they can generate per unit time, decreasing spectral width by increasing filter thicknesses comes at the cost of decreased number photons used to generate K-edge-subtracted images. This, coupled with inefficient production of x-rays at low applied tube voltages, often results in a severe reduction in the number of photons incident on the x-ray detector, sometimes as low as 1/60th that of DSA.^[88] Early attempts were therefore limited to imaging peripheral vasculature where the x-ray path is much shorter than in coronary applications. Furthermore, balancing benefits of soft-tissue and bone suppression with detriments of low photon-flux rates requires use of sub-optimal x-ray spectra that result in incomplete tissue suppression and reduced image signal-to-noise ratio (SNR) compared to DSA.^[39,88,97,98,131] To overcome these problems, approaches that better suppress soft-tissue and bone structures were proposed. Because these approaches use three x-ray exposures at different average energies to estimate contributions of soft-tissue, bone, and iodine to the total attenuation of an incident x-ray beam, they are referred to as triple-energy approaches.

1.5.1.2 Triple-energy approaches

As described in Sec. 1.3, x-ray photons in the diagnostic energy range interact primarily through photoelectric absorption and Compton-scattering. Alvarez and Macovski^[11] demonstrated that contributions of photoelectric and Compton interactions to total attenuation can be estimated from two x-ray images acquired at different average energies. With this approach, the linear attenuation coefficient of an object is represented as a sum of photoelectric and Compton attenuation coefficients, called basis functions. Lehman *et al.*^[107] generalized this approach and showed that, because attenuation in soft tissue and bone is uniquely characterized by the relative contributions of photoelectric and Compton scatter, attenuation coefficients of water and bone can also be used as basis functions. Subtracting low and high-energy images therefore enables decomposition of an image into soft-tissue and bone components and is particularly helpful in removing lungs from chest radiographs.^[11,36,208] However, using water and bone basis materials assumes that x rays do not travel through materials with absorption edges in the diagnostic energy range^[11,36,107] and is therefore not suitable for subtraction angiography where the goal is to separate iodinated vasculature from surrounding soft-tissue and bone structures.

Application of basis-material-decomposition approaches to angiography requires including a third basis function equal to the mass attenuation coefficient of iodine.^[97,98,153,165] Complete suppression of soft-tissue and bone variations using a three-material approach requires estimation of the contributions of soft tissue, bone, and iodine to the total attenuation of an incident x-ray beam and

therefore requires three exposures acquired using x-ray spectra with different average energies.^[97,98] Early triple-energy efforts by Kelcz *et al.*^[97,98] used a three-filter, three-kV approach and substantially reduced pixel-intensity variations caused by residual soft-tissue and bone variations. However, like K-edge subtraction approaches, triple-energy approaches are rarely used in coronary angiography.

Limitations of early triple-energy studies Similar to K-edge subtraction angiography, early triple-energy efforts implemented thick filters to produce non-overlapping x-ray spectra. Kelcz *et al.*^[97,98] implemented a three-spectrum approach with 46-kV, 54-kV, and 62-kV x-ray spectra filtered with iodine, cerium, and lead, respectively (Fig. 1.5.1). While this approach suppressed soft-tissue and bone from angiographic images, because of power limitations of x-ray tubes, iodine-specific images suffered from severely reduced SNR. In some cases there were so few photons reaching the x-ray detector that iodine-specific images were severely compromised by noise associated with detector electronics.^[97,98] Subsequently, dual-energy approaches that use thinner filters and higher-energy x-ray spectra were developed.

1.5.1.3 Dual-energy approaches

The goal of dual-energy approaches is to suppress either soft-tissue or bone from angiographic images by subtracting two images acquired with x-ray spectra having different average energies. This is most commonly performed using applied tube voltages of 50-70 kV and 120-130 kV for low and high-energy spectra, respectively, with 2-2.5 mm of copper filtration on the high-energy spectrum.^[75,76,112-116,134-136] Because movement of soft tissue, for example, cardiac, bowel, and pulmonary motion, is the primary source of motion artifacts, most two-material approaches aim to suppress soft-tissue structures. Since bone is not suppressed from these images, early investigators subtracted pre-injection dual-energy images from post-injection dual-energy images to remove overlying bone structures.^[75,76,114,135] Guthaner *et al.*^[75,76] demonstrated that in cooperative patients this approach combines the benefits of bone suppression offered by DSA with the benefits of soft-tissue suppression and reduced motion artifacts offered by dual-energy subtraction. Molloy *et al.*^[135] used a dual-energy approach to quantify canine coronary arteries and, while bone was not suppressed from images, soft-tissue suppression resulted in superior iodine visualization compared to non-subtraction approaches. Similar approaches have been useful in quantifying left-ventricular ejection fraction.^[115,136] Dual-energy approaches use thinner filters than K-edge subtraction and three-material approaches, but early studies still suffered from reduced SNR compared to DSA,

sometimes by a factor of 2-5. [75,76,121,135,136]

Limitations of early dual-energy studies Similar to K-edge subtraction and triple-energy approaches, when limited by the output of x-ray generators, early dual-energy studies had severely reduced SNR compared to DSA and non-subtraction approaches [75,76,112,113,115,116,134-136] due to the combination of inefficient production of low-energy x-ray spectra and filtering of high-energy spectra. In addition, early dual-energy studies used x-ray detectors consisting of image intensifiers that convert x-ray energy to photons with wavelengths in the visible range in combination with a video camera used to detect visible photons. Cameras used in many of these systems suffered from substantial read-out lag that decreased the dual-energy iodine signal by 30-50% in some studies. [112,130,131,134] Read-out lag, however, has minimal affect on DSA image signal because pre and post-contrast exposures are acquired many seconds apart. In addition, because many of these systems were initially designed for DSA studies where pre and post-injection images are acquired using the same x-ray exposure levels, early studies were often performed using equal exposures for low and high-energy images which could have resulted in an SNR reduction of up to a factor of 4 compared to optimal exposure ratios. [113]

1.5.1.4 Current state of energy-subtraction angiography

As described above, early ESA efforts were compromised by poor image SNR compared to DSA, sometimes by a factor of 2 to 5. For this reason, it is generally accepted that ESA provides sub-optimal image quality, and this approach is not currently used for imaging coronary arteries. However, early studies assessed ESA using technology of the time and it is therefore unclear whether reduced image quality was a result of technological limitations or of the fundamental physics of ESA. X-ray source and detector technologies have improved substantially over the past three decades and the limitations described above may no longer apply, suggesting that it may be the right time to revisit ESA for coronary imaging with a focus on the image quality that can be achieved for a given radiation dose to the patient and how this compares to DSA. However, since this approach requires two images, it may still be susceptible to motion artifacts although to a much lower extent than DSA. Energy-resolved approaches that extract the iodine signal from analysis of the spectral shape of a single post-injection transmission would be insensitive to motion artifacts.

1.5.2 Energy-resolved angiography

Advances in x-ray detector technology are leading to the development of a new generation of x-ray detectors that are capable of measuring the energy of each x-ray photon interacting in each x-ray detector element with the goal of estimating the spectrum of interacting photons, which may enable implementation of energy-resolved angiography. Energy-resolving photon-counting (EPC) x-ray imaging was conceived as early as 1976 by Alvarez *et al.*^[11] who was a pioneer of energy-dependent approaches for computed tomography. However, until recently, this concept never gained widespread interest for medical imaging applications because of limitations of x-ray detector technology. Recent advances in EPC x-ray detector technology have revived interest in this approach and these detectors may become available for medical imaging applications in the near future.

1.5.2.1 State-of-the-art energy-resolving photon-counting x-ray detectors

Modern digital x-ray detectors typically consist of a conversion layer, such as a phosphor or photoconductor, that converts x-ray energy into secondary quanta, such as optical photons or electrical charges, and a sensor that measures the number of liberated secondaries. In large-area direct-conversion approaches, x-ray energy is converted to electrical charges in a photoconductive converter material, such as amorphous selenium (*a*-Se), that is electrically coupled to a capacitive element. Charge integrated by the capacitive element is amplified by a semiconductor device, usually a thin-film transistor (TFT), located in each detector element and read out by peripheral electronics to generate a two-dimensional image.^[129,157,216] In conventional energy-integrating systems, many x-ray photons interact in the converter material during the integration time, which is determined by the x-ray exposure time, producing an image signal proportional to the total energy deposited by all interacting x-ray photons. Recent development of fast low-noise electronic readout systems equipped with thresholding circuits are capable of identifying signals generated from individual x-ray interactions.^[12,15,18,102,110,111,206,215]

Single photon-counting (SPC) systems produce an image signal proportional to the number of interacting photons by incrementing a counter when the signal from a detector element is greater than electronic noise levels. This approach has been used in positron emission tomography (PET) and single photon emission tomography (SPECT) since the 1970s but, until recent developments, higher count rates and stricter spatial-resolution requirements have restricted their use in x-ray imaging. Detector technology has advanced and there are now a number of prototype x-ray detectors^[44,70,89,91,102,103,110,124] and systems^[16,61,67,68,90,109,165,173,174,177] equipped with photon-counting

technology. State-of-the-art readout electronics are capable of counting 10^7 - 10^8 photons per second per detector element which may be adequate for some applications including mammography^[30,68,168] and breast computed tomography^[173,175,176,181] but may not yet be adequate for general CT applications.^[7,15,91,165,174,205,210,211,220] In addition, charge sharing between neighboring detector elements causes a substantial degradation of image quality^[4,5,31,126] and spectral information.^[31,44,70,101,102,110,174,178] Techniques that sum charge from neighboring elements and assign a count to the element with the largest signal, such as those discussed by Bornefalk *et al.*^[31] and implemented in the MEDIPIX3 prototype^[18] may mitigate this effect. We call these methods “adaptive binning” which will almost certainly be required to achieve high-quality images. When these approaches are implemented, it may be possible to estimate the total energy deposited by each interacting x-ray photon.^[18,31]

Since the number of liberated secondary quanta is proportional to deposited photon energy, use of multiple thresholds enables estimation of the number of interacting photons having energies within in a specified energy range. Incrementing a counter for one of a number of energy bins following each interaction yields an estimate of the spectrum of interacting photon energies.^[15,18,24,91,101,102,128,129,198] There are now a number of prototype mammography,^[16,67,68] computed tomography,^[61,165,173,176,177] and micro-computed-tomography^[81,205] systems with energy-resolving capabilities. Schlomka *et al.*^[165] used EPC measurements to generate iodine-specific CT images of a PMMA phantom containing bone-mimicking material and an iodinated contrast agent. Wang *et al.*^[205] performed a similar experiment using a micro-CT system equipped with a cadmium telluride (CdTe) EPC x-ray detector. Fredenberg *et al.*^[67] demonstrated that energy-resolved mammography has the potential to remove unwanted background variations and improve conspicuity of small low-contrast breast lesions. While EPC detectors used in these systems are single-line scanning detectors that are not suitable for angiography, area detectors such as the MEDIPIX prototypes^[18,44,70,102,110,124] may enable energy-resolved angiography.

1.5.2.2 Potential advantages of energy-resolved angiography

Energy-resolved angiography would use energy-bin data acquired using EPC x-ray detectors to estimate contributions of iodine, soft tissue, and bone to the total attenuation of an incident x-ray spectrum with the goal of producing an image showing only the distribution of iodinated contrast material. This approach would have the advantage that iodine-specific images could be generated from a single x-ray exposure and therefore would be less susceptible to motion artifacts that compromise DSA procedures. In addition, because this approach would not require the use of thick

filters, it may not be limited by generator output restrictions that compromised early ESA studies. Furthermore, this approach would enable rejection of electronic noise through the use of thresholding techniques, which is important at low x-ray exposure levels. In summary, the advent of EPC detectors may enable high-SNR subtraction images of the coronary arteries that are not degraded by electronic noise sources or motion artifacts.

1.6 Research problem

While ERA and ESA are exciting angiographic approaches that may overcome limitations of DSA, it is unclear whether iodine-specific images obtained with these approaches will provide image quality equal to or better than conventional subtraction approaches. In addition, EPC x-ray detectors are at an early stage in their development and present a number of new imaging challenges that will need to be overcome before routine energy-resolved x-ray imaging is possible. These issues lead to the following research questions:

1. What are the fundamental signal and noise limits of energy-resolved and energy-subtraction angiography and how do they compare with temporal-subtraction approaches for the same radiation and iodine dose?
2. How will the random nature of x-ray interaction and detection processes affect the performance of energy-resolving photon-counting x-ray detectors?
3. How can we optimize the performance of both EPC and conventional energy-integrating systems to maximize ERA and ESA image quality?

These questions are important because they indicate how much research effort should be invested in design and development of ERA and ESA systems for coronary angiography. Answering these questions requires a thorough understanding of image formation in photon-counting and material-specific imaging and how various image forming processes affect ERA and ESA image quality.

1.7 Research goal

The goal of this thesis is to determine the potential of energy-dependent approaches to provide equal or better image quality than conventional subtraction approaches, in terms of iodine signal-to-noise ratio, and to identify the impact of non-ideal detector performance on ERA and ESA image quality. The results of this thesis will provide imaging scientists and system manufacturers with (i)

knowledge of the ultimate potential of ERA and ESA; (ii) knowledge of the fundamental signal and noise limitations of energy-resolving photon-counting x-ray detectors; and (iii) tools necessary for design and optimization of ERA and ESA systems.

1.8 Research objectives

The objectives of this thesis are:

1. To develop a method of comparing image quality in terms of iodine signal-to-noise ratio (SNR) obtained using ESA and ERA with DSA assuming ideal instrumentation for each.
2. To develop a method of describing detector performance and image quality that can be obtained with photon-counting detectors.
3. To assess the potential of ESA and ERA by comparing the available iodine SNR with that of DSA including the effects of non-ideal detector performance.

1.9 Thesis outline

The goal of this thesis is addressed in a series of 4 papers (Chapters 2 to 5) that have either been submitted for publication or are in preparation for publication. Each paper corresponds to a specific thesis objective as described in the following sections.

Chapter 2: A theoretical comparison of x-ray angiographic image quality obtained with energy-dependent and conventional subtraction methods

While many researchers have investigated image quality in energy-resolved mammography,^[29,30,67] general radiography,^[174] and computed tomography,^[172,173,176,205] a direct image-quality comparison of ERA and ESA with DSA has not been performed. It is therefore unknown whether or not energy-dependent methods will generate iodine-specific images with image quality comparable to DSA. Comparing these techniques is difficult because currently there is no general theoretical framework for estimating signal and noise in x-ray subtraction angiography.

Chapter 2 describes a theoretical framework for characterizing angiographic image quality obtained with energy-resolved, energy-subtraction, and temporal-subtraction approaches. Inspired by Cardinal and Fenster's^[43] power series expansion of log-transmission signals, it is demonstrated

that iodine-specific images can be generated by weighted-log subtraction of x-ray transmission measurements acquired using energy-resolved, energy-subtraction, or temporal-subtraction approaches. Pixel values in log-subtracted images are proportional to estimated iodine area density (g cm^{-2}). Large-area quantum noise, expressed in terms of the pixel variance in an iodine-specific image, is calculated using an error propagation technique. This formalism is used to compare ERA and ESA with DSA for the task of isolating large iodine objects embedded in uniform water-only objects, with the surprising result that in some situations both ERA and ESA can provide iodine SNR within 10% that of DSA for the same patient entrance exposure, assuming ideal instrumentation for each method.

[This chapter was published as the article “A theoretical comparison of x-ray angiographic image quality using energy-dependent and conventional subtraction methods” by J. Tanguay, Ho Kyung Kim, and Ian A. Cunningham, published in *Medical Physics* 2012; 39(1): 132.]

Chapter 3: Fundamental signal and noise limits of photon counting x-ray detectors

Chapter 2 demonstrated the potential of ERA to provide angiographic image quality equal to DSA for the same patient entrance exposure. However, this comparison was based on the assumption of ideal EPC detector technology and therefore did not consider the effects of stochastic energy-deposition and conversion to secondary quanta in an x-ray convertor material, collection of secondary quanta by collecting electrodes, and additive electronic read-out noise, all of which are known to degrade detector performance in conventional energy-integrating x-ray detectors. X-ray detector performance is commonly characterized in terms of the Fourier-based detective quantum efficiency (DQE),^[54,169,170] which is a measure of how efficiently an x-ray detector converts incident x-ray quanta to a final image signal. Over the past three decades, a cascaded-systems approach has been developed to describe how image-forming processes, such as those described above, affect the DQE of conventional energy-integrating x-ray detectors. While this approach has been successful in the development of theoretical models that describe the DQE of many current systems, cascaded-systems analysis (CSA) of single-photon-counting systems is still preliminary and does not account for many factors known to degrade image quality in conventional approaches.

Chapter 3 describes an extension of CSA to include a description of the DQE of photon-counting x-ray detectors. Point-process theory is used to develop a method of propagating the mean image signal and noise, expressed in terms of the Wiener noise power spectrum (NPS), through a thresh-

olding stage required to identify x-ray interaction events. It is demonstrated that under certain conditions, the CSA approach can be applied to SPC systems with the additional requirement of propagating the probability density function describing the total number of image-forming quanta through each stage of a cascaded model. The new transfer relationships are used to describe the zero-frequency DQE of a hypothetical SPC detector including the effects of stochastic conversion to secondary quanta, secondary quantum sinks, additive noise, and threshold level. Theoretical results are compared with Monte Carlo calculations.

It is demonstrated that in some situations $DQE_{\text{SPC}}(0) = \alpha I_{\text{SPC}}$ where α represents the quantum efficiency and I_{SPC} is a new SPC noise factor equal to the true positive fraction of counting interacting photons and accounts for degradation in image quality due to stochastic energy deposition, conversion, and collection processes, electronic noise, and thresholding. A CSA analysis demonstrates that in some situations there is a narrow range of acceptable thresholds required to avoid reduced I_{SPC} values.

[This chapter was published as the article “The detective quantum efficiency of photon-counting x-ray detectors using cascaded systems analyses” by J. Tanguay, Ho Kyung Kim, and Ian A. Cunningham, published in *Medical Physics* 2012; 40(4): 041913-1.]

Chapter 4: Modeling signal and noise propagation in energy-resolving photon-counting x-ray detectors

The formalism developed in Chapter 3 was useful in understanding the importance and utility of using a PDF-transfer approach, but is restricted to the simplistic case where all the energy of an interacting photon is deposited at a primary interaction site, ignoring photoelectric and Compton emission/scatter photons that escape the detector or are reabsorbed at a remote interaction site. The goal of Chapter 4 is to extend the capabilities of PDF transfer theory to include the effects x-ray reabsorption on the PDF of image-forming quanta to enable a description of the zero-frequency DQE of SPC systems. This is accomplished by developing a general expression for the PDF of the total number of image quanta for a parallel cascade of quantum processes. The utility of the parallel cascades approach is demonstrated in an analysis of the zero-frequency DQE and imprecision in measurements of photon energy of hypothetical selenium-based photon-counting x-ray detectors.

A CSA model of the SPC Swank factor I_{SPC} using an x-ray interaction and detection model that incorporates stochastic energy deposition through photoelectric and Compton interactions, liberation and collection of secondary quanta, electronic noise, and thresholding shows that the DQE can be

degraded by each of these processes. It is demonstrated that there is a narrow range of acceptable thresholds that depends on photon energy, the energy required to liberate an electron-hole pair, collection efficiency, and electronic noise level. For Se-based systems with thresholds that adequately suppress electronic noise without thresholding out interaction events, the DQE is approximately equal to the quantum efficiency. In this case, as expected, the DQE is not compromised by Swank noise or electronic noise. However, it is demonstrated that in some cases this condition cannot be satisfied, such as at lower mammography energies, higher levels of additive noise, and poor collection efficiencies.

Chapter 5: Cascaded-systems analysis of angiographic image quality obtained using energy-dependent and conventional subtraction approaches

Chapter 5 describes a theoretical comparison of angiographic image quality that could be achieved using energy-dependent and conventional subtraction approaches including the effects of electronic noise sources and stochastic energy-depositing, conversion, and collection processes in real x-ray detectors. Iodine SNR is determined for energy-resolved, energy-subtraction, and digital subtraction angiography using cascaded-systems analysis developed in Chapters 3 and 4 in combination with the linearized noise propagation approach developed in Chapter 2. This enables a direct comparison of ERA image quality that could be achieved using state-of-the-art photon-counting x-ray detectors with energy integrating approaches, including ESA and DSA. It is demonstrated that under certain conditions, both ERA and ESA could result in image quality within 25% of that of DSA at angiographic exposure levels. Requirements for successful implementation of ERA systems that use novel cadmium-zinc-telluride-based EPC x-ray detectors are discussed.

Chapter 2

A theoretical comparison of x-ray angiographic image quality obtained with energy-dependent and conventional subtraction methods

This chapter is adapted from a manuscript entitled “A theoretical comparison of x-ray angiographic image quality using energy-dependent and conventional subtraction methods” by Jesse Tanguay, Ho Kyung Kim, and Ian A. Cunningham, published in *Medical Physics* 2012; 39: 132-142.

2.1 Introduction

Cardiovascular diseases (CVDs) are the leading causes of death worldwide.^[117] In 2004, an estimated 17.1 million people died from CVDs, representing 29% of all global deaths. Of these, an estimated 7.2 million were due to coronary heart disease (CHD) and 5.7 million to stroke. Accurate imaging of CVD patients is critical for clinical decision making such as guiding and planning surgical interventions, where disease classification requires arterial lesions be categorized based on length and location.^[87,104,159] Carotid luminal stenoses can be an indicator of an unstable (“vulnerable”) plaque with increased risk of thrombosis and stroke.^[62]

Investigations for diagnosis and treatment planning may include x-ray digital subtraction angiography (DSA), magnetic resonance angiography (MRA), computed tomography angiography

(CTA), or duplex ultrasonography (DU). DU is often used as a screening tool and follow-up DSA, CTA, or MRA investigations are usually performed to confirm diagnosis and plan surgical interventions.^[142,189,190] CTA and MRA have seen increased use due to improvements in spatial and temporal resolution made over the past decade.^[144,160,190] In spite of these great advances, DSA, developed over two decades ago,^[34,56,96,133,149] remains the reference standard for imaging near-stationary vasculature such as the peripheral and the neuro-vasculature.^[144,190] With this technique, an image acquired prior to injection of an iodinated contrast agent is subtracted from a series of post-injection images, thereby largely removing overlapping anatomical structures. However, the need for both pre and post-injection exposures, often many seconds apart, can result in severe motion artifacts and failed or compromised diagnostic procedures.^[200]

Although large movements during image acquisition are largely avoided with a cooperative patient, respiratory and cardiac motions are common. Involuntary motions such as swallowing after a carotid injection can impair image quality^[37,47,200] and movement of extremities can degrade visualization of peripheral arteries.^[75,188] In coronary angiography, subtraction methods are almost never employed, and high quality images are obtained using relatively high radiation exposures and iodine concentrations to ensure that both large and small arteries are clearly distinguished over background structures. Image processing techniques have been helpful for retrospective registration, particularly for simpler motions.^[23,122,123]

An alternative approach may come from the development of a new generation of x-ray detectors capable of estimating the energy of each interacting x-ray photon. An exciting aspect of energy-resolved photon-counting (EPC) imaging is the potential to generate “DSA-like” images from a single exposure that are not susceptible to motion artifacts. Energy-resolved angiography (ERA) would use measurements of the spectrum of interacting x-ray energies in each pixel to estimate the iodine attenuation along each path.^[61,165]

Many technical barriers must be overcome before EPC detectors are ready for use in ERA. For example, they must operate at very high count rates that cannot be achieved at present. In addition, angiography requires high spatial resolution but the use of small detector elements will result in reabsorption of characteristic and Compton-scatter x rays and therefore charge sharing in near-by elements. This may result in increased image noise^[5,18,31,126,178,191,201,203] although fast coincidence detection algorithms, such as that implemented in the Medipix-3 prototype detector,^[18] may prevent these effects.

Another approach, originally proposed in the 1980s, is the use of dual-energy methods to produce an iodine-specific image^[75,113,115,116,121,136] based on two (or more) x-ray images acquired at different

average energies to enhance or suppress materials of a particular atomic number.^[43,107,154] While not in use at present, energy-subtraction angiography (ESA) could be implemented using fast kV-switching to generate “DSA-like” images with reduced or eliminated motion artifacts.

While early dual-energy studies suggested that iodine signal-to-noise ratio (SNR) would be much less than that of DSA (by a factor of 2 to 5),^[112,113,115,135] these studies did not specifically address whether reduced SNR was a result of technological limitations or the fundamental physics of dual-energy imaging. For example, early dual-energy cardiac studies used smaller x-ray tubes with low heat capacity that forced operation at lower patient exposures and could not control exposure times independently. These limitations resulted in decreased SNR but may be less restrictive at present.

While ERA and ESA are exciting alternatives, their potential success depends largely on the image quality that can be achieved for a given exposure (or effective dose) to the patient. In this article, we use linearized expressions of image signal and noise to develop a theoretical framework to enable this comparison, with the unexpected result that both ERA and ESA have the potential to produce similar image quality to DSA.

2.2 Theory

We consider the task of isolating contrast agents (iodine) embedded in a soft-tissue and/or bony environment. The goal is to produce an image showing only the spatial distribution of the contrast agent. The attenuation of x rays through a patient is determined from the line integral of the linear attenuation coefficient $\mu(s; E)$ along the x-ray path which we express as a linear combination of basis-material mass-attenuation coefficients:^[11,43,152,165]

$$\int \mu(s; E) ds = \sum_{b=1}^m \frac{\mu}{\rho}_b(E) A_b = \mathbf{A}^T \frac{\boldsymbol{\mu}}{\boldsymbol{\rho}}(E), \quad (2.2.1)$$

where b identifies the basis material, m is the number of basis materials, s represents position along the x-ray path as shown in Fig. 2.2.1, E is the photon energy, and

$$\mathbf{A} = \begin{bmatrix} A_1 \\ \vdots \\ A_m \end{bmatrix} \quad \text{and} \quad \frac{\boldsymbol{\mu}}{\boldsymbol{\rho}}(E) = \begin{bmatrix} \frac{\mu}{\rho}_1(E) \\ \vdots \\ \frac{\mu}{\rho}_m(E) \end{bmatrix}. \quad (2.2.2)$$

The coefficients of the expansion, A_b , represent the area densities of each basis material such as soft tissue (A_S), bone (A_B), and iodine (A_I). The mass-attenuation coefficients of possible basis materials

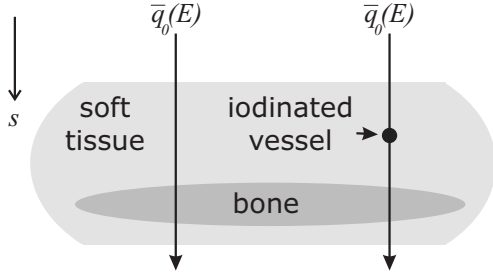


Figure 2.2.1: Schematic showing x-ray paths through iodinated and background regions of a patient for the incident spectrum $\bar{q}_0(E)$.

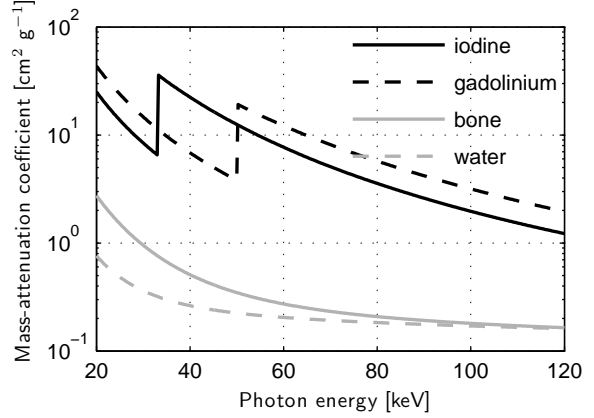


Figure 2.2.2: Plots of the mass-attenuation coefficients for potential basis materials for angiographic applications.

are shown in Fig. 2.2.2. An image showing any of the basis materials can be generated by estimating \mathbf{A} at each pixel location. In the following subsections we provide a general mathematical formalism for estimating \mathbf{A} from x-ray transmission measurements acquired using either energy-integrating or photon-counting x-ray detectors. We use an over-head tilde (eg. \tilde{x}_i) to represent random variables (RVs) and $E(\tilde{x}_i)$, $\text{Var}(\tilde{x}_i)$, and $\text{Cov}(\tilde{x}_i, \tilde{x}_j)$ to represent the expected value, variance, and covariance, respectively.

2.2.1 Angiographic image signal

The angiographic image signal A_I is derived from two or more images where, for linear detectors, the expected pixel value measured in image i , is given by

$$E(\tilde{M}_i) = ka \int_0^{kV_i} S_i(E) \bar{q}_i(E) e^{-\mathbf{A}^T \frac{\mu}{\rho}(E)} dE; \quad i = 1..n \quad (2.2.3)$$

where k is a constant of proportionality, $\bar{q}_i(E)$ and kV_i describe the spectral distribution of x-ray photons incident on the patient [$\text{mm}^{-2} \text{keV}^{-1}$] corresponding to image i , and $S_i(E)$ is a weighting function describing the detector response associated with image i . The form of $S(E)$ requires some explanation. For a conventional detector that produces a single image with a signal proportional to absorbed energy, $S(E) = \alpha(E)E_{ab}(E)$ where α and E_{ab} are the detector quantum efficiency and absorbed energy respectively for a photon of energy E . For an ideal photon counting detector, $S_i(E) = \alpha(E)$ for energies within bin i and is zero otherwise. For the dual-energy approach, $n = 2$

and $S_i(E)$ corresponds to the conventional detector described above where i indicates the spectrum.

Attenuation of the spectral distribution of x rays $\bar{q}_i(E)$ through a patient is determined from the log signal, \tilde{l}_i , given by

$$\tilde{l}_i = -\log \frac{\tilde{M}_i}{\tilde{M}_{i0}}; \quad i = 1..n, \quad (2.2.4)$$

where $\tilde{M}_i/\tilde{M}_{i0}$ is an image of x-ray transmission values and $\tilde{M}_{i0} = \tilde{M}_i|_{\mathbf{A}=\mathbf{0}}$ (corresponding to no patient). The above relationship represents a system of n non-linear equations in the m unknowns $A_1 \dots A_m$. The solution to Eq. (2.2.4) provides an estimate of the area density of each basis material. However, in general, Eq. (2.2.4) has no analytic solution. We apply a simple linearization technique similar to Le and Molloy^[105] and Cardinal and Fenster^[43] to obtain an approximate analytic solution. We let $\mathbf{A}_0 = [A_{10} \dots A_{m0}]$ represent the point about which we expand the log signal \tilde{l}_i and $\tilde{l}_{i0} = \tilde{l}_i|_{\mathbf{A}=\mathbf{A}_0}$. In the appendix we show that the linearized version of Eq. (2.2.4) about $\mathbf{A} = \mathbf{A}_0$ is given by

$$\mathbf{L} - \mathbf{L}_0 = \mathbf{J}(\mathbf{A} - \mathbf{A}_0) \quad (2.2.5)$$

where

$$\mathbf{L} - \mathbf{L}_0 = \begin{bmatrix} \tilde{l}_i - \tilde{l}_{i0} \\ \vdots \\ \tilde{l}_n - \tilde{l}_{n0} \end{bmatrix} \quad (2.2.6)$$

and \mathbf{J} is the Jacobian matrix with elements given by

$$J_{ib} = \frac{\bar{\mu}}{\rho}_{ib}; \quad i = 1..n, \quad b = 1..m \quad (2.2.7)$$

where $\frac{\bar{\mu}}{\rho}_{ib}$ denotes the average value of the mass-attenuation coefficient of basis material b weighted by $S_i(E) \bar{q}_i(E) e^{-\mathbf{A}_0^T \frac{\mu}{\rho}(E)}$:

$$\frac{\bar{\mu}}{\rho}_{ib} = \frac{\int_0^{kV_i} \frac{\mu}{\rho}_b(E) S_i(E) \bar{q}_i(E) e^{-\mathbf{A}_0^T \frac{\mu}{\rho}(E)} dE}{\int_0^{kV_i} S_i(E) \bar{q}_i(E) e^{-\mathbf{A}_0^T \frac{\mu}{\rho}(E)} dE}. \quad (2.2.8)$$

In practice \mathbf{L}_0 could be determined from either theoretical calculations or a series of calibration scans. Equation (2.2.5) has a unique solution for $n = m$ and no solution for $n > m$, which occurs, for example, when using EPC x-ray detectors with more energy bins than basis materials. In the latter case, we use a simple least-squares technique similar to that of Le and Molloy.^[105] The

estimated area-density vector is then expressed as

$$\mathbf{A} = \mathbf{A}_0 + \mathbf{W}(\mathbf{L} - \mathbf{L}_0) \quad (2.2.9)$$

where

$$\mathbf{W} = \begin{cases} \mathbf{J}^{-1} & \text{for } n = m \\ (\mathbf{J}^T \mathbf{J})^{-1} \mathbf{J}^T & \text{for } n > m \end{cases}. \quad (2.2.10)$$

Equations (2.2.9) and (2.2.10) give an estimate of the area density of each basis material for all three techniques considered in this study. They may also be used to determine area densities from hybrid detectors that use some combination of energy-resolving, photon-counting, and energy-integrating measurements, such as those described by Alvarez.^[9] For $\mathbf{A}_0 = \mathbf{0}$, this result is equivalent to commonly used expressions for linear dual-energy,^[108] temporal-subtraction,^[59,209] and energy-resolved^[105] approaches. An angiographic image is obtained by solving for the iodine-specific signal \tilde{A}_I .

2.2.2 Angiographic image noise

Random variations in the number of interacting photons, the energy deposited by each photon, and the number of secondary quanta collected in a detector element will result in random variations in \tilde{M}_i and therefore noise in the material-specific images. Roessl *et al.*^[152,154] and Wang and Pelc^[201,203] both used error propagation techniques and the Cramér Rao lower bound to estimate large-area basis-image noise for EPC detectors. In this article, we generalize the error-propagation approach used by Roessl *et al.*^[154] to describe the signal-to-noise ratio in basis-material images for both energy-integrating and EPC detectors to allow for a direct comparison of image SNR.

The covariance matrix of the basis-material images $\mathbf{V}(\mathbf{A})$ is related to the covariance matrix of the log signals $\mathbf{V}(\mathbf{L})$ by:^[49,154,202]

$$\mathbf{V}(\mathbf{A}) = \mathbf{W} \mathbf{V}(\mathbf{L}) \mathbf{W}^T \quad (2.2.11)$$

where \mathbf{W} is given by Eq. (2.2.10) and

$$V_{ij}(\mathbf{L}) = \begin{cases} \text{Cov}(\tilde{l}_i, \tilde{l}_j) & i \neq j \\ \text{Var}(\tilde{l}_i) & i = j \end{cases}, \quad (2.2.12)$$

with a similar result for $\mathbf{V}(\mathbf{A})$.

We separate our analysis of basis-image noise into two cases, corresponding to independent and cross-correlated measurements \tilde{M}_i . While in most cases \tilde{M}_i will correspond to independent measurements and will therefore be statistically uncorrelated, cross correlations may occur when, for example, an x-ray detector records both the total energy deposited and the total number of photons interacting in a detector element from the same exposure.^[9,154] Note that these correlations are not spatial correlations within a single image - they are cross correlations between the two or more measurements used to derive \mathbf{A} .

2.2.2.1 General case: Cross-correlated measurements

In the Appendix A ("Supplemental material for Chapter 2") we show that

$$\text{Cov}(\tilde{l}_i, \tilde{l}_j) = \frac{\text{Cov}(\tilde{M}_i, \tilde{M}_j)}{\text{E}(\tilde{M}_i) \text{E}(\tilde{M}_j)} \quad (2.2.13)$$

and

$$\text{Var}(\tilde{l}_i) = \frac{\text{Var}(\tilde{M}_i)}{\text{E}(\tilde{M}_i)^2} = \frac{1}{\text{SNR}_{M_i}^2} \quad (2.2.14)$$

where SNR_{M_i} represents the signal-to-noise ratio (SNR) for \tilde{M}_i . The analytical form of $\text{Var}(\tilde{M}_i)$ has been extensively described in the literature, for example, see Swank^[184] or Alvarez and Macovski.^[11] For each of the three methods considered in this article $\text{Cov}(\tilde{M}_i, \tilde{M}_j) = 0$. We refer the interested reader to Roessl *et al.*^[154] or Alvarez^[9] for details on calculating $\text{Cov}(\tilde{M}_i, \tilde{M}_j)$ in the case that it is non zero.

Combining Eqs. (2.2.11)-(2.2.14), the covariance between material-specific images for basis materials b and b' is given by

$$V_{bb'}^{\text{cor}}(\mathbf{A}) = \sum_{i=1}^n \sum_{j=1}^n \frac{W_{b_i} \text{Cov}(\tilde{M}_i, \tilde{M}_j) W_{b'_j}}{\text{E}(\tilde{M}_i) \text{E}(\tilde{M}_j)}. \quad (2.2.15)$$

The above equation gives the variance ($b = b'$) and covariance ($b \neq b'$) of the material-specific images for the general case of cross-correlated measurements \tilde{M}_i .

2.2.2.2 Special case: Independent measurements

For the case of independent measurements \tilde{M}_i , $\text{Cov}\{\tilde{M}_i, \tilde{M}_j\} = \delta_{ij}\text{Var}\{\tilde{M}_i\}$ where δ_{ij} is the Kronecker delta equal to one for $i = j$ and zero otherwise. Therefore:

$$V_{bb'}^{\text{indep}}(\mathbf{A}) = \sum_{i=1}^n \frac{W_{bi}W_{b'i}}{\text{SNR}_{M_i}^2}. \quad (2.2.16)$$

The above equation gives the variance and covariance of basis-material estimates when the measured (raw) image signals \tilde{M}_i and \tilde{M}_j are statistically independent, including the three methods compared in this article. This calculation accommodates cross correlations between material-specific images as described by the $b \neq b'$ case, such as may occur with dual-energy methods or between calcium and soft-tissue images using EPC detectors as described by Wang and Pelc. [201–203]

2.2.3 Iodine Detectability

The ability to visualize iodinated vasculature is related to the iodine signal-to-noise ratio (SNR), and this ratio is different for each of the methods compared in this work. We compare the three methods in terms of a performance metric related to the detectability index, [1] defined as the iodine SDNR per square-root of patient entrance exposure:

$$P_I = \frac{\text{SNR}_I}{\sqrt{X}} = \frac{1}{\sqrt{X}} \frac{\text{E}\{\tilde{A}_I - \tilde{A}_I^N\}}{\sqrt{\text{Var}\{\tilde{A}_I - \tilde{A}_I^N\}}}, \quad (2.2.17)$$

where X is the patient entrance exposure, [17] and \tilde{A}_I and \tilde{A}_I^N are the iodine signals from iodinated and non-iodinated regions of the images, respectively. In this study we ignore spatial correlations in an image, in which case $\sqrt{\text{Var}\{\tilde{A}_I - \tilde{A}_I^N\}} = \sqrt{\text{Var}\{\tilde{A}_I\} + \text{Var}\{\tilde{A}_I^N\}}$.

2.3 Methods and materials

2.3.1 Theoretical comparison of energy-resolved, energy-subtraction and digital-subtraction angiography

The method described above was used to theoretically compare image quality that can be obtained with each of the three methods for the same exposure. For each method we consider the task of isolating iodine embedded in water. In all cases, our model assumes ideal energy resolution and unity

quantum efficiency. Non-ideal energy resolution will likely increase the variance of basis-material estimates for each of the techniques considered. This effect may be more pronounced in the case of ERA, where non-ideal energy resolution may result in “cross-talk” (correlations) between energy bins. All sources of noise apart from Poisson quantum noise are considered negligible, and an ideal anti-scatter grid (ie. complete transmission of primary photons and complete rejection of scattered photons) is assumed. Our analysis therefore represents an optimistic estimate of image quality achievable with each method.

In the following sections, all x-ray spectra are generated using an in-house MATLAB routine that implements algorithms published by Tucker and Barnes^[199] for a tungsten-target x-ray tube.

2.3.1.1 Digital subtraction angiography, DSA

DSA requires subtraction of a post-injection image from a pre-injection (mask) image. For each, the expected signal from a conventional energy-integrating detector element is proportional to the total energy deposited by the x-ray spectrum incident on the detector:

$$\mathbb{E} \left(\tilde{M}_{\text{pre}} \right) = ka \int_0^{kV} E \bar{q}_0(E) e^{-\frac{\mu}{\rho} w(E) A_W} dE \quad (2.3.1)$$

$$\mathbb{E} \left(\tilde{M}_{\text{post}} \right) = ka \int_0^{kV} E \bar{q}_0(E) e^{-\frac{\mu}{\rho} w(E) A_W - \frac{\mu}{\rho} I(E) A_I} dE \quad (2.3.2)$$

where A_W is the area density of water. We theoretically calculated image signal (Eqs. (2.2.9) and (2.2.10)), noise (Eq. (2.2.16)) and P_I (Eq. (5.2.28)) for applied-tube voltages ranging from 50 to 100 kV with an additional 2 mm of aluminum filtering.

2.3.1.2 Energy-subtraction angiography, ESA

We consider a dual-energy approach that makes use of two post-injection images with different high and low average energies to isolate the iodine signal from background:

$$\mathbb{E} \left(\tilde{M}_L \right) = ka \int_0^{kV_L} E \bar{q}_L(E) e^{-\frac{\mu}{\rho} w(E) A_W - \frac{\mu}{\rho} I(E) A_I} dE \quad (2.3.3)$$

$$\mathbb{E} \left(\tilde{M}_H \right) = ka \int_0^{kV_H} E \bar{q}_H(E) e^{-\frac{\mu}{\rho} w(E) A_W - \frac{\mu}{\rho} I(E) A_I} dE. \quad (2.3.4)$$

Previous studies suggest that optimal SNR is obtained when the low-energy applied tube voltage is in the range of 50-60 kV and the high energy applied tube voltage is in the range of 100-130 kV.^[113,135] These studies also suggest that filtering the output of the high-energy applied tube voltage with and

Imaging Technique	DSA	ERA	ESA
Applied tube voltage [kV]	63	150	50/130
Al filtration per image [mm]	2/2	2	2/2
Cu filtration per image [mm]	0/0	0	0/2.1
Tube current per image [mAs]	9.25/9.25	3	28.5/11.1
Heat units [mAs×kV]	1166	450	2733
Entrance exposure per image [mR]	20/20	40	28.7/11.3

Table 2.1: Exposure parameters used for the Monte Carlo study.

addition 2-2.5 mm of copper (Cu) provides optimal SNR. We therefore fixed the low-energy applied tube voltage at 50 kV and varied both the high-energy applied tube voltage and low-to-high-energy mAs ratio to maximize P_I . For each spectral combination, both the low and high-energy spectra were filtered with 2 mm of Al with an additional 2.1 mm of Cu on the high energy spectrum. For each combination of exposure parameters the theoretical technique developed in the theory section was used to calculate image signal, noise and P_I .

2.3.1.3 Energy-resolved angiography, ERA

ERA requires only a single post-contrast-injection transmission and binning of x-ray photons into pre-specified energy bins to isolate the iodine signal from background. The signal from each energy bin is given by:

$$E(\tilde{M}_i) = ka \int_{E_i}^{E_{i+1}} \bar{q}_i(E) e^{-\frac{\mu}{\rho} w(E) A_w - \frac{\mu}{\rho} I(E) A_I} dE; \quad i = 1 \dots n \quad (2.3.5)$$

where n is the number of energy bins. We calculated image signal and noise for 2 and 3-bin ERA approaches (using a least-squares solution for the 3-bin method). For both approaches we varied the applied tube voltage from 50 to 150 kV and applied a numerical optimization using Matlab's patternsearch function to determine the location of the energy thresholds that maximize P_I . For each combination of exposure parameters, the theoretical technique developed in the theory section was used to calculate image signal, noise, and P_I .

2.3.2 Monte Carlo Validation

The theoretical formalism developed in Section II was validated with a simple Monte Carlo calculation. The number of incident x-ray photons in each energy interval (1 keV) was determined for the desired exposure using a Poisson random number generator. A virtual phantom with iodine area densities of 0, 10, 20, 30, 40, and 50 mg cm⁻² embedded in 20 cm of water was used for numerical

Imaging technique	DSA	ESA
Applied tube voltage [kV]	63	50/130
Cu filtration per image [mm]	0/0	0/2.1
Tube current per image [mAs]	4/4	10/4
Heat units [mAs×kV]	504	1020
Entrance exposure per image [mR]	9/9	11/4

Table 2.2: Exposure parameters used for the experimental study.

comparison with theoretical results. A second virtual phantom consisting of iodinated vasculature with diameters of 0.2 and 0.5 cm filled with 0.10 g cm^{-3} of iodine embedded in 20 cm of water with an extra 2 cm of water placed over the right half of the image was used to compare the background removal capabilities of each technique. For each virtual phantom, a 128×128 grid of 0.2×0.2 -mm detector elements was simulated, giving a 2.56×2.56 -cm image. Transmissions were calculated using tabulated values of the mass-attenuation coefficients for water and iodine. For each technique, we used the exposure parameters (summarized in Table 2.1) that maximized P_I .

To simulate energy-integrating images, we weighted each transmitted x-ray photon by its energy and then summed over the entire spectral distribution. To simulate EPC images, we summed the number of transmitted photons between the lower and upper energy thresholds for each energy bin. Iodine-specific images for DSA, ESA and ERA were then generated using the contrast separation technique developed in the theory section.

2.3.3 Visual comparison of ESA with DSA

A visual comparison of ESA with DSA was obtained experimentally using a simple static vascular phantom consisting of two tubes of variable inner diameters (steps of 0.15, 0.4 and 0.8 cm) filled with 0.10 g cm^{-3} of iodine. The tubes were placed in 20 cm of water with an extra thickness of 2.5 cm of PMMA placed over the left tube to provide background (non-iodinated) contrast.

We acquired a series of contrasted and mask images (with and without the tubes). For the ESA experiment we also acquired open-field images at both kV values required for the log-transform in Eq. (2.2.4). Ten open-field images were acquired (at lower mAs values to prevent detector saturation and then scaled to match the mAs of the contrast images) and averaged. The contrast separation technique developed in the theory section was then used to generate iodine-specific images for both DSA and ESA. In all cases we linearized the image signals about zero water thickness. We were unable to perform an ERA experiment because our laboratory currently does not have access to an EPC x-ray detector.

All images were acquired using a General Electric Revolution XR/d x-ray system with a 1 m

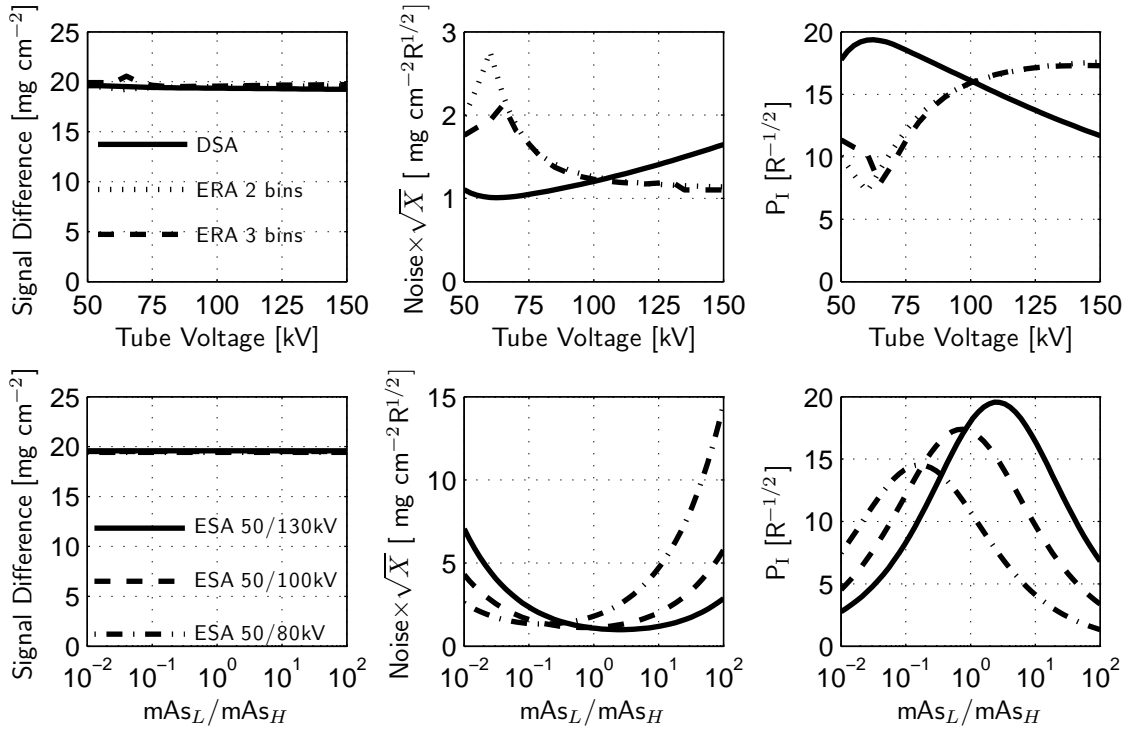


Figure 2.4.1: Dependence of iodine SNR on exposure parameters. The top row illustrates the dependence of DSA and ERA on the applied tube voltage. The bottom row illustrates the dependence of ESA on both the high-energy applied tube voltage and the low-to-high-energy mAs ratio.

source-image distance. This system uses a conventional x-ray tube (General Electric MX-100, General Electric Medical Systems) and generator (General Electric SCPU-80, General Electric Medical Systems) with a CsI based flat-panel detector. Exposure parameters are shown in Table 2.2.

2.4 Results

2.4.1 Dependence on imaging parameters

2.4.1.1 Exposure technique

Figure 2.4.1 illustrates the dependence of iodine signal, noise $\times \sqrt{X}$, and the performance metric P_1 for each of the three methods on exposure parameters for 20 cm of water and 20 mg cm⁻² of iodine. In all cases, the log signals were expanded about 20 cm of water. In general, there is little variation in signal with variable exposure parameters for each of the three techniques.

In the case of DSA, the performance metric reaches a maximum when the applied tube voltage is approximately equal to 63 kV. This is consistent with previous studies. See, for example, Gkanatsios *et al.*^[72] Pre and post-injection x-ray spectra for 20 cm of water and 40 mg cm⁻² of iodine are

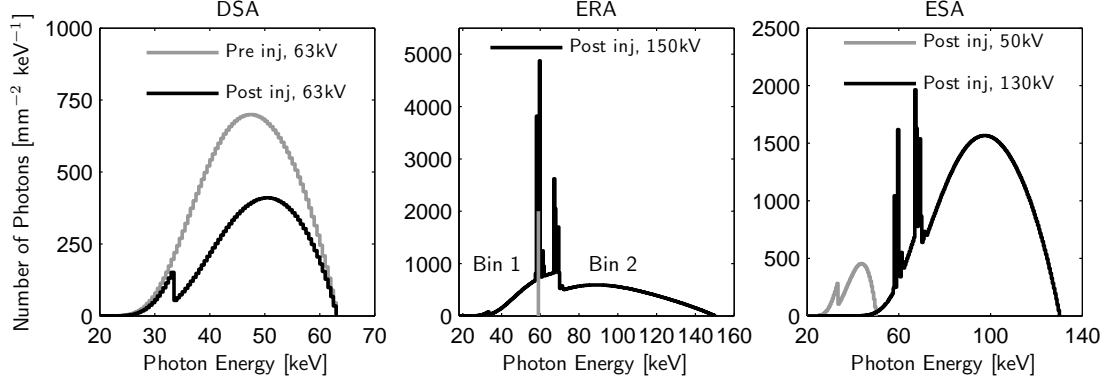


Figure 2.4.2: X-ray spectra for DSA, ERA, and ESA. The pre-injection DSA spectrum has been transmitted through 20 cm of water and all post-injection spectra have been transmitted through 20 cm of water and 40 mg cm^{-2} of iodine. The total entrance exposure for each spectral combination is 40 mR.

illustrated in Fig. 2.4.2 for a 40 mR entrance exposure.

In the case of ERA, there is little difference in P_I between the 2 and 3-bin approaches. This is consistent with the findings of Shikhaliev^[177] who demonstrated that there is little change in iodine contrast-to-noise ratio (CNR) between 2 and 5-bin approaches. For both approaches, iodine SNR reaches a minimum when the applied tube voltage is in the range of 55-65 kV and then increases with increasing applied tube voltage. Because there is little difference between the 2 and 3-bin approaches, from this point forward we present the results of the 2-bin approach in comparison with ESA and DSA. We used a 150 kV applied tube voltage with an energy threshold at 59 keV which was determined to be optimal and is consistent with that found by Nik *et al.*^[138] The post-injection transmitted x-ray spectrum is illustrated in Fig. 2.4.2 for a 40 mR entrance exposure.

In the case of ESA, applied-tube voltages of 50 and 130 kV (with the high-energy spectrum additionally filtered by 2.1 mm of Cu) with a low-to-high-energy mAs ratio of 2.3 provided the highest SNR of the spectral combinations considered. These parameters are similar to those used in previous studies.^[113,135] Post-injection high and low-energy spectra are illustrated in Fig. 2.4.2 for a 40 mR entrance exposure.

2.4.1.2 Taylor-expansion point

Figure 2.4.3 illustrates the dependence of iodine signal and P_I on the Taylor-expansion point $\mathbf{A}_0 = [A_{I0}, A_{W0}]$ for 20 cm of water and iodine concentrations of 20 mg cm^{-2} and 50 mg cm^{-2} of iodine. In all cases we expanded about $A_{I0} = 0$. In general, iodine signal becomes more inaccurate as the expansion point increases or decreases from the true area densities for all three techniques. This

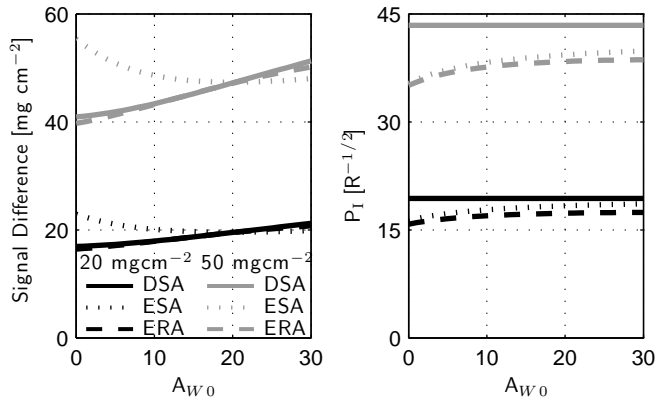


Figure 2.4.3: Dependence of iodine signal (left) and performance index P_I (right) on the Taylor-expansion point $\mathbf{A}_0 = [A_{I0}, A_{W0}]$ for 20 cm of water and iodine area densities of 20 mg cm^{-2} and 50 mg cm^{-2} . For each technique we have expanded about zero iodine area density, ie. $A_{I0} = 0$.

effect could likely be reduced by using more energy bins in the ERA approach. While the image signals show variation with expansion point, P_I for all three techniques shows very little dependence on A_{W0} . In the case of DSA, P_I is independent of A_{W0} . For all remaining theoretical and simulation results presented, the log signals were expanded about 20 cm of water.

2.4.1.3 Iodine concentration

Iodine-specific images, generated using the exposure parameters in table I for various iodine concentrations in 20 cm of water, are shown in Fig. 2.4.4. The iodine signal \tilde{A}_I for each concentration is given by the pixel value in these images. The iodine signal and performance metric P_I , determined using Eq. (5.2.28) is compared with theoretical predictions in Fig. 2.4.5. Excellent agreement was obtained between our theoretical method and the Monte Carlo calculations.

All three methods show a linear response with near-unity slope with increasing iodine concentration as illustrated in the upper plot of Fig. 2.4.5. Surprisingly, for this particular choice of exposure parameters, the performance metric P_I for ESA is slightly higher than that of ERA and both are within 5-10 % of DSA under these conditions.

2.4.1.4 Water thickness

The upper plot of Fig. 2.4.6 demonstrates that there is little variability in iodine signal with increasing water thickness for each of the three methods. However, as described earlier, as the actual water thickness increases or decreases from the expansion point ($\mathbf{A}_0 = [0, 20]$) the signals become slightly inaccurate.

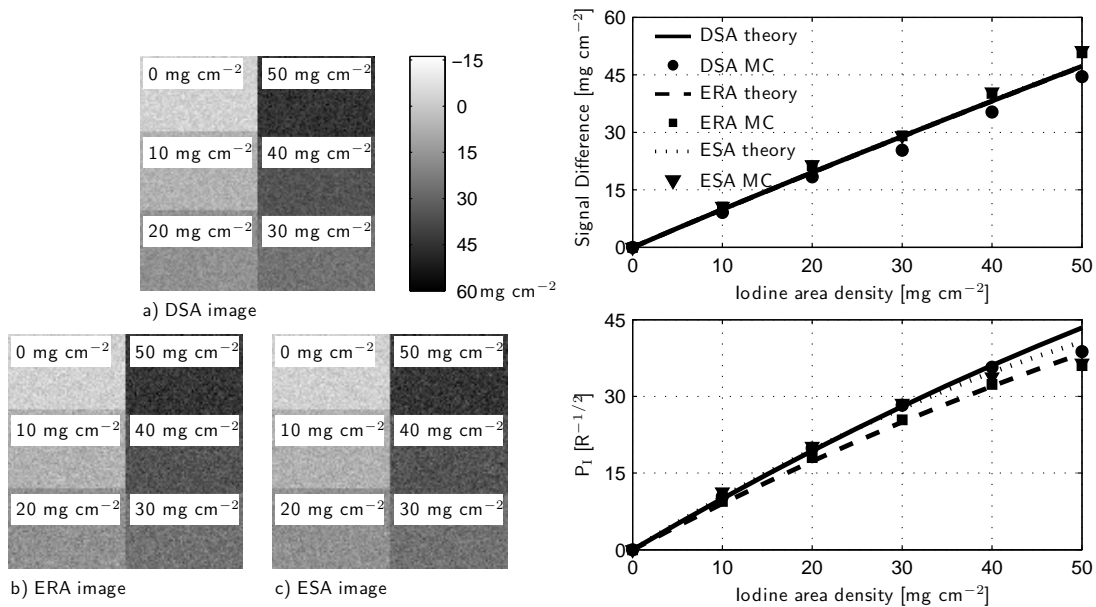


Figure 2.4.4: Simulated iodine-specific images of various iodine concentrations in 20 cm of water generated by Monte Carlo calculations.

Figure 2.4.5: Illustration of iodine signal and P_I for 20 cm of water and various iodine concentrations. Solid lines represent theoretical calculations and symbols represent Monte Carlo calculations.

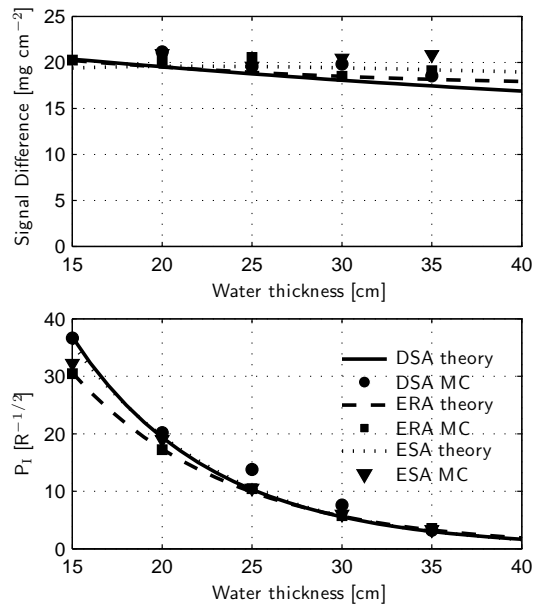


Figure 2.4.6: Illustration of the dependence of iodine signal and P_I on water thickness for 20 g cm⁻² of iodine. Solid lines represent theoretical calculations and symbols represent Monte Carlo calculations.

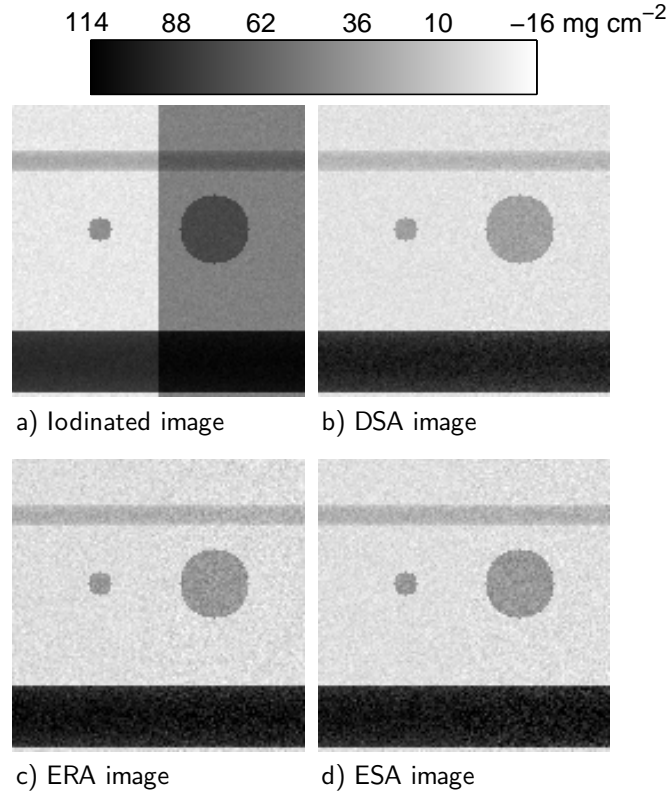


Figure 2.4.7: Comparison of simulated iodine-specific images containing 20 cm of water with two horizontal vessels having diameters of 0.2 and 0.5 cm filled with 0.1 g cm^{-3} of iodine and two circular vessels with diameters of 0.2 and 0.5 cm. A 2-cm thick layer of water is overlaid on the right half of the image to provide background contrast.

The lower plot of Fig. 2.4.6 shows that all three methods have similar P_I values over a wide range of water thickness values, although DSA is slightly better below 20 cm. However, it must be emphasized that the spectral methods shown here are not necessarily optimized and may be improved further. The important observation is to note how similar they are to each other.

2.4.2 Background suppression

The ability of each method to suppress (non-iodinated) background structures is illustrated in Fig. 2.4.7 where an extra 2 cm of water was placed in the right half of each image in the Monte Carlo calculation. All three methods show excellent suppression with only minor noise modulation caused by reduced x-ray transmission through the additional water thickness.

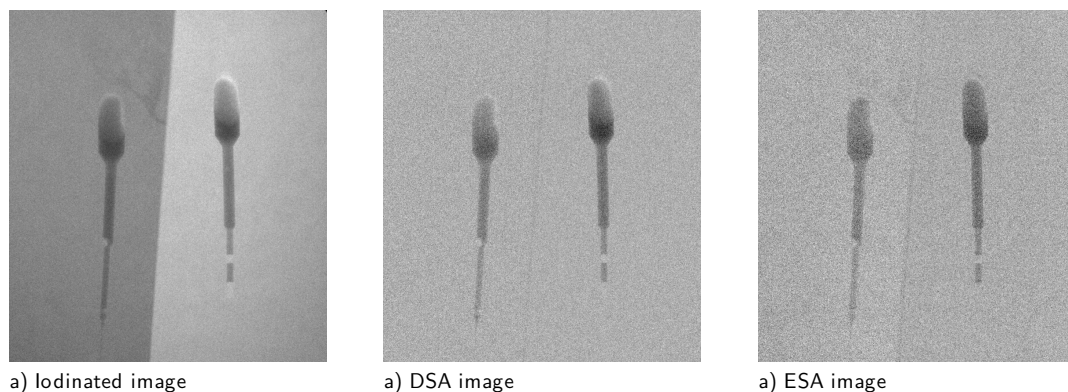


Figure 2.4.8: Visual comparison of ESA with DSA using a vascular phantom consisting of two tubes of variable inner diameter (steps of 0.15, 0.4 and 0.8 cm) containing 0.1 g cm^{-3} of iodine in 20 cm of water. An extra 2.5 cm of PMMA was placed over the left tube to provide background (non-iodinated) contrast. a) Iodinated image (63 kV, 9 mR). b) DSA image (63 kV, 18 mR). c) ESA image (50/130 kV, 15 mR).

2.4.3 Visual comparison of ESA with DSA

Experimental DSA and ESA images are shown in Fig. 2.4.8. The background PMMA structure has been effectively removed and a series of very small air bubbles, adhering to the top section of each vessel, appear as increased brightness in the DSA image but do not appear at all in the ESA image (ESA is a true iodine-specific method). The ESA image appears slightly noisier than the DSA image for two reasons: 1) the x-ray exposure used to acquire the ESA image was 17% lower than that used to acquire the DSA image; and 2) the ESA method requires an open-field image to determine \tilde{M}_{i0} as described in Sec. III.C and an insufficient number of images were averaged (10 at a reduced mAs) to avoid adding noise to the iodine image. In practice, it would be necessary to average a large number of open images (no patient) to ensure maximal iodine SNR.

2.5 Discussion

Energy-resolved and energy-subtraction angiography are exciting alternatives to DSA and their potential success depends largely on the image quality that can be achieved for a given exposure (or effective dose) to the patient. We have presented a theoretical framework for such a comparison based on linear estimates of basis-material area densities. It is sufficiently general to include either energy-integrating or energy-resolving photon-counting x-ray detectors, or a combination such as that described by Alvarez.^[9]

While the tube heat load for ESA was higher than that of DSA by 2x to 4x, and photon-counting

detectors are not yet ready for angiographic imaging, the available iodine SNR for both methods as tested is within 10% of that of conventional DSA for the same patient exposure over a wide range of patient thicknesses and iodine concentrations. This was an unexpected result as it is generally regarded that image quality (iodine SNR) obtained with ESA is less than that of DSA. Early dual-energy studies may have suffered from technological limitations that are less of an issue now.

It must also be noted that the results shown here apply only to the methods as tested. There may be alternative approaches that could improve each method, such as increasing the number of energy bins used for decomposition in ERA, or using a weighted linear least-squares approach to estimate iodine signal that takes into consideration the statistics of the energy bins. Also, while the linearized methods compared in this study are commonly used in energy-subtraction,^[58,108,213] temporal-subtraction,^[59] and energy-resolved^[67,105,166,167] approaches, we have not compared non-linear iterative methods such as those of Lehmann *et al.*^[107] and Schlomka *et al.*^[165] Suppression of more than one material (such as bone and soft tissue) might require additional images for ESA or energy bins for ERA and likely reduce SNR, but has not been compared.

For each technique considered in this study we assumed ideal x-ray detector technology for both theoretical and simulation studies. For example, in the case of ERA, pulse pile up will likely reduce SNR but was not considered. In addition, the random processes of x-ray interactions (eg. conversion to secondary quanta, characteristic escape, etc.) that degrade the detective quantum efficiency (and SNR) of all x-ray detectors^[60,77,78,221] will reduce image quality for DSA, ESA, and ERA, and have not been addressed.

2.6 Conclusions

The linearized noise-propagation analysis described here provides a framework for optimizing and evaluating iodine SNR that may be obtained using novel energy-based methods. Using this framework, energy-resolved photon-counting angiography and dual-energy angiography were compared with conventional digital-subtraction angiography. Theoretical models were validated with Monte Carlo calculations, and a qualitative comparison of dual-energy angiography with DSA showed similar image quality. While the energy-based methods are not necessarily optimized and further improvements are likely, it is concluded that both dual-energy and photon-counting approaches have the potential to provide similar iodine SNR to DSA for the same x-ray exposure.

Chapter 3

Fundamental signal and noise limits of photon counting x-ray detectors

This chapter is adapted from a manuscript entitled “The detective quantum efficiency of photon-counting x-ray detectors using cascaded-systems analyses” by Jesse Tanguay, Seungman Yun, Ho Kyung Kim, and Ian A. Cunningham, published in *Medical Physics* 2013; 40(4): 041913-1.

3.1 Introduction

Innovative advances in x-ray detector technology are leading to the development of single-photon-counting (SPC) energy-resolving x-ray detectors. [5,15,18,28,41,91,118,129,198,215,216] These have the potential for advanced spectroscopic applications such as energy-resolved angiography using measurements of the x-ray spectrum to generate angiographic images from a single exposure^[192] with reduced risk of motion artifacts, and improved image quality by reducing detector noise from stochastic conversion gain, poor collection efficiency, additive noise, and broad-spectrum imaging (Swank noise).^[129]

There are many challenges that must be overcome before the full benefits of SPC imaging can be achieved. These include materials engineering, count rate limitations,^[155,186,197] detector-element size^[18,212] and others.^[15,24] However, direction must also come from signal and noise considerations to ensure the performance of these new systems will produce superior image quality. For example, variability in deposited photon energy due to random escape of Compton scatter and characteristic emissions will degrade the precision of energy measurements.^[191] Scatter reabsorption and spreading of secondary image quanta (e.g., charge pairs in a photoconductor or optical quanta in a phosphor)

may result in cross-talk between detector elements^[178] and a decrease in the detective quantum efficiency (DQE).^[5] Adaptive binning approaches that sum signals from a number of elements surrounding each primary interaction to determine the total deposited energy, such as one implemented in the Medipix-3 prototype,^[18,139,198] may mitigate this effect, although use of broad x-ray spectra, statistical variations in conversion to secondary quanta, optical or charge collection efficiency, additive noise and other considerations may still compromise SPC detector performance.

Over the past several years, a cascaded-systems approach has been developed to describe how these considerations affect the DQE of conventional energy-integrating detectors. By propagating metrics of signal and noise through a cascade of fundamental image-forming processes^[6,53,54,125,146,164,214,218] the DQE^[170] of a complex cascade is given by^[52]

$$\text{DQE}(\mathbf{k}) = \frac{\bar{d}^2 T^2(\mathbf{k})}{\bar{q}_o \text{NPS}(\mathbf{k})} \quad (3.1.1)$$

where $\mathbf{k} = (u, v)$ [cycles/mm] represents a spatial-frequency vector with components in x and y directions, \bar{q}_o [mm⁻²] represents the mean distribution of incident x-ray quanta, \bar{d} represents the mean detector signal, $T(\mathbf{k})$ represents the modulation transfer function (MTF), and $\text{NPS}(\mathbf{k})$ [mm²] represents the image Wiener noise-power spectrum (NPS). Since the DQE is a Fourier-based metric, it is applicable for linear and shift-invariant (LSI) systems having wide-sense stationary (WSS) or wide-sense cyclo-stationary (WSCS) noise processes.^[33,52,143]

Cascaded-systems analysis (CSA) has been successful in the development of theoretical models that describe the DQE of many current systems and identify physical processes that determine detector performance and image quality.^[77,78,148,180,218] However, while the success of SPC detectors will depend in part on how the DQE compares with that of conventional systems, existing methods of analysis for SPC detectors remain preliminary and do not account for many factors known to be important in conventional systems including secondary quantum sinks^[53] and the statistical nature of other imaging-forming processes. In this first contribution on CSA methods and the DQE of SPC detectors, we describe stochastic conversion of incident photons to secondary quanta, collection of secondary quanta into detector elements, secondary quantum sinks, additive noise, and thresholding. It is shown that the DQE of SPC systems can be determined using the CSA approach by cascading the probability density function (PDF) of the number of image-forming quanta through each process in addition to conventional metrics of signal and noise. This gives rise to the necessary conditions on these design parameters to ensure an optimal DQE.

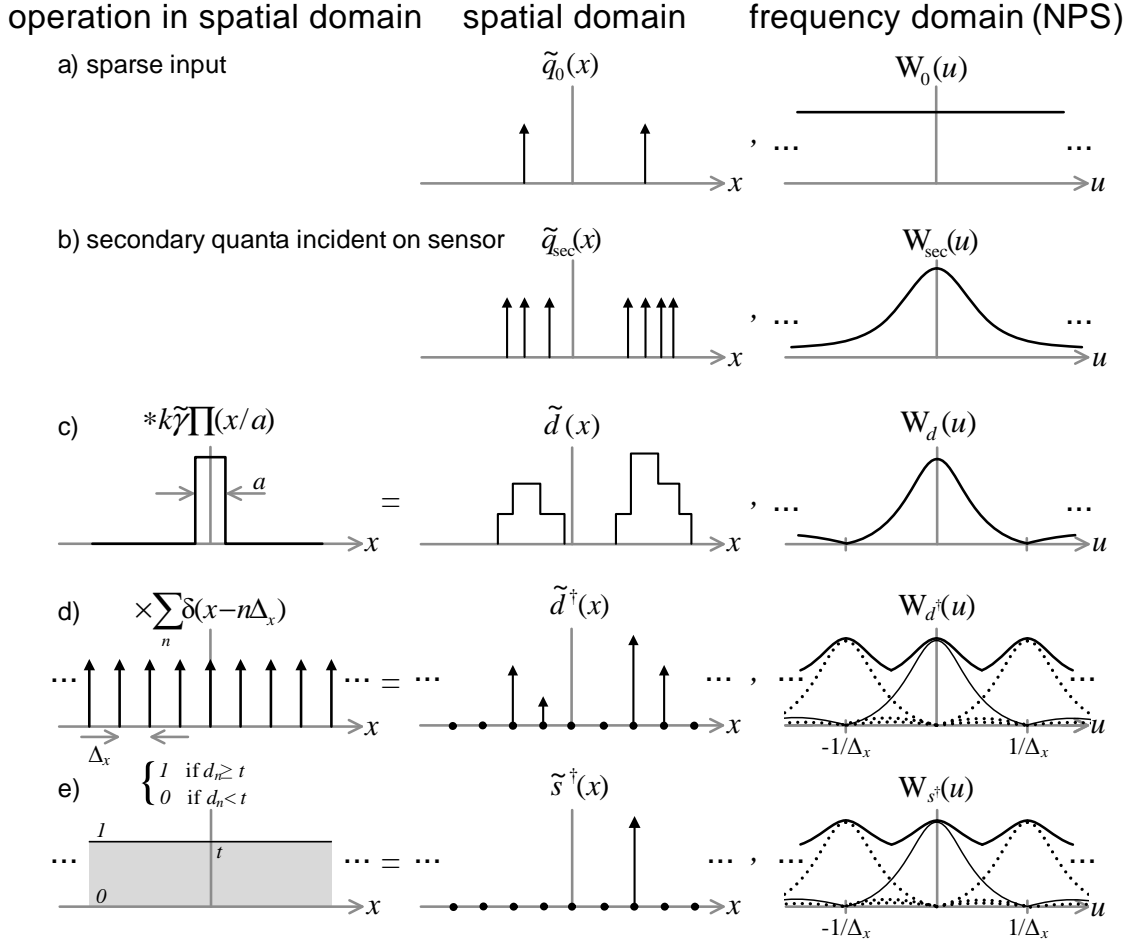


Figure 3.2.1: One-dimensional schematic representation of the process of converting a distribution of incident x-ray quanta (\tilde{q}_0) to secondary quanta such as liberated charges in a photoconductor (\tilde{q}_{sec}) incident on the sensors, to the detector presampling signal \tilde{d} , and then to the thresholded signal \tilde{s}^\dagger from one detector readout. The superscript \dagger indicates a function consisting of a uniform sequence of delta functions scaled by discrete detector values and superscript j has been omitted for simplicity.

3.2 Theory

3.2.1 Signal and noise in SPC detectors

Photon-counting detectors are essentially conventional detectors operating with very low noise and fast electronic readout such that there is little chance of more than one photon interacting in any one detector element in each readout. Images are generated by acquiring multiple readouts and counting the number of photons interacting in each element. Our CSA model of the SPC detector is therefore based on a conventional (energy-integrating) detector consisting of converter (e.g. photoconductor or phosphor/scintillator) and sensor (e.g. CMOS) layers with fast readout and thresholding electronics

as illustrated in Fig. 3.2.1. The following sections describe signal and noise transfer through this model assuming WSS/WSCS conditions.

3.2.1.1 Incident x-ray quanta, \tilde{q}_o

The description starts with a sparse distribution of x-ray quanta incident during the j th readout, represented by the random point process $\tilde{q}_o^j(\mathbf{r})$ [mm^{-2}] consisting of non-overlapping Dirac δ impulses^[20,22,214] (Fig. 3.2.1a). Therefore,

$$\tilde{q}_o^j(\mathbf{r}) = \sum_{i=1}^{\tilde{N}_o^j} \delta(\mathbf{r} - \tilde{\mathbf{r}}_i^j) \quad (3.2.1)$$

where overhead tilde denotes a random variable (RV), \tilde{N}_o^j is an integer-valued RV giving the number of quanta incident during readout j and $\{\tilde{\mathbf{r}}_i^j, i = 1.. \tilde{N}_o^j\}$ is the set of independent and identically-distributed RVs indicating quanta coordinates in image space. The mean is given by $\bar{q}_o^j = \tilde{N}_o^j/A = \bar{q}_o a_t$ [mm^{-2}] where A [mm^2] is the detector area, \bar{q}_o [$\text{mm}^{-2}\text{s}^{-1}$] is the mean rate of x-ray quanta incident on the detector, and a_t [s] is the integration time of one readout assuming no dead time between readouts. The NPS is given by $\text{NPS}_o^j(\mathbf{k}) = \bar{q}_o^j$ [mm^{-2}].^[20,52]

3.2.1.2 Conversion to secondary image-forming quanta, \tilde{q}_{sec}

Deposited x-ray energy will liberate secondary image quanta (charge pairs or optical quanta) in the converter layer at the primary interaction site and possibly at a nearby location if a scatter/emission photon is reabsorbed. We let \tilde{q}_{sec}^j (Fig. 3.2.1b) represent the resulting spatial distribution of secondary quanta incident on the sensor layer with associated MTF and NPS given by $T_{\text{sec}}(\mathbf{k})$ and $\text{NPS}_{\text{sec}}(\mathbf{k})$.

3.2.1.3 Collection of secondary quanta by sensor elements

The readout signal from each detector element is proportional to the number of secondary quanta collected in the element plus a random contribution from readout electronics. In the CSA approach, this is represented by a selection of those secondaries that contribute to the sensor signals followed by the collection of these secondaries into a signal from each element. These are described as a quantum-selection process with probability γ (the sensor quantum efficiency) and convolution with a rectangular aperture function respectively (Fig. 3.2.1c). Therefore,

$$\tilde{d}^j(\mathbf{r}) = k \tilde{\gamma} \tilde{q}_{\text{sec}}^j(\mathbf{r}) * \Pi\left(\frac{\mathbf{r}}{\mathbf{a}}\right) + \tilde{e}(\mathbf{r}) \quad (3.2.2)$$

where k is a constant of proportionality, $\tilde{\gamma}$ is a Bernoulli RV with mean γ and sample values 0 or 1 for each secondary describing whether the secondary contributes to sensor signal or not, and $\Pi(\mathbf{r}/\mathbf{a})$ represents a two-dimensional rectangular aperture function having area a and dimension $a_x \times a_y$ in x and y directions respectively defining the active area of a sensor element centered at $(x, y) = (0, 0)$. Additive noise \tilde{e} is represented as a WSS zero-mean noise density with the property that the NPS integral over all frequencies is equal to the variance σ_e^2 . The presampling readout signal corresponds to an element centered at position \mathbf{r} but is physically meaningful only at locations corresponding to the centers of the elements. The corresponding presampling NPS is given by^[52]

$$\text{NPS}_d(\mathbf{k}) = [\gamma^2 (\text{NPS}_{\text{sec}}(\mathbf{k}) - \bar{q}_{\text{sec}}) + \gamma \bar{q}_{\text{sec}}] a_x^2 a_y^2 \text{sinc}^2(a_x u) \text{sinc}^2(a_y v). \quad (3.2.3)$$

3.2.1.4 Detector-element signals, $\tilde{d}^{\dagger j}$

The process of determining signals from each element is represented as multiplication with a series of Dirac δ functions (Fig. 3.2.1d) and the sampled signal $\tilde{d}^{\dagger j}(\mathbf{r})$ is given by

$$\tilde{d}^{\dagger j}(\mathbf{r}) = \tilde{d}^j(\mathbf{r}) \sum_{n=-\infty}^{\infty} \sum_{m=-\infty}^{\infty} \delta(\mathbf{r} - \mathbf{r}_{nm}) \quad (3.2.4)$$

where $\mathbf{r}_{nm} = (n\Delta_x, m\Delta_y)$ and $\mathbf{\Delta} = (\Delta_x, \Delta_y)$ represents the center-to-center element spacing (pixel pitch).

3.2.1.5 Thresholded signal, $\tilde{s}^{\dagger j}$

Photon counting is achieved by applying a threshold to distinguish interaction events from noise in each readout. Ideally, each readout interval is short such that the probability of multiple photon interactions in the same element is small (i.e., $a_t \ll 1/\bar{q}_0 a$). Pile-up occurs when this condition is not satisfied and the detected count rate will be decreased.^[100,217] In either case, the result is a Bernoulli RV \tilde{s}_{nm}^j having sample values of 1 or 0 (Fig. 3.2.1e) where

$$\tilde{s}_{nm}^j = \begin{cases} 1 & \text{for } \tilde{d}_{nm}^j \geq t \\ 0 & \text{for } \tilde{d}_{nm}^j < t \end{cases} \quad (3.2.5)$$

in the j th readout for threshold t . We assume a lag-free detector such that \tilde{s}_{nm}^j and \tilde{s}_{nm}^i are independent RVs for $i \neq j$ and define $\tilde{s}^{\dagger j}(\mathbf{r})$ [mm⁻²] as the sampled and thresholded image signal:

$$\tilde{s}^{\dagger j}(\mathbf{r}) = \tilde{s}^j(\mathbf{r}) \sum_{n=-\infty}^{\infty} \sum_{m=-\infty}^{\infty} \delta(\mathbf{r} - \mathbf{r}_{nm}) \quad (3.2.6)$$

where $\tilde{s}^j(\mathbf{r})$ is a continuous presampling representation of \tilde{s}_{nm}^j . An SPC image is produced after M readouts using \tilde{s}_{nm}^j to increment a counter for each element, resulting in image $\tilde{c}^{\dagger}(\mathbf{r})$:

$$\tilde{c}^{\dagger}(\mathbf{r}) = \sum_{j=1}^M \tilde{s}^{\dagger j}(\mathbf{r}) \quad (3.2.7)$$

represented as a sequence of scaled δ -functions.

3.2.1.6 Mean SPC signal, \bar{c} :

The mean SPC image signal is given by

$$\mathbb{E}(\tilde{c}^{\dagger}(\mathbf{r})) = \sum_{n=-\infty}^{\infty} \sum_{m=-\infty}^{\infty} \mathbb{E}(\tilde{c}(\mathbf{r})) \delta(\mathbf{r} - \mathbf{r}_{nm}). \quad (3.2.8)$$

Following the notation of Papoulis,^[143] we let $p_c(c; \mathbf{r})$ represent the PDF of $\tilde{c}(\mathbf{r})$ and therefore $\mathbb{E}(\tilde{c}(\mathbf{r})) = \int_{-\infty}^{+\infty} c p_c(c; \mathbf{r}) dc$. Since \tilde{c} is equal to the summation of M Bernoulli RVs, the binomial distribution gives^[143]

$$p_c(c; \mathbf{r}) = \sum_{i=0}^M \binom{M}{i} \zeta^i (1 - \zeta)^{M-i} \delta(\tilde{c}(\mathbf{r}) - i) \quad (3.2.9)$$

where ζ is equal to the probability that $\tilde{d}^j \geq t$ and is the same for each readout. Therefore,

$$\mathbb{E}\{\tilde{c}(\mathbf{r})\} = \sum_{i=0}^M i \binom{M}{i} \zeta^i (1 - \zeta)^{M-i} \quad (3.2.10)$$

$$= M \mathbb{P}(\tilde{d}(\mathbf{r}) \geq t) \quad (3.2.11)$$

where $\mathbb{P}(\cdot)$ represents the probability of observing the specified event. Since \tilde{d} is WSS, it has the PDF $p_d(d; \mathbf{r}) = p_d(d)$, and thus while \tilde{d} is a function of \mathbf{r} , its PDF is not, giving

$$\mathbb{E}(\tilde{c}(\mathbf{r})) = \bar{c} = M \int_t^{\infty} p_d(d) dd. \quad (3.2.12)$$

Equation (3.2.12) is a key intermediate result of this work. It shows that the mean signal from an SPC detector is shift invariant and, more importantly, can be determined simply from the PDF of \tilde{d} . In Sec. 3.2.4 it will be shown that this PDF can be determined by propagating the PDF for the total number of image-forming quanta through each process in a cascade of image-forming processes.

3.2.1.7 SPC autocovariance and Wiener noise power spectrum:

The sampled SPC signal $\tilde{c}^\dagger(\mathbf{r})$ has an autocovariance given by^[52,143]

$$K_{c^\dagger}(\mathbf{r}, \mathbf{r} + \boldsymbol{\tau}) = \sum_{n=-\infty}^{\infty} \sum_{m=-\infty}^{\infty} \sum_{n'=-\infty}^{\infty} \sum_{m'=-\infty}^{\infty} K_c(\mathbf{r}, \mathbf{r} + \boldsymbol{\tau}) \delta(\mathbf{r} - \mathbf{r}_{nm}) \delta(\mathbf{r} + \boldsymbol{\tau} - \mathbf{r}_{n'm'}) \quad (3.2.13)$$

where K_c represents the autocovariance of \tilde{c} :

$$K_c(\mathbf{r}, \mathbf{r} + \boldsymbol{\tau}) = R_c(\mathbf{r}, \mathbf{r} + \boldsymbol{\tau}) - \bar{c}^2 \quad (3.2.14)$$

where $R_c(\mathbf{r}, \mathbf{r} + \boldsymbol{\tau}) = \text{E}(\tilde{c}(\mathbf{r})\tilde{c}(\mathbf{r} + \boldsymbol{\tau}))$ is the autocorrelation of \tilde{c} given by:

$$R_c(\mathbf{r}, \mathbf{r} + \boldsymbol{\tau}) = \text{E} \left(\sum_{i=1}^M \sum_{j=1}^M \tilde{s}^i(\mathbf{r}) \tilde{s}^j(\mathbf{r} + \boldsymbol{\tau}) \right) \quad (3.2.15)$$

$$= \sum_{j=1}^M R_s^j(\mathbf{r}, \mathbf{r} + \boldsymbol{\tau}) + \sum_{i=1}^M \sum_{\substack{j=1 \\ j \neq i}}^M \text{E}(\tilde{s}^i(\mathbf{r}) \tilde{s}^j(\mathbf{r} + \boldsymbol{\tau})) \quad (3.2.16)$$

where we have separated the double summation into terms for which $i = j$ and $i \neq j$,^[22] $\text{E}(\tilde{s}^i(\mathbf{r}) \tilde{s}^j(\mathbf{r} + \boldsymbol{\tau})) = \bar{s}^2$, and R_s^j is the autocorrelation of \tilde{s}^j :

$$R_s^j(\mathbf{r}, \mathbf{r} + \boldsymbol{\tau}) = \int_{-\infty}^{+\infty} \int_{-\infty}^{+\infty} s^j s'^j p_s(s^j, s'^j; \mathbf{r}, \mathbf{r} + \boldsymbol{\tau}) ds^j ds'^j \quad (3.2.17)$$

where $p_s(s^j, s'^j; \mathbf{r}, \mathbf{r} + \boldsymbol{\tau})$ represents the joint PDF^[143] for $s^j(\mathbf{r})$ and $s'^j(\mathbf{r} + \boldsymbol{\tau}) = s^j(\mathbf{r} + \boldsymbol{\tau})$ and is the same for all j :

$$p_s(s^j, s'^j; \mathbf{r}, \mathbf{r} + \boldsymbol{\tau}) = \sum_{i=0}^1 \sum_{l=0}^1 \zeta_{il} \delta(s^j(\mathbf{r}) - i) \delta(s^j(\mathbf{r} + \boldsymbol{\tau}) - l) \quad (3.2.18)$$

where ζ_{il} represents the probability that $\tilde{s}(\mathbf{r})$ equals i and $\tilde{s}(\mathbf{r} + \boldsymbol{\tau})$ equals l . Therefore

$$R_s^j(\mathbf{r}, \mathbf{r} + \boldsymbol{\tau}) = \text{P} \left\{ \tilde{d}(\mathbf{r}) \geq t \text{ and } \tilde{d}(\mathbf{r} + \boldsymbol{\tau}) \geq t \right\} \quad (3.2.19)$$

$$= \int_t^\infty \int_t^\infty p_d(d, d'; \mathbf{r}, \mathbf{r} + \boldsymbol{\tau}) dd dd'. \quad (3.2.20)$$

Similar to the PDF for \tilde{d} , the joint PDF is a function of separation $\boldsymbol{\tau}$ and independent of \mathbf{r} ,^[143] and can be expressed as $p_d(d, d'; \boldsymbol{\tau})$. Combining this with Eqs. (3.2.14) and (3.2.16) yields

$$K_c(\mathbf{r}, \mathbf{r} + \boldsymbol{\tau}) = K_c(\boldsymbol{\tau}) = M \int_t^\infty \int_t^\infty p_d(d, d'; \boldsymbol{\tau}) dd dd' - M \left[\int_t^\infty p_d(d) dd \right]^2. \quad (3.2.21)$$

The above expression shows that the presampling SPC image signal \tilde{c} is WSS and, therefore, the sampled signal \tilde{c}^\dagger is a WSCS sequence of scaled δ -functions. Therefore,^[52,143]

$$K_{c^\dagger}(\mathbf{r}, \mathbf{r} + \boldsymbol{\tau}) = K_{c^\dagger}(\boldsymbol{\tau}) = \sum_{n=-\infty}^{\infty} \sum_{m=-\infty}^{\infty} K_c(\boldsymbol{\tau}) \delta(\boldsymbol{\tau} - \mathbf{r}_{nm}). \quad (3.2.22)$$

This is the second important result of this work and shows that the SPC autocovariance is determined by the joint PDF of $\tilde{d}(\mathbf{r})$ and $\tilde{d}(\mathbf{r} + \boldsymbol{\tau})$.

In general, the presampling NPS is given by the Fourier transform of the autocovariance, $\text{NPS}_c(\mathbf{k}) = \mathcal{F}\{K_c(\boldsymbol{\tau})\}$, and the NPS including the effects of sampling (noise aliasing) is given by

$$\text{NPS}_{c^\dagger}(\mathbf{k}) = \text{NPS}_c(\mathbf{k}) + \sum_{n=1}^{\infty} \sum_{m=1}^{\infty} \text{NPS}_c(\mathbf{k} \pm \mathbf{k}_{nm}) \quad (3.2.23)$$

where $\mathbf{k}_{nm} = (\Delta_x/n, \Delta_y/m)$. Therefore, for LSI systems with only WSS or WSCS noise processes (discussed further below), the DQE of SPC systems is given by

$$\text{DQE}_{\text{SPC}}(\mathbf{k}) = \frac{\bar{c}^2 T^2(\mathbf{k})}{\bar{q}_o \text{NPS}_{c^\dagger}(\mathbf{k})} \quad (3.2.24)$$

where \bar{c} and NPS_{c^\dagger} are the mean pixel value and NPS in an SPC image as given by Eqs. (3.2.12) and (3.2.23), respectively. This is equivalent in form to the DQE of a conventional detector in Eq. (3.1.1) after substituting \bar{c} with \bar{d} , although the NPS of \tilde{c} is different to that of \tilde{d} since they are determined by statistical fluctuations in the number of interacting photons (a Poisson RV) and deposited energy for each photon, respectively.

3.2.2 Special Case: Low count rates and no charge sharing

As a special case, we consider a low-count-rate limit where the probability that two photons deposit energy in the same element during a single readout is negligible (no pulse pile-up) and no charge sharing between elements. This may be a good assumption for photoconductor-based detectors such as Se, but possibly not for CsI-based systems where optical scatter will share x-ray quantum energy between more than one element. However, if adaptive binning is implemented to sum signals from elements surrounding a primary interaction, this assumption may also be valid as discussed in the Discussion section. The signal \tilde{d}^j therefore corresponds either to the case of all deposited energy from one photon, or no deposited energy. We continue to assume WSS/WSCS noise processes.

3.2.2.1 Mean signal, \bar{c}

The mean signal \bar{c} is obtained by combining Eqs. (3.2.12) with $p_d(d)$ which is calculated in Appendix B:

$$\bar{c} = \bar{q}_o a \xi_1(t) \left[1 + \frac{1 - \lambda \xi_0(t)}{\lambda \xi_1(t)} \right], \quad (3.2.25)$$

where $\lambda = \bar{q}_o a_T a$ and

$$\xi_0(t) = \int_t^{+\infty} p_d(d|_0) dd \quad (3.2.26)$$

$$\xi_1(t) = \int_t^{+\infty} p_d(d|_1) dd \quad (3.2.27)$$

representing the probability that \tilde{d} is greater than the threshold for the case of zero or one photons incident on an element, respectively. The second term in brackets in Eq. (3.2.25) corresponds to false-count events.

This result shows that for fast readouts and negligible secondary scatter, calculation of \bar{c} requires the PDF for \tilde{d} given one and zero incident photons. In addition, unlike conventional energy-integrating detectors but consistent with expectation, this result shows how zero-mean additive electronic noise may result in an increase in the mean SPC image signal.

3.2.2.2 Wiener noise power spectrum

The Wiener NPS requires calculation of the joint PDF for $\tilde{d}(\mathbf{r})$ and $\tilde{d}(\mathbf{r} + \boldsymbol{\tau})$ as described by Eq. (3.2.16). In Appendix B we show that for our special case it can be expressed in terms of the

PDF for the case of zero and one incident photons. The presampling NPS is derived Appendix B and is given by

$$\text{NPS}_c(\mathbf{k}) = \sigma_c^2 a \text{sinc}^2(a_x u) \text{sinc}^2(a_y v) \quad (3.2.28)$$

where σ_c^2 is the variance in the number of counts from a single element, given by

$$\sigma_c^2 = \bar{q}_o a \xi_1(t) \left[1 + \frac{(1-\lambda)^2}{\lambda} \left(\frac{1}{1-\lambda} - \xi_0(t) \right) \frac{\xi_0(t)}{\xi_1(t)} - 2(1-\lambda) \xi_0(t) \right]. \quad (3.2.29)$$

3.2.3 PDF transfer through elementary processes

In this section, we show that the PDF of \tilde{d} can be determined by cascading the PDF through elementary image-forming processes and describe the transfer relationships for each. This is a key result as it means the cascaded approach can be applied to photon-counting systems with the additional step of cascading the PDF of the total number of image quanta at each stage.

We let $p_{\text{in}}(N_{\text{in}})$ and $p_{\text{out}}(N_{\text{out}})$ represent the PDFs of the total number of input quanta \tilde{N}_{in} and output quanta \tilde{N}_{out} , respectively. In general, the PDF of \tilde{N}_{out} is given by

$$p_{\text{out}}(N_{\text{out}}) = \int_0^\infty p_{\text{out}}(N_{\text{out}}|N_{\text{in}}) p_{\text{in}}(N_{\text{in}}) dN_{\text{in}} \quad (3.2.30)$$

where $p_{\text{out}}(N_{\text{out}}|N_{\text{in}})$ is the PDF for \tilde{N}_{out} given \tilde{N}_{in} . Since \tilde{N}_{in} and \tilde{N}_{out} assume integer values only, $p_{\text{out}}(N_{\text{out}})$ can be expressed as point processes:

$$p_{\text{out}}(N_{\text{out}}) = \sum_{n'=0}^\infty \text{pr}_{\text{out}}(N_{\text{out}} = n') \delta(N_{\text{out}} - n') \quad (3.2.31)$$

where

$$\text{pr}_{\text{out}}(N_{\text{out}}) = \sum_{n''=0}^\infty \text{pr}_{\text{out}}(N_{\text{out}}|N_{\text{in}} = n'') \text{pr}_{\text{in}}(N_{\text{in}} = n'') \quad (3.2.32)$$

is the PMF for \tilde{N}_{out} . This is a general result that we now use to determine PDF transfer relationships for the elementary processes of quantum selection, quantum gain, and quantum scatter.

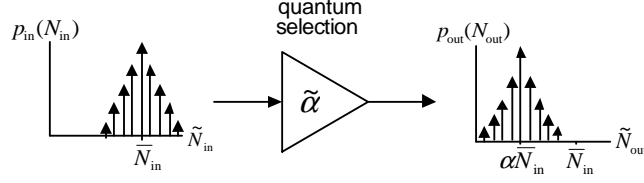


Figure 3.2.2: Schematic illustration of transfer of the PDF describing the total number of image quanta through a quantum selection stage. The PDF for \tilde{N}_{out} is shifted to the left relative of that for \tilde{N}_{in} and approaches a Poisson distribution for small α .

3.2.3.1 Quantum selection

A quantum selection stage describes the process of randomly selecting quanta from a distribution and can be used to describe a quantum efficiency or collection probability.^[52] The total number of quanta following a quantum selection stage is given by

$$\tilde{N}_{\text{out}} = \sum_{i=1}^{\tilde{N}_{\text{in}}} \tilde{\alpha}_i \quad (3.2.33)$$

where $\tilde{\alpha}_i$ is a Bernoulli RV that assumes values of either 1 (with probability α) or zero (with probability $1 - \alpha$). Since \tilde{N}_{out} is equal to the summation of \tilde{N}_{in} Bernoulli RVs, the mean total number of quanta following a quantum selection stage is given by $\alpha\tilde{N}_{\text{in}}$. The PDF describing \tilde{N}_{out} is therefore shifted towards the origin (relative to $p_{\text{in}}(N_{\text{in}})$) as illustrated in Fig. 3.2.2, and $\text{pr}_{\text{out}}(N_{\text{out}} = j | N_{\text{in}} = i)$ is given by the binomial distribution:^[143]

$$\text{pr}_{\text{out}}(N_{\text{out}} = n' | N_{\text{in}} = n'') = \begin{cases} \binom{n''}{n'} \alpha^{n'} (1 - \alpha)^{n'' - n'} & n' \in \{0, 1, \dots, n''\} \\ 0 & \text{otherwise} \end{cases} \quad (3.2.34)$$

Combining Eqs. (3.2.31), (3.2.32) and (3.2.34) gives the PDF transfer relationship for quantum selection.

3.2.3.2 Quantum gain

Quantum gain represents the process of replacing the i th quantum in an input distribution with \tilde{g}_i quanta in the output, such as liberation of electron-hole pairs in a semiconductor by an x-ray

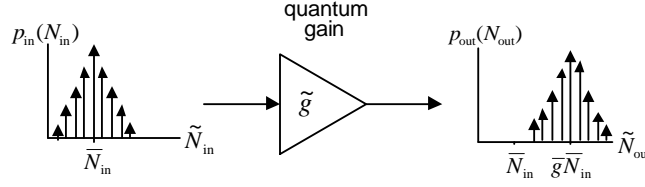


Figure 3.2.3: Schematic illustration of PDF transfer through a quantum gain stage. The PDF for \tilde{N}_{out} is shifted to the right relative to that for \tilde{N}_{in} and the shape of $p_{\text{out}}(N_{\text{out}})$ depends in part on the PDF describing \tilde{g} .

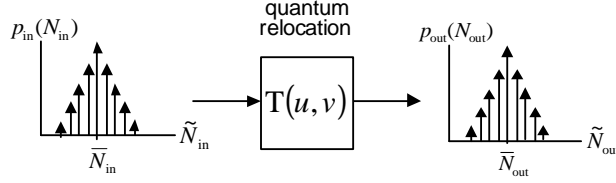


Figure 3.2.4: Schematic illustration of PDF transfer through a quantum relocation stage where the PDFs for \tilde{N}_{out} and \tilde{N}_{in} are always the same.

interaction, giving

$$\tilde{N}_{\text{out}} = \sum_{i=1}^{\tilde{N}_{\text{in}}} \tilde{g}_i. \quad (3.2.35)$$

Since \tilde{N}_{out} is the sum of \tilde{N}_{in} RVs and the set $\{\tilde{g}_i, i = 1.. \tilde{N}_{\text{in}}\}$ are independent and identically-distributed RVs, $\bar{N}_{\text{out}} = \bar{g}\bar{N}_{\text{in}}$. The PDF describing \tilde{N}_{out} is therefore right-shifted relative to $p_{\text{in}}(N_{\text{in}})$, as illustrated in Fig. 3.2.3, and the PMF for \tilde{N}_{out} given \tilde{N}_{in} is^[143]

$$\text{pr}_{\text{out}}(N_{\text{out}} = n' | N_{\text{in}} = n'') = \left(\text{pr}_g *^{(n''-1)} \text{pr}_g \right) \Big|_{g=n'} \quad (3.2.36)$$

where $\text{pr}_g(g)$ is the PMF for \tilde{g} and $(\text{pr}_g *^{(n''-1)} \text{pr}_g) \Big|_{g=n'}$ represents the discrete convolution of $\text{pr}_g(g)$ with itself $n'' - 1$ times evaluated at $\tilde{g}=n'$. Combining Eqs. (3.2.31), (3.2.32) and (3.2.36) yields the PDF transfer relationship for a quantum gain stage.

3.2.3.3 Quantum relocation

Quantum relocation represents the process of randomly relocating quanta in an input distribution. This does not change the total number of image quanta and therefore (Fig. 3.2.4):

$$\text{pr}_{\text{out}}(N_{\text{out}} = n' | N_{\text{in}} = n'') = \delta(n' - n'') \quad (3.2.37)$$

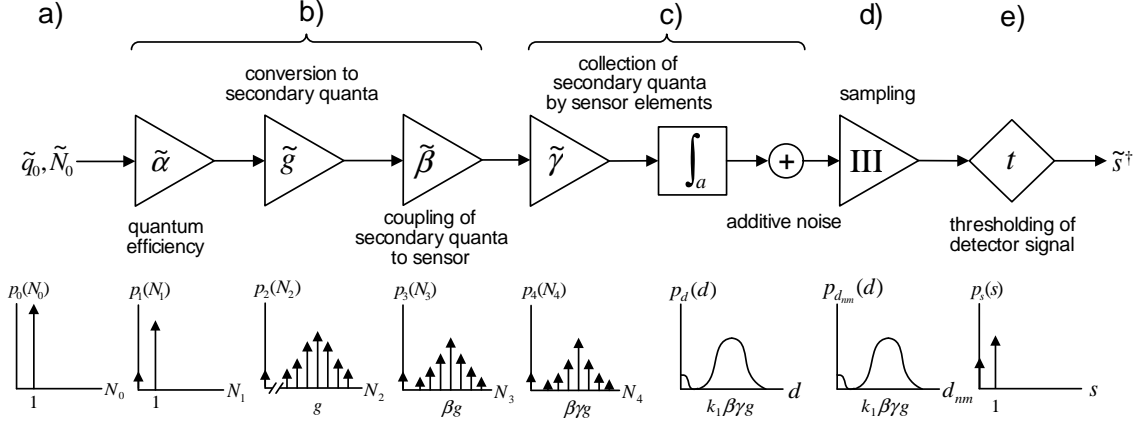


Figure 3.2.5: Schematic representation of the CSA model used to describe transfer of signal, noise and PDF of image quanta through an SPC x-ray detector. Letters a) to e) correspond to labels in Fig. 3.2.1. Figures in bottom row represent PDFs at output of each stage.

3.2.4 Application to simple SPC detector model

We apply the theoretical formalism developed above to the description of the simple SPC detector illustrated in Fig. 3.2.5. We assume mono-energetic x-rays, no pile-up and negligible secondary quanta relocation as described above. Limitations of this model for describing prototype SPC detectors in a clinical environment are addressed in the Discussion.

Stage 1: Interaction of incident x-ray quanta in convertor. Each incident x-ray photon interacts in the convertor material with probability α equal to the detector quantum efficiency. The PDF of the total number of interacting x-ray photons \tilde{N}_1 is obtained using Eq. (3.2.32) with $\text{pr}_{N_1}(N_1|N_0=1)$ given by Eq. (3.2.34) and $p_0(N_0) = \delta(N_0 - 1)$:

$$\text{pr}_1(N_1 = n' | N_0 = 1) = \alpha^{n'} (1 - \alpha)^{n'' - n'} . \quad (3.2.38)$$

The PDF describing the number of interacting x-ray photons given one incident is given by

$$p_1(N_1 | N_0 = 1) = (1 - \alpha) \delta(N_1) + \alpha \delta(N_1 - 1) . \quad (3.2.39)$$

The above expression is illustrated schematically in Fig. 3.2.5.

Stage 2: Liberation of secondary quanta in convertor. We assume that the i th interacting x-ray photon liberates \tilde{g}_i secondary quanta (e-h pairs or optical quanta) and that this process obeys Poisson statistics. The PDF for \tilde{g}_i is then given by the Poisson distribution and Eq. (3.2.36) becomes

$$\text{pr}_2(N_2 = n' | N_1 = n'') = \begin{cases} 1 & n'' = 0 \\ \text{pr}_g(n') & n'' = 1 \end{cases}. \quad (3.2.40)$$

The PDF describing the number of liberated secondaries given one incident photon is

$$p_2(N_2 | N_0 = 1) = (1 - \alpha) \delta(N_2) + \alpha \sum_{n''=0}^{\infty} \text{pr}_g(N_2) \delta(N_2 - n''). \quad (3.2.41)$$

Stage 3: Coupling of secondary quanta to sensor elements. A fraction β of liberated secondaries are coupled to the sensor elements. This could reflect losses due to charge recombination in a photoconductor^[83,94,100] or optical attenuation in a phosphor/scintillator.^[52,86,157,180,182,221] We assume β is independent of depth, giving

$$\text{pr}_3(N_3 = n' | N_2 = n'') = \begin{cases} 1 & n'' = 0 \\ \binom{n''}{n'} \beta^{n'} (1 - \beta)^{n'' - n'} & n'' \geq 1 \end{cases} \quad (3.2.42)$$

and

$$p_3(N_3 | N_0 = 1) = (1 - \alpha) \delta(N_3) + \alpha \sum_{n''=0}^{\infty} \sum_{n'=1}^{n''} \text{pr}_g(g = n'') \binom{n''}{n'} \beta^{n'} (1 - \beta)^{n'' - n'} \delta(N_3 - n'). \quad (3.2.43)$$

Stage 4: Collection of secondary quanta in detector elements and additive noise.

a) Each secondary incident on the sensor elements has a probability γ of contributing to the measured signal, accounting for sensor quantum efficiency.^[52,86,157,180,182,221] The PMF of \tilde{N}_4 given \tilde{N}_3

has a form similar to Eq. (3.2.42) with the substitution of γ for β , giving

$$p_4(N_4|N_0=1) = \sum_{n''=0}^{\infty} \sum_{n'=0}^{n''} \binom{n''}{n'} \gamma^{n'} (1-\gamma)^{n''-n'} \text{pr}_3(N_3=n''|N_0=1) \delta(N_4-n') \quad (3.2.44)$$

b) The readout signal \tilde{d} is proportional to the number of secondaries that are collected in each detector element plus an additive component due to the detector electronics as described in Appendix B, giving^[143]

$$p_d(d|_1) = \frac{1}{k} p_4\left(\frac{d|_1}{k}\right) * p_e(d|_1) \quad (3.2.45)$$

where $p_e(d|_1)$ represents the PDF of \tilde{e} evaluated at $d|_1$. In all cases we assume that \tilde{e} is a zero-mean normally-distributed RV with variance σ_e^2 .

Stage 5: Sampling of detector elements. Generating a discrete output signal for each element is represented as a sampling process (Fig. 3.2.1) and does not change the PDF for \tilde{d} .

Stage 6: Thresholding of sampled detector signals. Calculation of both the mean signal and NPS following a thresholding stage requires the integral of $p_d(d|_1)$ and $p_d(d|_0)$ from t to infinity, represented by $\xi_1(t)$ and $\xi_0(t)$, respectively:

$$\xi_1(t) = (1-\alpha)\xi_F(t) + \alpha\xi_T(t) \quad (3.2.46)$$

$$\xi_0(t) = \xi_F(t) \quad (3.2.47)$$

where ξ_T and ξ_F represent contributions from true-count and false-count events, respectively, as developed in Appendix B.

3.2.4.1 Mean signal, \bar{c}

Combining Eqs. (3.2.25), (3.2.46), and (3.2.47) yields

$$\bar{c} = \bar{q}_o a \alpha \xi_T(t) \left[1 + \frac{1-\lambda\alpha}{\lambda\alpha} \frac{\xi_F(t)}{\xi_T(t)} \right], \quad (3.2.48)$$

demonstrating that false counts due to additive noise will increase average image signal. This can be avoided by choosing a threshold that satisfies the inequality:

$$\frac{\xi_T(t)}{\xi_F(t)} \gg \frac{1 - \lambda\alpha}{\lambda\alpha}. \quad (3.2.49)$$

3.2.4.2 Noise power spectrum and individual element noise

Combining Eqs. (3.2.28), (3.2.46), and (3.2.47) yields the presampling NPS and integrating over all spatial frequencies gives the image pixel variance: ^[143]

$$\sigma_c^2 = \int_{\mathbb{R}^2} \text{NPS}_c(\mathbf{k}) d^2\mathbf{k} \quad (3.2.50)$$

$$= \bar{q}_o a \alpha \xi_T(t) \left[1 + \frac{\xi_F(t)}{\xi_T(t)} \left(\frac{1 - \lambda\alpha}{\lambda\alpha} - \frac{(1 - \lambda)^2}{\lambda\alpha} \xi_F(t) \right) - 2(1 - \lambda) \xi_F(t) \left(\frac{1 - \alpha}{\alpha} \frac{\xi_F(t)}{\xi_T(t)} + 1 \right) \right] \quad (3.2.51)$$

$$\approx \bar{q}_o a \alpha \xi_T(t) \left[1 + \frac{\xi_F(t)(1 - \xi_F(t))}{\xi_T(t)\lambda\alpha} - 2\xi_F(t) \left(\frac{1 - \alpha}{\alpha} \frac{\xi_F(t)}{\xi_T(t)} + 1 \right) \right] \quad (3.2.52)$$

where we used $\lambda \ll 1$ in the approximation. This demonstrates that the SPC pixel variance is equal to the variance in the number of true-count events plus the variance in the number of false-count events.

3.2.4.3 Photon-counting $DQE(0)$

Combining Eqs. (3.2.24), (3.2.28), and (3.2.48), and assuming a threshold that satisfies Eq. (3.2.49), the zero-frequency DQE for the model considered in this work is given by

$$\text{DQE}(0) = \frac{\bar{c}^2}{\text{NPS}_{c^+}(0)} = \alpha \xi_T(t) \quad (3.2.53)$$

where $\xi_T(t) \in [0, 1]$. This is an important result and demonstrates that the zero-frequency DQE of an SPC detector with no pile-up is given by the product of the detector quantum efficiency and a new noise factor equal to the true-count probability given by the probability that the signal generated by one interacting x-ray photon is greater than the threshold t .

3.3 Monte Carlo Validation

A simple Monte Carlo analysis was performed to test the theoretical derivation described above. Using the same assumptions and assumed values of α , β , γ , \bar{g} , and σ_e , x-ray images were simulated using the following seven-step algorithm:

1. For each readout, generate the total number of incident Poisson-distributed photons.
2. Select photons that interact in the detector with probability of interaction α .
3. Randomly determine the position of each interacting photon in the image plane.
4. Generate the number of secondary quanta liberated per-interaction by randomly sampling the Poisson distribution with mean \bar{g} .
5. Select the subset of liberated secondaries that are collected by sampling the binomial distribution with number of trials equal to the number of generated secondaries and probability of success equal to $\beta\gamma$.
6. Simulate additive noise by adding or subtracting normally-distributed secondary quanta with zero mean and variance σ_e^2 .
7. If the number of secondaries collected in each element and readout is greater than t , increment the element signal by one.

We performed the above calculations for each element in a 32×32 -element image and then calculated DQE(0) using the expression $\text{DQE}(0) = \text{SNR}_{\text{det}}^2 / \text{SNR}_{\text{ideal}}^2$ where SNR_{det} is the detected signal-to-noise ratio calculated from the mean and variance of the final image and $\text{SNR}_{\text{ideal}}$ is the ideal signal-to-noise ratio calculated from the mean and variance of the distribution of incident photons per detector element.

3.4 Results

3.4.1 Optimal threshold t

Figures 3.3.1 and 3.3.2 illustrate the dependence of normalized average pixel value $\bar{c}_o = \bar{c}/\bar{q}_0 a$ [counts per incident photon] and normalized pixel variance $\sigma_o^2 = \sigma_c^2/\bar{q}_0 a$ on threshold t for selected values of $\beta\gamma\bar{g}$, σ_e , and $\lambda = \bar{q}_0 a_T a$ for $\alpha = 1$. In all cases, theoretical results are consistent with observed statistical fluctuations in the MC calculations. For example, the average differences between MC

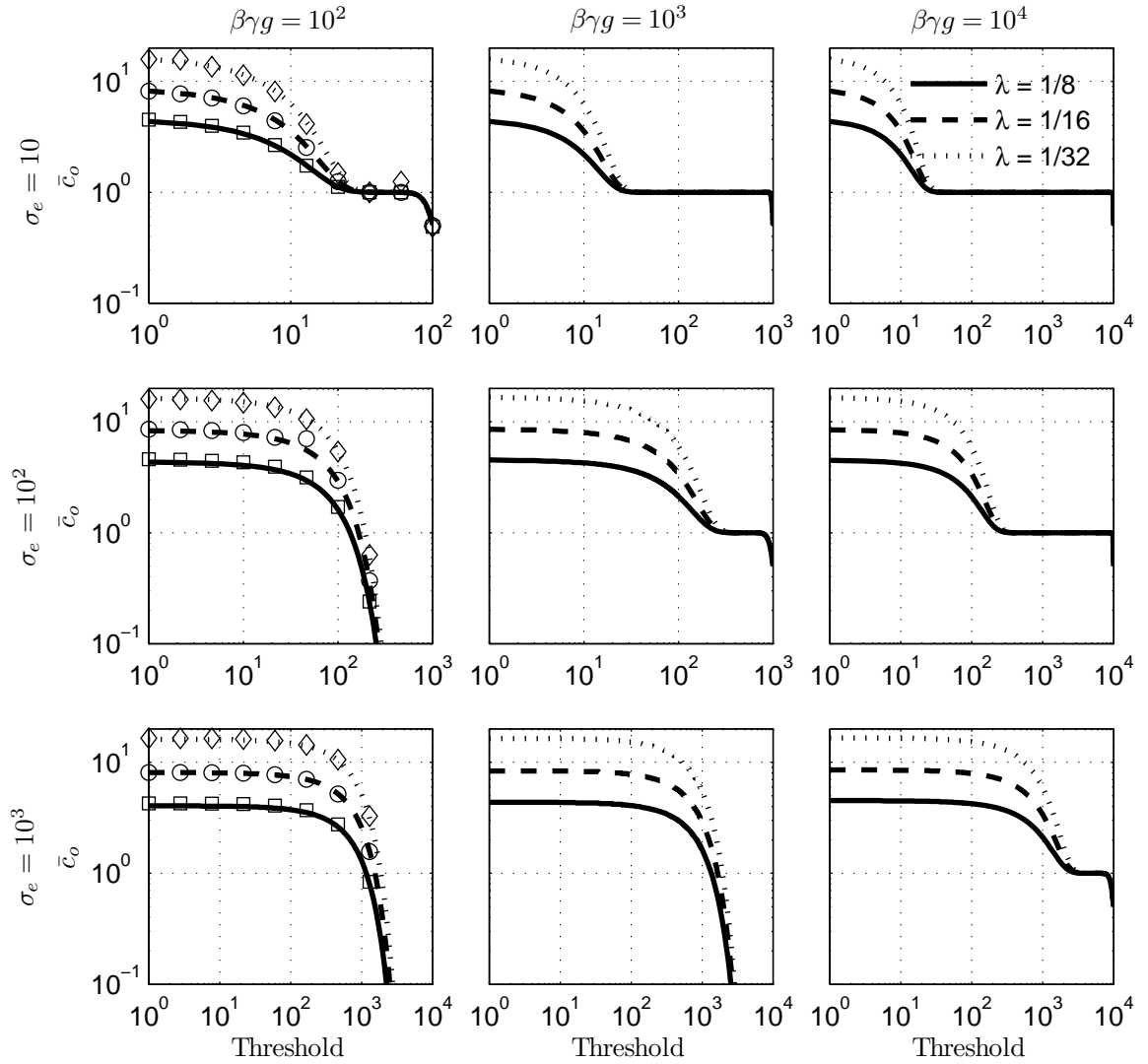


Figure 3.3.1: Graphical illustration of the dependence of normalized pixel value \bar{c}_o (counts per incident photon) on threshold t for selected values of $\beta\gamma\bar{g}$, σ_e , and $\lambda = \bar{q}_0 a_t a$. The detector quantum efficiency has been set to unity for all calculations. Lines and symbols represent theoretical and MC calculations, respectively.

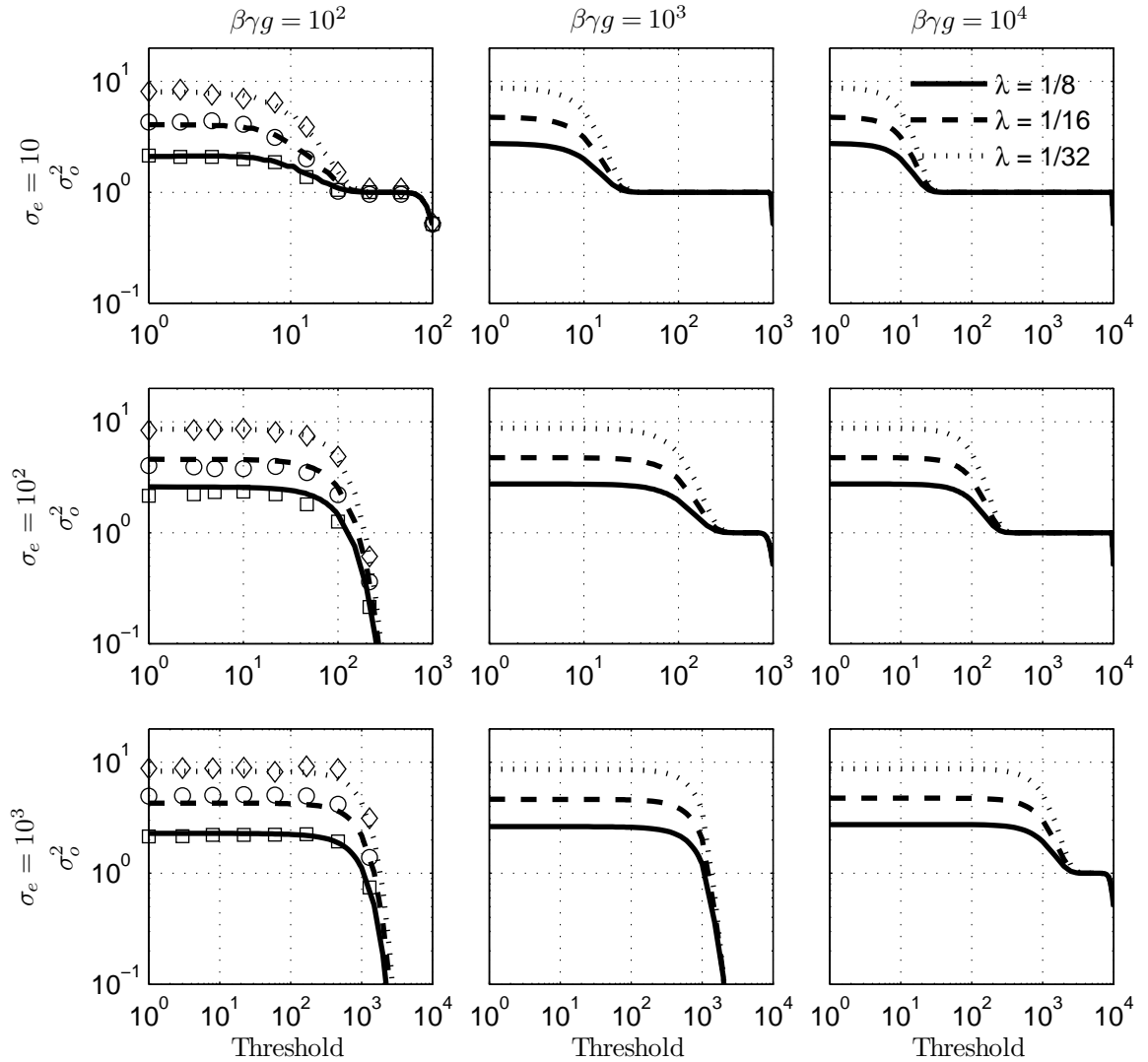


Figure 3.3.2: Graphical illustration of the dependence of σ_c^2 normalized by $\bar{q}_0 a$ (number of incident quanta) on threshold t for selected values of $\beta\gamma\bar{g}$, σ_e , and $\lambda = \bar{q}_0 a_t a$. The detector quantum efficiency has been set to unity for all calculations. Lines and symbols represent theoretical and MC calculations, respectively.

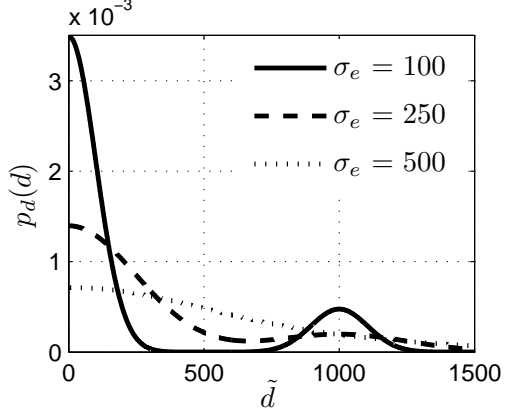


Figure 3.3.3: Graphical illustration of the PDF of \tilde{d} for $\beta\gamma\bar{g} = 10^3$, $\lambda = \bar{q}_0 a_t a = 1/8$ and various values of σ_e .

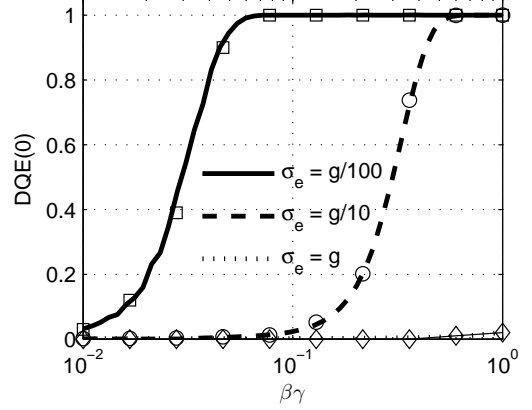


Figure 3.3.4: DQE(0) as a function of coupling and collection efficiency $\beta\gamma$ for selected values of σ_e/\bar{g} . The detector quantum efficiency has been set to unity for all calculations. Lines and symbols represent theoretical and MC calculations, respectively.

and theory in the top left plot of Fig. 3.3.1 are 1-3%. For the top left plot of Fig. 3.3.2, the average differences are 4-7%.

It is shown that low threshold values result in false counts and an increase in mean pixel value due to additive noise. While this may increase pixel SNR, it is not desirable and corresponds to a non-linear response (analogous to a conventional detector saturating at high exposure levels). High threshold values will cause missed true counts and hence a decrease in SNR. The acceptable range of threshold values is therefore strongly dependent on the number of collected secondaries per interacting photon relative to additive noise levels, and this range can be fairly small depending on the PDF of \tilde{d} as illustrated in Fig. 3.3.3. In general, higher mean gain results in a wider range of acceptable thresholds and higher additive noise results in a smaller range. From Fig. 3.3.3, the threshold t must satisfy the condition

$$3\sigma_e < t < \bar{d}|_{\text{int}} - 3\sigma_d|_{\text{int}} \quad (3.4.1)$$

where $\bar{d}|_{\text{int}}$ represents the mean readout signal given one interaction and $\sigma_d|_{\text{int}}$ is the corresponding standard deviation. For the specific SPC detector described here, $\bar{d}|_{\text{int}} = k\beta\gamma\bar{g}$ and $\sigma_d|_{\text{int}}$ is calculated from the PDF for \tilde{d} (Eq. 3.2.45), giving

$$3\sigma_e < t < k\beta\gamma\bar{g} - 3k\sqrt{\beta\gamma\bar{g} \left(1 + \frac{\sigma_e^2}{k\beta\gamma\bar{g}}\right)} \quad (3.4.2)$$

which simplifies to

$$3\sigma_e < t < k\beta\gamma\bar{g} \left(1 - \frac{3}{\sqrt{\beta\gamma\bar{g}}}\right) \quad (3.4.3)$$

for the case of high collection efficiencies and/or large gain ($k\beta\gamma\bar{g} \gg \sigma_e^2$). When this expression is satisfied, the inequality in Eq. (3.2.49) is also satisfied. However, for low gains or high additive noise levels, there may be no acceptable threshold value.

3.4.2 DQE(0) dependence on additive noise, collection efficiency, and mean gain

Figure 3.3.4 illustrates the dependence of the zero-frequency DQE value on collection and coupling efficiencies $\beta\gamma$ for selected values of σ_e/\bar{g} for $\alpha = 1$. For each curve, the threshold has been set equal to $t = 3\sigma_e$ to avoid false additive-noise counts. It is shown that in general, detectors with high levels of additive noise will require higher collection efficiencies to ensure a high DQE(0) value. In the worst-case scenario when the additive noise is on the same order of magnitude as the mean gain, the DQE is close to zero because the threshold required to avoid false counts is greater than the signal generated by the interacting photons. For detectors with low levels of additive noise ($\sigma_e \leq \bar{g}/100$), a collection efficiency greater than approximately 5 % will be required so that the DQE(0) is not degraded by the combination of additive noise and thresholding. This can be achieved by satisfying the inequality in Eq. (3.4.3).

3.5 Discussion

A theoretical framework is presented for describing propagation of the mean signal and Wiener NPS through elementary image forming processes for SPC x-ray detectors including a thresholding stage that converts the detector signal (proportional to absorbed energy) to sample values of 1 or 0 (counts) in each readout. While thresholding is generally non-linear, the mean SPC image signal maintains a linear relationship with the mean number of incident x-ray quanta for the case of fast readouts, negligible image lag, and thresholds chosen to avoid false electronic noise counts.

Under these conditions, CSA can be applied to the description of signal and noise propagation in SPC x-ray detectors with the additional requirement for the PDF of detector-element signals and the joint PDF describing spatial correlations between elements. While general expressions for these quantities may be difficult to compute, for the limiting case of fast readouts and negligible secondary-quantum relocation, the joint PDF simplifies to the PDF which is easily determined for elementary

processes. General PDF-transfer relationships are developed for quantum selection, quantum gain, and quantum scatter processes.

We apply the new CSA concepts to the description of a simple SPC x-ray detector assuming fast readouts and negligible quantum scatter. While this ignores possible spatial correlations between neighboring elements due to charge sharing, charge sharing is known to reduce the DQE substantially if not addressed^[5] and it is believed that any successful design will implement some form of adaptive element binning to determine total absorbed energy. In addition, pulse pile-up is known to cause spectral distortion artifacts,^[155,186] reduce image quality in energy-resolved applications,^[204] and, if not corrected, will likely reduce the DQE. The model presented here will be valid only when pile-up effects can be avoided, with typical count-rates dependent on the application. For example, the readout interval in some state-of-the-art silicon-based SPC detectors is approximately 200×10^{-9} sec^[68] which would result in negligible pile-up in mammography applications where count rates are relatively low ($< 5 \times 10^7$ mm⁻²sec⁻¹).^[15] However, in computed tomography applications where count rates are much higher ($1-10 \times 10^8$ mm⁻²sec⁻¹) pulse pile-up may result in substantial DQE degradation despite the shorter readout interval (30×10^{-9} s)^[91] of cadmium telluride and cadmium-zinc-telluride convertor materials. Our model also did not consider the effects of broad x-ray spectra, but these are easily incorporated by averaging mono-energetic results over given spectra. It is expected the model will correctly show DQE improvements that real SPC systems will have over conventional energy-integrating systems due to reduced Swank noise.

3.6 Conclusions

A signal and noise analysis is described that provides a framework for optimizing and evaluating the DQE that may be achieved using novel SPC x-ray detectors for medical imaging applications. The main change required to apply a cascaded-systems approach to SPC detectors is the need to compute the probability density function describing signals generated by individual detector elements for each readout of the x-ray detector. Using this framework, the zero-frequency DQE of a hypothetical SPC x-ray detector was calculated including the effects of stochastic conversion gain, poor collection efficiency, additive noise, and thresholding. It was demonstrated that in some cases there is a narrow band of allowable thresholds t ($3\sigma_e < t < k\beta\gamma\bar{g} - 3k\sqrt{\beta\gamma\bar{g} + \sigma_e^2}$) for high-DQE performance and that secondary quantum sinks will still degrade the DQE of SPC systems.

Chapter 4

Modeling signal and noise transfer in photon-counting and energy-resolving photon-counting x-ray detectors

This chapter is adapted from a manuscript entitled “Energy precision and detective quantum efficiency of photon-counting x-ray detectors using a cascaded-systems approach: Large elements with x-ray reabsorption” by Jesse Tanguay, Seungman Yun, Ho Kyung Kim, and Ian A. Cunningham, in preparation for submission to Medical Physics.

4.1 Introduction

Advances in x-ray detector technology are leading to the development of energy-resolving photon-counting (EPC) x-ray detectors^[5,15,18,28,41,91,102,118,129,198,215,216] with the ability to estimate the energy of each interacting x-ray photon. The resulting spectral-distribution of energy-depositing events may enable advanced spectroscopic procedures such as energy-resolved angiography^[192] and other applications.^[28,30,61,174] Even for general radiography, EPC methods are expected to improve image quality by reducing image noise from random physical processes including Swank and additive detector readout noise.^[15,129]

While photon-counting methods are receiving a great deal of interest, EPC detectors are at an early stage in their development and there remain many challenges to overcome before the full benefits can be achieved. State-of-the-art readout electronics are capable of count rates of 10^7 - 10^8 photons s^{-1} mm^{-2} which may be adequate for some applications including mammogra-

phy^[30,68,168] and breast computed tomography^[173,175,176,181] but may not yet be adequate for general CT applications.^[7,15,91,165,174,205,210,211,220] In addition, charge sharing between neighboring detector elements can cause substantial degradation of image quality^[4,5,31,126] and loss of spectral information.^[31,44,70,110,174,178] This effect is mitigated with techniques that sum charges in neighboring elements and assigns them to the element with the largest signal, such as those described by Bornefalk *et al.*^[31] and implemented in the MEDIPIX3 prototype.^[18] We call these methods “adaptive binning” and some form of adaptive binning will almost certainly be required to achieve high-quality images. In addition, it is also true that these systems will produce the best possible images only when they are optimized to produce the best possible detective quantum efficiency (DQE).

Cascaded-systems analysis^[6,52–54,77,78,125,146,148,180,218] (CSA) has been successful in the development of theoretical models of the DQE, important in the development of new conventional energy-integrating systems, and has recently been extended to include a description of the zero-frequency DQE of single-photon-counting (SPC) detectors that implement adaptive binning.^[193–195] In particular, we showed that $DQE(0)$ can be expressed in terms of the mean photon-counting signal and associated Wiener noise power spectrum (NPS) and that both can be obtained from the probability density function (PDF) of detector signals resulting in the zero-frequency DQE of SPC systems given by^[195]

$$DQE(0) = \alpha I_{\text{SPC}} \tag{4.1.1}$$

where α represents the detector quantum efficiency and $I_{\text{SPC}} (\leq 1)$ is a noise factor equal to the probability that a true photon count is observed by the system given an interaction event (the true-positive fraction). This form has a pleasing symmetry to the Swank noise factor^[184,185] for conventional energy-integrating systems with I_{SPC} being the SPC Swank factor accounting for degradation in image quality due to stochastic energy deposition, conversion, and collection processes. Equation (4.1.1) is a good description of SPC detector performance when effective adaptive binning approaches are implemented and a threshold is chosen such that false counts due to additive electronic noise are suppressed.

A formalism for determining I_{SPC} from the PDF of the total number of detected image quanta per interaction was described in which the PDF of image-forming quanta is propagated through each stage in a serial cascade of quantum processes, enabling a description of $DQE(0)$ using Eq. (4.1.1).^[195] This result was useful in understanding the importance and utility of using a PDF-transfer approach, but is restricted to the simplistic case where all the energy of an interacting photon is deposited

at the primary interaction site, ignoring photoelectric and Compton emission/scatter photons that escape the detector or are reabsorbed at a remote interaction site. In the case of reabsorption, photon energy is converted to secondary quanta at both primary-interaction and reabsorption sites resulting in a complicated energy response function.^[219] Also, liberation of secondary quanta is a stochastic process and the PDF when energy is deposited at one site differs to that when the same energy is deposited at multiple sites. Furthermore, generation and reabsorption of emission/scatter photons is only one of many possible energy-depositing processes and a description of the PDF of image-forming quanta must consider all important events.

The purpose of this chapter is to extend the capabilities of PDF transfer theory to include the effects x-ray reabsorption on the PDF of image-forming quanta to enable a description of the zero-frequency DQE of SPC systems and energy imprecision of EPC systems. This is accomplished by developing a general expression for the PDF of the total number of image quanta for a parallel cascade of quantum processes. It is shown that a relatively simple closed-form expression for the PDF exists under conditions of importance for SPC and EPC imaging. The utility of the parallel cascades approach is demonstrated in an analysis of the zero-frequency DQE and imprecision in measurements of photon energy of hypothetical selenium-based detectors.

4.2 Theory

4.2.1 SPC noise factor and energy response function

The factor I_{SPC} is equal to the true-positive fraction of counting interaction events.^[194,195] For an interacting photon having energy E , the detector signal after adaptive binning and prior to thresholding \tilde{d} is used to determine the estimated photon energy \tilde{e} where, for a linear x-ray detector, $\tilde{e} = \kappa\tilde{d}$ for some constant κ . It is convenient to characterize the system response in terms of the energy response function $R(\varepsilon, E)$ which is equal to the probability density of \tilde{e} given interacting energy E . Letting $p_d(d|E)$ represent the PDF of \tilde{d} given an interaction yields

$$R(\varepsilon, E) = \frac{1}{\kappa} p_d(d|E)|_{d=\varepsilon/\kappa} \quad (4.2.1)$$

showing how the energy-response function and PDF of \tilde{d} are related. The SPC noise factor is then given by^[195]

$$I_{\text{SPC}} = \int_{\kappa t}^{\infty} R(\varepsilon, E) d\varepsilon = \int_t^{\infty} p_d(d|E) dd \quad (4.2.2)$$

where t is a threshold used to separate x-ray interaction events from additive electronic noise. This result shows that I_{SPC} can be determined from a knowledge of the PDF of binned detector signals.

4.2.2 EPC energy imprecision and energy response function

When photon counting detectors are equipped with multiple thresholds, it is possible to bin photons based on estimated photon energy $\tilde{\epsilon}$. The relative root-mean-square (RMS) energy measurement imprecision is given by the coefficient of variation of $\tilde{\epsilon}$:^[191]

$$\sigma_{rel} = \frac{\sigma_{\tilde{\epsilon}}}{\tilde{\epsilon}} = \sqrt{\frac{\mathfrak{R}_2(E)}{\mathfrak{R}_1^2(E)} - 1} \quad (4.2.3)$$

where $\mathfrak{R}_n(E)$ is the n th energy moment of the energy response function:

$$\mathfrak{R}_n(E) = \int_0^\infty \epsilon^n R(\epsilon, E) d\epsilon = \kappa^n \int_0^\infty d^n p_d(d|E) dd \quad (4.2.4)$$

The above equation shows that the moments of $\tilde{\epsilon}$ are directly related to moments of \tilde{d} which can be determined from the PDF of \tilde{d} .

4.2.3 Determining the energy response function from the PDF of image quanta

Equations (4.2.2) to (E.2.1) demonstrate that both the SPC noise factor and EPC energy imprecision can be determined from the energy response function which, in turn, requires the PDF of \tilde{d} . Recently, Yun *et al.*^[219] described $R(\epsilon, E)$ for selected x-ray convertor materials including the effects of random x-ray energy depositing processes. This approach is useful in describing the situation of deterministic conversion of x-ray energy to secondary quanta for negligible pulse pile up.^[155,186,204] In the following sections we describe a method of obtaining $R(\epsilon, E)$ from the PDF of \tilde{d} that includes the effects of stochastic conversion and collection processes, and x-ray reabsorption. We start by summarizing existing PDF transfer relationships and then extend to include a description of x-ray reabsorption.

4.2.3.1 PDF of image quanta following a cascade of quantum processes

Letting \tilde{N}_i represent the total number of image quanta after the i th stage of a serial cascade of quantum gain or selection processes, the PDF of \tilde{N}_i is given by^[195]

$$p_{N_i}(N_i) = \int p_{N_i}(N_i|N_{i-1}) p_{N_{i-1}}(N_{i-1}) dN_{i-1} \quad (4.2.5)$$

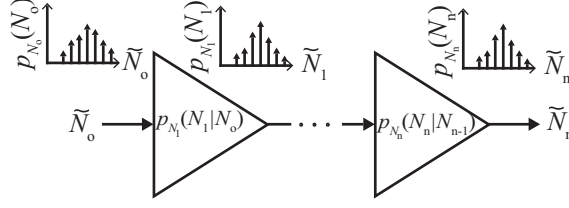


Figure 4.2.1: Schematic representation of PDF transfer (describing total number of image quanta) through a cascade of quantum gain or loss processes. Each PDF consists of a series of δ -functions describing the probability of integer-only number of quanta.

where $p_{N_i}(N_i|N_{i-1})$ represents the conditional PDF of \tilde{N}_i given \tilde{N}_{i-1} . The specific form of $p_{N_i}(N_i|N_{i-1})$ depends on the process and has been described for quantum gain, selection, and scatter processes. ^[195]

A serial cascade of n elementary processes is represented schematically in Fig. 4.2.1 with each process characterized by a conditional PDF $p_{N_i}(N_i|N_{i-1})$. Recursive application of Eq. (4.2.5) yields the PDF after n processes:

$$p_{N_n}(N_n) = \int p_{N_o}(N_o) \int p_{N_1}(N_1|N_o) \dots \dots \int p_{N_{n-1}}(N_{n-1}|N_{n-2}) p_{N_n}(N_n|N_{n-1}) dN_{n-1} \dots dN_1 dN_o \quad (4.2.6)$$

where $p_{N_o}(N_o)$ is the PDF describing the number of incident (x-ray) quanta \tilde{N}_o .

a) Poisson gain Quantum gain represents the process of replacing the j th quantum in an input distribution with \tilde{g}_j quanta in the output, such as liberation of electron-hole pairs in a semiconductor by an x-ray interaction. In the case of Poisson-distributed gain with mean \bar{g}_j , the conditional PDF $p_{N_i}(N_i|N_{i-1})$ is given by

$$p_{N_i}(N_i|N_{i-1}) = \sum_j \text{pr}_{N_i}(N_i = j|N_{i-1}) \delta(N_i - j) \quad (4.2.7)$$

where the summation is over all possible values of N_i , $\delta(\cdot)$ represents the Dirac delta function, and ^[194]

$$\text{pr}_{N_i}(N_i = j|N_{i-1}) = \frac{1}{j!} \left(\sum_{j'=1}^{N_{i-1}} \bar{g}_{j'} \right)^j \exp \left(- \sum_{j'=1}^{N_{i-1}} \bar{g}_{j'} \right). \quad (4.2.8)$$

The above expression demonstrates that $\text{pr}_{N_i}(N_i|N_{i-1})$ is equal to the Poisson distribution with mean $\sum_{j=1}^{N_{i-1}} \bar{g}_j$.

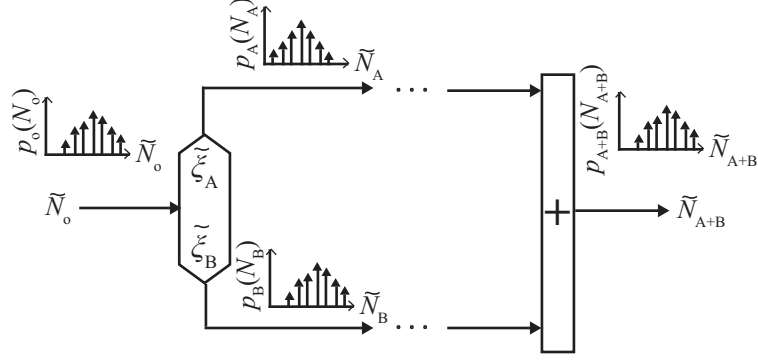


Figure 4.2.2: Schematic representation PDF transfer where \tilde{N}_o is separated into two different cascaded (A and B) and then combined.

b) Gaussian gain We let $G(\tilde{g}; \bar{g}, \sigma_g)$ represent a Gaussian distribution describing all possible gain values \tilde{g} with mean \bar{g} and variance σ_g^2 . Then^[143,195]

$$p_{N_i}(N_i | N_{i-1}) = (G *^{N_{i-1}-1} G)(N_i). \quad (4.2.9)$$

where $(G *^{N_{i-1}-1} G)(N_i)$ denotes a convolution of $G(\tilde{g}; \bar{g}, \sigma_g)$ with itself $N_{i-1} - 1$ times and is a function N_i . Only integer values of \tilde{g} are allowed which may require re-normalization of $p_{N_i}(N_i | N_{i-1})$ for small gain values.

c) Deterministic gain For the special case that $\sigma_g \rightarrow 0$, Eq. (4.2.9) becomes

$$pr_{N_i}(N_i | N_{i-1}) = \delta(N_i - \bar{g}) *^{N_{i-1}-1} \delta(N_i - \bar{g}) = \delta(N_i - \bar{g}N_{i-1}) \quad (4.2.10)$$

where we have used the translation property of the delta function.

Equation (4.2.6) provides a complete description of the PDF of the total number of quanta when there is only one possible path of energy deposition. However, Eq. (4.2.6) will be inadequate when there are multiple possible paths, in which case a parallel-cascades approach is required.

4.2.3.2 PDF of image quanta from parallel cascades

In the case of multiple energy-depositing paths, the total number of quanta contributing to an image signal is equal the total number of quanta from all paths.^[214] Each path may, for example, represent conversion to secondary image quanta through one of a number of energy-depositing processes as required to describe scatter reabsorption.

We consider a sum from two paths (illustrated in Fig. 4.2.2) and let $\tilde{N}_{A+B} = \tilde{N}_A + \tilde{N}_B$ represent

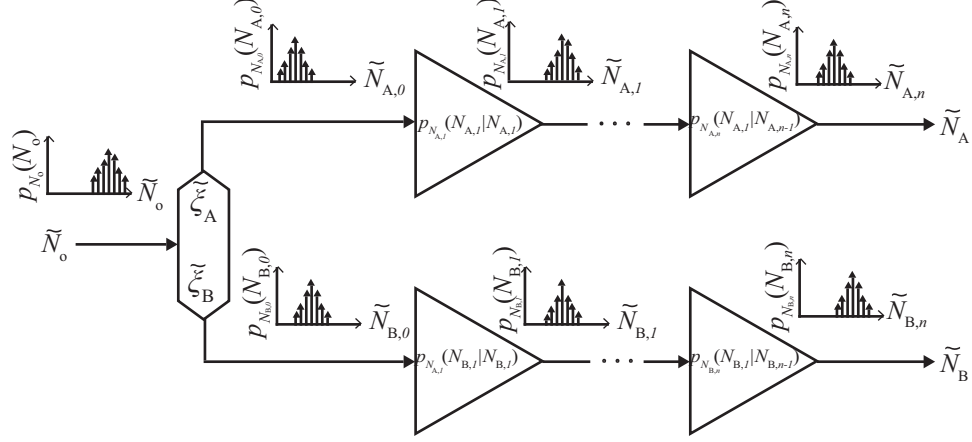


Figure 4.2.3: Schematic representation of PDF transfer through parallel cascades of quantum gain and loss processes. $\tilde{N}_{A,0}$ and $\tilde{N}_{B,0}$ represent the number of quanta in each subset of the input process.

the sum of input paths A and B. The PDF of \tilde{N}_{A+B} is given by^[143]

$$p_{N_{A+B}}(N_{A+B}) = \int_{-\infty}^{+\infty} p_{N_A, N_B}(N_{A+B} - N_B, N_B) dN_B \quad (4.2.11)$$

where $p_{N_A, N_B}(N_A, N_B)$ is the joint PDF for paths A and B describing the probability of observing \tilde{N}_A quanta from path A and \tilde{N}_B quanta from path B. The above expression demonstrates that calculation of the PDF of a sum of quanta from parallel paths requires the joint PDF $p_{N_A, N_B}(N_A, N_B)$ of \tilde{N}_A and \tilde{N}_B .

Special case: \tilde{N}_A independent of \tilde{N}_B In the case that \tilde{N}_A and \tilde{N}_B are independent RVs, $p_{N_A, N_B}(N_A, N_B) = p_{N_A}(N_A)p_{N_B}(N_B)$ and Eq. (4.2.11) simplifies to

$$p_{N_A, N_B}(N_{A+B}) = p_{N_A}(N_{A+B}) * p_{N_B}(N_{A+B}) \quad (4.2.12)$$

where $*$ represents the convolution operator.

Equations (4.2.11) and (4.2.12) give the PDF of a sum of quanta from two correlated or uncorrelated paths, respectively. Of particular importance is when the input to each path is a subset of a common input distribution, as illustrated in Fig. 4.2.2. The process of selecting quanta for each path is called branch point.

a) Joint PDF and branch points A branch point, illustrated in Fig. 4.2.2, represents a sequence of independent trials where each trial is a random selection of one point of an input distribution

to follow paths A and/or B with probabilities $\bar{\xi}_A$ and $\bar{\xi}_B$, respectively, that are the same for each trial.^[214] This process may, for example, represent separation of incident x-ray photons that interact through either the photoelectric or Compton effect. The number of trials is equal to the number of quanta in the input distribution and is therefore a RV. Each trial is described in terms of the two Bernoulli RVs $\tilde{\xi}_{j,A}$ and $\tilde{\xi}_{j,B}$ where each can have a value of either 0 or 1. Each trial is independent of all others but correlations may exist between $\tilde{\xi}_{j,A}$ and $\tilde{\xi}_{j,B}$ as described by the joint PDF $p_{\xi_{j,A},\xi_{j,B}}(\xi_{j,A},\xi_{j,B})$ which is the same for each trial and is given by^[143]

$$p_{\xi_{j,A},\xi_{j,B}}(\xi_{j,A},\xi_{j,B}) = \sum_{k=0}^1 \sum_{l=0}^1 P(\xi_{j,A} = k \text{ and } \xi_{j,B} = l) \delta(\xi_{j,A} - k) \delta(\xi_{j,B} - l) \quad (4.2.13)$$

where $P(\xi_{j,A} = k \text{ and } \xi_{j,B} = l)$ represents the probability that $\tilde{\xi}_{j,A} = k$ and $\tilde{\xi}_{j,B} = l$. Noting that $p_{\xi_{j,A},\xi_{j,B}}(\xi_{j,A},\xi_{j,B}) = p_{\xi_A,\xi_B}(\xi_A,\xi_B)$ is the same for all trials, we show in Appendix C that following a branch point the joint PDF of \tilde{N}_A and \tilde{N}_B given \tilde{N}_o input quanta is given by

$$p_{N_A,N_B}(N_A,N_B|\tilde{N}_o) = (p_{\xi_A,\xi_B} *^{\tilde{N}_o-1} p_{\xi_A,\xi_B})(N_A,N_B) \quad (4.2.14)$$

where $(p_{\xi_A,\xi_B} *^{\tilde{N}_o-1} p_{\xi_A,\xi_B})(N_A,N_B)$ denotes a two dimensional convolution of $p_{\xi_A,\xi_B}(\xi_A,\xi_B)$ with itself $\tilde{N}_o - 1$ times where the result is a function of N_A and N_B . Averaging over \tilde{N}_o yields

$$p_{N_A,N_B}(N_A,N_B) = \int (p_{\xi_A,\xi_B} *^{\tilde{N}_o-1} p_{\xi_A,\xi_B})(N_A,N_B) p_{N_o}(N_o) dN_o. \quad (4.2.15)$$

The above expression shows that the joint PDF of the number of quanta in two random subsets of the same common input distribution is completely described by the joint PDF of selection variables $\tilde{\xi}_{j,A}$ and $\tilde{\xi}_{j,B}$.

b) Joint PDF following cascades of elementary processes A more general case involves the joint statistics of the number of quanta in two paths after undergoing serial cascades of elementary processes, as illustrated in Fig. 4.2.3. The RVs $\tilde{N}_{A,i}$ and $\tilde{N}_{B,i}$ in Fig. 4.2.3 represent the number of quanta after the i th elementary process of each path and \tilde{N}_A and \tilde{N}_B represent the two outputs. In all cases the elementary processes of each path must be independent of the other.

In Appendix C we show that the joint PDF of \tilde{N}_A and \tilde{N}_B given \tilde{N}_o is given by

$$p_{N_A, N_B} (N_A, N_B | \tilde{N}_o) = \langle p_{N_A} (N_A | \xi_A) p_{N_B} (N_B | \xi_B) \rangle_{\xi_A, \xi_B} *_{\tilde{N}_o}^{-1} \langle p_{N_A} (N_A | \xi_A) p_{N_B} (N_B | \xi_B) \rangle_{\xi_A, \xi_B} \quad (4.2.16)$$

where $\langle \rangle_{\xi_A, \xi_B}$ represents an average over all possible values of $\tilde{\xi}_{j,A}$ and $\tilde{\xi}_{j,B}$:

$$\langle p_{N_A} (N_A | \xi_A) p_{N_B} (N_B | \xi_B) \rangle_{\xi_A, \xi_B} = \iint p_{N_A} (N_A | \xi_A) p_{N_B} (N_B | \xi_B) p_{\xi_A, \xi_B} (\xi_A, \xi_B) d\xi_A d\xi_B \quad (4.2.17)$$

where $p_{N_A}(N_A|\xi_A)$ and $p_{N_B}(N_B|\xi_B)$ represent the PDFs of \tilde{N}_A and \tilde{N}_B given $\tilde{\xi}_{j,A}$ and $\tilde{\xi}_{j,B}$ for one trial and are obtained using Eq. (4.2.6):

$$p_{N_A}(N_A|\tilde{\xi}_A) = \int p_{N_{A,0}}(N_{A,0}|\tilde{\xi}_A) \int p_{N_{A,1}}(N_{A,1}|N_{A,0}) \dots \int p_{N_{A,n-1}}(N_{A,n-1}|N_{A,n-2}) p_{N_{A,n}}(N_{A,n}|N_{A,n-1}) dN_{A,n-1} \dots dN_{A,1} dN_{A,0} \quad (4.2.18)$$

and similarly for $p_B(N_B|\tilde{\xi}_B)$. Averaging Eq. (4.2.16) over all possible values of \tilde{N}_o yields

$$p_{N_A, N_B} (N_A, N_B) = \int \left[\langle p_{N_A} (N_A | \xi_A) p_{N_B} (N_B | \xi_B) \rangle_{\xi_A, \xi_B} *_{\tilde{N}_o}^{-1} \langle p_{N_A} (N_A | \xi_A) p_{N_B} (N_B | \xi_B) \rangle_{\xi_A, \xi_B} \right] p_{N_o} (N_o) dN_o. \quad (4.2.19)$$

The above equation is a generic PDF transfer relationship between $p_{N_A, N_B}(N_A, N_B)$ and $p_o(N_o)$ and demonstrates that the joint statistics of \tilde{N}_A and \tilde{N}_B depend on how $\tilde{\xi}_A$ and $\tilde{\xi}_B$ are correlated, the elementary processes involved in each path, and the input PDF.

c) Special case: One incident quantum, $N_o = 1$ An important situation occurs when the number of input quanta is equal to either 0 or 1. In this case, \tilde{N}_o may represent the number photons interacting in a detector element (after adaptive binning) during one integration period. For $N_o = 1$, the PDF of input quanta can be represented as $p_o(N_o) = \delta(N_o - 1)$. Equation (4.2.19) then reduces to

$$p_{N_A, N_B} (N_A, N_B) = \langle p_{N_A} (N_A | \xi_A) p_{N_B} (N_B | \xi_B) \rangle_{\xi_A, \xi_B}. \quad (4.2.20)$$

The above equation demonstrates that $p_{N_A, N_B}(N_A, N_B) \neq p_{N_A}(N_A)p_{N_B}(N_B)$ and therefore the number of quanta from each path are dependent RVs.

Two important situations are when each input quantum is selected for *either* path A *or* B, called a Bernoulli branch, and when each input quantum is selected for *both* paths A *and* B, called a cascade fork .^[214]

Bernoulli branch A Bernoulli branch may, for example, describe separation of photoelectric interactions that produce a characteristic emission from those that do not.^[77,148,214,218] Equation (4.2.13) for the joint PDF of selection variables $\tilde{\xi}_{j,A}$ and $\tilde{\xi}_{j,B}$ is given by

$$p_{\xi_A, \xi_B}(\xi_A, \xi_B) = \bar{\xi}_A \delta(\xi_A - 1) \delta(\xi_B) + \bar{\xi}_B \delta(\xi_A) \delta(\xi_B - 1). \quad (4.2.21)$$

Combining the above equation with Eq. (4.2.20) yields the joint PDF of \tilde{N}_A and \tilde{N}_B following a Bernoulli branch for one input quantum:

$$p_{N_A, N_B}(N_A, N_B) = \bar{\xi}_A p_A(N_A | \xi_A = 1) p_B(N_B | \xi_B = 0) + \bar{\xi}_B p_A(N_A | \xi_A = 0) p_B(N_B | \xi_B = 1) \quad (4.2.22)$$

where $p_{N_A}(N_A | \xi_A = 0) = \delta(N_A)$ and $p_{N_B}(N_B | \xi_B = 0) = \delta(N_B)$. Combining Eqs. (4.2.11) and (4.2.22) yields

$$p_{N_{A+B}}(N_{A+B}) = \bar{\xi}_A p_A(N_{A+B} | \xi_A = 1) + \bar{\xi}_B p_B(N_{A+B} | \xi_B = 1). \quad (4.2.23)$$

The above expression describes the expected result that when an input quantum is selected for only one path or the other, the PDF of the total number of output quanta is equal to the summation of PDFs of quanta for each path weighted by the probability of selection for each path.

Cascade fork A cascade fork may, for example, describe the situation where a photon that has interacted through the Compton effect deposits energy the site of primary interaction and at a remote site following reabsorption of a Compton-scatter x ray. In this case, the joint PDF of selection variables is given by

$$p_{\xi_A, \xi_B}(\xi_A, \xi_B) = \delta(\xi_A - 1) \delta(\xi_B - 1) \quad (4.2.24)$$

and the joint PDF of \tilde{N}_A and \tilde{N}_B for one incident quantum is given by

$$p_{N_A, N_B}(N_A, N_B) = p_{N_A}(N_A | \xi_A = 1) p_{N_B}(N_B | \xi_B = 1). \quad (4.2.25)$$

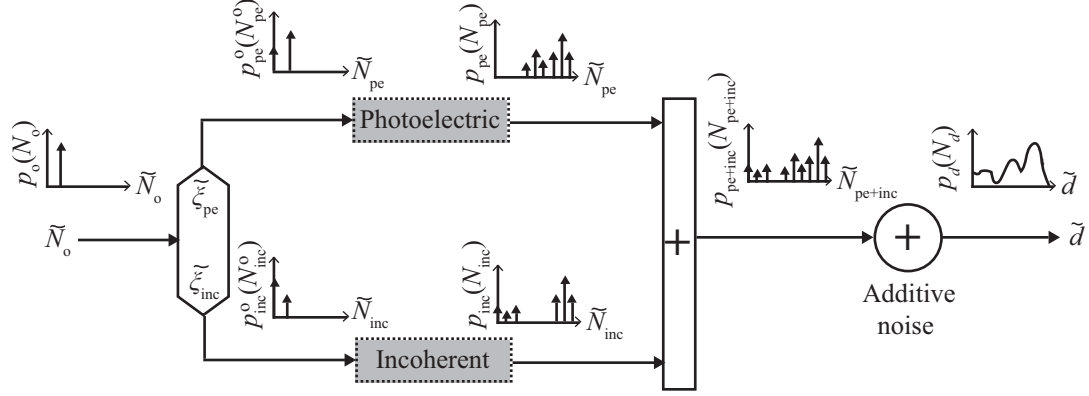


Figure 4.2.4: Schematic illustration of the CSA model describing PDF transfer of the total number of secondary quanta through photoelectric and incoherent interactions using parallel cascades. The RV \tilde{N}_o is the total number of incident x-ray quanta in one readout and is chosen to be unity. The RVs \tilde{N}_{pe} and \tilde{N}_{inc} describe the total number of secondary quanta collected from photoelectric and incoherent interactions.

Equations (4.2.22) and (4.2.25) demonstrate that for the special case of one incident quantum, the joint PDF of parallel cascades of elementary processes following a Bernoulli branch or cascade fork is described in terms of $p_{N_A}(N_A|\xi_A = 1)$ and $p_{N_B}(N_B|\xi_B = 1)$ both of which are obtained using Eq. (4.2.18). Combining Eqs. (4.2.11) and (4.2.25) yields

$$p_{N_{A+B}}(N_{A+B}) = p_{N_A}(N_{A+B}|\xi_A = 1) * p_{N_B}(N_{A+B}|\xi_B = 1). \quad (4.2.26)$$

In the following section we use these results to determine the energy response function and in turn the energy imprecision and zero-frequency DQE of hypothetical selenium-based EPC and SPC x-ray detectors.

4.2.4 Liberation of secondary quanta in x-ray convertor

Figure 4.2.4 is a schematic representation of the parallel cascade model we use to describe energy-deposition in an x-ray convertor material including the effects of stochastic energy deposition through either photoelectric or incoherent scattering, conversion to secondary quanta, and collection of secondary quanta, similar to that described by Yun *et al.*^[218] Our goal is to describe the PDF of the total number of secondary quanta \tilde{N}_{tot} collected by detector elements per interacting x-ray photon. We therefore let $p_{N_o}(N_o) = \delta(N_o - 1)$. In all cases, we assume large pixels such that the probability of reabsorption of characteristic or Compton-scatter x rays in neighboring elements is negligible. This may be a good approximation for systems that use an adaptive binning approach to sum signals from neighboring pixels to get the total energy deposited for every interacting x-ray photon.

The output from each path is the total number of quanta collected from either photoelectric or incoherent interactions. From Eq. (4.2.11), the total number of collected secondaries $\tilde{N}_{\text{tot}} = \tilde{N}_{\text{pe}} + \tilde{N}_{\text{inc}}$ is given by

$$p_{N_{\text{tot}}}(N_{\text{tot}}) = \int_{-\infty}^{+\infty} p_{N_{\text{pe}}, N_{\text{inc}}}(N_{\text{tot}} - N_{\text{pe}}, N_{\text{pe}}) dN_{\text{pe}} \quad (4.2.27)$$

where $p_{N_{\text{pe}}, N_{\text{inc}}}(N_{\text{pe}}, N_{\text{inc}})$ is the joint PDF of \tilde{N}_{pe} and \tilde{N}_{inc} . From Eq. (4.2.20), $p_{N_{\text{pe}}, N_{\text{inc}}}(N_{\text{pe}}, N_{\text{inc}})$ is given by

$$p_{N_{\text{pe}}, N_{\text{inc}}}(N_{\text{pe}}, N_{\text{inc}}) = \iint p_{N_{\text{pe}}}(N_{\text{pe}} | \tilde{\xi}_{\text{pe}}) p_{N_{\text{inc}}}(N_{\text{inc}} | \tilde{\xi}_{\text{inc}}) p_{\xi_{\text{pe}}, \xi_{\text{inc}}}(\xi_{\text{pe}}, \xi_{\text{inc}}) d\xi_{\text{pe}} d\xi_{\text{inc}}. \quad (4.2.28)$$

Since each photon interacts through either photoelectric or incoherent scattering, the branch point in Fig. 4.2.4 represents a Bernoulli branch. Therefore, from Eq. (4.2.22),

$$p_{N_{\text{tot}}}(N_{\text{tot}}) = \bar{\xi}_{\text{pe}} p_{N_{\text{pe}}}(N_{\text{tot}} | \xi_{\text{pe}} = 1) + \bar{\xi}_{\text{inc}} p_{N_{\text{inc}}}(N_{\text{tot}} | \xi_{\text{inc}} = 1) \quad (4.2.29)$$

where $\bar{\xi}_{\text{pe}}$ and $\bar{\xi}_{\text{inc}}$ represent the probabilities of photoelectric absorption and incoherent scattering, respectively:

$$\bar{\xi}_{\text{pe}} = \frac{\mu_{\text{pe}}(E)}{\mu_{\text{pe}}(E) + \mu_{\text{inc}}(E)} \quad \text{and} \quad \bar{\xi}_{\text{inc}} = \frac{\mu_{\text{inc}}(E)}{\mu_{\text{pe}}(E) + \mu_{\text{inc}}(E)} \quad (4.2.30)$$

Equation (4.2.29) shows that a description of $p_{N_{\text{tot}}}(N_{\text{tot}})$ requires the PDFs of the number of collected secondaries resulting from photoelectric and incoherent interactions. These processes are similar in that they both may result in emission of a fluorescent/scatter photon. It is therefore convenient to describe photoelectric and incoherent interactions as two special cases of a generalized interaction process.

4.2.4.1 Generalized interaction process

Each shaded box in Fig. 4.2.4 is a special case of a generalized interaction process illustrated in Fig. 4.2.5. The subscript t in Fig. 4.2.5b represents the interaction type, photoelectric (pe) or incoherent (inc). As illustrated in Fig. 4.2.5a, an incident photon interacts at depth \tilde{z}_1 in the x-ray convertor material and may generate a scatter photon with probability S_t at scatter angle $\tilde{\theta}$ and azimuthal angle $\tilde{\phi}$ that may be reabsorbed at depth \tilde{z}_2 . Secondary quanta (electron-hole pairs in a photoconductor) are liberated at both primary-interaction and reabsorption sites unless the scatter

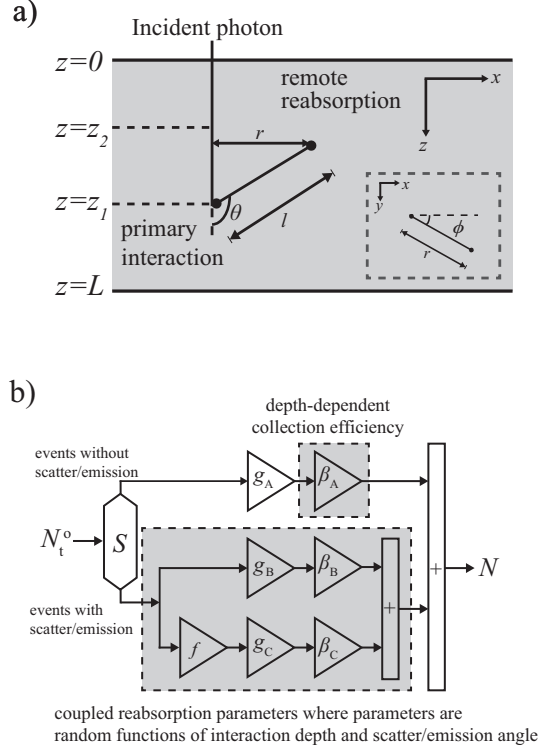


Figure 4.2.5: Schematic illustration of the interaction model used in this work showing: (a) an incident x-ray photon interacting in the x-ray converter and subsequent production of a scatter photon at polar θ and azimuthal angle ϕ ; and (b) CSA model. The three paths in (b) represent events that liberate charges from: (path A) primary interaction site when no scatter/emission photon is generated; (path B) primary interaction site when a scatter/emission photon is generated; and (path C) remote reabsorption of scatter/emission photon.

photon escapes the detector. While this model is similar to that presented by Yun *et al.*,^[218] it also allows for depth-dependent collection efficiency.

Depth-dependent collection efficiency Electrons and holes may recombine in the x-ray converter material prior to collection by collecting electrodes. We assume the collection efficiency β has a depth dependence given by the Hecht relationship.^[83] Therefore, the average fraction of charge collected given an interaction at depth z is given by^[83,94,100]

$$\beta(z) = \frac{\mu_e \tau_e \epsilon}{L} \left(1 - e^{-\frac{L-z}{\mu_e \tau_e \epsilon}} \right) + \frac{\mu_h \tau_h \epsilon}{L} \left(1 - e^{-\frac{z}{\mu_h \tau_h \epsilon}} \right) \quad (4.2.31)$$

where L [cm] represents the converter thickness, $\mu_e \tau_e$ and $\mu_h \tau_h$ [cm² V⁻¹] are mobility-lifetime products for electrons and holes, respectively, ϵ [V cm⁻¹] is the applied electric field, and we have assumed that the electrons travel towards the entrance surface and holes travel towards the exit surface. The collection efficiency of Se-based detectors with material properties listed in Tab. 4.1 is

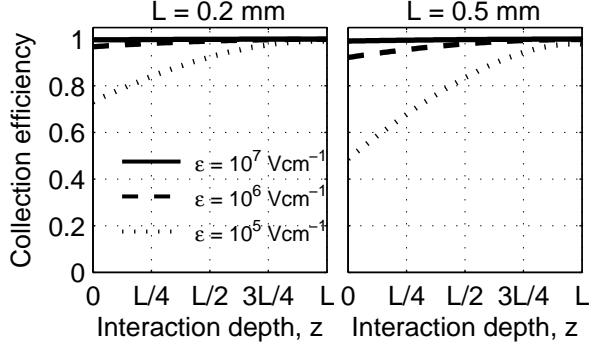


Figure 4.2.6: Collection efficiency β as a function of interaction depth z for a Se x-ray converter material with material properties listed in Tab. 4.1.

illustrated in Fig. 4.2.6. We show below that depth-dependent collection of secondaries may result in substantial broadening of the distribution of detected photon energies and reduced DQE.

PDF of number of quanta The collection efficiency β_A of path A in Fig. 4.2.3 is a function the depth of primary interaction \tilde{z}_1 , which is a RV. The concept of gain and/or selection variables that are themselves functions of random variables was first introduced by Van Metter and Rabbani^[125] who called these input-labelled random processes. We adopt this idea to describe the depth-dependent collection efficiency in the top shaded path of Fig. 4.2.5 where we let the interaction depth \tilde{z}_1 be a RV with the appropriate exponential PDF. However, in the lower shaded box of Fig. 4.2.5 all processes are functions of either depth \tilde{z}_1 and/or scatter angle $\tilde{\theta}$. In addition, these processes are coupled because they are dependent on the same \tilde{z}_1 and $\tilde{\theta}$ for each individual interacting photon. In Appendix C we generalize the previous derivation of the PDF of the total number of image quanta from parallel cascades to include a description of these input-labelled parallel processes. The result is used to calculate the PDF of the number of quanta for the generic interaction model in illustrated in Fig. 4.2.5. Letting \tilde{N}_t represent the total number of image quanta for the generic interaction model, it is shown that

$$\begin{aligned}
 p_{N_t}(N_t) = & (1 - S_t) \langle \mathcal{B}_A(N_t; \beta) \rangle_{z_1} + S_t \langle (1 - f_t) \mathcal{B}_B(N_t; \beta) \rangle_{\theta, z_1} \\
 & + S_t \langle f_t \mathcal{B}_B(N_t; \beta) * \langle \mathcal{B}_C(N_t; \beta) \rangle_{z_2} \rangle_{\theta, z_1}
 \end{aligned} \tag{4.2.32}$$

where $\langle \rangle_{\theta, z_1}$ denotes an average over \tilde{z}_1 and $\tilde{\theta}$, $f_t = f_t(\tilde{z}_1, \tilde{\theta})$ represents the fluorescent/scatter reabsorption probability for interaction type t , given by

$$f_t(\tilde{z}_1, \tilde{\theta}) = \begin{cases} \int_0^{(L-\tilde{z}_1)/|\cos(\tilde{\theta})|} p_l(l) dl & 0 \leq \theta \leq \pi/2 \\ \int_0^{\tilde{z}_1/|\cos(\tilde{\theta})|} p_l(l) dl & \pi/2 < \theta \leq \pi \end{cases} \quad (4.2.33)$$

where $p_l(l) = \mu(E_s) \exp[-\mu(E_s)l]$ where E_s represents fluorescent/scatter photon energy, and

$$\mathcal{B}_A^t(N_t; \beta) = \int \mathcal{B}(N_t; g_A, \beta(z_1)) p_{g_A}(g_A) dg_A \quad (4.2.34)$$

$$\mathcal{B}_B^t(N_t; \beta) = \int \mathcal{B}(N_t; g_B, \beta(z_1)) p_{g_B}(g_B; \theta) dg_B \quad (4.2.35)$$

$$\mathcal{B}_C^t(N_t; \beta) = \int \mathcal{B}(N_t; g_C, \beta(z_2)) p_{g_C}(g_C; \theta) dg_C \quad (4.2.36)$$

where $p_{g_A}(g_A; \theta)$ represents the PDF of \tilde{g}_A which may depend on angle θ , $\mathcal{B}(N_t; g_A, \beta(z_1))$ represents the binomial distribution with number of trials equal to g_A and probability of success $\beta(z_1)$ given by Eq. (4.2.31).

The average over \tilde{z}_2 in Eq. (4.2.32) requires the PDF of \tilde{z}_2 given \tilde{z}_1 and $\tilde{\theta}$ which is derived in Appendix C. Averages over \tilde{z}_1 and $\tilde{\theta}$ require the joint PDF $p_{z_1, \theta}^t(z_1, \theta)$ of \tilde{z}_1 and $\tilde{\theta}$, which for a given incident photon energy is given by^[143]

$$p_{z_1, \theta}^t(z_1, \theta) = p_{z_1}(z_1) p_{\theta}^t(\theta) \quad (4.2.37)$$

where $p_{\theta}^t(\theta)$ depends on the interaction type and has been described in detail by Hajdok *et al.*^[79] and Yun *et al.*^[218, 219] for both photoelectric and incoherent interactions, and $p_{z_1}(z_1)$ is given by

$$p_{z_1}(z_1) = \frac{\mu(E) e^{-\mu(E)z_1}}{1 - e^{-\mu(E)L}}. \quad (4.2.38)$$

The first term in Eq. (4.2.32) represents the PDF of image quanta for those events that do not result in production of fluorescent/scatter x rays. The second term represents the PDF of image quanta for events that result in production of a fluorescent/scatter photon that escapes the detector, and the third term represents the PDF of image quanta for events that result in production of a fluorescent/scatter photon that is reabsorbed within the detector.

In the following sections we apply the above equations to the description of the PDFs of the total number of quanta for photoelectric and incoherent interactions. Table 4.2 gives mean values

Table 4.1: Physical and electrical properties including mass density, electron and hole mobility-lifetime products, effective ionization energy, K-fluorescent energy, K-shell participation fraction, and K-fluorescence yield for *a*-Se. Mobility-lifetime products for Se are taken from Ref. 94 and effective ionization energies are taken from Ref. 157.

	Symbol	Se
Mass density (g cm ⁻³)	ρ	4.3
K-fluorescent energy	E_K	11.2
K-shell participation fraction	ρ_K	0.864
K-fluorescence yield	ω_K	0.589
Average ionization energy (eV)	w	45
Electron mobility-lifetime product [cm ² V ⁻¹]	$\mu_e\tau_e$	3×10^{-7}
Hole mobility-lifetime product [cm ² V ⁻¹]	$\mu_h\tau_h$	1.2×10^{-5}

Table 4.2: Random variables and PDFs defining the type of x-ray interaction used in the generic model shown in Fig. 4.2.5.

RV	Photoelectric		Incoherent	
	Mean	PDF	Mean	PDF
\tilde{S}_t	$\omega_K Y_K$	Bernoulli	1	δ -function
\tilde{g}_A	E/w	Poisson		
\tilde{g}_B	$(E - E_K)/w$	Poisson	$(E - E')/w$	Poisson
\tilde{g}_C	E_K/w	Poisson	E'/w	Poisson
$\tilde{\beta}_A$	$\beta(z_1)$	Bernoulli	$\beta(z_1)$	Bernoulli
$\tilde{\beta}_B$	$\beta(z_1)$	Bernoulli	$\beta(z_1)$	Bernoulli
$\tilde{\beta}_C$	$\beta(z_2)$	Bernoulli	$\beta(z_2)$	Bernoulli

and PDFs used for selection and gain variables for each interaction type, where ρ_K , ω_K , E_K , E' , w , and f_t represent the K-shell participation fraction, K-fluorescence yield, K-fluorescence photon energy, incoherent-scatter energy, effective energy required to liberate one electron-hole pair, and scatter/emission reabsorption probability, respectively.

4.2.4.2 Photoelectric interactions

In a photoelectric event, path A of Fig. 4.2.5 corresponds to those events that do not produce a fluorescent photon, and incident energy E is assumed to be completely absorbed at the primary interaction site liberating \tilde{g}_A secondaries with PDF $p_{g_A}(g_A)$ (see Table 4.2). Paths B and C describe events that produce a fluorescent photon, resulting in \tilde{g}_B secondaries emitted locally and \tilde{g}_C liberated remotely with probability $f_{pe} = f_{pe}(z_1, \theta)$ given by Eq. (4.2.33) with $E_s = E_K$. From Eq. (4.2.32),

the PDF of \tilde{N}_{pe} is given by

$$p_{N_{\text{pe}}}(N_{\text{pe}}) = (1 - \rho_{\text{K}\omega_{\text{K}}}) \langle \mathcal{B}_{\text{A}}^{\text{pe}}(N_{\text{pe}}; \beta) \rangle_{z_1} + \rho_{\text{K}\omega_{\text{K}}} \langle (1 - f_{\text{pe}}) \mathcal{B}_{\text{B}}^{\text{pe}}(N_{\text{pe}}; \beta) \rangle_{\theta, z_1} \\ + \rho_{\text{K}\omega_{\text{K}}} \langle f_{\text{pe}} \mathcal{B}_{\text{B}}^{\text{pe}}(N_{\text{pe}}; \beta) * \langle \mathcal{B}_{\text{C}}^{\text{pe}}(N_{\text{pe}}; \beta) \rangle_{z_2} \rangle_{\theta, z_1} \quad (4.2.39)$$

where $p_{z_1, \theta}^{\text{pe}}(z_1, \theta)$ is given by Eq. (4.2.37) with $p_{\theta}^{\text{pe}}(\theta) = \sin(\theta)/2$.^[77,218] The first and third terms in Eq. (4.2.39) contribute to the photo peak and the second term contributes to the K-escape peak.

4.2.4.3 Incoherent interactions

In an incoherent event, an incident photon interacts with a loosely bound (free) electron producing a Compton photon and recoil electron. The energy of the Compton photon E' is a function of both incident photon energy and scatter polar angle θ :^[17]

$$E' = \frac{E}{1 + \alpha(1 - \cos(\theta))} \quad (4.2.40)$$

where $\alpha = E/m_{\text{o}}c^2$ represents the incident photon energy in units of the electron rest-mass energy ($m_{\text{o}}c^2 = 511 \text{ keV}$). The recoil electron deposits its energy at the primary interaction site with mean conversion gain $\bar{g}_{\text{B}} = (E - E')/w$. The scatter photon is reabsorbed with probability $f_{\text{inc}} = f_{\text{inc}}(z_1, \theta)$ given by Eq. (4.2.33). From Eq. (4.2.32), the PDF of \tilde{N}_{inc} is given by

$$p_{N_{\text{inc}}}(N_{\text{inc}}) = \langle (1 - f_{\text{inc}}) \mathcal{B}_{\text{B}}^{\text{inc}}(N_{\text{inc}}; \beta) \rangle_{\theta, z_1} + \langle f_{\text{inc}} \mathcal{B}_{\text{B}}^{\text{inc}}(N_{\text{inc}}; \beta) * \langle \mathcal{B}_{\text{C}}^{\text{inc}}(N_{\text{inc}}; \beta) \rangle_{z_2} \rangle_{\theta, z_1} \quad (4.2.41)$$

where $p_{z_1, \theta}^{\text{inc}}(z_1, \theta)$ is given by Eq. (4.2.37) with $p_{\theta}^{\text{inc}}(\theta)$ described in detail by Hajdok *et al.*^[79] and Yun *et al.*^[218,219] The first term in Eq. (4.2.41) represents the distribution of secondaries collected from energy deposition by the recoil electron and the second term contributes to the photo-peak.

4.2.4.4 PDF of detector element signal \tilde{d}

Combining Eqs. (4.2.27), (4.2.39), and (4.2.41) yields the PDF of $\tilde{N}_{\text{tot}} = \tilde{N}_{\text{pe}} + \tilde{N}_{\text{inc}}$:

$$\begin{aligned}
p_{N_{\text{tot}}}(\tilde{N}_{\text{tot}}) &= \bar{\xi}_{\text{pe}}(1 - \rho_K \omega_K) \langle \mathcal{B}_A^{\text{pe}}(N_{\text{tot}}; \beta) \rangle_{z_1} + \bar{\xi}_{\text{pe}} \rho_K \omega_K \langle (1 - f_{\text{pe}}) \mathcal{B}_B^{\text{pe}}(N_{\text{tot}}; \beta) \rangle_{\theta, z_1} \\
&+ \bar{\xi}_{\text{pe}} \rho_K \omega_K \left\langle f_{\text{pe}} \mathcal{B}_B^{\text{pe}}(N_{\text{tot}}; \beta) * \langle \mathcal{B}_C^{\text{pe}}(N_{\text{tot}}; \beta) \rangle_{z_2} \right\rangle_{\theta, z_1} \\
&+ \bar{\xi}_{\text{inc}} \langle (1 - f_{\text{inc}}) \mathcal{B}_B^{\text{inc}}(N_{\text{tot}}; \beta) \rangle_{\theta, z_1} \\
&+ \bar{\xi}_{\text{inc}} \left\langle f_{\text{inc}} \mathcal{B}_B^{\text{inc}}(N_{\text{tot}}; \beta) * \langle \mathcal{B}_C^{\text{inc}}(N_{\text{tot}}; \beta) \rangle_{z_2} \right\rangle_{\theta, z_1}. \tag{4.2.42}
\end{aligned}$$

The above equation describes the PDF of the number of collected secondary quanta not including the effects of additive electronic noise. The PDF of \tilde{d} given interacting photon energy E including the effects of additive electronic noise is obtained by convolving the above equation with the PDF describing the distribution of the additive electronic noise component: ^[194,195]

$$p_d(d|E) = \frac{1}{k} p_{\text{tot}}(d/k) * p_e(d) \tag{4.2.43}$$

where $p_{N_{\text{tot}}}(d/k) = p_{N_{\text{tot}}}(\tilde{N}_{\text{tot}})|_{\tilde{N}_{\text{tot}}=d/k}$, $p_e(d)$ represents the PDF of the signal resulting from additive electronic noise, and k is a constant of proportionality that converts number of quanta to detector element units.

Equations (4.2.42) and (4.2.43) describe the PDF of element signals after adaptive binning prior to thresholding for single-Z detector materials. We use these expressions to calculate the zero-frequency DQE (Eq. (4.1.1)) and relative energy imprecision (Eq. (E.2.4)) of a hypothetical Se-based photon-counting x-ray detector that implements adaptive element binning.

4.2.5 Mean number of photon counts

For fast readouts, the mean number of photon counts \bar{c} for detectors that implement adaptive element binning was described in detail in Chapter 3 and is given by

$$\bar{c} = \bar{q}_o a \alpha I_{\text{SPC}} \left[1 + \frac{\xi_0}{\lambda I_{\text{SPC}}} \right] \tag{4.2.44}$$

where $\lambda = \bar{q}_o a_T a \ll 1$, I_{SPC} is the SPC noise factor, and ξ_0 represents the probability of observing a false count due to electronic noise. In the following sections \bar{c} is used to identify thresholds that result in suppression of false noise counts without loss of actual interaction events. Since $\lambda \ll 1$,

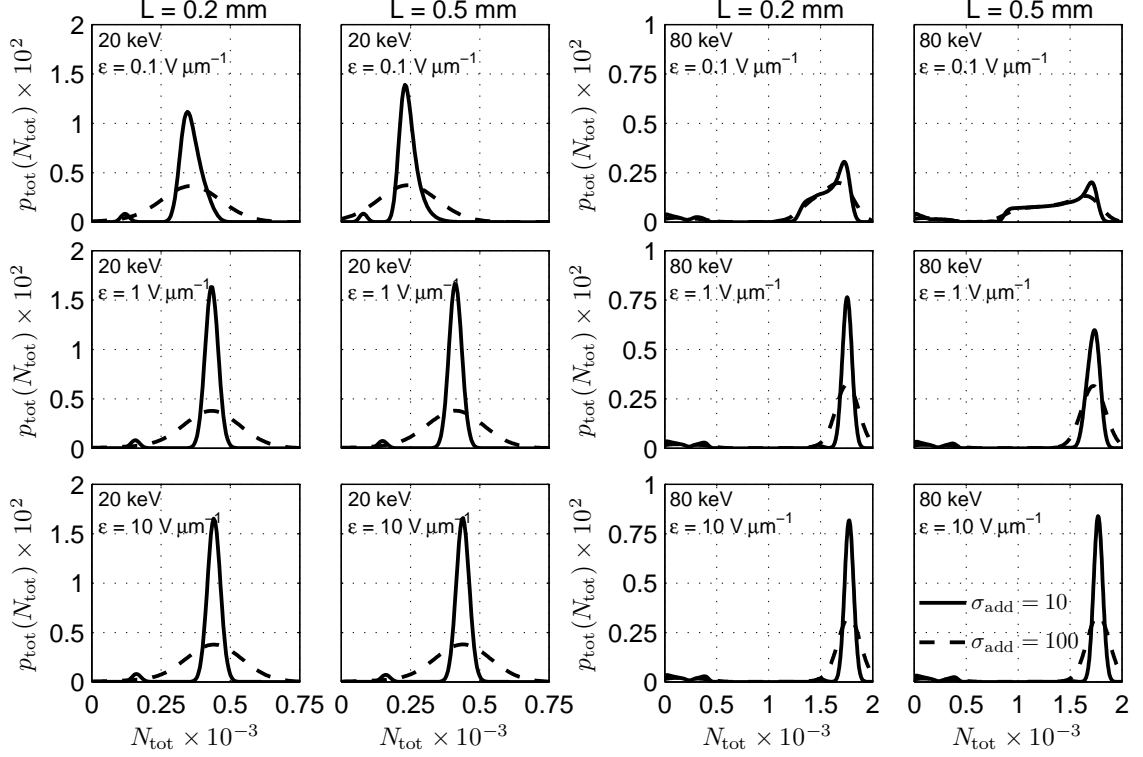


Figure 4.3.1: Probability density functions of the total number of quanta collected by detector elements for 20-keV (left) and 80-keV (right) photons incident on Se-based convertor materials for selected thicknesses and applied electric fields.

this will require thresholds such that ξ_0 tends to zero while I_{SPC} remains non-zero.

4.3 Results

4.3.1 PDF of detector element signals, $p_d(d|E)$

Figure 4.3.1 illustrates $p_d(d|E)$ for the model illustrated in Fig. 4.2.4 calculated using Eq. (4.2.43) for 20-keV and 80-keV photons incident on a Se-based x-ray detector for selected convertor thicknesses, applied electric fields, and electronic noise levels. All calculations were performed using material properties listed in Table 4.1 with mean gain values and PDFs listed in Tab. 4.2.

In general, low applied electric fields ($\sim 10^5$ V cm $^{-1}$) result in broad and asymmetric photo-peaks due to depth-dependent collection efficiencies. This effect is more severe for thicker convertor materials, where the collection efficiency has a stronger dependence on interaction depth (Fig. 4.2.6), and higher-energy photons, where the distribution of interaction depths is more uniform over the convertor layer. As expected, increasing additive noise levels also results in photo-peak broadening. For systems with sufficiently low additive-noise levels and high electric fields, stochastic energy

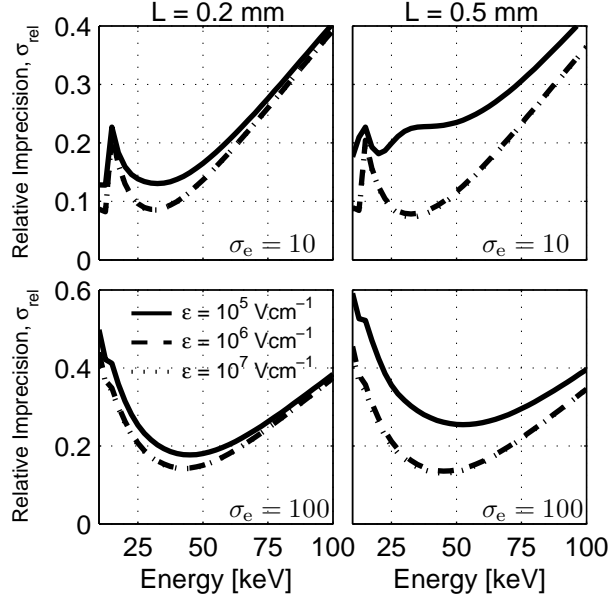


Figure 4.3.2: Graphical illustration of the dependence of relative imprecision σ_{rel} on incident photon energy for selected convertor thicknesses, applied electric fields, and additive noise levels.

deposition and conversion processes are primary causes of spectral distortion, resulting in finite-width photo-peaks, K-escape peaks, and a distribution of low-energy deposition events.

4.3.2 Relative energy imprecision of EPC detectors

The relative energy imprecision σ_{rel} is shown in Fig. 4.3.2 for selected convertor thicknesses, applied electric fields, and additive noise levels.

In the case of low additive noise levels, there is low relative imprecision below the K-edge energy. Similar to previous studies,^[191] at energies above the k edge, relative energy imprecision increases due to random escape of characteristic emissions. Compton scatter becomes important at energies above approximately 45 keV resulting in a substantial increase in imprecision at higher energies. In addition, imprecision increases with decreasing applied electric field due to broadening of photo-peaks (Fig. 4.3.2) caused by depth-dependent collection efficiency. This effect is more pronounced for thicker convertor layers.

In the case of high additive noise levels, as expected, energy imprecision is generally worse than that for low additive noise levels. In addition, relative imprecision is high for both lower and higher photon energies with imprecision increasing with decreasing applied electric field and increasing thickness for the same previously-discussed reasons.

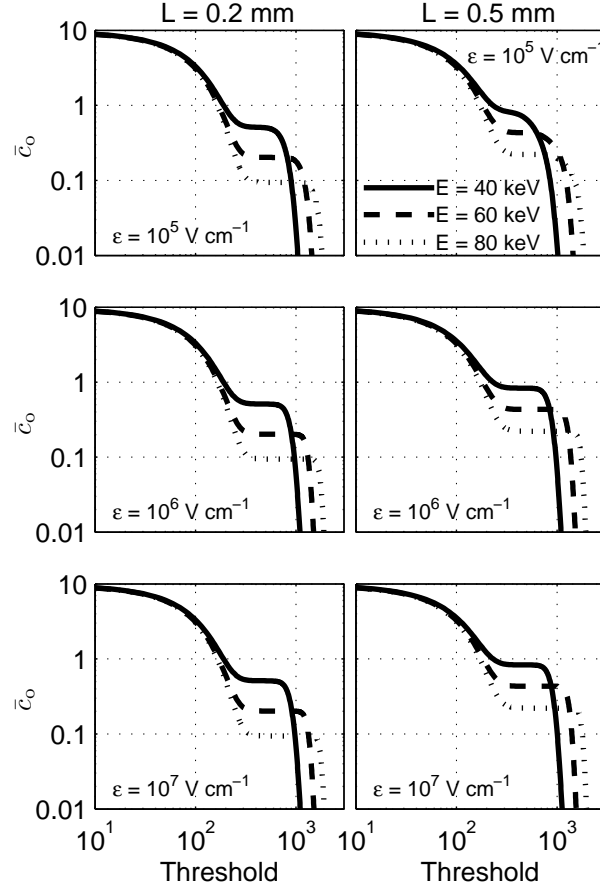


Figure 4.3.3: Illustration of the dependence of normalized SPC pixel value \bar{c}_o (counts per incident photon) on threshold t for selected convertor thicknesses, incident photon energies, and applied electric fields. Curves are calculated for $\sigma_e = 100$ e-h pairs and $\lambda = 1/10$.

4.3.3 Optimal SPC threshold

Figure 4.3.3 illustrates the dependence of normalized SPC pixel value ($\bar{c}/\bar{q}_o a$) on threshold level for selected convertor thicknesses, photon energies, and applied electric fields. All curves in Fig. 4.3.3 were calculated assuming $\sigma_e = 100$ e-h pairs and $\lambda = \bar{q}_o a a_T = 1/10$.

In all cases, as expected, threshold values lower than approximately $3\sigma_e$ result in an inflated image signal due to false electronic noise counts. For threshold values greater than $3\sigma_e$, a plateau is reached with height approximately equal to the quantum efficiency. The width of the plateau depends on the number of secondaries collected per interacting x-ray photon and in general is narrower for lower-energy photons than for higher-energy photons. In addition, decreasing the applied electric field narrows the range of acceptable threshold values because of secondary quantum sink issues.

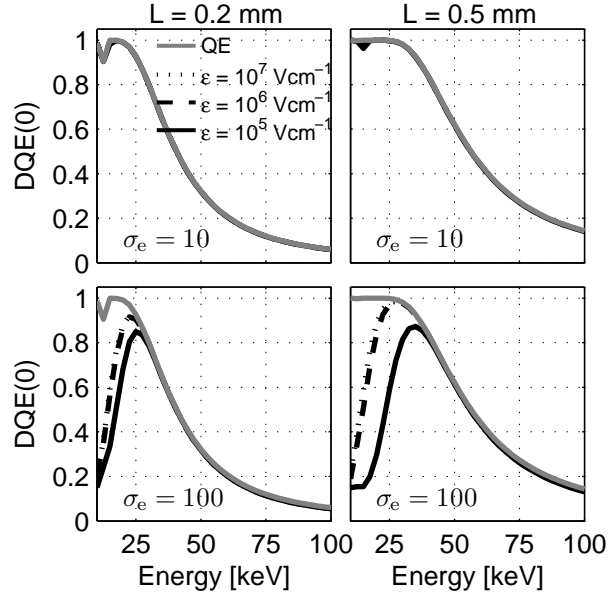


Figure 4.3.4: Illustration of the dependence of $DQE(0)$ on incident photon energy for selected convertor thicknesses, applied electric fields, and additive noise levels. The gray curve indicates the quantum efficiency.

4.3.4 Zero-frequency DQE of SPC detectors

Figure 4.3.4 illustrates the dependence of $DQE(0)$ on incident photon energy for selected convertor thicknesses and applied electric fields. In all cases we have assumed $\sigma_e = 100$ e-h pairs, $t = 3\sigma_e$, $\lambda \ll 1$, and large detector elements.

At fluoroscopic and radiographic energies (>40 keV), $DQE(0)$ is approximately equal to the quantum efficiency for all convertor thicknesses, applied electric fields, and additive noise levels considered. However, for higher levels of additive noise and mammographic photon energies (<40 keV), $DQE(0)$ is substantially degraded due to loss of energy-deposition events below the the electronic noise floor ($3\sigma_e$). This effect is caused by a combination of lower gain at lower energies, poor collection efficiency, and thresholding.

4.4 Discussion and Conclusions

A theoretical framework is presented for obtaining the energy-response function of photon-counting x-ray detectors. This was made possible by the introduction of new relationships that describe propagation of the PDF of the total number of image-forming quanta through complicated parallel cascades of image forming processes for photon-counting x-ray detectors. It is shown that the PDF of image quanta from parallel cascades can be obtained from the joint PDF of quanta from

parallel paths. This is required when there is more than one image-forming process that contributes to an image signal, such as in the case of reabsorption of fluorescent and Compton-scatter photons. Using this approach, the relative energy imprecision and zero frequency DQE of hypothetical selenium-based EPC and SPC detectors were determined including the effects of escape and reabsorption of fluorescent and Compton-scatter photons, stochastic conversion to secondary quanta, depth-dependent collection of secondary quanta, and electronic noise.

Similar to recent studies,^[194,195] it is shown that for systems that implement adaptive element binning, the zero-frequency SPC DQE is equal to the quantum efficiency multiplied by a new SPC noise factor I_{SPC} that is equal to the probability of counting a photon given an interaction event, ie. the true-positive fraction of photon counts. A CSA model of I_{SPC} based on a generalized depth-dependent interaction model incorporating the statistics of liberation and collection of secondary quanta showed that the DQE is degraded by escape of fluorescent and Compton-scatter photons, depth-dependent collection efficiency, and electronic noise. It was demonstrated that for Se-based SPC systems, there is a narrow range of acceptable thresholds that depends on photon energy, collection efficiency, and electronic noise level. In addition, for Se-based systems with thresholds that adequately suppress electronic noise without thresholding out interaction events, the DQE is approximately equal to the quantum efficiency. In this case, as expected, the DQE is not compromised by Swank noise or additive electronic noise. However, in some cases this condition cannot be satisfied, such as at lower mammographic energies, higher levels of additive noise, and poor collection efficiency, and the SPC DQE is severely degraded suggesting that it may be difficult to provide high-DQE photon-counting images at low energies.

Similar to a Monte Carlo analysis presented in Appendix E, precision in photon-energy measurements by energy-resolving photon-counting (EPC) detectors that implement adaptive binning is shown to be compromised by escape of fluorescent and Compton-scatter photons. In addition, it was demonstrated that depth-dependent collection efficiency can also result in a large increase in energy imprecision. This is particularly important for thick convertor materials with lower mobility-lifetime products for electrons and/or holes. Even with the use of adaptive-binning algorithms to sum energy deposited in detector elements surrounding a primary interaction to estimate total deposited energy, the combined effects of characteristic emission, Compton scatter escape, and depth-dependent collection efficiency can result in relative energy imprecision of 20-40%. Electronic noise results in a further increase in relative imprecision, particularly at lower mammographic photon energies.

In all cases, we assumed an adaptive binning approach where all interacting photon energy was assumed to be collected in a single large element. In Se-based detectors, Compton scatter accounts

for $\approx 20\%$ of all x-ray interactions which may require adaptively-binned element areas up to 4 mm^2 which will lower the tolerable flux rates. Even if electronic readout systems are fast such clinical flux rates can be tolerated with these element areas, this may require summing up to 100 or more detector elements (depending on element size) which would result in a substantial increase in additive noise per adaptively-binned element per readout. As demonstrated in the analysis here, this will likely result in loss of a substantial number of interaction events below the additive noise floor, and therefore reduced DQE. This suggests that Se-based detectors with this type of adaptive-binning approach may not be suitable for EPC applications. Alternative binning techniques, and the trade off between suppression of false counts caused by reabsorption of fluorescent and Compton-scatter x rays and increased additive noise levels caused by adaptive element binning were not analyzed in this thesis and require further study to assess whether Se-based detectors are suitable for EPC applications. Alternative x-ray convertor materials that have low Compton cross sections and relatively high conversion gains may be more suitable candidates for photon-counting systems.

Chapter 5

Cascaded-systems analysis of angiographic image quality obtained using energy-dependent and conventional subtraction approaches

This chapter is adapted from a manuscript entitled “Cascaded-systems analysis of angiographic image quality obtained using energy-dependent and conventional subtraction approaches” by Jesse Tanguay, Seungman Yun, Ho Kyung Kim, and Ian A. Cunningham, in preparation for submission to Medical Physics.

5.1 Introduction

X-ray digital subtraction angiography^[34,56,96,133,149] (DSA) is a vascular imaging technique that is commonly used for visualization of arterial diseases. With this technique, an image acquired prior to injection of an iodinated contrast agent is subtracted from a post-injection image, thereby largely removing overlapping anatomic structures. While DSA is extremely successful at imaging structures that are near-stationary over a period of several seconds, the need for both pre and post-injection exposures can result in severe motion artifacts and failed or compromised diagnostic procedures.^[32,37,47,75,95,119,149,188,200] For this reason, DSA is rarely used in coronary applications.

Alternative methods of generating iodine-specific images with reduced motion artifacts might

exploit the energy-dependence of x-ray attenuation in a patient. This could be performed either by acquiring two or more post-injection images at different x-ray energies [75,76,88,97-99,112-116,130-133] or from an analysis of the spectral shape of a single post-injection transmitted spectrum. [9-11,67,152,165] The first method, energy-subtraction angiography (ESA), was introduced as a dual-energy alternative to DSA over two decades ago but technological limitations of the time resulted in poor image quality. [75,76,88,97,98,130,131] The second potential method, energy-resolved angiography (ERA), requires energy-resolving photon-counting (EPC) x-ray detectors that are under development in a number of laboratories. [5,15,18,28,41,91,101,102,118,129,198,215,216] Both approaches would use energy-dependent information to estimate iodine attenuation along each x-ray path with the goal of generating iodine-specific images that are less sensitive to patient motion.

It was recently demonstrated [192] that both ESA and ERA have the potential to produce iodine-specific images with iodine SNR within 10% of DSA for the same patient x-ray exposure assuming ideal instrumentation for each. While this provides strong motivation to pursue energy-dependent angiographic approaches, stochastic x-ray interaction and detection processes are known to degrade the performance of conventional energy-integrating systems, and are also expected to degrade iodine SNR obtained with both ESA and DSA.

In the case of EPC systems, charge sharing between neighboring detector elements can cause substantial degradation of image quality [4,5,31,126] and loss of spectral information. [31,44,70,110,174,178] While this effect is mitigated with techniques that sum charges in neighboring elements and assigns them to the element with the largest signal, such as those described by Bornefalk *et al.* [31] and implemented in the MEDIPIX3 prototype, [18] poor collection efficiency of secondary quanta and escape of fluorescent and Compton-scatter photons will continue degrade to spectral information [29,94,106,158,174,178,191] and may result in loss of photon counts below the electronic noise floor, as discussed in Chapters 3 and 4 of this thesis. It is well known that poor spectral information will also result in noisy estimates of contrast material densities obtained using EPC detectors, [152,203] and are also expected to degrade ERA image quality.

It is therefore important to understand and quantify how x-ray interaction and detection processes will affect ERA, ESA, and DSA image quality to identify the conditions required for successful implementation of energy-based approaches. Cascaded-systems analysis [6,52-54,77,78,125,146,148,180,218] (CSA) has been an important tool in development of theoretical models of signal and noise performance of energy-integrating systems, and was extended to include a description of photon-counting image quality in Chapters 3 and 4 of this thesis. The goal of this study is to apply CSA concepts for both energy-integrating and photon-counting detectors to the description of iodine SNR that could

be achieved with each of these approaches for both fluoroscopic and angiographic imaging conditions, including the influence of stochastic x-ray interaction, conversion, and collection processes, and electronic noise.

5.2 Theory

The goal of subtraction angiography, including ERA, ESA, and DSA, is to enhance visualization of diseased vasculature, most often peripheral or coronary arteries, by producing an image showing only those vessels that were opacified by an iodine contrast agent. [32,35,47,56,75,88,97,115,130] As described in Chapter 2, each of ERA, ESA, and DSA, are similar in that they all require weighted subtraction of two or more x-ray images. It is therefore convenient to describe image signal and noise for each of these processes using a generic formalism, described in detail by Tanguay *et al.*, [192] and summarized below.

5.2.1 Angiographic image signal

For ERA, ESA, and DSA, the angiographic image signal obtained from an estimate of iodine area density A_I [g cm⁻²] for each x-ray path, which is derived from two or more images where, assuming linear x-ray detectors, the expected pixel value measured in image i is given by

$$\bar{M}_i = \int_0^{kV} s_i(E) \bar{q}_i(E) e^{-\mathbf{A}^T \frac{\boldsymbol{\mu}}{\rho}(E)} dE; \quad i = 1 \dots n \quad (5.2.1)$$

where

$$\mathbf{A} = \begin{bmatrix} A_W \\ A_B \\ A_I \end{bmatrix} \quad \text{and} \quad \frac{\boldsymbol{\mu}}{\rho}(E) = \begin{bmatrix} \frac{\mu}{\rho}_W(E) \\ \frac{\mu}{\rho}_B(E) \\ \frac{\mu}{\rho}_I(E) \end{bmatrix} \quad (5.2.2)$$

and $s_i(E)$ is a weighting function describing the detector response associated with image i . [192] The angiographic image signal is obtained by weighted log-subtraction of images \tilde{M}_i :

$$\tilde{A}_I = - \sum_{i=1}^n W_{I,i} \log \frac{\tilde{M}_i}{M_{i0}} \quad (5.2.3)$$

where image weights $W_{I,i}$ are related to the mass-attenuation coefficients of basis materials and M_{i0} is given by Eq. (5.2.1) evaluated at a known set of basis-material area densities. See Tanguay *et al.*, [192] for details on calculation of $W_{I,i}$ and M_{i0} for ERA, ESA, and DSA. Equation (5.2.3) gives

an estimate of iodine area density for each image pixel.

5.2.2 Angiographic image noise

We characterize angiographic image noise in terms of the variance of \tilde{A}_I , given by^[192]

$$\text{Var}(\tilde{A}_I) = \sum_{i=1}^n \frac{W_{Ii}^2}{\text{SNR}_{M_i}^2} + \sum_{i=1}^n \sum_{\substack{j=1 \\ j \neq i}}^n \frac{W_{Ii}W_{Ij}}{\tilde{M}_i\tilde{M}_j} \text{Cov}(\tilde{M}_i, \tilde{M}_j) \quad (5.2.4)$$

where $\text{SNR}_{M_i}^2 = \tilde{M}_i^2/\text{Var}(\tilde{M}_i)$, $\text{Cov}(\tilde{M}_i, \tilde{M}_j)$ is the covariance between \tilde{M}_i and \tilde{M}_j . In the following sections $\text{Var}(\tilde{M}_i)$ and $\text{Cov}(\tilde{M}_i, \tilde{M}_j)$ are described for DSA, ESA, and ERA. We use \tilde{d}_i and \tilde{c}_i when referring specifically to energy-integrating and energy-resolved photon-counting measurements, respectively.

5.2.2.1 Energy-integrating systems

In the case of conventional DSA and ESA, \tilde{d}_i represent signals from energy-integrating detector elements. The expected value of \tilde{d}_i is proportional to the mean number of secondary quanta, such as electron-hole pairs in direct conversion detectors, detected in a detector element. In this case, the quantity $s_i(E)$ is proportional to the mean gain of the system. We let $G(E) = \bar{d}(E)/\bar{q}_{i,o}(E)$ represent the mean gain for incident photon energy E and number of quanta $\bar{q}_{i,o}(E)$ [$\text{mm}^{-2} \text{keV}^{-1}$] incident at the detector plane. Equation (5.2.1) is then expressed as^[52-54,180]

$$\text{E}(\tilde{d}_i) = \bar{d}_i = \int_0^{kV} G(E)\bar{q}_i(E) e^{-\mathbf{A}^T \frac{\mu}{\rho}(E)} dE. \quad (5.2.5)$$

Since separate readouts of the x-ray detector are independent, $\{\tilde{d}_i, i = 1..n\}$ are uncorrelated for both ESA and DSA, the covariance between \tilde{d}_i and \tilde{d}_j is given by

$$\text{Cov}(\tilde{d}_i, \tilde{d}_j) = \delta_{ij} \text{Var}(\tilde{d}_i). \quad (5.2.6)$$

where δ_{ij} represents the Kronecker delta function equal to 1 for $i = j$ and zero otherwise. Assuming wide-sense-stationary (WSS) noise processes, $\text{Var}(\tilde{d}_i)$ is obtained from the presampling Wiener noise-power-spectrum (NPS), $\text{NPS}_{d_i}(u, v)$:^[52-54,143]

$$\text{Var}(\tilde{d}_i) = \iint_{\mathbb{R}^2} \text{NPS}_{d_i}(u, v) dudv \quad (5.2.7)$$

where u and v represent spatial frequencies in the x and y directions, respectively, and $\iint_{\mathbb{R}^2} dudv$ represents a two-dimensional integral over all spatial frequencies. The form of $\text{NPS}_{d_i}(u, v)$ depends on specifics of the x-ray detector and x-ray spectrum incident on the detector. In Sec.5.2.3 we use CSA to determine both $G(E)$ and $\text{NPS}_{d_i}(u, v)$.

5.2.2.2 Energy-resolving systems

Energy-resolved photon counting is achieved by incrementing a counter for one of n energy bins based on the energy deposited in detectors element during one fast readout. Ideally, each readout interval is short such that the probability of multiple photon interactions in the same element is small. Pile-up occurs when this condition is not satisfied and results in a decrease in detected count rates.^[100,217] We show in Appendix D that in the case of large detector elements, fast readouts, and thresholds chosen to suppress false counts due to additive electronic noise, the mean number of photon counts in bin i is given by^[194,195]

$$\bar{c}_i = \lambda T \int_0^{kV} \alpha(E) \left[\int_{t_i}^{t_{i+1}} p_d(d|E) dd \right] p_E(E) e^{-\mathbf{A}^T \frac{\mu}{\rho}(E)} dE \quad (5.2.8)$$

where $\lambda = \bar{q}aa_t$ represents the mean number of photons incident on a detector element of area a during readout time a_t for mean fluence rate \bar{q} [$\text{mm}^{-2} \text{s}^{-1}$], T [s] represent the total exposure time, t_i and t_{i+1} represent lower and upper thresholds for bin i , $\alpha(E)$ represents the detector quantum efficiency, $p_d(d|E)$ represents the PDF of prethesholding signals \tilde{d} given one interacting photon having energy E , and $p_E(E)$ represents the PDF of incident photon energies E . Equation (5.2.8) assumes low count rates and therefore is valid for $\lambda \ll 1$. Conditions required to meet this constraint are discussed in Section 5.3.

In Appendix D we show that, also in the case of large detector elements, fast readouts, and thresholds chosen to suppress false counts due to additive electronic noise, the covariance of \tilde{c}_i and \tilde{c}_j is expressed as

$$\text{Cov}(\tilde{c}_i, \tilde{c}_j) = \begin{cases} -c_i c_j \times \frac{a_t}{T} & i \neq j \\ c_i & i = j \end{cases} \quad (5.2.9)$$

where T/a_t is equal to the total number of readouts. For fast readouts, $a_t/T \ll 1$. The above expressions shows that both the mean number of counts in each energy bin and covariance between counts detected in two separate bins are directly related to the PDF describing the readout signal \tilde{d} . In the following section we use a PDF-transfer approach to describe $p_d(d|E)$ and therefore \bar{c}_i and

Table 5.1: Mean gain values for photoelectric and incoherent interactions. The variables E_K and E' represent fluorescent and Compton-scatter photon energy, respectively.

Variable	Photoelectric	Incoherent
	Mean	Mean
\bar{g}_A	E/w	
\bar{g}_B	$(E - E_K)/w$	$(E - E')/w$
\bar{g}_C	E_K/w	E'/w

$\text{Cov}(\tilde{c}_i, \tilde{c}_j)$.

5.2.3 Cascaded model of mean gain, variance, and PDF of \tilde{d}

In this section we described how to use CSA to obtain $G(E)$, $\text{NPS}_d(u, v)$, and $p_d(d|E)$ required for calculation of angiographic image signal and noise, as described above. Calculations are based on a CdZnTe x-ray detector with material properties listed in Tab. 5.2.

5.2.3.1 Mean gain

The detector signal from a conventional energy-integrating x-ray detector element is proportional to the total number of collected secondaries \tilde{q}_{sec} [mm^{-2}]. Therefore,

$$\bar{d}(E) = ka\bar{q}_{\text{sec}}(E) \quad (5.2.10)$$

where we have dropped the subscript i for notational convenience, k is a constant of proportionality and $a = a_x a_y$ represents the area of a detector element. We determine $\bar{q}_{\text{sec}}(E)$ using the CSA model illustrated Fig. 5.2.1. In this model, each incident photon may interact with Cd, Te, or Zn atoms, yielding

$$\bar{q}_{\text{sec}}(E) = \bar{q}_{\text{Cd,sec}}(E) + \bar{q}_{\text{Zn,sec}}(E) + \bar{q}_{\text{Te,sec}}(E) \quad (5.2.11)$$

where $\bar{q}_{\text{Cd,sec}}(E)$, $\bar{q}_{\text{Zn,sec}}(E)$, and $\bar{q}_{\text{Te,sec}}(E)$ represent the number of collected secondaries resulting from interactions with Cd, Zn, and Te atoms, respectively. We determine each of these using the single-Z CSA model described in Chapter 4. A similar model has been shown to accurately describe \bar{q}_{sec} and $\text{NPS}_{\text{sec}}(u, v)$ for single-Z energy-integrating detectors.^[218] In all cases, we ignore characteristic emission from lower-Z atoms following reabsorption of higher-Z characteristic photons. Since these x rays may escape the detector, this model likely overestimates \bar{q}_{sec} . The mean number

of secondaries for atom l is given by^[218]

$$\bar{q}_{l,\text{sec}}(E) = \bar{q}_{l,\text{sec}}^{\text{pe}}(E) + \bar{q}_{l,\text{sec}}^{\text{inc}}(E) \quad (5.2.12)$$

where $l \in \{\text{Cd}, \text{Zn}, \text{Te}\}$ identifies the atom, and $\bar{q}_{l,\text{sec}}^{\text{pe}}(E)$ and $\bar{q}_{l,\text{sec}}^{\text{inc}}(E)$ represent the mean number of secondaries collected from photoelectric and incoherent interactions. A simple extension of the model presented by Yun *et al.*^[218] to include depth-dependent collection processes in energy-integrating x-ray detectors can be used to show that $\bar{q}_{l,\text{sec}}^{\text{pe}}(E)$ and $\bar{q}_{l,\text{sec}}^{\text{inc}}(E)$ are given by

$$\begin{aligned} \bar{q}_{l,\text{sec}}^{\text{pe}}(E) = \bar{q}_o(E) F_{l,\text{pe}} & \left[(1 - P_{K_l} \omega_{K_l}) \langle \beta \rangle_{z_1} \bar{g}_{l,\text{pe,A}} \right. \\ & \left. + P_{K_l} \omega_{K_l} \left(\langle \beta \rangle_{z_1} \bar{g}_{l,\text{pe,B}} + \langle f_{l,\text{pe}} \langle \beta \rangle_{z_2} \rangle_{z_1, \theta} \bar{g}_{l,\text{pe,C}} \right) \right] \end{aligned} \quad (5.2.13)$$

and

$$\bar{q}_{l,\text{sec}}^{\text{inc}}(E) = \bar{q}_o(E) F_{l,\text{inc}} \left\langle \langle \beta \rangle_{z_1} \bar{g}_{l,\text{inc,B}} + \langle f_{l,\text{inc}} \langle \beta \rangle_{z_2} \rangle_{z_1} \bar{g}_{l,\text{inc,C}} \right\rangle_{\theta} \quad (5.2.14)$$

respectively, where $\bar{q}_o(E)$ [$\text{mm}^{-2}\text{keV}^{-1}$] represents the spectrum of photons incident on the x-ray detector, P_{K_l} and ω_{K_l} represent the K-shell participation fraction and fluorescence yield, respectively, $f_{l,\text{pe}}$ and $f_{l,\text{inc}}$ represent reabsorption probabilities of fluorescent and Compton-scatter x rays for atom l , respectively, $\bar{g}_{\text{pe},l,\text{A}}$, $\bar{g}_{\text{pe},l,\text{B}}$, and $\bar{g}_{\text{pe},l,\text{C}}$ represent gain factors describing conversion of x-ray energy to secondary quanta through photoelectric interactions for atom l , $\langle \rangle_x$ represents an average over the RV \tilde{x} , and $F_{l,\text{pe}}$ and $F_{l,\text{inc}}$ represent probabilities that an incident photon interacts in atom l through photoelectric and incoherent interaction given by

$$F_{l,\text{pe}} = \left(1 - e^{\mu_{\text{tot}}(E)L} \right) \times \frac{\mu_{l,\text{pe}}}{\mu_{l,\text{tot}}} \times \nu_{l,w} \quad (5.2.15)$$

$$F_{l,\text{inc}} = \left(1 - e^{\mu_{\text{tot}}(E)L} \right) \times \frac{\mu_{l,\text{inc}}}{\mu_{l,\text{tot}}} \times \nu_{l,w} \quad (5.2.16)$$

where ν_l represents the atomic weight fraction for atom l , $\mu_{l,\text{pe}}$, $\mu_{l,\text{inc}}$, and $\mu_{l,\text{tot}}$ represent the photoelectric, incoherent and total linear attenuation coefficient for atom l , respectively, μ_{tot} represents the total linear attenuation coefficient of CdZnTe, and L represents detector thickness.

Probability density functions required for all averages in the above equations have been described in detail in Chapter 4 and by Yun *et al.*^[218,219] Mean conversion gains \tilde{g} for photoelectric and incoherent interactions are summarized in Tab. 5.1. Note that many of the variables in the above expressions are energy-dependent although we have only explicitly expressed $\bar{q}_o(E)$ as a function of

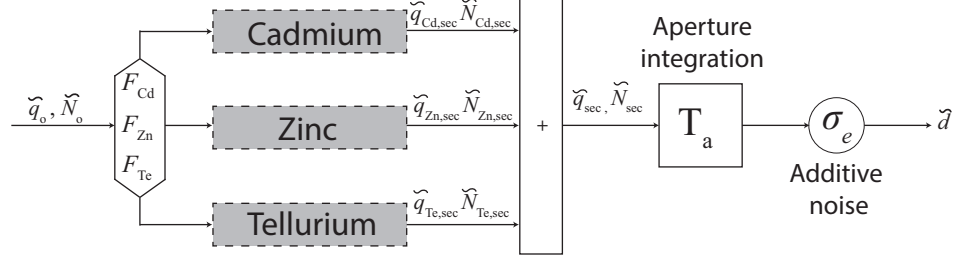


Figure 5.2.1: Schematic illustration of the CSA model used to describe energy deposition and conversion to secondaries in CdZnTe detectors. Transfer of the mean, NPS, and PDF of the number of quanta through each path is described using the generic interaction model described in Chapter 5.

energy.

Combining Eqs. (5.2.13) and (5.2.14) with (5.2.10) yields the mean gain $G(E)$:

$$G(E) = G_{\text{Cd}}(E) + G_{\text{Zn}}(E) + G_{\text{Te}}(E) \quad (5.2.17)$$

where $G_l(E)$ is given by

$$G_l(E) = ka \left[\bar{q}_{l,\text{sec}}^{\text{pe}}(E) + \bar{q}_{l,\text{sec}}^{\text{inc}}(E) \right] \quad (5.2.18)$$

with $\bar{q}_{l,\text{sec}}^{\text{pe}}(E)$ and $\bar{q}_{l,\text{sec}}^{\text{inc}}(E)$ given by Eqs. (5.2.13) and (5.2.14), respectively, for atom l . Combining the above expressions with Eq. (5.2.5) yields the mean detector element signal \bar{d} for energy-integrating systems. Substituting \bar{d}_i for \bar{M}_i in Eq. (5.2.3) yields the subtracted image signal for DSA and ESA.

5.2.3.2 Energy-integrating pixel variance

The pixel variance for energy-integrating systems, given by Eq. (5.2.7), requires determination of $\text{NPS}_{d_i}(u, v)$. Ignoring the influence of spatial relocation of fluorescent photons, the CSA model illustrated in Fig. 5.2.1 gives

$$\text{NPS}_d(u, v) \approx k^2 \text{NPS}_{\text{sec}}(0, 0) a^2 \text{sinc}^2(a_x u) \text{sinc}^2(a_y v) + \text{NPS}_{\text{add}}(u, v) \quad (5.2.19)$$

where we have dropped the subscript i , $\text{sinc}(a_x u)$ represents the sinc function, $\text{NPS}_{\text{sec}}(0, 0)$ represents the zero-frequency NPS of the number of collected secondary quanta \bar{q}_{sec} , and $\text{NPS}_{\text{add}}(u, v)$ represents the presampling additive noise NPS accounting for random variations in the image signal resulting from noisy detector electronics. Combining the above expression with Eq. (5.2.7) gives

$$\text{Var}(\bar{d}) = k^2 a \text{NPS}_{\text{sec}}(0, 0) + \sigma_{\text{add}}^2 \quad (5.2.20)$$

where $\sigma_{\text{add}}^2 = \iint_{\mathbb{R}^2} \text{NPS}_{\text{add}}(u, v) du dv$. Note that σ_{add} represents the electronic noise level for a single detector element over the entire length of the x-ray exposure. The above expression shows that in the limit of large detector elements $\text{Var}(\tilde{d})$ can be obtained by characterizing $\text{NPS}_{\text{sec}}(0, 0)$ and σ_{add} .

Since the number of secondaries liberated for one photon of energy E is independent of those for a different energy, $\text{NPS}_{\text{sec}}(0, 0)$ is given by

$$\text{NPS}_{\text{sec}}(0, 0) = \int_0^{kV} \text{NPS}_{\text{sec}}(0, 0; E) dE \quad (5.2.21)$$

$$\begin{aligned} &= \int_0^{kV} \text{NPS}_{\text{Cd,sec}}(0, 0; E) dE + \int_0^{kV} \text{NPS}_{\text{Zn,sec}}(0, 0; E) dE \\ &+ \int_0^{kV} \text{NPS}_{\text{Te,sec}}(0, 0; E) dE \end{aligned} \quad (5.2.22)$$

where $\text{NPS}_{l,\text{sec}}(0, 0; E)$ represents the energy-dependent zero-frequency NPS of the number of secondaries generated by an interaction with atom l . The second inequality in the previous equation follows because the number of secondaries collected from interactions with one atom is independent of the number collected from interactions with another atom. We obtain the zero-frequency NPS of atom l using the approach describe by Yun *et. al.*:^[218]

$$\text{NPS}_{l,\text{sec}}(0, 0; E) = \text{NPS}_{l,\text{sec}}^{\text{pe}}(0, 0; E) + \text{NPS}_{l,\text{sec}}^{\text{inc}}(0, 0; E) \quad (5.2.23)$$

where $\text{NPS}_{l,\text{sec}}^{\text{pe}}(0, 0; E)$ and $\text{NPS}_{l,\text{sec}}^{\text{inc}}(0, 0; E)$ represent the zero-frequency NPS of secondaries collected from photoelectric and incoherent interactions, respectively, for incident photon energy E . Extending the model described by Yun *et. al.*^[218] to include depth-dependent collection processes yields

$$\begin{aligned} \text{NPS}_{l,\text{sec}}^{\text{pe}}(0, 0; E) &= \bar{q}_o(E) F_{l,\text{pe}} \left[(1 - P_{K_l} \omega_{K_l}) \langle \beta \rangle_{z_1}^2 \bar{g}_{l,\text{pe,A}}^2 \left(1 + \frac{1}{\bar{g}_{l,\text{pe,A}}} + \frac{1 - \langle \beta \rangle_{z_1}}{\langle \beta \rangle_{z_1} \bar{g}_{l,\text{pe,A}}} \right) \right. \\ &+ P_{K_l} \omega_{K_l} \left[\langle \beta \rangle_{z_1} \bar{g}_{l,\text{pe,B}}^2 \left(1 + \frac{1}{\bar{g}_{l,\text{pe,B}}} \right) + \langle f_{l,\text{pe}} \langle \beta \rangle_{z_2} \rangle_{z_1, \theta} \bar{g}_{l,\text{pe,C}}^2 \left(1 + \frac{1}{\bar{g}_{l,\text{pe,C}}} \right) \right. \\ &\left. \left. + 2 \langle f_{l,\text{pe}} \beta \langle \beta \rangle_{z_2} \rangle_{z_1, \theta} \bar{g}_{l,\text{pe,B}} \bar{g}_{l,\text{pe,C}} \right] \right] \end{aligned} \quad (5.2.24)$$

and

$$\begin{aligned}
\text{NPS}_{l,\text{sec}}^{\text{inc}}(0, 0; E) &= \bar{q}_o(E) F_{l,\text{pe}} \left[\left\langle \beta \bar{g}_{l,\text{inc},\text{B}}^2 \left(1 + \frac{1}{\bar{g}_{l,\text{inc},\text{B}}} \right) \right\rangle_{z_1, \theta} \right. \\
&\quad + \left\langle f_{l,\text{inc}} \langle \beta \rangle_{z_2} \bar{g}_{l,\text{inc},\text{C}}^2 \left(1 + \frac{1}{\bar{g}_{l,\text{inc},\text{C}}} \right) \right\rangle_{z_1, \theta} \\
&\quad \left. + 2 \left\langle \left\langle f_{l,\text{pe}} \beta \langle \beta \rangle_{z_2} \right\rangle_{z_1} \bar{g}_{l,\text{inc},\text{B}} \bar{g}_{l,\text{inc},\text{C}} \right\rangle_{\theta} \right] \quad (5.2.25)
\end{aligned}$$

respectively. Combining the above expressions with Eq. (5.2.20) yields the variance of \tilde{d} for energy-integrating systems. Substituting $\text{Var}(\tilde{d}_i)$ for $\text{Var}(\tilde{M}_i)$ in Eq. (5.2.4) yields an expression for image noise for DSA and ESA.

5.2.3.3 PDF of prethresholding detector element signals

The mean EPC signal and variance are given by Eqs. (5.2.8) and (5.2.9), respectively, both of which are expressed in terms of $p_d(d|E)$ which is equal to the PDF of prethresholding adaptively-binned signal \tilde{d} given one interacting photon with energy E . In Chapters 3 and 4 a PDF transfer approach was used to obtain $p_d(d|E)$:

$$p_d(d|E) = \frac{1}{k} p_{\text{tot}}^1(d/k) * p_e(d) \quad (5.2.26)$$

where $p_{\text{tot}}^1(d/k)$ represents the PDF of the total number of collected secondaries given one interacting x ray photon, and $p_e(d)$ represents the PDF of the signal resulting from electronic noise which, similar to Chapters 3 and 4 is assumed to be Gaussian with standard deviation $\sqrt{j}\sigma_e$ where σ_e represents electronic noise of a single prebinning detector element for one fast readout and j is the number of binned detector elements. The number of binned elements j required to collect the total energy deposited per interaction is discussed in Sec. 5.3. The PDF of collected secondaries, $p_{\text{tot}}^1(d/k)$, is given by

$$p_{\text{tot}}^1(d/k) = \nu_{\text{Cd},w} p_{\text{Cd,tot}}^1(d/k) + \nu_{\text{Zn},w} p_{\text{Zn,tot}}^1(d/k) + \nu_{\text{Te},w} p_{\text{Te,tot}}^1(d/k) \quad (5.2.27)$$

where $\nu_{l,w}$ represents the atomic weight fraction of atom l . We use the CSA model described in Chapter 4 to determine $p_{l,\text{tot}}^1(d/k)$ for each atom. Combining the above two equations with Eqs. (5.2.8) and (5.2.9) yields the mean number of photon counts in each energy bin and covariance between energy bins, respectively. Image signal and noise for ERA are then given by Eqs. (5.2.3) and (5.2.4) with the replacement of \bar{M}_i , $\text{Var}(\bar{M}_i)$, and $\text{Cov}(\bar{M}_i, \bar{M}_j)$ with \bar{c}_i , $\text{Var}(\bar{c}_i)$, and $\text{Cov}(\bar{M}_i, \bar{M}_j)$,

Table 5.2: Physical and electrical properties used for CdZnTe calculations. Atomic number, mass density, fractional atom No, fractional atomic weight, Average K-fluorescent energy [keV], K-shell participation fraction, and K-fluorescence yield are take from Ref. 106. Electron and hole mobility-lifetime products are taken from Ref. 158.

Parameter	Symbol	Cd	Zn	Te
Atomic number	Z	48	30	52
Mass density [g cm ⁻²]	ρ	8.65	7.61	6.25
Fractional atom No.	ν_a	0.45	0.05	0.5
Fractional atomic weight	ν_w	0.43	0.028	0.54
Average K-fluorescent energy [keV]	E_K	24	8.9	29
K-shell participation fraction	P_K	0.85	0.87	0.84
K-fluorescence yield	ω_K	0.84	0.48	0.88
Electron mobility lifetime product [cm ² V ⁻¹]	$\mu_e\tau_e$		2×10^{-3}	
Electron mobility lifetime product [cm ² V ⁻¹]	$\mu_h\tau_h$		2×10^{-5}	

respectively.

5.2.4 Iodine Detectability

We quantify the ability to visualize iodinated vasculature in terms of a performance metric related to the detectability index,^[4] defined as the iodine SNR per square-root of patient entrance exposure:

$$\frac{\text{SNR}_I}{\sqrt{X}} = \frac{1}{\sqrt{X}} \frac{\text{E}(\tilde{A}_I - \tilde{A}_I^N)}{\sqrt{\text{Var}(\tilde{A}_I - \tilde{A}_I^N)}}, \quad (5.2.28)$$

where X is the patient entrance exposure, and \tilde{A}_I and \tilde{A}_I^N are the iodine signals from iodinated and non-iodinated regions of the images, respectively. In this study we ignore spatial correlations in an image, in which case $\text{Var}(\tilde{A}_I - \tilde{A}_I^N) = \text{Var}(\tilde{A}_I) + \text{Var}(\tilde{A}_I^N)$.

5.3 Methods

5.3.1 Monte Carlo simulation of upper-limit of side-escape fraction

It is well understood that lateral escape of characteristic and/or Compton-scatter x rays from a detector element results in degradation of spatial resolution, image quality, and spectral resolution, and that some form of adaptive binning will be required to minimize these effects. We assume an adaptive-binning approach similar to one implemented in the Medipix3^[18] prototype. With this approach, charge liberated in a cluster of j neighboring elements is summed and a count attributed to the element with the largest signal.

In the case of CdZnTe convertor materials, less than 1 % of all x-ray interactions result in generation of a Compton-scatter x ray. Therefore, reabsorption of Compton scatter x rays outside adaptively-binned elements will result in negligible degradation of both image quality and energy imprecision. Estimating total deposited energy will therefore only require summing all secondaries resulting from photoelectric interactions, including those produced following reabsorption of fluorescent photons. We perform a simple Monte Carlo simulation to determine the adaptively-binned element size required to minimize lateral escape of fluorescent photons. We assume that each x ray arrives normal to the detector and establish an upper limit of the side-escape fraction per interacting x ray by considering the worst-case scenario where characteristic photons are emitted at a polar angle of $\pi/2$ radians, as illustrated in Fig. 5.3.1.

Since the fractional atomic number of Zn is negligible compared to that for Cd and Te, we only consider interactions with either Cd or Te atoms with probabilities determined by fractional atomic numbers. In the case of interaction with a Cd atom, the probability of characteristic emission is determined from the product of the K-shell participation fraction and the K-shell fluorescence yield. In the case of characteristic emission, azimuthal angle $\tilde{\phi}$ is determined by sampling a uniform distribution over the domain $\tilde{\phi} \in [0, 2\pi]$. Reabsorption distance \tilde{l}_1 is determined by sampling the distribution $p_{l_1}(l_1) = \mu(E_K^{\text{Cd}})\exp(-\mu(E_K^{\text{Cd}})l_1)$. When an interaction occurs with a Te atom, probability of fluorescence, azimuthal angle $\tilde{\phi}$, and reabsorption distance \tilde{l}_1 are determined in a similar manner as that for Cd. We also account for emission of a second characteristic photon following interaction of a Te characteristic x ray in a Cd atom, as illustrated in Fig. 5.3.1. We tally the total number of reabsorption events occurring inside the element for element widths ranging from 0.1-2 mm. All Monte Carlo calculations were performed using the material properties listed in Tab. 5.2.

5.3.2 Theoretical comparison of angiographic image quality

The method described above for calculating image signal and noise is used to theoretically compare image quality that can be obtained with each of ERA, ESA, and DSA for the same patient entrance exposure. For each method we consider the task of isolating iodine embedded in water. In all cases, we assume a source-to-object distance of 20 cm, source-to-detector distance of 80 cm, 30-cm thick patient, and a 0.5-mm thick CdZnTe x-ray convertor with material properties listed in Tab. 5.2. We assume pre-binning element widths of 0.2×0.2 mm and ignore distortions in object size caused by fan-beam projection as this will affect each technique equally. All x-ray spectra are generated using

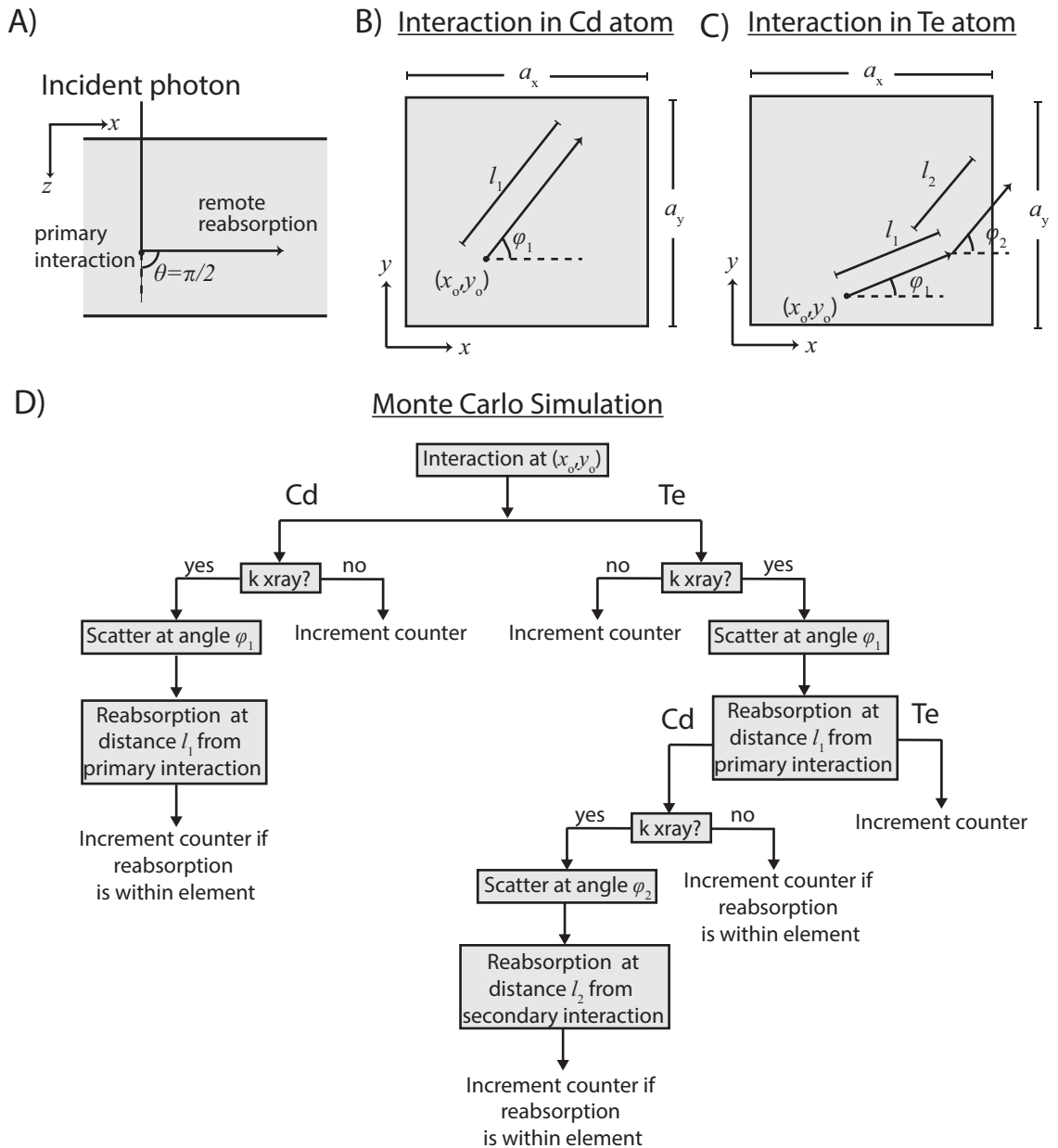


Figure 5.3.1: Schematic illustration of the Monte Carlo simulation used to determine the upper limit of the fraction of x-ray interactions that result in lateral escape of characteristic photons from an adaptively-binned CdZnTe element. A) Illustration of emission of characteristic x ray at a polar angle of $\pi/2$ radians. B) Illustration of reabsorption of a Cd characteristic x ray. C) Illustration of reabsorption of a Te characteristic x-ray and subsequent production of a Cd characteristic x ray. D) Flow-chart representation of the Monte Carlo simulation.

an in-house MATLAB routine that implements algorithms published by Tucker and Barnes^[199] for a tungsten-target x-ray tube.

5.3.2.1 Energy-resolved angiography, ERA

We implement a two-material decomposition approach^[192] in which the object is assumed to be composed of water and iodine. Interacting photon energy estimated from binned elements is assigned to one of two energy bins using thresholds t_1 and t_2 . We let $t_1 = 3 \times \sqrt{j}\sigma_e$, where j is the number of binned elements, in order to suppress false noise counts from binned elements and choose t_2 such that P_I is maximized. In all cases we assume an adaptively-binned element size such the upper limit of the side-escape fraction (determined from Monte Carlo calculations) is $\leq 5\%$, and readout intervals of length $a_t = 10^{-7}$ sec which is in the range of what is possible with state-of-the-art readout electronics for CdZnTe-based photon-counting systems.^[30,68,91,102,168,173,175,176,181] We consider x-ray exposures typical for fluoroscopy (0.001 mR/image at the detector) and angiography (0.1 mR/image at the detector).^[55] As discussed below, for 1/30 sec exposure time and 10^{-7} sec readout time, this results in negligible pulse pile up in EPC detectors. Image signal (Eq. (5.2.3)), noise (Eq. (5.2.4)), and SNR per root exposure_I (Eq. (5.2.28)) are calculated for an applied tube voltage of 100 kV for the imaging geometry and patient thickness described above, and selected additive noise levels and applied electric fields.

5.3.2.2 Digital subtraction angiography, DSA

Digital subtraction angiography requires subtraction of a post-injection image from a pre-injection (mask) image. The mean gain and zero-frequency NPS of secondary quanta used for calculation of the mean pre and post-injection exposures are plotted as a function of incident photon energy in Fig. 5.4.1. We assume an exposure time of 1/30 sec for both pre and post-injection images resulting in a total exposure time $T = 1/15$ sec. To compare DSA with ERA for the same additive noise level, we let $\sigma_{\text{add}} = \sigma_e T / a_t$ where, σ_e is the additive noise level corresponding to one fast readout of one 0.2×0.2 mm² element. Note that EI detectors do not perform fast readouts and expressing σ_{add} in terms of a_t and σ_e is only required to compare image quality with ERA for the same levels of additive noise. We theoretically calculate image signal (Eq. (5.2.3)), noise (Eq. (5.2.4)), and SNR per root exposure (Eq. (5.2.28)) for an applied tube voltage of 65 kV for imaging geometry, patient thickness, and exposure levels described above, for selected convertor thicknesses and additive noise levels.

5.3.2.3 Energy subtraction angiography, ESA

We consider a dual-energy approach that implements weighted subtraction of low and high-energy post-injection images with total exposure time of $T = T_L + T_H = 1/30$ sec where T_L and T_H represent low and high-energy exposure times, respectively. Additive noise levels in low and high-energy images are then given by $\sigma_{L,\text{add}} = \sigma_e \times T_L/a_t$ and $\sigma_{H,\text{add}} = \sigma_e \times T_H/a_t$, respectively. We theoretically calculate image signal (Eq. (5.2.3)), noise (Eq. (5.2.4)), and SNR per root exposure (Eq. (5.2.28)) for low and high-energy applied tube voltages of 50 kV and 130 kV with 2.1 mm of copper filtration on the 130-kV spectrum and a low-to-high-mAs ratio that maximizes SNR per root exposure. We assume the optimal mAs ratio is obtained by varying T_L and T_H for constant mA.

5.4 Results

5.4.1 Performance characteristics of CdZnTe detectors

5.4.1.1 Mean gain and zero-frequency NPS of collected secondaries

Figure (5.4.1) illustrates the dependence of the mean gain and normalized zero-frequency NPS of secondaries ($\bar{q}_o \text{NPS}_{\text{sec}}(0,0)/\bar{q}_{\text{sec}}$) on incident photon energy and applied electric field. In general, as expected, lower electric fields result in lower mean gain values and higher normalized NPS values for all incident photon energies. This is due to poor charge collection efficiency at lower electric fields resulting in a secondary quantum sink.^[53] This effect is modest under all conditions considered and, therefore, will likely to have minimal effect on iodine SNR for DSA and ESA. At higher photon energies the mean gain decreases and normalized NPS increases because of low quantum efficiency at these energies.

5.4.1.2 Fraction of fluorescent x rays reabsorbed in neighboring elements

Figure 5.4.2 illustrates the results of MC calculations of the upper limit of the number of x-ray interactions that result in reabsorption of a characteristic x ray outside of adaptively-binned elements. As expected, the side-escape fraction decreases with increasing element width. For small element sizes (0.1-0.5 mm) the upper limit of side-escape fraction can be greater than 10 % suggesting that at these element widths reabsorption of characteristic x rays may result in multiple photon counts per interacting x-ray photon. At an adaptive-element width of 1.0 mm, the upper limit of side-escape fraction reduces to approximately 5-6 %. Since the actual number of side-escape events will be lower than this, we assume an adaptively-binned element size of $1.0 \times 1.0 \text{ mm}^2$ in all subsequent

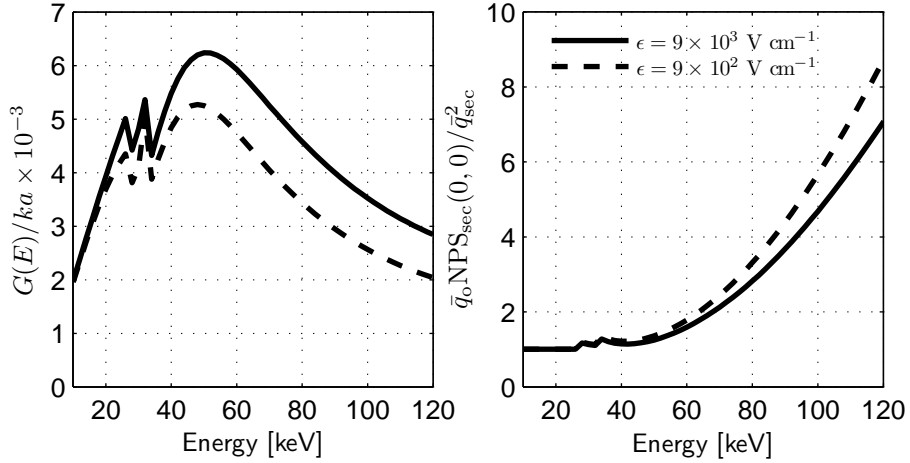


Figure 5.4.1: Dependence of mean gain $G(E)$ and normalized zero-frequency NPS of secondaries $\bar{q}_0 \text{NPS}_{\text{sec}}(0, 0) / \bar{q}_{\text{sec}}^2$ on incident photon energy.

calculations. For prebinning-element width of 0.2 mm this requires binning into 5×5 element clusters. The additive noise level for adaptively-binned prethresholding signals is then equal to $5 \times \sigma_e$ where σ_e is the additive noise for one prebinning element.

Figure 5.4.3 illustrates the dependence of the mean number of incident photons per element per readout on element size for selected detector exposure levels. Each curve is calculated based on a 100 kV x-ray spectrum transmitted through 30 cm of water and 10^{-7} s readout intervals. This figure demonstrates that at fluoroscopic exposure levels (<0.01 mR) and adaptive-element widths of 1.0 mm, pulse pile up can be ignored. At angiographic exposure levels (0.1-0.5 mR) $\lambda \sim 10^{-2} - 10^{-1}$ suggesting that even at these higher exposures pulse pile up will not degrade image quality.

5.4.1.3 Response function

Figure 5.4.4 illustrates $p_d(d|E)$ for the model illustrated in Fig. 5.2.1 calculated using Eqs. (5.2.26) and (5.2.27) for a 50-keV photon incident on a 0.5-mm thick CdZnTe-based x-ray detector for selected applied electric fields and electronic noise levels, and an adaptively-binned element size of 1.0 mm². All calculations were performed using material properties listed in Table 5.2.

Similar to the results of Le Claire *et al.*^[106], Fig. 5.4.4 shows that low applied electric fields ($\sim 10^2$ V cm⁻¹) result in broader and more asymmetric photo-peaks and escape peaks compared to higher electric fields. This is caused by a stronger depth dependence of the collection efficiency at lower electric fields. In addition, as expected, increasing additive noise levels also results in photo and escape-peak broadening. Since photo-peak broadening is known to increase noise in basis material

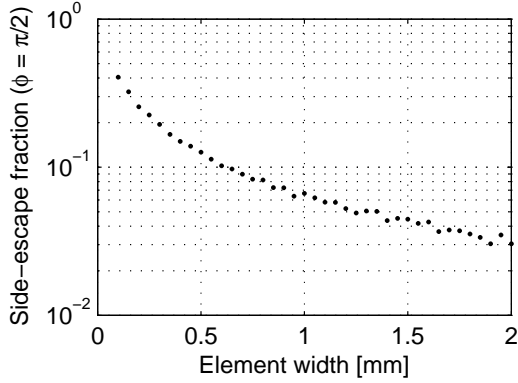


Figure 5.4.2: Upper limit of the fraction of interactions that result in lateral escape of characteristic photons from an adaptively-binned element. All values were obtained using the Monte Carlo simulation illustrated in Fig. 5.3.1 with material properties listed in Tab. 5.2.

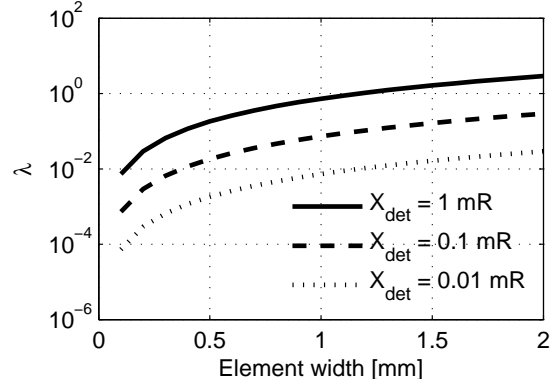


Figure 5.4.3: Dependent of mean number of photons incident per element per readout λ on element width for selected detector exposure levels. Numbers are calculated assuming a total exposure time of 1/30 sec and readout time of 100 ns and a 100 kV spectrum transmitted through 30 cm of water.

estimates,^[152,201,203] it is expected that the combined effects of low electric fields and high electronic noise levels will result in degraded iodine SNR, as described below. For systems with sufficiently low additive-noise levels and high electric fields, escape of fluorescent scatter photons and stochastic conversion gain are primary causes of spectral distortion.

5.4.2 Comparison of iodine SNR obtained with ERA, ESA, and DSA assuming CdZnTe x-ray detectors for each

Figure 5.4.5 illustrates the dependence of P_I on iodine area density [mg cm^{-2}] for selected electronic noise levels, applied electric fields, and detector exposures for ERA, ESA, and DSA. For exposure levels and readout times considered in this study, pulse pile up is expected to have a negligible effect on image quality, in which case ERA is independent of exposure.

5.4.2.1 Influence of depth-dependent collection efficiency

In the case of ESA and DSA, as expected based on Fig. 5.4.1, Fig. 5.4.5 demonstrates that iodine SNR per root exposure varies very little with applied electric field for all imaging conditions considered. In addition, at angiographic exposure levels (~ 0.5 mR), SNR/\sqrt{X} for ESA is within approximately 25 % of that of DSA for all iodine concentrations and additive noise levels considered.

In the case of ERA, SNR/\sqrt{X} shows a strong dependence on electric field. In particular, as

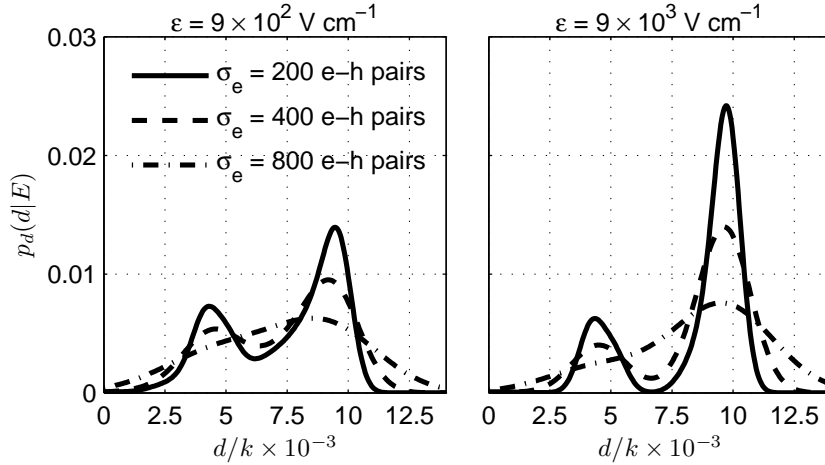


Figure 5.4.4: Probability density functions of prethresholding detector element signals for 50 keV photons incident on a 0.5-mm thick CdZnTe-based x-ray detector for selected applied electric fields and additive noise levels.

suggested by the response functions in Fig. 5.4.4, iodine SNR for ERA is degraded at low electric field levels. The influence of low electric fields on ERA image quality is two-fold. Firstly, low electric fields result in photo-peak broadening that is known to degrade SNR in basis material images. Secondly, low electric fields reduce the mean number of secondaries collected per x-ray interaction potentially resulting in prethresholding signals below the additive noise floor. Successful CdZnTe-based photon-counting systems for ERA will likely have to be designed such that collection efficiencies are near-uniform over the x-ray convertor layer. When this condition is satisfied, and additive noise levels are sufficiently low ($\leq 5 \times 200$ e-h pairs for per adaptively-binned element), Fig. 5.4.5 demonstrates that ERA has the potential to provide iodine SNR within approximately 25-30 % of that DSA for the same patient entrance exposure.

5.4.2.2 Dependence on exposure and electronic noise levels

Figure 5.4.5 illustrates that for both ESA and DSA, as expected, SNR/\sqrt{X} is reduced when exposure levels are reduced from angiographic levels (~ 0.5 mR) to fluoroscopic levels ($1 \mu\text{R}$) with the degree of degradation depending on electronic noise levels. This occurs because at lower exposure levels electronic noise becomes a substantial fraction of image noise and angiographic image quality is no longer determined solely by noise associated with the random number of collected secondaries, i.e. image quality is no longer quantum noise limited. While SNR/\sqrt{X} for ESA may only be 30-50 % of that of DSA at fluoroscopic exposures, pre and post-injection images for DSA may be acquired many seconds apart which may result in substantial motion artifacts in real-time subtracted images.

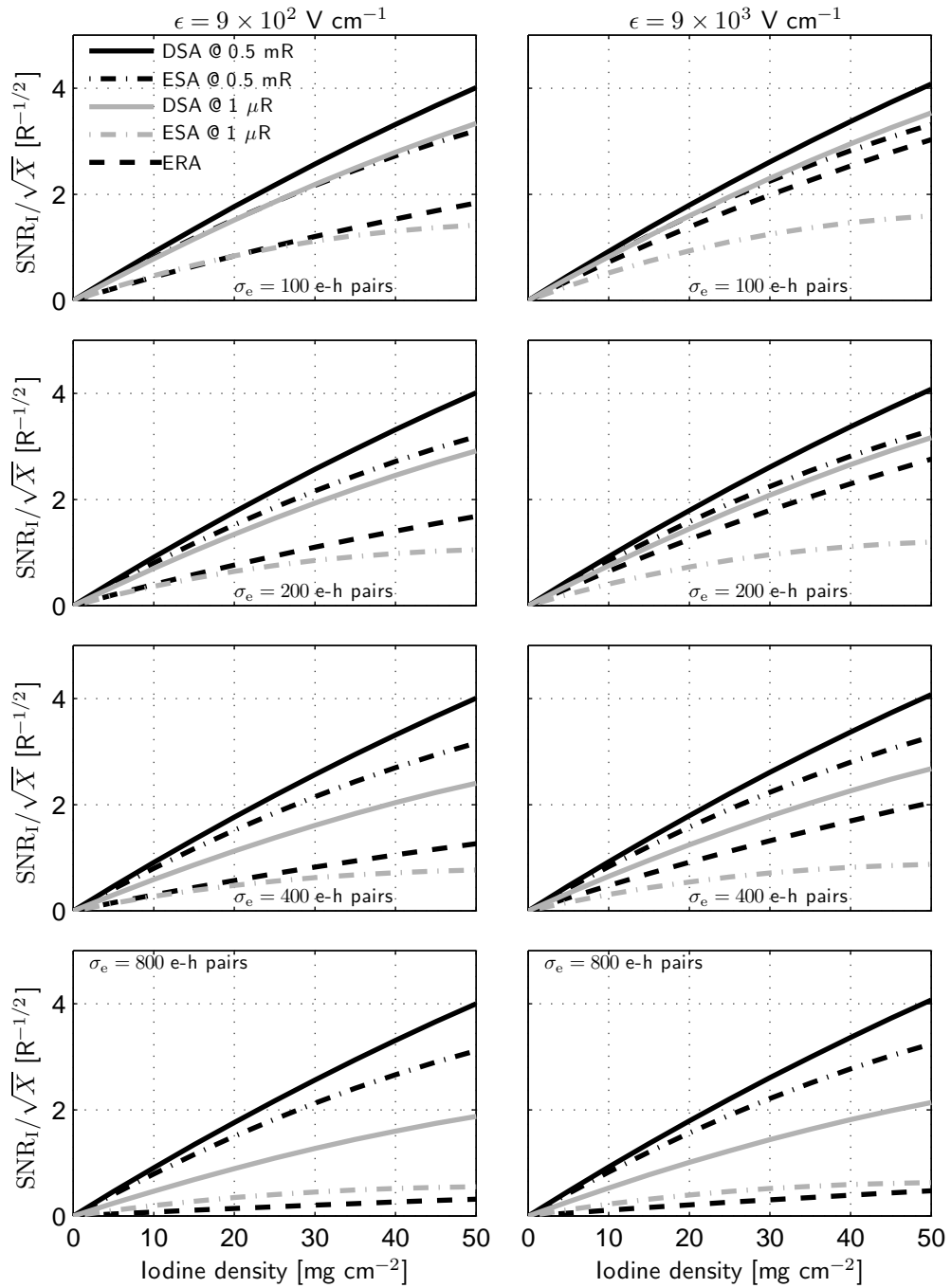


Figure 5.4.5: Dependence of SNR_I / \sqrt{X} on iodine density $[\text{mg cm}^{-2}]$ for 30 cm of water and selected additive noise levels, exposure levels, and applied electric fields. Exposure levels indicated are those at the x-ray detector.

In the case of ERA, since this technique thresholds out electronic noise, SNR/\sqrt{X} is independent of exposure levels for exposure and readout times considered here. However, Fig. 5.4.5 illustrates that high additive noise levels ($\geq 5 \times 400$ e-h pairs per adaptively-binned element) will result in a substantial reduction of iodine SNR for all imaging conditions considered. This is due to the fact that for higher additive noise levels, a higher threshold must be chosen to suppress false noise counts. When additive noise per adaptively-binned element reaches the same order of magnitude (or greater) as the mean number of secondaries collected per x-ray interaction (Fig. 5.4.1), this results in loss of signals generated below the additive noise floor. In some situations, this results in ERA iodine SNR that is only 10 % that of DSA for the same patient entrance exposure and additive noise level.

5.5 Discussion

We have presented a novel theoretical comparison of angiographic image quality that could be achieved using energy-dependent and conventional subtraction approaches including the effects of electronic noise sources and stochastic energy-depositing, conversion, and collection processes. Iodine SNR was determined for energy-resolved, energy-subtraction, and digital subtraction angiography using cascaded-systems analysis in combination with a recently-described linearized noise propagation.^[192] This enabled a direct comparison of ERA image quality that could be achieved using state-of-the-art CdZnTe-based photon-counting x-ray detectors, with ESA and DSA also assuming CdZnTe detectors. Our analysis demonstrates that both energy-subtraction and energy-resolved approaches have the potential to provide iodine SNR within 25% of that of DSA using realistic x-ray detectors at angiographic exposure levels.

In the case of ERA, we assumed an adaptive-binning approach where signals from neighboring elements are summed into a larger composite element to estimate total deposited photon energy, and a count attributed to the element with the largest signal. A Monte Carlo simulation demonstrated that clustering elements into 1.0 mm^2 adaptively-binned elements would result in reabsorption of fluorescent photons outside binned elements in less than 5% of all x-ray interactions. All calculations were therefore based on 1.0 mm^2 adaptively binned element sizes. With this assumption, it was demonstrated that iodine SNR is within 25% of DSA when electric fields are chosen such that collection of e-h pairs is nearly uniform over the x-ray convertor layer, and additive noise levels do not exceed 1000 e-h pairs per 1.0 mm^2 composite element. Recently, a cadmium-telluride-based EPC detector was constructed with element areas of 0.165 mm^2 with additive noise levels less than 200 e-h pairs per element per readout,^[101] suggesting that it may therefore be possible to achieve

the imaging performance predicted in this analysis with contemporary EPC technologies.

For each technique considered in this study we assumed CdZnTe x-ray detector technology and, in all cases, ignored the influence of spatial relocation of characteristic photons. The analysis presented here, therefore, likely overestimates image quality achievable with each technique. However, it is unlikely that this assumption will influence the comparison between ESA and DSA since it is expected that reabsorption will affect spatial resolution and image NPS similarly for these approaches. In the case of ERA, since we have assumed an adaptive binning approach, spatial relocation of quanta will only result in loss of resolution when reabsorption of fluorescent photons is outside adaptively-binned elements, which occurs in less than 5% of all interactions, or when reabsorption occurs within adaptively-binned elements but energy deposited at a reabsorption site is greater than that deposited at a primary interaction site, which may occur for interacting photon energies less than approximately 65 keV. In the latter case, a count may incorrectly be attributed to the element where a fluorescent photon is reabsorbed. The relative influence of spatial relocation of reabsorbed characteristic x rays on DSA, ESA, and ERA requires further study.

While CdZnTe is currently being developed for EPC x-ray detection systems, DSA and ESA would likely be implemented using more common x-ray convertor materials, such as cesium iodide. Many of the image-forming processes discussed in this analysis are common to all detector materials, and the ESA and DSA results presented here will likely still apply.

5.6 Conclusions

The cascaded-systems approach combined with the linearized noise-propagation analysis provides a framework for optimizing and evaluating iodine SNR that may be obtained using novel energy-based methods in realistic imaging conditions. Using this framework, energy-resolved angiography and energy-subtraction angiography were compared with conventional digital-subtraction angiography, assuming CdZnTe-based x-ray detectors for each. While the energy-based methods are not necessarily optimized and further improvements are likely, it is concluded that both dual-energy and photon-counting approaches have the potential to provide iodine SNR within 25% of that of DSA for the same x-ray exposure using realistic x-ray detectors.

For CdZnTe-based photon-counting systems, a Monte Carlo simulation demonstrated that binning detector elements into 1.0 mm^2 composite elements would suppress greater than 95% of interaction events that result in reabsorption of fluorescent x-rays outside of adaptively-binned elements. For readout times in the range of what is possible with state-of-the art CdZnTe EPC detectors, this

will result in negligible pulse pile up at fluoroscopic and angiographic exposure levels. In addition to adaptive binning, successful CdZnTe-based ERA systems will require electronic noise levels less than ~ 1000 e-h pairs per 1.0 mm^2 adaptively-binned element and applied electric fields chosen such that collection of e-h pairs is nearly uniform over the x-ray convertor layer.

Chapter 6

Conclusions

Energy-resolved and energy-subtraction angiography are exciting vascular imaging approaches that may enable DSA-like imaging of moving structures, such as coronary arteries, that are not susceptible to motion artifacts. Similar to any innovation in medical imaging, understanding and quantifying the ultimate potential of these new imaging approaches to overcome limitations of existing methods, and provide high-quality images, is critical and identifies how much research effort and resources should be focused on design and development of new systems. This requires development of new theories and frameworks for comparing with conventional approaches by theory, simulation, and experiment, and was the focus of this thesis.

In this thesis, a theoretical framework for describing angiographic image quality that could be obtained with energy-resolved and conventional subtraction approaches was developed and used to compare iodine SNR available with each of these approaches. A simple analysis assuming ideal instrumentation suggested that both ERA and ESA could provide iodine SNR within 5-10% that of DSA. This was a surprising result because it is generally accepted that ESA approaches result in image SNR that is 3-5 times lower than DSA. The difference between the analysis described in Chapter 2 and previous studies is that we considered the available iodine SNR per root exposure independent of source and detector technology, where early studies performed in the 1980s assessed the potential of ESA with technologies of the time that were often limited by power restrictions of x-ray tubes and generators. Modern x-ray generators are capable of power outputs on the order of 80 kW, and Fig. 6.0.1 illustrates that it may be possible to obtain ESA images in less than 0.2 s that satisfy this requirement. In coronary applications, images would be acquired in the diastolic phase that is ≈ 0.25 -0.3 s (depending on heart rate), during which coronary arteries are near-stationary.

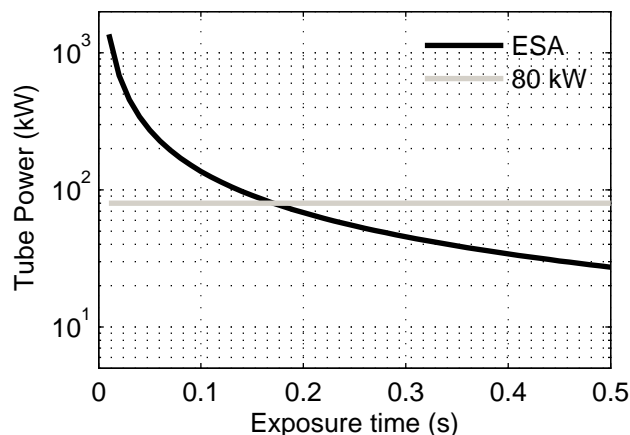


Figure 6.0.1: A plot of the applied tube power required to generate ESA images at angiographic exposure levels (~ 0.5 mR at the detector) as a function of total exposure time. Calculations are based on the imaging geometry, exposure parameters, and patient thickness described in Chapter 5. The horizontal line indicates 80 kW.

Combining these numbers with the results of Chapter 5, it is concluded that ESA images of coronary arteries could be generated with *reduced* motion artifacts compared to DSA and iodine SNR within 25% of that of DSA using modern x-ray source and detector technology. Depending on the degree of motion-artifact reduction, this may result “DSA-like” coronary angiograms with higher iodine sensitivity than conventional non-subtraction angiography.

Energy-subtraction angiography could be implemented using fast-kV-switching x-ray generators and modern cesium-iodide-based energy-integrating x-ray detectors. Such a system is currently under development in Dr. Cunningham’s research laboratory at the Robarts Research Institute. This system will be used in follow-up studies that quantitatively assess the influence of motion and tube power on ESA image quality. It is expected that for higher heart rates, ESA may not completely suppress motion artifacts and provide SNR within 25% of DSA. Energy-resolved approaches on the other hand would only require a single post-injection exposure and would not be limited by power restrictions.

While prototype EPC detectors are currently strip or small-area detectors, it was demonstrated that ERA also has the potential to provide iodine SNR within 25% of that of DSA for the same patient entrance exposure using CdZnTe-based photon-counting x-ray detectors. This will require adaptively binning elements into 1.0 mm^2 composite elements, electronic noise levels lower than ≈ 1000 e-h pairs per 1.0-mm^2 adaptively-binned element, and applied electric fields that result in collection efficiency of secondary quanta that is near-uniform over the convertor layer. Some prototype CdZnTe-based systems are capable of satisfying the last two requirements, but electronic readout

systems will need to be further developed in order to bin elements into larger 1.0 mm^2 adaptively-binned elements. The results of this thesis suggests that research effort and resources should be focused on design and development of large-area low-noise EPC detectors with adaptive-binning capabilities for implementation in future ERA systems. When these technological requirements are satisfied, ERA is expected to provide motion-artifact-free images with iodine SNR comparable to that of DSA. In the interim, ESA could be developed as a dual-energy alternative that would reduce motion artifacts for patients with lower heart rates.

Subtraction imaging of coronary arteries has been a long-term goal of cardiac imaging and the results of this thesis suggest that this may become possible with energy-dependent imaging approaches in the near future. Both energy-dependent approaches considered in this thesis have the potential to improve visibility of diseased coronary arteries compared to conventional non-subtraction approaches. This could enable imaging studies of the coronary anatomy that use lower iodine doses and reduced x-ray exposures compared to current approaches. However, a limitation of this thesis is that a direct comparison of angiographic image quality obtained using energy-dependent subtraction and conventional non-subtraction approaches was not performed. As discussed in the Future Work section, such a comparison would require quantifying the ability of ERA and ESA to remove image intensity variations caused by density and thickness variations of soft-tissue and bone structures. Whether or not suppression of background variations with ERA and ESA will result in superior iodine visualization compared to non-subtraction angiography remains an unanswered question and will be the focus of future studies, such as the one outlined in the Future Work section.

Chapter 7

Future work I: Comparison of energy-dependent angiography with conventional non-subtraction angiography

7.1 Introduction

For patients suspected of having coronary artery disease (CAD), determining the location and severity of atherosclerotic plaques is critical for predicting risk of myocardial infarction and identifying patients that may benefit from revascularization procedures. [42,66,71,150,207] In spite tremendous advances made in three-dimensional imaging techniques, including computed tomography and magnetic resonance imaging approaches, conventional two-dimensional non-subtraction coronary angiography remains the most widely used imaging technique for visualizing coronary anatomy. In Canada, the United States, and Europe, with the exception of low-risk groups, the majority of patients suspected of CAD will undergo x-ray angiography for both confirmation of diagnosis of CAD and assessment of suitability for revascularization procedures. [66,71,150]

Non-subtraction angiography procedures require acquisition of an x-ray image of cardiac anatomy after injection of a contrast agent, usually iodine-based, into one or more coronary arteries. While iodine injection enhances visualization of coronary arteries, projection of over and under-lying

anatomic structures causes intensity variations that can obscure arterial visualization.^[141] Pixel-intensity variations caused by projection of soft-tissue and bone structures (with different densities and thicknesses) onto a two-dimensional image plane is commonly referred to as anatomic noise.^[19,27,162,163] Minimizing the influence of anatomic noise on arterial visualization with non-subtraction angiography requires using relatively high doses of iodine-based contrast material that, when used in excess, can impair kidney and left ventricular function.^[63,84,85,119,120]

Digital subtraction angiography^[34,35,38,50,51,56,132,133,149] (DSA) was introduced in the 1970s with the goal of improving visualization of diseased vasculature and reducing contrast-material doses. While DSA is extremely successful at imaging structures that are near-stationary over a period of several seconds, the need for subtraction of pre and post injection images results in motion artifacts in studies of coronary arteries.^[96]

In this thesis we revisited energy-subtraction approaches, originally proposed in the late 1970s as a dual-energy alternative to DSA, and proposed the use of energy-resolved approaches for coronary imaging. These approaches would be less sensitive to patient motion and, as demonstrated in Chapter 5, both energy-subtraction angiography and energy-resolved angiography have the potential to provide iodine SNR within 25% of that of DSA for the same patient entrance exposure. While this result suggests that these approaches have the potential to improve iodine detectability relative to conventional non-subtraction angiography, a direct comparison between energy-dependent and non-subtraction angiography was not performed. It therefore remains an unanswered question as to whether or not these approaches will improve image quality in coronary angiography.

Performing a direct comparison of ESA and ERA image quality with non-subtraction angiography requires quantification of potential improvements in iodine visualization that would be gained by suppression of soft-tissue and/or bone structures from angiographic images. In the following sections a theoretical framework that describes the influence of both anatomic and quantum noise sources is described. Results from a preliminary comparison of soft-tissue suppression capabilities of energy-dependent and conventional subtraction approaches are presented. In addition, a preliminary comparison of the iodine detectability index^[1] obtained with energy-dependent and non-subtraction angiography is presented.

7.2 Theoretical framework for comparing subtraction and non-subtraction angiography

The goal of both subtraction and non-subtraction angiography is to enhance visualization of diseased vasculature by injecting a patient with a contrast-enhancing agent such as iodine. Assuming an object composed of water, bone, and iodine, the line-integral of attenuation along an x-ray path through a patient is given by

$$\int \tilde{\mu}(\mathbf{r}, s; E) ds = \sum_{b=1}^m \frac{\mu}{\rho}_b(E) \tilde{A}_b(\mathbf{r}) = \tilde{\mathbf{A}}(\mathbf{r})^T \frac{\boldsymbol{\mu}}{\boldsymbol{\rho}}(E) \quad (7.2.1)$$

where s represents position along the x-ray path, E represents photon energy, \mathbf{r} represents position in the image plane and

$$\tilde{\mathbf{A}}(\mathbf{r}) = \begin{bmatrix} \tilde{A}_W(\mathbf{r}) \\ \tilde{A}_B(\mathbf{r}) \\ A_I(\mathbf{r}) \end{bmatrix} \quad \text{and} \quad \frac{\boldsymbol{\mu}}{\boldsymbol{\rho}}(E) = \begin{bmatrix} \frac{\mu}{\rho}_W(E) \\ \frac{\mu}{\rho}_B(E) \\ \frac{\mu}{\rho}_I(E) \end{bmatrix} \quad (7.2.2)$$

where $\frac{\mu}{\rho}(E)$ [$\text{cm}^2 \text{g}^{-1}$] represents the mass-attenuation coefficient and $\tilde{A}_W(\mathbf{r})$, $\tilde{A}_B(\mathbf{r})$, and $A_I(\mathbf{r})$ [g cm^{-2}] represent area densities of water, bone, and iodine, respectively. Note that the difference between the above expressions and similar expressions presented in chapters 2 and 5, is the here area densities are expressed as random functions of position. This enables analyses of the effects of variations in soft-tissue and bone density encountered in real patients. In this chapter we only consider anatomic variability due to changes in soft-tissue area density $\tilde{A}_W(\mathbf{r})$. In order to quantify the influence of background variability on iodine detectability we use a statistical model of $\tilde{A}_W(\mathbf{r})$.

7.2.1 Modeling anatomic fluctuations

Modeling background variability is important for determining potential benefits that subtraction approaches may have over conventional non-subtraction approaches. We consider the effects of soft-tissue variations using the ‘‘lumpy-background’’ model described by Rolland *et al.*^[156] and Myers *et al.*^[137] With this approach, anatomic variations are simulated by superimposing two-dimensional Gaussian functions on a uniform background with mean area density \bar{A}_W . We let \tilde{K} and $\{\tilde{\mathbf{r}}_i, i =$

1... \tilde{K} } be RVs representing the number and locations of Gaussian “lumps:”

$$\tilde{A}_W(\mathbf{r}) = \bar{A}_W + \sum_{i=1}^{\tilde{K}} \frac{\tilde{\nu}_i b}{\pi \rho^2} \exp\left(-\frac{|\mathbf{r} - \tilde{\mathbf{r}}_i|^2}{\rho^2}\right) \quad (7.2.3)$$

where $\tilde{\nu}_i$ is a Bernoulli RV that takes on values of +1 or -1 with equal probability, and b [g] and ρ [cm] represent the height and $1/e$ width of each lump. Figure 7.2.1 illustrates some examples of simulated anatomic backgrounds generated using Eq. (7.2.3) for Poisson-distributed \tilde{K} . While real anatomic backgrounds may be more complicated than those in Fig. 7.2.1, this model enables analyses of thickness and density variations of variable width and magnitude.

Rolland *et al.*^[156] demonstrated that when \tilde{K} is Poisson-distributed, anatomic variations described using Eq. (7.2.3) satisfy the properties of wide sense stationarity (WSS) with noise power spectrum (NPS) is given by

$$\text{NPS}_{A_W}(u, v) = \kappa b^2 e^{-2\pi^2 \rho^2 |u^2 + v^2|} \quad (7.2.4)$$

[g² cm⁻²] where u and v represent spatial frequencies in the x and y directions and $\kappa = \bar{K}/A$ [cm⁻²] represents the mean number of Gaussian lumps per unit area where A represents image area. The global variance σ_W^2 [g² cm⁻⁴] of the anatomic background is expressed in terms of the integral of the NPS over all spatial frequencies:^[143]

$$\sigma_W^2 = \int_{-\infty}^{+\infty} \int_{-\infty}^{+\infty} \text{NPS}_{A_W}(u, v) dudv = \frac{\kappa b^2}{2\pi \rho^2} \quad (7.2.5)$$

Equation (7.2.5) demonstrates that the variance of $\tilde{A}(\mathbf{r})$ depends on the number, height, and width of Gaussian lumps. In the following sections, the NPS of both subtraction and non-subtraction angiographic images is expressed in terms of $\text{NPS}_{A_W}(u, v)$.

7.2.2 Angiographic image signal

7.2.2.1 Non-subtraction angiography

Conventional non-subtraction angiography uses a single image acquired after injection of an iodine-based contrast agent to visualize diseased vasculature. Contrast between iodinated and non-iodinated regions of an image is the result of increased attenuation through iodine. Assuming linear x-ray detectors, the mean pixel value is proportional to the total energy deposited by all interacting x-ray

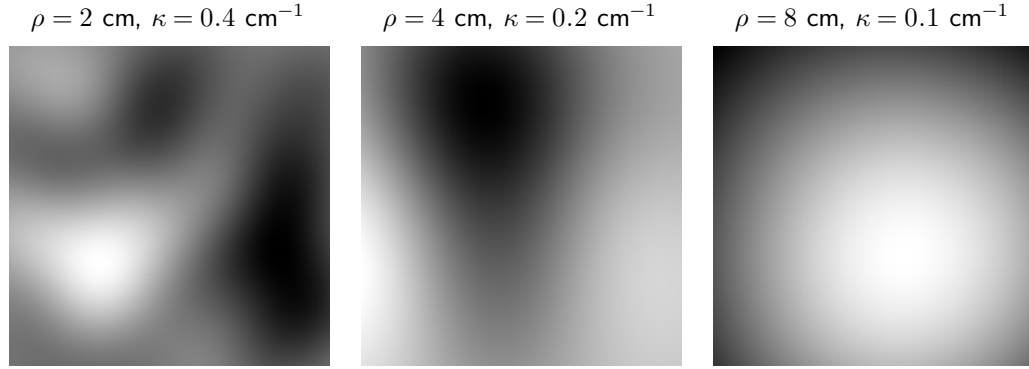


Figure 7.2.1: Examples of anatomic backgrounds simulated using Eq. (7.2.3) for selected values of $\kappa = \bar{K}/A$ and ρ for $\sigma_W = 5$.

photons. The mean signal from a detector element centered at \mathbf{r} given \tilde{A}_W is given by

$$\mathbb{E} \left(\tilde{M}(\mathbf{r}) \mid \tilde{A}_W \right) = k \int_0^{kV} s(E) \bar{q}(E) \int_{a(\mathbf{r})} e^{-\tilde{\mathbf{A}}(\mathbf{r}')^T \frac{\mu}{\rho}(E)} d^2 \mathbf{r}' dE \quad (7.2.6)$$

where $\int_{a(\mathbf{r})} d^2 \mathbf{r}'$ represents a two-dimensional integral over an element of area $a = a_x a_y$ centered at \mathbf{r} , k is a constant of proportionality, a [mm^2] represents element area, $\bar{q}(E)$ [$\text{mm}^{-2} \text{keV}^{-1}$] and kV describe the spectral distribution of x-ray photons incident on the patient, and $s(E) = G(E)$ where $\alpha(E)$ and $E_{\text{dep}}(E)$ represent the quantum efficiency and deposited energy for incident photon energy E . Averaging over all possible values of \tilde{A}_W yields^[143]

$$\bar{M} = \mathbb{E} \left(\tilde{M}(\mathbf{r}) \right) = k \int_0^{kV} s(E) \bar{q}(E) \int_{a(\mathbf{r})} \mathbb{E} \left(e^{-\tilde{\mathbf{A}}(\mathbf{r}')^T \frac{\mu}{\rho}(E)} \right) d^2 \mathbf{r}' dE. \quad (7.2.7)$$

For the lumpy-background model, \tilde{A}_W is approximately Gaussian-distributed and $\exp(-\tilde{A}_W \frac{\mu}{\rho}(E))$ is therefore approximately log-normally-distributed. Assuming small variations of \tilde{A}_W about \bar{A}_W , the mean subtracted angiographic image signal \bar{M} is therefore given by

$$\bar{M} = ka \int_0^{kV} s(E) \bar{q}(E) e^{-\bar{\mathbf{A}}^T \frac{\mu}{\rho}(E)} dE. \quad (7.2.8)$$

7.2.2.2 Subtraction angiography

The goal of subtraction angiography is to produce an image showing only the spatial distribution of iodine contrast agent. This is accomplished by estimating \tilde{A}_I for each image pixel. The angiographic

image signal \tilde{A}_I is derived from two or more images where, similar to Eq. (7.2.8), the expected pixel value measured in image i , is given by

$$\bar{M}_i = ka \int_0^{kV} s_i(E) \bar{q}_i(E) e^{-\bar{\mathbf{A}}^T \frac{\mu}{\rho}(E)} dE; \quad i = 1 \dots n \quad (7.2.9)$$

where, as described in Chapter 2, $s_i(E)$ is a weighting function describing the detector response associated with image i . The angiographic image signal is obtained by weighted log-subtraction of raw images \tilde{M}_i :

$$\tilde{A}_I = - \sum_{i=1}^n W_{I,i} \log \frac{\tilde{M}_i}{M_{i0}} \quad (7.2.10)$$

where image weights $W_{I,i}$ are related to the mass-attenuation coefficients of basis materials and M_{i0} is given by Eq. (7.2.9) evaluated at a known set of basis-material area densities. See Chapter 2 for further details on calculation of $W_{I,i}$ and M_{i0} . Equation (7.2.10) gives an estimate of iodine area density for each image pixel.

7.2.3 Image noise power spectrum including both quantum and anatomic fluctuations

As discussed above, the ability to detect iodinated objects may be degraded by both quantum and anatomic noise. Quantum fluctuations are the result random variations in the number of interacting photons, the energy deposited by each photon, and the number of secondary quanta collected in a detector element, and were described in Chapters 2-5 of this thesis. Anatomic fluctuations are the result of variations in density and thickness of over and under-lying soft-tissue structures. In this section the approach for calculating image noise presented in Chapter 2 is generalized to accommodate calculation of the image NPS of both subtracted and subtracted images enabling a direct comparison of image noise and iodine detectability for both subtraction and non-subtraction angiography. Similar to Chapter 2, in all cases we assume ideal x-ray detectors. Results presented here will therefore likely underestimate image noise for each technique.

Barret *et al.*,^[19] showed that the the presampling NPS of an imaging system can be represented as

$$\text{NPS}(u, v) = \text{NPS}^q(u, v) + \text{NPS}^{\text{an}}(u, v) \quad (7.2.11)$$

where $\text{NPS}^q(u, v)$ and $\text{NPS}^{\text{an}}(u, v)$ represent quantum and anatomic contributions, respectively. We separate our analysis of image noise into non-subtraction and subtraction approaches.

7.2.3.1 Non-subtraction angiography

Quantum NPS The full derivation for the quantum and anatomical NPS terms is omitted here, but it can be shown that the quantum NPS for non-subtraction angiography is given by

$$\text{NPS}_M^q(u, v) = \mathcal{F} \{ \text{E} (K_{M|A_W}(\tau_x, \tau_y)) \} \quad (7.2.12)$$

where $\mathcal{F} \{ \}$ represents the Fourier transform operator and $K_{M|A_W}(\tau_x, \tau_y)$ represents the autocovariance of \tilde{M} for fixed \tilde{A}_W . The expected value in the above equation represents an average over all possible values of \tilde{A}_W . For small variations about \bar{A}_W and ideal energy-integrating x-ray detectors, Eq. (7.2.12) can be written as

$$\text{NPS}_M^q(u, v) = \text{Var}_q(\tilde{M}) a^2 \text{sinc}^2(au) \text{sinc}^2(av) \quad (7.2.13)$$

where $\text{Var}_q(\tilde{M})$ represents the variance of \tilde{M} due to quantum fluctuations, given by

$$\text{Var}_q(\tilde{M}) = \text{E} \left(\text{Var}(\tilde{M}|\tilde{A}_w) \right) \quad (7.2.14)$$

where $\text{Var}(\tilde{M}|\tilde{A}_w)$ represents the variance in detector element values for a fixed background level and is given by: [184,185]

$$\text{Var}(\tilde{M}|\tilde{A}_w) = k \int_0^{kV} \alpha(E) E_{\text{dep}}^2(E) \bar{q}(E) \int_{a(\mathbf{r})} e^{-\tilde{\mathbf{A}}(\mathbf{r}')^T \frac{\mu}{\rho}(E)} d^2\mathbf{r}' dE. \quad (7.2.15)$$

The expectation operator in Eq. (7.2.14) represents an average over all possible values of \tilde{A}_W . Similar to Eq. (7.2.8), averaging over all values of \tilde{A}_w yields

$$\text{Var}_q(\tilde{M}) = ka \int_0^{kV} \alpha(E) E_{\text{dep}}^2(E) \bar{q}(E) e^{-\bar{\mathbf{A}}^T \frac{\mu}{\rho}(E)} dE. \quad (7.2.16)$$

Equations (7.2.12)-(7.2.16) demonstrate that for small fluctuations of \tilde{A}_W about \bar{A}_W , the quantum NPS is that which would be observed for a uniform water background with mean \bar{A}_W .

Anatomic NPS The anatomic NPS (derivation omitted) for non-subtraction angiography is given by

$$\text{NPS}_M^{\text{an}}(u, v) = \mathcal{F} \{ K_{E(M|A_W)}(\tau_x, \tau_y) \} \quad (7.2.17)$$

where $K_{E(M|A_W)}(\tau_x, \tau_y)$ represents the autocovariance function of $E(\tilde{M}|\tilde{A}_W)$:

$$K_{E(M|A_W)}(\tau_x, \tau_y) = E \left(E \left(\tilde{M}(\mathbf{r}) \middle| \tilde{A}_W(\mathbf{r}) \right) E \left(\tilde{M}(\mathbf{r} + \boldsymbol{\tau}) \middle| \tilde{A}_W(\mathbf{r} + \boldsymbol{\tau}) \right) \right) - \bar{M}^2 \quad (7.2.18)$$

where $\boldsymbol{\tau} = (\tau_x, \tau_y)$. Similar to Fredenberg *et al.*,^[67] we consider small fluctuations of \tilde{A}_W about \bar{A}_W , in which case the first term in the above equation is given by

$$\begin{aligned} & E \left(E \left(\tilde{M}(\mathbf{r}) \middle| \tilde{A}_W(\mathbf{r}) \right) E \left(\tilde{M}(\mathbf{r} + \boldsymbol{\tau}) \middle| \tilde{A}_W(\mathbf{r} + \boldsymbol{\tau}) \right) \right) \\ &= \frac{\bar{M}^2 \bar{\mu}^2}{a^2 \rho_W} K_{A_W}(\tau_x, \tau_y) * \Pi \left(\frac{\tau_x}{a_x}, \frac{\tau_y}{a_y} \right) * \Pi \left(\frac{\tau_x}{a_x}, \frac{\tau_y}{a_y} \right) + \bar{M}^2 \end{aligned} \quad (7.2.19)$$

where $K_{A_W}(\tau_x, \tau_y)$ represents the autocovariance function of \tilde{A}_W and $*\Pi(\frac{\tau_x}{a_x}, \frac{\tau_y}{a_y})$ represents convolution with a two-dimensional rectangle function. Combining Eqs. (7.2.17)-(7.2.19) yields

$$\text{NPS}_M^{\text{an}}(u, v) = \bar{M}^2 \frac{\bar{\mu}^2}{\rho_W} \text{NPS}_{A_W}(u, v) \text{sinc}^2(au) \text{sinc}^2(av) \quad (7.2.20)$$

where $\frac{\bar{\mu}}{\rho_W}$ denotes the average value of the mass-attenuation coefficient of basis material b weighted by $s(E) \bar{q}(E) e^{-\bar{\mathbf{A}}^T \frac{\mu}{\rho}(E)}$. Equation (7.2.20) demonstrates that for small fluctuations of \tilde{A}_W about \bar{A}_W , the anatomic NPS is that which would be observed when an input distribution with NPS equal to $\frac{\bar{\mu}^2}{\rho_W} \text{NPS}_{A_W}(u, v)$ is transferred through a deterministic x-ray detection system with MTF equal to a two-dimensional sinc-squared function. Equations (7.2.13) and (7.2.20) described the combined effects of quantum and anatomic fluctuations on image noise.

Individual pixel noise Pixel noise is expressed in terms of the variance of an individual pixel, $\text{Var}(\tilde{M})$. While pixel variance does not give information concerning noise correlations within an image, it is useful in comparing the magnitude of image noise and the relative levels of quantum and anatomic noise sources. Combining Eqs. (7.2.11), (7.2.13), and (7.2.20), and integrating over all spatial frequencies yields $\text{Var}(\tilde{M})$:^[52-54,143]

$$\text{Var}(\tilde{M}) = \int_{-\infty}^{+\infty} \int_{-\infty}^{+\infty} \text{NPS}(u, v) dudv = \text{Var}_q(\tilde{M}) + \text{Var}_{\text{an}}(\tilde{M}) \quad (7.2.21)$$

where $\text{Var}_q(\tilde{M})$ is given by Eq. (7.2.16) and $\text{Var}_{\text{an}}(\tilde{M})$ is given by

$$\text{Var}_{\text{an}}(\tilde{M}) = \bar{M}^2 \frac{\bar{\mu}^2}{\rho_W} \int_{-\infty}^{+\infty} \int_{-\infty}^{+\infty} \text{NPS}_{A_W}(u, v) \text{sinc}^2(au) \text{sinc}^2(av) dudv. \quad (7.2.22)$$

7.2.3.2 Subtraction angiography

Quantum NPS The quantum NPS for subtraction angiography is similar in form to Eq. (7.2.13) with the replacement of $\text{Var}_q(\tilde{M})$ with $\text{Var}_q(\tilde{A}_I)$:

$$\text{NPS}_M^q(u, v) = \text{Var}_q(\tilde{A}_I) a^2 \text{sinc}^2(au) \text{sinc}^2(av) \quad (7.2.23)$$

where $\text{Var}_q(\tilde{A}_I)$ is given by

$$\text{Var}_q(\tilde{A}_I) = \text{E} \left(\text{Var}(\tilde{A}_I | \tilde{A}_W) \right) = \sum_{i=1}^n W_{I,i}^2 \frac{\text{Var}_q(\tilde{M}_i)}{\tilde{M}_i^2} = \sum_{i=1}^n \frac{W_{I,i}^2}{\text{SNR}_{q,i}^2} \quad (7.2.24)$$

where $\text{Var}_q(\tilde{M}_i)$ is similar in form to Eq. (7.2.16) with the replacement of $s(E)$ with $s_i(E)$. The above equation is identical to the expression for image noise that was derived in Chapter 2 and demonstrates that increasing the SNR of “raw” images decreases quantum noise in iodine-specific angiographic images.

Anatomic NPS Similar to non-subtraction angiography, the anatomic NPS for subtraction angiography is proportional to $\text{NPS}_{A_W}(u, v)$ modulated by a sinc-squared function:

$$\text{NPS}_{A_I}^{\text{an}}(u, v) = \left(\sum_{i=1}^n W_{I,i} \frac{\bar{\mu}}{\rho w_i} \right)^2 \times \text{NPS}_{A_W}(u, v) \text{sinc}^2(au) \text{sinc}^2(av) \quad (7.2.25)$$

where $\frac{\bar{\mu}}{\rho w_i}$ denotes the average value of the mass-attenuation coefficient of basis material b weighted by $s_i(E) \bar{q}_i(E) e^{-\bar{A}^T \frac{\mu}{\rho}(E)}$. While $\text{NPS}_{A_I}^{\text{an}}(u, v)$ has the same frequency components as that for non-subtraction angiography, we will see that the magnitude of $\text{NPS}_{A_I}^{\text{an}}(u, v)$ is often much less than that of $\text{NPS}_M^{\text{an}}(u, v)$ for a wide range of anatomic variations.

Individual pixel noise Combining Eqs. (7.2.11), (7.2.23), and (7.2.25), and integrating over all spatial frequencies yields $\text{Var}(\tilde{A}_I)$:^[52-54,143]

$$\text{Var}(\tilde{A}_I) = \int_{-\infty}^{+\infty} \int_{-\infty}^{+\infty} \text{NPS}(u, v) dudv = \text{Var}_q(\tilde{A}_I) + \text{Var}_{\text{an}}(\tilde{A}_I)$$

where $\text{Var}_q(\tilde{A}_I)$ is given by Eq. (7.2.24) and $\text{Var}_{\text{an}}(\tilde{A}_I)$ is given by

$$\text{Var}_{\text{an}}(\tilde{A}_I) = \left(\sum_{i=1}^n W_{I,i} \frac{\bar{\mu}}{\rho_{W_i}} \right)^2 \times \int_{-\infty}^{+\infty} \int_{-\infty}^{+\infty} \text{NPS}_{A_w}(u, v) \text{sinc}^2(au) \text{sinc}^2(av) \, dudv.$$

7.2.4 Task-based iodine detectability

The ability to visualize iodinated vasculature depends on x-ray exposure, vessel size, and the magnitude and correlation length of anatomic variations. The detectability index d_I is a figure of merit that enables analyses of each of these considerations on iodine detectability. [1] We compare the performance of subtraction and non-subtraction approaches in terms of the detectability index per unit entrance exposure (X):

$$\frac{d_I}{X} = \frac{1}{X} \int_{-u_N}^{+u_N} \int_{-v_N}^{+v_N} \frac{F^2(u, v) \text{MTF}^2(u, v)}{\sum_{n=-\infty}^{+\infty} \sum_{m=-\infty}^{+\infty} \text{NPS}\left(u + \frac{n}{\Delta_x}, v + \frac{m}{\Delta_x}\right)} \, dudv \quad (7.2.26)$$

where the denominator is the image NPS including the effects of noise aliasing, Δ_x and Δ_y represent the image sample spacing in the x and y directions, respectively, $u_N = 1/(2\Delta_x)$ and $v_N = 1/(2\Delta_y)$ represent the Nyquist frequencies in the x and y directions, respectively, $\text{MTF}(u, v) = \text{sinc}(au) \text{sinc}(av)$, and $F(u, v)$ is a task function equal to the Fourier transform of the object to be detected. In all cases, we assume the sample spacing is equal to element width, ie. $\Delta_x = \Delta_y = a_x = a_y$.

We consider detection of low contrast iodinated vessels with lengths L_y ranging from 1 cm to 5 cm and widths L_x ranging from 0.01 cm to 1 cm. In the spatial domain, the imaging task is then represented as a two dimensional rectangle function with length L_y , width L_x , and height equal to the average difference between iodinated and non-iodinated regions of the image. Therefore

$$F(u, v) = |\bar{M} - \bar{M}^{\text{NI}}| L_x L_y \text{sinc}(L_x u) \text{sinc}(L_y v) \quad \text{non subtraction} \quad (7.2.27)$$

$$F(u, v) = |\bar{A}_I - \bar{A}_I^{\text{NI}}| L_x L_y \text{sinc}(L_x u) \text{sinc}(L_y v) \quad \text{subtraction} \quad (7.2.28)$$

where \bar{M} and \bar{M}^{NI} represent the mean subtracted image signals (Eq. (7.2.8)) from iodinated and non-iodinated regions of the image, respectively, and similarly for \bar{A}_I and \bar{A}_I^{NI} .

7.3 Monte Carlo simulation of quantum and anatomic noise

7.3.1 Simulating variations in soft-tissue density

Anatomic backgrounds were simulated using Eq. (7.2.3). As described by Eq. (7.2.5), the global variance is determined by the mean number of Gaussian “lumps” per unit area $\kappa = \bar{K}/A$, the $1/e$ width ρ and the strength b of each lump. The number of lumps per unit area is simulated by sampling a Poisson distribution with mean \bar{K} for image area A . Each lump is either added or subtracted, with equal probability, from a uniform background with mean \bar{A}_W . We assume width ρ and strength b are the same for each lump, in which case the NPS of the background is given by Eq. (7.2.4).

7.3.2 Imaging simulation

X-ray images were simulated using a Monte Carlo method similar to that described in Chapter 2. With this approach, x-ray spectra were generated using an in-house MATLAB routine that implements algorithms published by Tucker *et al.*^[199] for a tungsten-target x-ray tube. The number of incident x-ray photons in each energy interval (1 keV) was determined for a desired exposure using a Poisson random number generator. For each background model (described above) a 128 x 128 grid of 0.02 x 0.02 cm² detector elements was simulated giving a 2.56 x 2.56 cm² image. Transmissions were calculated using tabulated values of the mass-attenuation coefficients for water and iodine. Conventional energy-integrating images were simulated by weighting each transmitted x-ray photon in proportion to its energy and then summing over the entire spectral distribution. For DSA this was performed on both pre and post-injection images. In the case of ESA, this technique was performed for both the high and low-energy images. We simulated EPC images by summing the number of transmitted x-ray photons between the lower and upper energy thresholds of each energy bin. We used the exposure parameters summarized in Chapter 2. In all cases we assumed unity quantum efficiency and ideal energy resolution. Therefore, the results of the theoretical and simulation studies will likely overestimate the image quality achievable with each technique.

7.4 Preliminary results: Soft-tissue suppression capabilities of energy-dependent angiography

Figure 7.4.1 illustrates the dependence of iodine detectability per unit exposure on vessel width for conventional non-subtraction angiography, ERA, ESA, and DSA assuming ideal instrumentation for

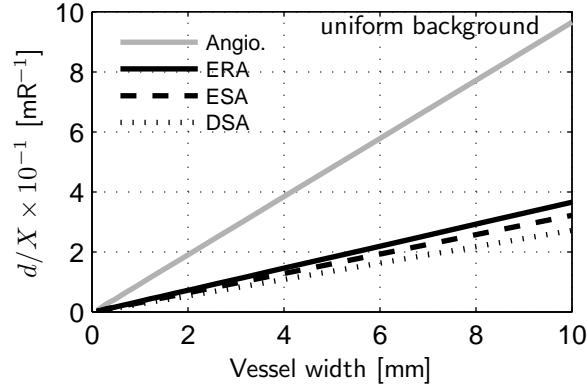


Figure 7.4.1: An illustration of the dependence of iodine detectability per unit exposure d/X on object size for subtraction and non-subtraction angiography for uniform background consisting of 30 g cm^{-2} of water. Calculations are based on 0.01 g cm^{-2} of iodine.

each. As expected, when a uniform iodinated object is embedded in a uniform water background, conventional non-subtraction angiography provides the highest detectability. This is an expected result because in this case performing either energy-dependent subtraction or conventional temporal subtraction does not enhance iodine visualization but does result in an increase in quantum noise relative to non-subtraction angiography for the same patient exposure.

7.4.1 Dependence on magnitude of soft-tissue variability

Figure 7.4.2 illustrates the dependence of iodine detectability on vessel width for selected levels of anatomic background variability σ_W and $1/e$ width ρ for both non-subtraction and subtraction angiography, including ERA, ESA, and DSA. Comparing Fig. 7.4.2 with Figure 7.4.1, we see that soft-tissue variations have very little effect on iodine detectability for ERA, ESA, and DSA for all levels of anatomic variability considered. On the other hand, iodine detectability for conventional non-subtraction angiography is substantially degraded when the $1/e$ width of soft-tissue variations ρ is on the same order of magnitude as vessel width. In this case, each of the subtraction approaches can provide higher iodine detectability per unit exposure than conventional non-subtraction angiography. When ρ is greater than the vessel width, iodine detectability with conventional angiography is not degraded by anatomic fluctuations because in this case the background intensity is near-uniform over the area of a vessel.

Figure 7.4.3 displays Monte-Carlo-simulated non-subtraction angiography, DSA, ESA, and ERA images for selected levels of background variability. These images show the same trends as those discussed above. In the case of a uniform background, the large iodinated object is better visualized

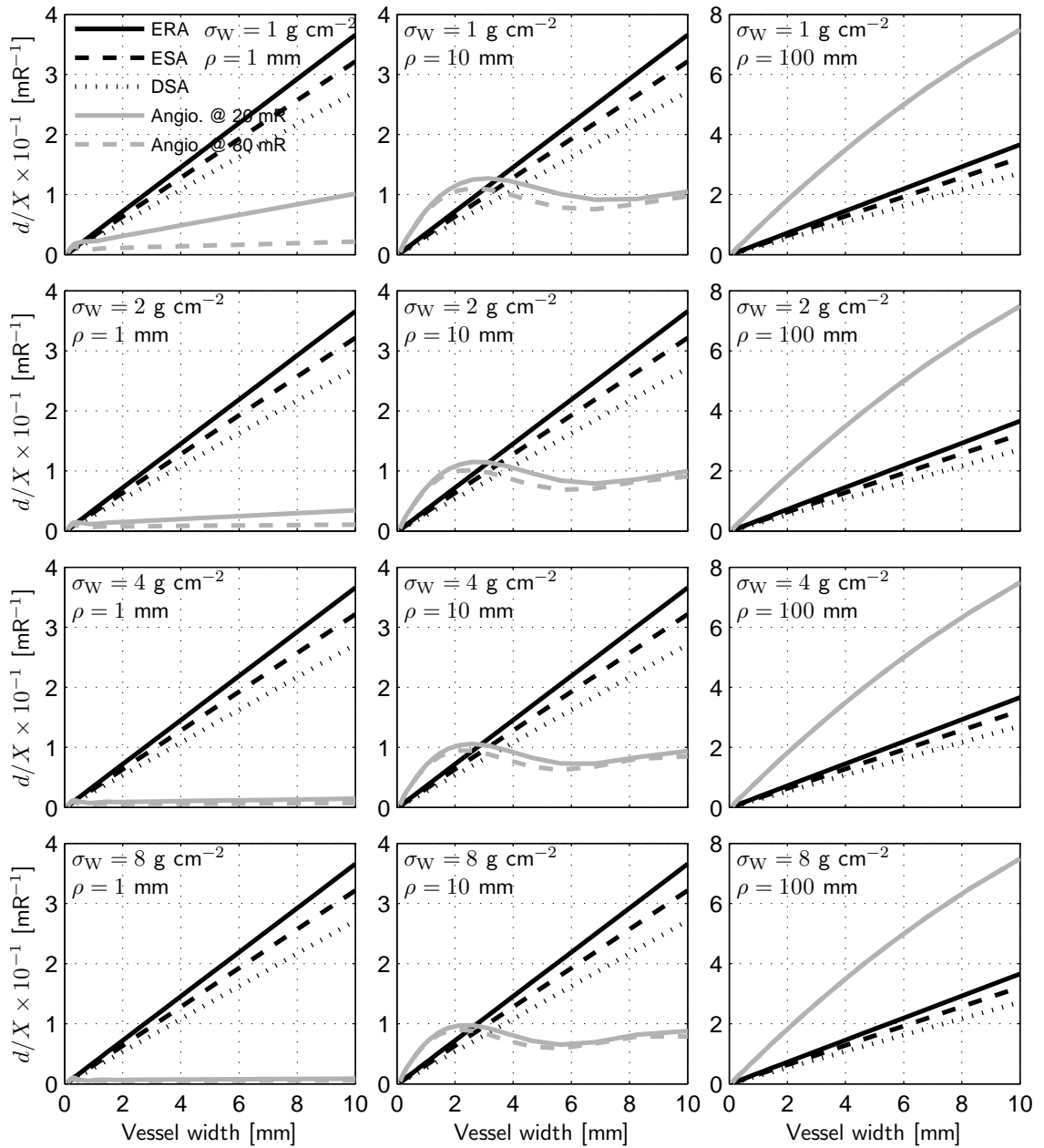


Figure 7.4.2: An illustration of the dependence of iodine detectability per unit exposure d/X on object size for subtraction and non-subtraction angiography for selected levels of background variability σ_W and correlation length ρ . Calculations are based on 0.01 g cm^{-2} of iodine, a mean background level of 30 g cm^{-2} of water, and 20 mR entrance exposure. Also, plotted is the detectability index for non-subtraction angiography at 80 mR entrance exposure.

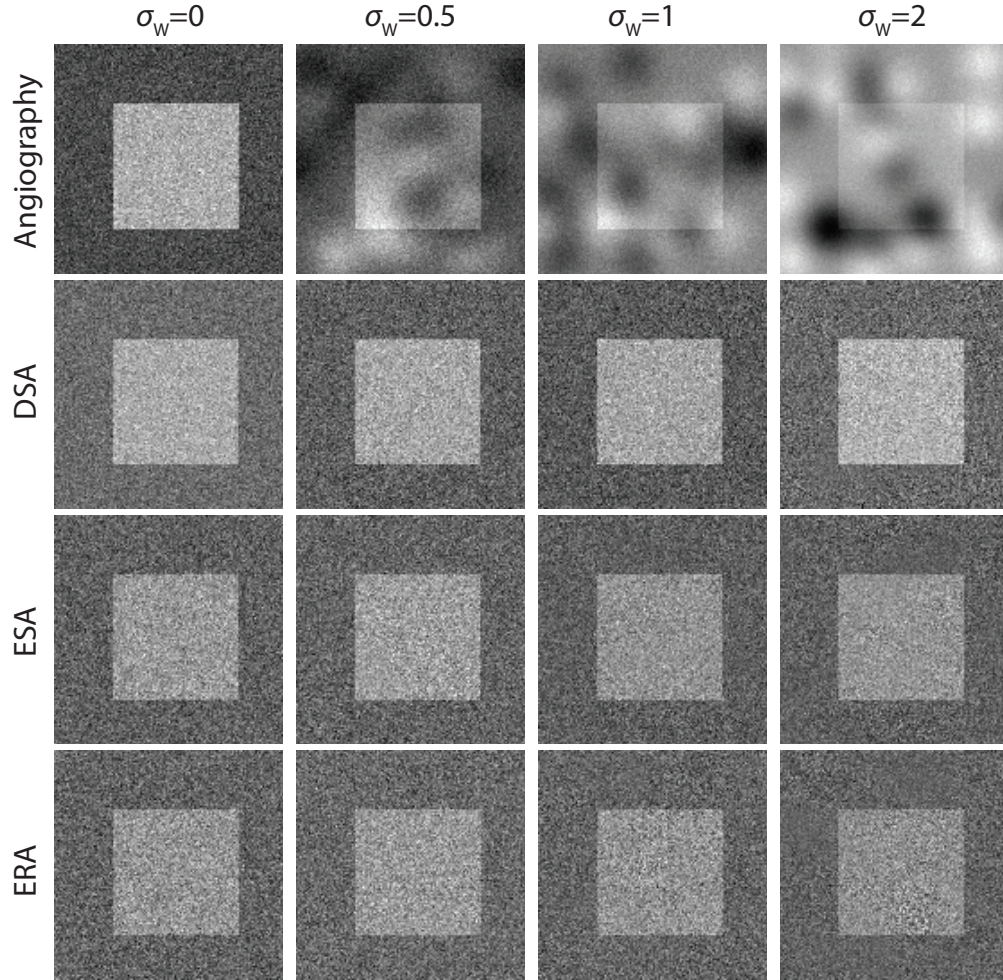


Figure 7.4.3: Comparison of simulated images of a large iodinated object (area density of 0.01 g cm^{-2}) in inhomogeneous backgrounds with increasing variability σ_w for conventional non-subtraction angiography, DSA, ESA, and ERA. Images were generated using a total entrance exposure of 20 mR assuming parallel beam x-ray geometry.

with angiography due to the superior quantum noise properties of this approach. However, as the level of background variability is increased, iodine visualization is degraded for non-subtraction angiography but not for DSA, ESA or ERA, as expected based on Fig. 7.4.2. Both ESA and ERA images show levels of background suppression similar to DSA images.

7.4.2 Dependence of iodine detectability on exposure level

Figure 7.4.3 displays another set of non-subtraction angiography, ERA, and ESA images generated from the Monte Carlo simulation. The high-contrast structure in the center of each image is 1.65 g cm^2 of bone and the vertical structures represent iodinated vessels with radii of $0.08 - 0.3 \text{ mm}$ filled with 0.1 g cm^{-3} of iodine. Since we have assumed a dual-energy approach for ESA,

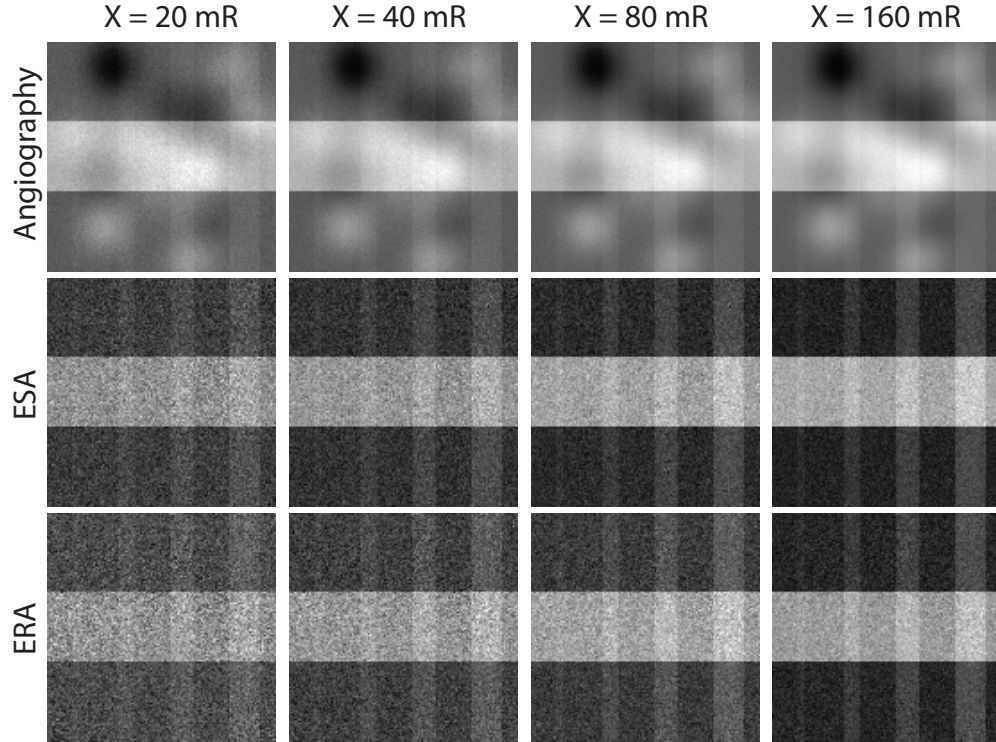


Figure 7.4.4: Comparison of simulated images containing 30 cm of water with background variance $\sigma_W = 1 \text{ g cm}^{-2}$ with vertical vessels having radii of 0.08 – 0.3 mm filled with 0.1 g cm^{-3} of iodine at 20-160 mR entrance exposures.

and a two-bin approach for ERA, neither of these approaches remove the overlying bone structure. However, both approaches have suppressed soft-tissue variations from the images. As expected, increasing the exposure level from 20 mR to 160 mR increases iodine visibility for both ERA and ESA. However, in the case of non-subtraction angiography, increasing the exposure level has little influence on the ability to visualize iodinated structures. This is expected for this approach since increasing the exposure level does not remove soft-tissue variations that degrade iodine detectability.

7.5 Discussion of preliminary comparisons

The framework presented above will be useful in future comparisons of energy-dependent subtraction angiography with conventional subtraction and non-subtraction approaches. While the formalism described above assumed ideal detectors, it could easily be extended to include the influence of stochastic energy-deposition, conversion, and collection processes, and electronic noise described in Chapters 2-5. The preliminary study described above demonstrated the utility of this approach for the quantification of soft-tissue suppression capabilities of energy-dependent approaches. The

results of this study suggest that both ERA and ESA have the potential to remove image intensity variations caused by spatial fluctuations in soft-tissue area density, resulting in iodine detectability similar to that of DSA. Since ideal detectors were assumed, it is expected that iodine detectability would be approximately 25-30% lower than DSA when the influence of stochastic image forming processes are considered, such as those discussed in Chapters 2-5.

A comparison between subtraction and non-subtraction approaches for the task of detecting low-contrast iodinated structures in a spatially varying background demonstrated that in some situations iodine detectability obtained with non-subtraction angiography will be degraded by anatomic fluctuations. It was demonstrated that when the correlation length of the anatomical background is on the same order of magnitude or smaller than object size, iodine detectability for angiography is substantially degraded. Conversely, when the correlation length of the background is much greater than object size, iodine detectability is not degraded. Since subtraction approaches remove anatomic noise sources, iodine detectability with these approaches was independent of anatomic noise levels.

It should be emphasized that the results presented here only apply to the task and anatomic background model considered, both of which may not be suitable for describing angiographic situations. In reality, an angiographer must be able to detect atherosclerotic lesions located in one or more coronary arteries. This requires visualization of one or more arteries of various lengths and diameters and is a more complicated task than detecting a single low-contrast iodinated structure. Furthermore, the comparisons here assumed the anatomic background satisfied the properties of wide-sense stationarity which may not be satisfied for real anatomic backgrounds. ^[26,27] Therefore, caution must be taken when interpreting the comparisons between subtraction and non-subtraction approaches presented here. Therefore, while the framework presented here may be used as a foundation for comparing energy-dependent angiography with and conventional non-subtraction coronary angiography, future studies must determine appropriate task functions and models of anatomic noise that accurately reflect realistic angiograms.

Chapter 8

Future work II: Theoretical analysis of charge sharing in photon-counting x-ray detectors using a cascaded-systems approach

8.1 Introduction

Prototype photon-counting detectors employ a direct detection approach where x-ray photons are converted to electron-hole (e-h) pairs in a semiconductor. Liberated charges migrate to the top and/or bottom surfaces of the convertor material where they are integrated by a capacitive element and then amplified by a semiconductor device located in each detector element.^[129,157,216] Due to Coulomb repulsion of charges of the same sign, electrons and holes may be relocated from the position of primary x-ray interaction which can result in charge-sharing between neighboring detector elements. Charge sharing between neighboring detector elements can cause substantial degradation of image quality^[4,5,31,126] and loss of spectral information.^[31,44,70,110,174,178] This effect is mitigated with techniques that sum charges in neighboring elements and assigns them to the element with the largest signal, such as those described by Bornefalk *et al.*^[31] and implemented in the MEDIPIX3 prototype.^[18] Determining optimal adaptive binning approaches will require quantification of how charge sharing and adaptive binning are expected to affect image signal, noise, and spatial resolution.

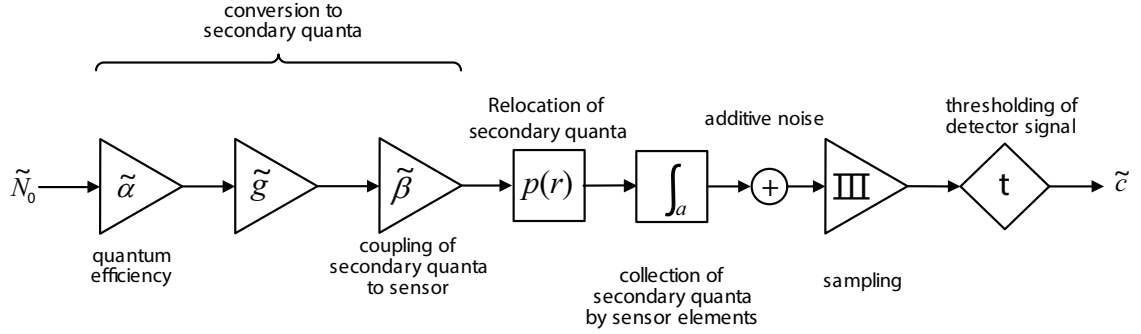


Figure 8.2.1: Cascaded model used to describe the influence of charge sharing in photon-counting x-ray detectors.

The following sections outline current progress made toward a description of the effects of charge sharing on recorded count rates and spatial resolution, expressed in terms of the photon-counting modulation transfer function (MTF).

8.2 Cascaded-systems analysis of charge sharing in photon-counting detectors

A simple CSA model of energy deposition in photon-counting x-ray detectors is illustrated in Fig. 8.2.1 and includes the effects of quantum efficiency, stochastic conversion gain, collection of secondary quanta by collecting electrodes, relocation of secondary quanta, integration in detector elements, electronic noise, and thresholding. This model does not include the emission of characteristic or Compton-scatter x rays considered in Chapters 4 and 5 and therefore may only be applicable to situations where Compton-scatter can be ignored and for energies below the K-edge energy of a convertor material.

The quantum relocation stage illustrated in Fig. 8.2.1 describes the situation where every secondary quantum is relocated by the same PSF. While the distance a quantum is relocated may depend on depth of interaction, these affects are ignored in this analysis. In the following sections the PDF of the total number of image quanta per x-ray interaction is calculated for the model shown in Fig. 8.2.1. As will be shown, this enables description of both the mean number of photon counts per detector element and the PSF and MTF of photon-counting systems.

8.2.1 PDF of the number of image quanta collected in detector elements

We let \tilde{N}_{tot} represent the total number that are collected somewhere in the detector given one x-ray interaction and let $\tilde{N}_{\text{del}}(\mathbf{r})$ represent the number of quanta collected in an element centered at \mathbf{r} . Since quantum relocation does not result in production or loss of secondary quanta, the PDF of \tilde{N}_{tot} is obtained using the PDF transfer approach described in Chapters 3 and 4. From the results of Chapter 3 and Appendix B, $p_{N_{\text{tot}}}(N_{\text{tot}})$ is given by

$$p_{N_{\text{tot}}}(N_{\text{tot}}) = \sum_{l=1}^{\infty} \sum_{i=1}^{\infty} \text{pr}_g(i) \binom{i}{N_{\text{tot}}} \beta^i (1-\beta)^{i-N_{\text{tot}}} \delta(N_{\text{tot}} - l) \quad (8.2.1)$$

where $\text{pr}_g(i)$ represents the probability mass function (PMF) of gain variable \tilde{g} , and β represents the collection efficiency of secondary quanta. We let $\text{PSF}(\mathbf{r})$ represent the probability density function of relocation position \mathbf{r} relative to the primary interaction site. The probability that a secondary quantum is detected in an element of area a centered at \mathbf{r} is then given by

$$\text{PSF}_{\text{del}}(\mathbf{r}) = \text{PSF}(\mathbf{r}) * \Pi\left(\frac{\mathbf{r}}{a}\right) \quad (8.2.2)$$

where $\Pi(\mathbf{r}/a)$ represents the 2-D rectangle function. The relationship between $\text{PSF}_{\text{del}}(\mathbf{r})$ and $\text{PSF}(\mathbf{r})$ is illustrated schematically in Fig. 8.2.2 for Gaussian PSF. Since each secondary quantum is either detected in an element centered at \mathbf{r} or is not, the PDF of the number of quanta collected in an a detector element centered at \mathbf{r} can be obtained from the binomial distribution. The full derivation is omitted here, but it can be shown that $p_{N_{\text{del}}}(N_{\text{del}})$ is given by

$$p_{N_{\text{del}}}(N_{\text{del}}) = \int p_{N_{\text{del}}}(N_{\text{del}}|N_{\text{tot}}) p_{N_{\text{del}}}(N_{\text{tot}}) dN_{\text{tot}} \quad (8.2.3)$$

where $p_{N_{\text{del}}}(N_{\text{del}}|N_{\text{tot}})$ represents the PDF of N_{del} given N_{tot} , given by

$$p_{N_{\text{del}}}(N_{\text{del}}|N_{\text{tot}}) = \sum_{n=0}^{\infty} \text{pr}_{N_{\text{del}}}(N_{\text{del}}|N_{\text{tot}}) \delta(N_{\text{del}} - n) \quad (8.2.4)$$

where $\text{pr}_{N_{\text{del}}}(N_{\text{del}}|N_{\text{tot}})$ represents the the PMF of N_{del} given N_{tot} , and is a complicated function of the point spread function $\text{PSF}_{\text{del}}(\mathbf{r})$ and total number of quanta N_{tot} :

$$\text{pr}_{\text{del}}(N_{\text{del}}|N_{\text{tot}}) = \frac{1}{A} \binom{N_{\text{tot}}}{N_{\text{del}}} \iint_{\mathbb{R}^2} (\text{PSF}_{\text{del}}(\mathbf{r}))^{N_{\text{del}}} (1 - \text{PSF}_{\text{del}}(\mathbf{r}))^{N_{\text{tot}} - N_{\text{del}}} d^2\mathbf{r} \quad (8.2.5)$$

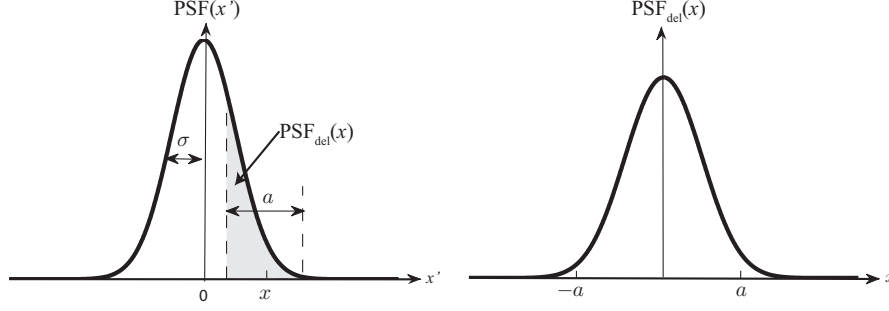


Figure 8.2.2: A 1-D schematic illustration of the relationship between $\text{PSF}(\mathbf{r})$ and $\text{PSF}_{\text{pix}}(\mathbf{r})$ for Gaussian-distributed secondary quanta with variance σ^2 . The PSF represents the probability density that a secondary quantum is detected at position \mathbf{r} where the pixel PSF represents the probability that a secondary quantum is detected in a pixel centered at \mathbf{r} .

where A represents image area, $\text{PSF}_{\text{del}}(\mathbf{r})$ is given by Eq. (8.2.2) and $\iint_{\mathbb{R}^2} d^2\mathbf{r}$ represents a two-dimensional integral over all space. Combining the above expressions yields

$$\begin{aligned}
 p_{N_{\text{del}}}(N_{\text{del}}) &= \sum_{i=0}^{\infty} \text{pr}_g(i) \sum_{l=0}^{\infty} \binom{i}{l} \beta^l (1-\beta)^{i-l} \\
 &\times \frac{1}{A} \sum_{n=0}^{\infty} \binom{l}{n} \iint_{\mathbb{R}^2} (\text{PSF}_{\text{del}}(\mathbf{r}))^n (1 - \text{PSF}_{\text{del}}(\mathbf{r}))^{l-n} d^2\mathbf{r} (N_{\text{del}} - n) \quad (8.2.6)
 \end{aligned}$$

The above expression shows that the PDF for the number of photons detected in an element is a complicated function of the point spread function, and importantly, is independent of position \mathbf{r} which is an important requirement for wide-sense stationarity.

8.2.2 Mean signal

Assuming fast readouts such that pulse pile up can be ignored, the mean number of photon counts is expressed as (derivation omitted):

$$\bar{c} = \bar{q}_0 a \alpha \kappa \left[1 + \frac{1 - \alpha \eta \lambda \xi}{\lambda \kappa} \right] \quad (8.2.7)$$

where α represents the quantum efficiency, $\lambda = \bar{q} a a_t \ll 1$ represents the mean number of incident photons per detector element for readout time a_t , ξ represents the probability of a false count, $\kappa \in [0, \infty)$ is given by

$$\kappa = \frac{A}{a} \int_t^{\infty} p_{N_{\text{del}}}(N_{\text{del}}) dN_{\text{del}} \quad (8.2.8)$$

and $\eta \in [1, \infty)$ is equal to the average number of detector elements that detect at least one secondary quantum given one x-ray interaction:

$$\eta = \frac{A}{a} \int_1^\infty p_{N_{\text{del}}} (N_{\text{del}}) dN_{\text{del}}. \quad (8.2.9)$$

To avoid pulse pile up issues, count rates must be chosen such that all secondaries detected in an element result from a single x-ray interaction event. The product $\eta\lambda$ in Eq. (8.2.7) is interpreted as an effective count rate that must be much less than unity to avoid pulse pile up. The factor κ in Eq. (8.2.7) is equal to the mean number of photon counts per x-ray interaction and may be larger than one depending on the amount of charge sharing and threshold level, and has been referred to as the ‘‘multiplicity’’ of SPC systems by some investigators. ^[126,127]

Equation (8.2.7) is an important result and demonstrates the expected result that, unlike energy-integrating systems, both charge sharing and electronic noise may result in incorrectly recording more photon counts than actual interactions. In the limit of no charge sharing, Eq. (8.2.7) reduces to the expression derived in Chapter 3 for large elements with negligible charge sharing.

8.2.3 Spatial resolution of photon-counting systems

In this section the PSF and MTF of photon counting systems that can be described using the CSA model illustrated in Fig. 8.2.1 are derived.

8.2.3.1 Photon-counting point spread function

Charge sharing may result in a non-negligible probability of detecting photons in an element located at some position \mathbf{r} from the primary interaction site. In the previous section we saw that this may result in multiple detected photons per interaction event. We define the photon-counting PSF as the probability density function of counting a photon at position \mathbf{r} relative to a primary interaction site, given one interacting photon. We start by considering the PMF of the number of secondaries detected in an element centered at \mathbf{r} , given a primary interaction at $\mathbf{r} = 0$ and N_{tot} collected secondaries. The binomial distribution gives

$$\text{pr}_{\tilde{N}_{\text{del}}} (\tilde{N}_{\text{del}} | N_{\text{tot}}; \mathbf{r}) = \binom{N_{\text{tot}}}{N_{\text{del}}} [\text{PSF}_{\text{del}}(\mathbf{r})]^{N_{\text{del}}} [1 - \text{PSF}_{\text{del}}(\mathbf{r})]^{N_{\text{tot}} - N_{\text{del}}} \quad (8.2.10)$$

where $\text{PSF}_{\text{del}}(\mathbf{r})$ represents the probability that a secondary quantum is collected in an element centered at \mathbf{r} and is given by Eq. (8.2.2). A count is incremented in an element centered at \mathbf{r} when $\tilde{N}_{\text{del}}(\mathbf{r}) \geq t$ where t is a threshold used to distinguish interaction events from electronic noise. Therefore, the probability of incrementing a count in an element centered at \mathbf{r} given \tilde{N}_{tot} secondaries is given by^[143]

$$P\left(\tilde{N}_{\text{del}}(\mathbf{r}) \geq t | N_{\text{tot}}\right) = \sum_{l=t}^{\infty} \binom{N_{\text{tot}}}{l} [\text{PSF}_{\text{del}}(\mathbf{r})]^l [1 - \text{PSF}_{\text{del}}(\mathbf{r})]^{N_{\text{tot}}-l}. \quad (8.2.11)$$

Averaging over all values of \tilde{N}_{tot} and normalizing to unity gives the PDF of detecting a photon in an element centered at \mathbf{r} :

$$\text{PSF}_{\text{del}}^{\text{SPC}}(\mathbf{r}) = \frac{1}{\kappa a} \sum_{i=0}^{\infty} \sum_{l=t}^{N_{\text{tot}}} \text{pr}_{N_{\text{tot}}}(N_{\text{tot}}) \binom{i}{l} [\text{PSF}_{\text{del}}(\mathbf{r})]^l [1 - \text{PSF}_{\text{del}}(\mathbf{r})]^{i-l} \quad (8.2.12)$$

where κ is given by Eq. (8.2.8) and $\text{pr}_{N_{\text{tot}}}(N_{\text{tot}})$ is given by Eq. (8.2.1).

8.2.3.2 Photon-counting modulation transfer function

The MTF is equal to the Fourier Transform of the point spread function. Using the binomial theorem, the SPC point spread functions is expressed as

$$\text{PSF}_{\text{del}}^{\text{SPC}}(\mathbf{r}) = \frac{1}{\kappa a} \sum_{i=0}^{\infty} \sum_{l=T}^{N_{\text{tot}}} \sum_{m=0}^{N_{\text{tot}}-l} b_{i,l,m} [\text{PSF}_{\text{del}}(\mathbf{r})]^l [\text{PSF}_{\text{del}}(\mathbf{r})]^m \quad (8.2.13)$$

where

$$b_{i,l,m} = \text{pr}_{N_{\text{tot}}}(N_{\text{tot}}) \binom{N_{\text{tot}}}{l} \binom{N_{\text{tot}}-l}{m} \Big|_{N_{\text{tot}}=i}. \quad (8.2.14)$$

Taking the Fourier transform of Eq. (8.2.13) yields the photon-counting MTF:

$$\text{T}_{\text{del}}^{\text{SPC}}(u, v) = \frac{1}{\kappa a} \sum_{N_{\text{tot}}=0}^{\infty} \sum_{l=T}^{N_{\text{tot}}} \sum_{m=0}^{N_{\text{tot}}-l} b_{i,l,m} [\text{T}_{\text{del}}(u, v) *^{l+m} \text{T}_{\text{del}}(u, v)] \quad (8.2.15)$$

where

$$\text{T}_{\text{del}}(u, v) = \text{T}(u, v) \text{sinc}(au) \text{sinc}(av)$$

and $\text{T}_{\text{del}}(u, v) *^{l+m} \text{T}_{\text{del}}(u, v)$ represents the convolution of $\text{T}_{\text{del}}(u, v)$ with itself $l + m$ times. The above equation illustrates the complicated relationship between the MTF of an SPC x-ray detector,

the threshold value, and $T_{\text{del}}(u, v)$.

8.3 Methods and Materials

8.3.1 Theoretical comparison of charge sharing effects in SPC and energy-integrating x-ray detectors

We use the above formalism to theoretically compare the effects of charge sharing between neighboring pixels on the MTF of both SPC and conventional energy-integrating x-ray detectors. For energy-integrating systems, the PSF and MTF are simply given by $\text{PSF}_{\text{del}}(\mathbf{r})$ and $T_{\text{del}}(u, v)$, respectively. We consider the simple case of a one-dimensional x-ray detector and Gaussian PSF(\mathbf{r}) with variance σ^2 . We assume that all photons interact through the photoelectric effect and no characteristic x rays are emitted. The results presented will therefore represent an upper limit of spatial resolution for both SPC and energy-integrating x-ray detectors.

8.3.2 Monte Carlo validation

Monte Carlo simulations have been performed to validate the theoretical description of the mean photon counting image signal and MTF described above. For simplicity we let $\beta = 1$ and assume Poisson-distributed \tilde{g} . Relocation distances for secondary quanta are assumed Gaussian-distributed with variance σ^2 . A counter is incremented in an element when the number of secondaries detected in the element is greater than threshold t .

The presampling pixel PSF and MTF were calculated by simulating x-ray incidence at 10 evenly spaced locations in a pixel centered at the origin. For each location, we simulated 1000 interacting x-ray photons and calculated the total number of photons counted in each detector element. The presampling MTF was then determined used the method described by Fujita *et al.*^[69] and Samei *et al.*^[161].

8.4 Preliminary results

8.4.1 Influence of charge sharing on recorded count rates

Figure 8.4.1 illustrates the dependence of normalized SPC pixel value $c_o = \bar{c}/\bar{q}_o a$ on threshold level for selected levels of charge sharing assuming Gaussian-distributed PSF for electronic noise level $\sigma_e = k\bar{g}/10$. Excellent agreement is obtained between theoretical and Monte Carlo calculations. As

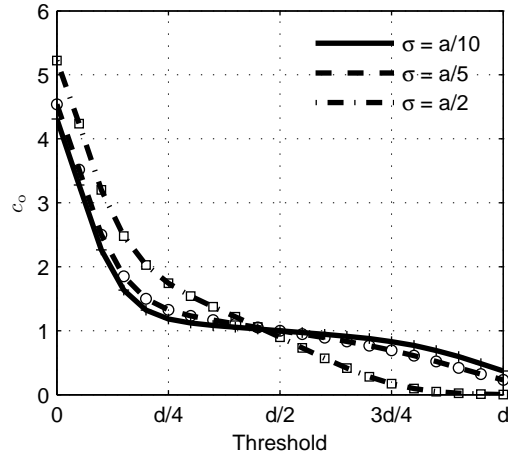


Figure 8.4.1: Plots of normalized SPC pixel value c_0 as a function of threshold value (expressed as a fraction of the mean prethresholding signal \bar{d}) for selected charge-sharing levels. All calculations have been performed for $\lambda = 1/8$, $\sigma_e = k\bar{g}/10$, and $\alpha = 1$. Lines and symbols represent theoretical and Monte Carlo calculations, respectively.

expected, charge sharing results in false counts for low threshold values. In general, the number of false counts increases as the width of the PSF of secondaries increases. In addition, charge sharing narrows the acceptable range of threshold values that adequately suppress false counts while at the same time preserving actual interaction events.

8.4.2 Influence of charge sharing on spatial resolution

Figure 8.4.2 illustrates results of theoretical and Monte Carlo calculations the one-dimensional PSF and MTF of SPC and EI systems. Excellent agreement is obtained between theoretical and Monte Carlo calculations. Notice that the shape of the PSF for SPC systems is different than that of EI systems. For lower levels of charge sharing, the PSF of both SPC and EI systems resembles a rectangle function that has been slightly “blurred.” In the case of SPC systems, as expected, the width of the PSF increases with decreasing threshold level. This results in an MTF that may be slightly degraded relative to that of an energy-integrating system, as illustrated in the right column of Fig. 8.4.2. As the level of charge sharing increases, the PSF for energy-integrating systems becomes more similar in shape to a Gaussian. However, in the case of SPC systems, the PSF remains more similar in shape to a rectangle function with width increasing as the threshold decreases. This is due to the fact that in SPC systems, for a given x-ray interaction, equal weighting is given to all elements that collect more secondaries than threshold t . This differs from EI where element signals are weighted in proportion to the number of collected secondaries.

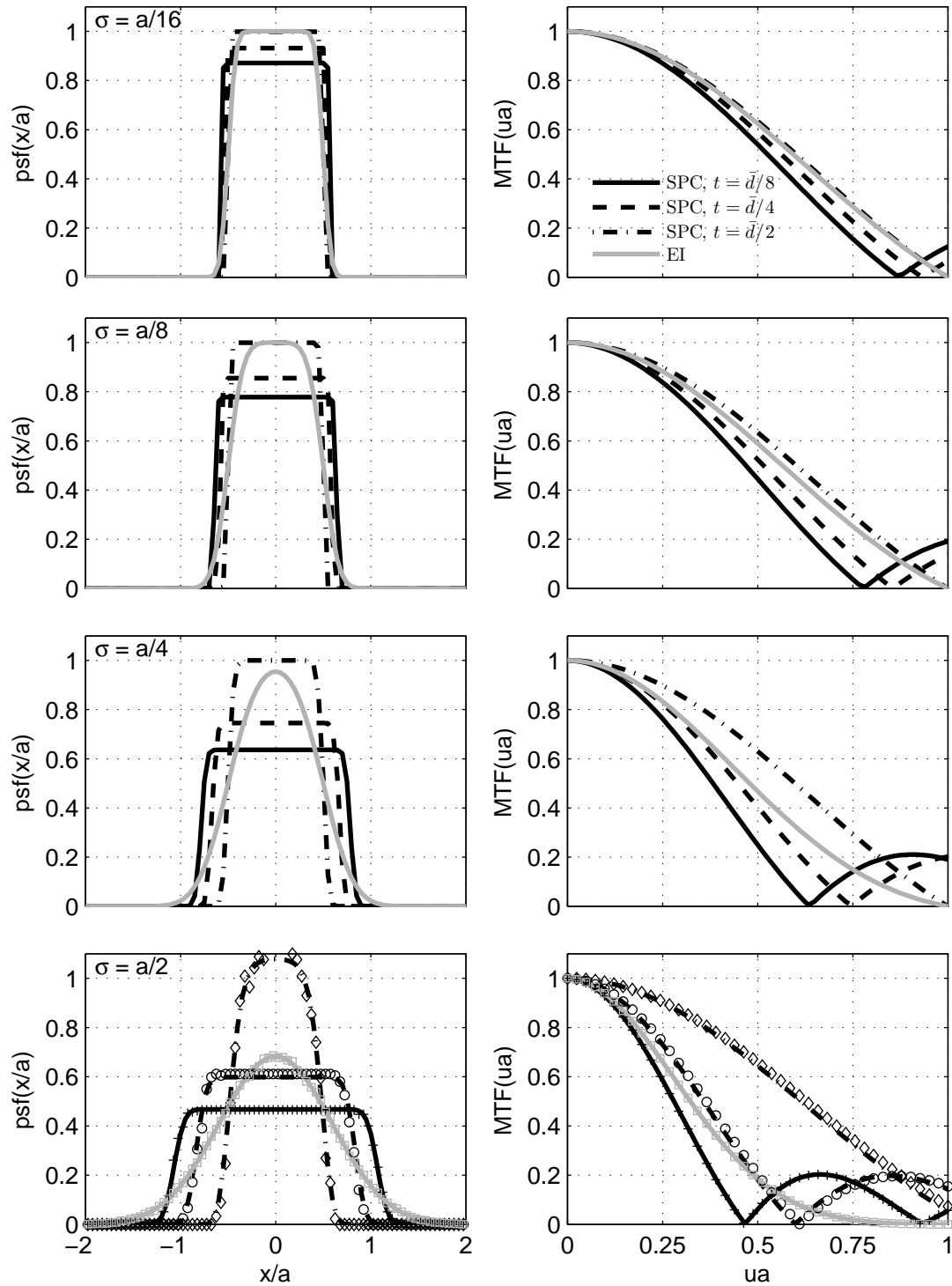


Figure 8.4.2: Plots of the PSF and MTF of photon counting systems for selected thresholds and levels of charge sharing. All calculations have been performed assuming $\sigma_e = k\bar{g}/10$. Lines and symbols represent theoretical and Monte Carlo calculations, respectively.

8.4.3 Optimal SPC threshold

In the case of SPC systems, Fig. 8.4.2 demonstrates that the shape of the MTF is strongly dependent on the threshold used to identify x-ray interaction events. For the model considered here, increasing the threshold level to one half of the mean prethresholding signal results in an MTF approximately equal to the sinc function for all levels of charge sharing considered. Surprisingly, even when the width of the relocation PDF was one-half of the element width, a threshold equal to $\bar{d}/2$ would result in negligible loss of photon counts, as illustrated in Fig. 8.4.1. This suggests that for photon-counting applications where energy information is not required, simple thresholding may adequately suppress false counts caused by charge sharing.

8.5 Discussion of preliminary results

The analysis presented here represents a first attempt at a theoretical understanding of the influence of charge sharing between neighboring detector elements on SPC count rates and spatial resolution expressed in terms of the modulation transfer function. While the description presented above is simplistic in the sense that it does not account for emission and reabsorption of fluorescent and Compton-scatter photons, or depth-dependent issues encountered in real SPC systems, it was useful in highlighting some of the fundamental relationships between charge-sharing levels, count rates, and spatial resolution of SPC systems. An interesting result from this first analysis is that when energy-information is not required, simple thresholding techniques may enable increasing the MTF of SPC systems without sacrificing count rates. However, this may not be the case when emission of fluorescent and Compton-scatter photons are considered. In this case, a combination of the techniques used in the analyses presented here and those presented in Chapters 4 and 5 will be required to understand the influence of reabsorption on count rates, spatial resolution, and image noise. This is the focus of an ongoing investigation.

The formalism presented above will become useful in design, evaluation, and identification of potential benefits of adaptive binning approaches that sum charge from neighboring pixels to estimate total deposited photon energy for each x-ray interaction, such as one implemented in the MEDIPIX3 prototype.^[18]

Appendix A

Supplemental material for Chapter 2

Material in this chapter is adapted from the Appendix of a manuscript entitled “A theoretical comparison of x-ray angiographic image quality using energy-dependent and conventional subtraction methods” by Jesse Tanguay, Ho Kyung Kim, and Ian A. Cunningham, published in *Medical Physics* 2012; 39: 132-142.

A.1 Linearization of the log signals

We let $\mathbf{A}_0 = [A_{10}, \dots, A_{m0}]$ represent the point about which we expand the log signal \tilde{l}_i and l_{i0} be the corresponding log signal. Then

$$\mathbb{E}(\tilde{l}_i - l_{i0}) = -\mathbb{E}\left(\ln \frac{\tilde{M}_i}{\tilde{M}_i|_{\mathbf{A}=\mathbf{A}_0}}\right). \quad (\text{A.1.1})$$

We linearize the right side of the above equation about $\tilde{M}_i/\tilde{M}_i|_{\mathbf{A}=\mathbf{A}_0} = 1$:

$$\mathbb{E}(\tilde{l}_i - l_{i0}) \approx 1 - \mathbb{E}\left(\frac{\tilde{M}_i}{\tilde{M}_i|_{\mathbf{A}=\mathbf{A}_0}}\right). \quad (\text{A.1.2})$$

The quantity $\tilde{M}_i|_{\mathbf{A}=\mathbf{A}_0}$ would be determined from an average of a series of calibration scans and we assume has negligible variability. Therefore

$$\mathbb{E}(\tilde{l}_i - l_{i0}) \approx 1 - \frac{\int_0^\infty S_i(E) \bar{q}_i(E) e^{-\mathbf{A}^T \frac{\mu}{\rho}(E)} dE}{\int_0^\infty S_i(E) \bar{q}_i(E) e^{-\mathbf{A}_0^T \frac{\mu}{\rho}(E)} dE}$$

Linearizing \tilde{M}_i about $\mathbf{A} = \mathbf{A}_0$ yields

$$\mathbb{E} \left(\tilde{l}_i - \tilde{l}_{i0} \right) \approx \sum_{b=1}^m (A_b - A_{b0}) \frac{\bar{\mu}}{\rho}_{ib}$$

where $\frac{\bar{\mu}}{\rho}_{ib}$ denotes the average value of the mass-attenuation coefficient of basis material b weighted by $S_i(E) \bar{q}_i(E) e^{-\mathbf{A}_0^T \frac{\mu}{\rho}(E)}$. In matrix notation the above expression can be written as

$$\mathbf{L} - \mathbf{L}_0 = \mathbf{J} (\mathbf{A} - \mathbf{A}_0). \quad (\text{A.1.3})$$

A.2 Log-signal covariance

In general, the covariance between log signals i and j , $\text{Cov}(\tilde{l}_i, \tilde{l}_j)$, is given by

$$\text{Cov} \left(\tilde{l}_i, \tilde{l}_j \right) = \mathbb{E} \left(\Delta \tilde{l}_i \Delta \tilde{l}_j \right) \quad (\text{A.2.1})$$

where $\Delta \tilde{l}_i = \tilde{l}_i - \mathbb{E}(\tilde{l}_i)$. A first order Taylor expansion of \tilde{l}_i about $\mathbb{E}(\tilde{M}_i)$ gives

$$\tilde{l}_i \approx \tilde{l}_i \Big|_{\tilde{M}_i = \mathbb{E}(\tilde{M}_i)} + \left(\tilde{M}_i - \mathbb{E}(\tilde{M}_i) \right) \frac{\partial \tilde{l}_i}{\partial \tilde{M}_i} \Big|_{\tilde{M}_i = \mathbb{E}(\tilde{M}_i)} \quad (\text{A.2.2})$$

$$\approx \mathbb{E} \left(\tilde{l}_i \right) - \frac{\tilde{M}_i - \mathbb{E}(\tilde{M}_i)}{\mathbb{E}(\tilde{M}_i)}. \quad (\text{A.2.3})$$

Therefore,

$$\Delta \tilde{l}_i = - \frac{\Delta \tilde{M}_i}{\mathbb{E}(\tilde{M}_i)}. \quad (\text{A.2.4})$$

where $\Delta \tilde{M}_i = \tilde{M}_i - \mathbb{E}(\tilde{M}_i)$. Combining Eqs. (A.2.1) and (A.2.4):

$$\text{Cov} \left(\tilde{l}_i, \tilde{l}_j \right) = \mathbb{E} \left(\frac{\Delta \tilde{M}_i}{\mathbb{E}(\tilde{M}_i)} \frac{\Delta \tilde{M}_j}{\mathbb{E}(\tilde{M}_j)} \right) = \frac{\text{Cov}(\tilde{M}_i, \tilde{M}_j)}{\mathbb{E}(\tilde{M}_i) \mathbb{E}(\tilde{M}_j)} \quad (\text{A.2.5})$$

where $\text{Cov}(\tilde{M}_i, \tilde{M}_j)$ is the covariance between \tilde{M}_i and \tilde{M}_j . The exact form of $\text{Cov}(\tilde{M}_i, \tilde{M}_j)$ depends on the specific imaging application.

Appendix B

Supplemental material for Chapter 3

Material in this chapter is adapted from the Appendix of a manuscript entitled “The detective quantum efficiency of photon-counting x-ray detectors using cascaded-systems analyses” by Jesse Tanguay, Seungman Yun, Ho Kyung Kim, and Ian A. Cunningham, published in *Medical Physics* 2013; 40(4): 041913-1.

B.1 PDF of readout signal, $p_d(d(\mathbf{r}))$

The PDF of readout signal \tilde{d}^j describes the relative probability of \tilde{d}^j taking particular values. In the limit of fast readout rates ($\bar{q}_o a_t a \ll 1$) with no scattering of secondary image quanta in the detector ($T_{\text{sec}}(\mathbf{k}) \approx 1$) and one photon incident at \mathbf{r}_i , \tilde{d}^j is given by

$$\tilde{d}^j(\mathbf{r}) = \begin{cases} \tilde{d}^j|_1 & \text{if } \mathbf{r}_i \text{ is in element centered at } \mathbf{r} \\ \tilde{d}^j|_0 & \text{otherwise} \end{cases} \quad (\text{B.1.1})$$

where the CSA model gives

$$\tilde{d}^j|_1 = k\tilde{q}_{\text{sec}} * \Pi\left(\frac{\mathbf{r}}{\mathbf{a}}\right) + \tilde{e} \quad (\text{B.1.2})$$

$$= k\tilde{N}_{\text{sec}}|_1 + \tilde{e} \quad (\text{B.1.3})$$

and

$$\tilde{d}^j|_0 = \tilde{e} \quad (\text{B.1.4})$$

where $\tilde{N}_{\text{sec}}|_1$ represents the total number of secondaries collected given one incident photon and \tilde{e} is a zero-mean Gaussian-distributed RV representing uncorrelated additive readout noise. Under

these conditions the probability that \tilde{d}^j is greater than t is given by the complementary cumulative distribution function (CDF) for \tilde{d} . The CDF for \tilde{d} given \tilde{N}_o^j incident photons with positions $\{\tilde{\mathbf{r}}_i^j, i = 1.. \tilde{N}_o^j\}$ is given by

$$\begin{aligned} P_d\left(d(\mathbf{r}) \geq t | \tilde{N}_o^j, \mathbf{r}_1^j, \dots, \mathbf{r}_{N_j}^j\right) &= P_d\left(\tilde{d}^j|_1 \geq t\right) \sum_{i=1}^{\tilde{N}_o^j} \Pi\left(\frac{\mathbf{r} - \mathbf{r}_i^j}{\mathbf{a}}\right) \\ &+ P_d\left(\tilde{d}^j|_0 \geq t\right) \left(1 - \sum_{i=1}^{\tilde{N}_o^j} \Pi\left(\frac{\mathbf{r} - \mathbf{r}_i^j}{\mathbf{a}}\right)\right) \end{aligned} \quad (\text{B.1.5})$$

where the two terms describe regions of \mathbf{r} where the readout signal is given by Eqs. (B.1.3) and (B.1.4) respectively. Averaging over all possible values of $\{\tilde{\mathbf{r}}_i^j, i = 1.. \tilde{N}_o^j\}$ yields

$$\begin{aligned} P_d\left(d(\mathbf{r}) \geq t | \tilde{N}_o^j\right) &= P_d\left(\tilde{d}^j|_1 \geq t\right) \sum_{i=1}^{\tilde{N}_o^j} \int_A \Pi\left(\frac{\mathbf{r} - \mathbf{r}_i^j}{\mathbf{a}}\right) p_{\mathbf{r}}\left(\mathbf{r}_i^j\right) d^2\mathbf{r}_i^j \\ &+ P_d\left(\tilde{d}^j|_0 \geq t\right) \int_A \left(1 - \sum_{i=1}^{\tilde{N}_o^j} \Pi\left(\frac{\mathbf{r} - \mathbf{r}_i^j}{\mathbf{a}}\right)\right) p_{\mathbf{r}}\left(\mathbf{r}_i^j\right) d^2\mathbf{r}_i^j \end{aligned} \quad (\text{B.1.6})$$

$$= P_d\left(\tilde{d}^j|_1 \geq t\right) \frac{\tilde{N}_o^j a}{A} + P_d\left\{\tilde{d}^j|_0 \geq t\right\} \left(1 - \frac{\tilde{N}_o^j a}{A}\right). \quad (\text{B.1.7})$$

Averaging over all possible values of \tilde{N}_o^j yields

$$P_d(d(\mathbf{r}) \geq t) = P_d\left(\tilde{d}^j|_1 \geq t\right) \bar{q}_o a_t a + P_d\left(\tilde{d}^j|_0 \geq t\right) (1 - \bar{q}_o a_t a) \quad (\text{B.1.8})$$

$$= \int_t^\infty \left[p_d\left(\tilde{d}^j|_1\right) \bar{q}_o a_t a + p_d\left(\tilde{d}^j|_0\right) (1 - \bar{q}_o a_t a) \right] dd. \quad (\text{B.1.9})$$

The integrand of the above equation is equal to the PDF for \tilde{d} :

$$p_d(d(\mathbf{r})) = p_d\left(d^j|_1\right) \bar{q}_o a_t a + p_d\left(d^j|_0\right) (1 - \bar{q}_o a_t a) \quad (\text{B.1.10})$$

which reduces to Eq. (3.2.25). The first term in Eq. (B.1.10) describes the primary peak in the PDF centered at $\bar{d}_{nm} = k_1 \beta \bar{g}$ in Fig. 3.2.5 giving the distribution in \tilde{d}^j values when a photon is incident in an element centered on the photon, while the second term gives the distribution when no photon is incident.

B.2 Joint PDF of readout signal, $p_d(d(\mathbf{r}), d(\mathbf{r} + \boldsymbol{\tau}))$

The Wiener NPS in a photon-counting image is given by the Fourier transform of the autocovariance of \tilde{c} from Eq. (3.2.21) and requires the joint PDF of $\tilde{d}(\mathbf{r})$ and $\tilde{d}(\mathbf{r} + \boldsymbol{\tau})$. It is important to emphasize that $\tilde{d}(\mathbf{r})$ is the *presampling* readout signal for an element centered at any \mathbf{r} value, including the non-physical situation of overlapping elements when $\boldsymbol{\tau}$ is less than the detector element spacing. In this case, one interacting photon may contribute to signals in both elements.

There are three possible scenarios to consider in the joint PDF: 1) photon incident on both elements; 2) photon incident on only one element; and 3) no photons are incident on either element. We let $P_{1,1}$, $P_{1,0}$, and $P_{0,0}$ represent the probability that both elements are above the threshold for each of these scenarios, giving

$$P(d(\mathbf{r}) \geq t \text{ and } d(\mathbf{r} + \boldsymbol{\tau}) \geq t) = P_{1,1} + 2P_{1,0} + P_{0,0}. \quad (\text{B.2.1})$$

$P_{1,1}$: The scenario of a photon incident on each element has two physically possible conditions, corresponding to complete overlap of the two elements or no overlap. When the elements completely overlap ($|\boldsymbol{\tau}| = 0$), there can be only one photon contributing to both elements and the probability that both signals are greater than t is then given by the complementary CDF for $\tilde{d}|_1$ defined above (see Eq. (B.1.8)). If the elements do not overlap, there must be two different photons incident on two uncorrelated elements, and the probability that both are greater than t is given by the square of the complementary CDF for $\tilde{d}|_1$. The probability that both elements are above the threshold is therefore given by

$$\begin{aligned} P_{1,1} = & P\left(\tilde{d}^j|_1 \geq t\right) \sum_{i=1}^{\tilde{N}_o^j} \Pi\left(\frac{\mathbf{r} - \mathbf{r}_i^j}{\mathbf{a}}\right) \Pi\left(\frac{\mathbf{r} + \boldsymbol{\tau} - \mathbf{r}_i^j}{\mathbf{a}}\right) \\ & + \left[P\left(\tilde{d}^j|_1 \geq t\right)\right]^2 \sum_{i=1}^{\tilde{N}_o^j} \sum_{\substack{l=1 \\ l \neq i}}^{\tilde{N}_o^j} \Pi\left(\frac{\mathbf{r} - \mathbf{r}_i^j}{\mathbf{a}}\right) \Pi\left(\frac{\mathbf{r} + \boldsymbol{\tau} - \mathbf{r}_l^j}{\mathbf{a}}\right) \end{aligned} \quad (\text{B.2.2})$$

where the two terms describe the two conditions above. While it will not matter what the model predicts for non-physical cases, Eq. (B.2.2) describes a convenient linear transition from complete overlap to no overlap in proportion to the overlap area. Averaging over all possible values of $\{\tilde{\mathbf{r}}_i^j, i =$

1.. \tilde{N}_o^j yields

$$\begin{aligned} P_{1,1} &= \frac{1}{A} P(\tilde{d}^j|_1 \geq t) \sum_{i=1}^{\tilde{N}_o^j} \int_A \Pi\left(\frac{\mathbf{r} - \mathbf{r}_i^j}{\mathbf{a}}\right) \Pi\left(\frac{\mathbf{r} + \boldsymbol{\tau} - \mathbf{r}_i^j}{\mathbf{a}}\right) d^2 \mathbf{r}_i^j \\ &+ \frac{1}{A^2} \left[P(\tilde{d}^j|_1 \geq t) \right]^2 \sum_{i=1}^{\tilde{N}_o^j} \sum_{\substack{l=1 \\ l \neq i}}^{\tilde{N}_o^j} \int_A \int_A \Pi\left(\frac{\mathbf{r} - \mathbf{r}_i^j}{\mathbf{a}}\right) \Pi\left(\frac{\mathbf{r} + \boldsymbol{\tau} - \mathbf{r}_l^j}{\mathbf{a}}\right) d^2 \mathbf{r}_i^j d^2 \mathbf{r}_l^j \end{aligned} \quad (\text{B.2.3})$$

$$= \frac{\tilde{N}_o^j}{A} P(\tilde{d}^j|_1 \geq t) \Pi\left(\frac{\boldsymbol{\tau}}{\mathbf{a}}\right) * \Pi\left(\frac{\boldsymbol{\tau}}{\mathbf{a}}\right) + \left(\tilde{N}_o^j\right)^2 \frac{a^2}{A^2} \left[P(\tilde{d}^j|_1 \geq t) \right]^2 \quad (\text{B.2.4})$$

$$= \frac{\tilde{N}_o^j}{A} P(\tilde{d}^j|_1 \geq t) a \Lambda\left(\frac{\boldsymbol{\tau}}{\mathbf{a}}\right) + \left(\tilde{N}_o^j\right)^2 \frac{a^2}{A^2} \left[P(\tilde{d}^j|_1 \geq t) \right]^2 \quad (\text{B.2.5})$$

where $\Lambda(\boldsymbol{\tau}/\mathbf{a}) = \Lambda(\tau_x/a_x)\Lambda(\tau_y/a_y)$ represents the two dimensional triangle function and $\Lambda(\tau_x/a)$ is equal to $(1 - |\tau_x/a_x|)$ for $|\tau_x| < a_x$ and zero otherwise and similarly for $\Lambda(\tau_y/a_y)$. Averaging over all possible values of \tilde{N}_o^j yields

$$\begin{aligned} P_{1,1} &= \bar{q}_o a_t P(\tilde{d}^j|_1 \geq t) a \Lambda\left(\frac{\boldsymbol{\tau}}{\mathbf{a}}\right) \\ &+ (\bar{q}_o a_t a)^2 \left[P(\tilde{d}^j|_1 \geq t) \right]^2. \end{aligned} \quad (\text{B.2.6})$$

$P_{0,0}$: For the case of no photon incident on either element, counts are triggered only when additive noise exceeds the threshold. For complete element overlap we have

$$P_{0,0}|_{|\boldsymbol{\tau}|=0} = P(\tilde{d}^j|_0 \geq t) \left(1 - \sum_{i=1}^{\tilde{N}_o^j} \Pi\left(\frac{\mathbf{r} - \mathbf{r}_i^j}{\mathbf{a}}\right) \right) \quad (\text{B.2.7})$$

where the term in parenthesis describes regions of \mathbf{r} where there are no incident x-ray photons. For no overlap, we have

$$\begin{aligned} P_{0,0}|_{\tau_x > a \text{ and } \tau_y > a} &= P_0\left(d(\mathbf{r}) \geq t | \tilde{N}_o^j, \mathbf{r}_1^j, \dots, \mathbf{r}_{\tilde{N}_o^j}^j\right) P_0\left(d(\mathbf{r} + \boldsymbol{\tau}) \geq t | \tilde{N}_o^j, \mathbf{r}_1^j, \dots, \mathbf{r}_{\tilde{N}_o^j}^j\right) \\ &= \left(1 - \sum_{i=1}^{\tilde{N}_o^j} \Pi\left(\frac{\mathbf{r} - \mathbf{r}_i^j}{\mathbf{a}}\right) \right) \left(1 - \sum_{i=1}^{\tilde{N}_o^j} \Pi\left(\frac{\mathbf{r} + \boldsymbol{\tau} - \mathbf{r}_i^j}{\mathbf{a}}\right) \right) \left[P(\tilde{d}^j|_0 \geq t) \right]^2. \end{aligned} \quad (\text{B.2.8})$$

Assuming a linear transition from non-overlapping elements to complete overlap as before gives

$$\begin{aligned}
P_{0,0} &= P\left(\tilde{d}^j|_0 \geq t\right) \left(1 - \sum_{i=1}^{\tilde{N}_o^j} \Pi\left(\frac{\mathbf{r} - \mathbf{r}_i^j}{\mathbf{a}}\right)\right) \Lambda\left(\frac{\boldsymbol{\tau}}{\mathbf{a}}\right) \\
&+ \left[P\left(\tilde{d}^j|_0 \geq t\right)\right]^2 \left(1 - \sum_{i=1}^{\tilde{N}_o^j} \Pi\left(\frac{\mathbf{r} - \mathbf{r}_i^j}{\mathbf{a}}\right)\right) \left(1 - \sum_{l=1}^{\tilde{N}_o^j} \Pi\left(\frac{\mathbf{r} + \boldsymbol{\tau} - \mathbf{r}_l^j}{\mathbf{a}}\right)\right) \left[1 - \Lambda\left(\frac{\boldsymbol{\tau}}{\mathbf{a}}\right)\right] \quad (\text{B.2.9})
\end{aligned}$$

and averaging over all possible values of $\{\tilde{\mathbf{r}}_i^j, i = 1.. \tilde{N}_o^j\}$ and \tilde{N}_o^j yields

$$\begin{aligned}
P_{0,0} &= (1 - \bar{q}_o a_t a) P\left(\tilde{d}^j|_0 \geq t\right) \Lambda\left(\frac{\boldsymbol{\tau}}{\mathbf{a}}\right) \\
&+ \left[P\left(\tilde{d}^j|_0 \geq t\right)\right]^2 (1 - \bar{q}_o a_t a)^2 \left[1 - \Lambda\left(\frac{\boldsymbol{\tau}}{\mathbf{a}}\right)\right]. \quad (\text{B.2.10})
\end{aligned}$$

$P_{1,0}$: In the non-overlapping case, $\tilde{d}(\mathbf{r})$ and $\tilde{d}(\mathbf{r} + \boldsymbol{\tau})$ are independent RVs. In the complete-overlap case, $P_{1,0}$ must be equal to 0 because an element cannot have both one and zero photons incident on it. We therefore represent $P_{1,0}$ as

$$P_{1,0} = P\left(\tilde{d}^j|_1 \geq t\right) P\left(\tilde{d}^j|_0 \geq t\right) \sum_{i=1}^{\tilde{N}_o^j} \Pi\left(\frac{\mathbf{r} - \mathbf{r}_i^j}{\mathbf{a}}\right) \left(1 - \sum_{l=1}^{\tilde{N}_o^j} \Pi\left(\frac{\mathbf{r} + \boldsymbol{\tau} - \mathbf{r}_l^j}{\mathbf{a}}\right)\right) \left[1 - \Lambda\left(\frac{\boldsymbol{\tau}}{\mathbf{a}}\right)\right]. \quad (\text{B.2.11})$$

Averaging over all possible values of $\{\tilde{\mathbf{r}}_i^j, i = 1.. \tilde{N}_o^j\}$ and \tilde{N}_o^j yields

$$P_{1,0} = \bar{q}_o a_t a (1 - \bar{q}_o a_t a) P\left(\tilde{d}^j|_1 \geq t\right) P\left(\tilde{d}^j|_0 \geq t\right) \left[1 - \Lambda\left(\frac{\boldsymbol{\tau}}{\mathbf{a}}\right)\right]. \quad (\text{B.2.12})$$

Combining Eqs. (B.2.6), (B.2.9), and (B.2.12) yields

$$\begin{aligned}
&P(d(\mathbf{r}) \geq t \text{ and } d(\mathbf{r} + \boldsymbol{\tau}) \geq t) \\
&= \bar{q}_o a_t P\left\{\tilde{d}^j|_1 \geq t\right\} a \Lambda\left(\frac{\boldsymbol{\tau}}{\mathbf{a}}\right) \\
&+ (\bar{q}_o a_t a)^2 \left[P\left\{\tilde{d}^j|_1 \geq t\right\}\right]^2 \\
&+ (1 - \bar{q}_o a_t a) P\left\{\tilde{d}^j|_0 \geq t\right\} \Lambda\left(\frac{\boldsymbol{\tau}}{\mathbf{a}}\right) \\
&+ (1 - \bar{q}_o a_t a)^2 \left[P\left\{\tilde{d}^j|_0 \geq t\right\}\right]^2 \left[1 - \Lambda\left(\frac{\boldsymbol{\tau}}{\mathbf{a}}\right)\right] \\
&+ 2\bar{q}_o a_t a (1 - \bar{q}_o a_t a) P\left\{\tilde{d}^j|_1 \geq t\right\} P\left\{\tilde{d}^j|_0 \geq t\right\} \left[1 - \Lambda\left(\frac{\boldsymbol{\tau}}{\mathbf{a}}\right)\right] \quad (\text{B.2.13})
\end{aligned}$$

and the joint PDF of $\tilde{d}(\mathbf{r})$ and $\tilde{d}(\mathbf{r} + \boldsymbol{\tau})$ can therefore be represented as

$$\begin{aligned}
p_d(d(\mathbf{r}), d(\mathbf{r} + \boldsymbol{\tau})) &= \delta(d(\mathbf{r}) - d(\mathbf{r} + \boldsymbol{\tau})) \bar{q}_o a_t p_d(d^j|_1)|_{d(\mathbf{r})} a \Lambda\left(\frac{\boldsymbol{\tau}}{\mathbf{a}}\right) \\
&\quad + (\bar{q}_o a_t a)^2 p_d(d^j|_1)|_{d(\mathbf{r})} p_d(d^j|_1)|_{d(\mathbf{r} + \boldsymbol{\tau})} \\
&\quad + \delta(d(\mathbf{r}) - d(\mathbf{r} + \boldsymbol{\tau})) (1 - \bar{q}_o a_t a) p_d(d^j|_0)|_{d(\mathbf{r})} \Lambda\left(\frac{\boldsymbol{\tau}}{\mathbf{a}}\right) \\
&\quad + (1 - \bar{q}_o a_t a)^2 p_d(d^j|_0)|_{d(\mathbf{r})} p_d(d^j|_0)|_{d(\mathbf{r} + \boldsymbol{\tau})} \left[1 - \Lambda\left(\frac{\boldsymbol{\tau}}{\mathbf{a}}\right)\right] \\
&\quad + 2\bar{q}_o a_t a (1 - \bar{q}_o a_t a) p_d(d^j|_0)|_{d(\mathbf{r})} p_d(d^j|_1)|_{d(\mathbf{r} + \boldsymbol{\tau})} \left[1 - \Lambda\left(\frac{\boldsymbol{\tau}}{\mathbf{a}}\right)\right] \quad (\text{B.2.14})
\end{aligned}$$

where $p_d(d^j|_1)|_{d(\mathbf{r})}$ indicates that the PDF of $\tilde{d}^j|_1$ is evaluated at $\tilde{d}(\mathbf{r})$ and similarly for $p_d(d^j|_1)|_{d(\mathbf{r} + \boldsymbol{\tau})}$.

B.3 Presampling NPS of SPC image $\tilde{c}(\mathbf{r})$

Building on Appendix B and combining Eqs. (3.2.21) and (B.2.14), gives the autocovariance $K_c(\boldsymbol{\tau})$:

$$\begin{aligned}
K_c(\boldsymbol{\tau}) &= M \left[\bar{q}_o a \int_t^\infty p_d(\tilde{d}^j|_1) dd \right. \\
&\quad + (1 - \bar{q}_o a_t a) \int_t^\infty p_d(\tilde{d}^j|_0) dd \\
&\quad - (1 - \bar{q}_o a_t a)^2 \left(\int_t^\infty p_d(\tilde{d}^j|_0) dd \right)^2 \\
&\quad - 2\bar{q}_o a_t a (1 - \bar{q}_o a_t a) \\
&\quad \left. \times \int_t^\infty p_d(\tilde{d}^j|_0) dd \int_t^\infty p_d(\tilde{d}^j|_1) dd \right] \Lambda\left(\frac{\boldsymbol{\tau}}{\mathbf{a}}\right). \quad (\text{B.3.1})
\end{aligned}$$

Taking the Fourier transform gives

$$\begin{aligned}
\text{NPS}_c(\mathbf{k}) &= M \left[\bar{q}_o a \int_t^\infty p_d(\tilde{d}^j|_1) dd \right. \\
&\quad + (1 - \bar{q}_o a_t a) \int_t^\infty p_d(\tilde{d}^j|_0) \\
&\quad - (1 - \bar{q}_o a_t a)^2 \left(\int_t^\infty p_d(\tilde{d}^j|_0) dd \right)^2 \\
&\quad - 2\bar{q}_o a_t a (1 - \bar{q}_o a_t a) \\
&\quad \left. \times \int_t^\infty p_d(\tilde{d}^j|_0) dd \int_t^\infty p_d(\tilde{d}^j|_1) dd \right] \\
&\quad \times a \text{sinc}^2(a_x u) \text{sinc}^2(a_y v) \quad (\text{B.3.2})
\end{aligned}$$

where $\text{sinc}(\theta) = \sin(\pi\theta)/\pi\theta$.

B.4 Calculation of $\xi_T(t)$ and $\xi_F(t)$

From Eqs. (3.2.43) and (3.2.45), the probability of a true count given a photon interaction $\xi_T(t)$ is given by

$$\xi_T(t) = \int_t^\infty \left[\sum_{i=0}^\infty \sum_{j=1}^i \sum_{l=1}^j \text{pr}_g(i) \binom{i}{j} \beta^j (1-\beta)^{i-j} \binom{j}{l} \gamma^l (1-\gamma)^{j-l} \delta\left(\frac{d}{k_1} - l\right) \right] * p_e(d) dd \quad (\text{B.4.1})$$

$$= \sum_{i=0}^\infty \sum_{j=1}^i \sum_{l=1}^j \text{pr}_g(i) \binom{i}{j} \beta^j (1-\beta)^{i-j} \binom{j}{l} \gamma^l (1-\gamma)^{j-l} \left[\int_t^\infty \delta\left(\frac{d}{k} - l\right) * p_e(d) dd \right] \quad (\text{B.4.2})$$

$$= \sum_{l=t}^\infty \sum_{j=1}^\infty \sum_{i=0}^\infty \text{pr}_g(i) \binom{i}{j} \beta^j (1-\beta)^{i-j} \binom{j}{l} \gamma^l (1-\gamma)^{j-l} p_e(kl) \quad (\text{B.4.3})$$

and the probability of a false count given no photon interaction $\xi_F(t)$ is simply given by

$$\xi_F(t) = \int_t^\infty p_e(d) dd \quad (\text{B.4.4})$$

where $p_e(k_1j)$ represents the PDF for \tilde{e} evaluated at k_1j and similarly for $p_e(d)$.

Appendix C

Supplemental material for Chapter 4

C.1 Joint PDF of parallel processes

C.1.1 Joint PDF and branch points

Random selection of points of an input distribution to follow one of two paths, or both paths, is illustrated in Fig. 4.2.2 where \tilde{N}_A and \tilde{N}_B represent the number of quanta in paths A and B, respectively, and $\tilde{\xi}_{j,A}$ and $\tilde{\xi}_{j,B}$ represent selection variables for the j th input quantum. We let $\tilde{\xi}_A = [\tilde{\xi}_{A,1} \dots \tilde{\xi}_{A,\tilde{N}_o}]$, $\tilde{\xi}_B = [\tilde{\xi}_{B,1} \dots \tilde{\xi}_{B,\tilde{N}_o}]$ and $p_{N_A,N_B}(N_A, N_B | \tilde{N}_o, \tilde{\xi}_A, \tilde{\xi}_B)$ represent the joint PDF of \tilde{N}_A and \tilde{N}_B given \tilde{N}_o , $\tilde{\xi}_A$, and $\tilde{\xi}_B$. For fixed \tilde{N}_o , $\tilde{\xi}_A$, and $\tilde{\xi}_B$, \tilde{N}_A and \tilde{N}_B are given by $\tilde{N}_A = \sum_{j=1}^{\tilde{N}_o} \tilde{\xi}_{j,A}$ and $\tilde{N}_B = \sum_{j=1}^{\tilde{N}_o} \tilde{\xi}_{j,B}$, respectively. Therefore

$$p_{N_A,N_B}(N_A, N_B | \tilde{N}_o, \tilde{\xi}_A, \tilde{\xi}_B) = \delta \left(N_A - \sum_{j=1}^{\tilde{N}_o} \tilde{\xi}_{j,A}, N_B - \sum_{j=1}^{\tilde{N}_o} \tilde{\xi}_{j,B} \right) \quad (\text{C.1.1})$$

where $\delta(\cdot)$ denotes the two-dimensional Dirac δ function. Using the translation property of the delta function, the above equation is expressed as

$$p_{N_A,N_B}(N_A, N_B | \tilde{N}_o, \tilde{\xi}_A, \tilde{\xi}_B) = \left[\delta \left(N_A - \tilde{\xi}_{A,1}, N_B - \tilde{\xi}_{B,1} \right) * \delta \left(N_A - \tilde{\xi}_{A,2}, N_B - \tilde{\xi}_{B,1} \right) * \dots \right. \\ \left. \dots * \delta \left(N_A - \tilde{\xi}_{A,\tilde{N}_o}, N_B - \tilde{\xi}_{B,\tilde{N}_o} \right) \right] \quad (\text{C.1.2})$$

where $*$ represents the convolution operator. Therefore

$$p_{N_A, N_B}(N_A, N_B | \tilde{N}_o) = \int \dots \int p_{A, B}(N_A, N_B | \tilde{N}_o, \boldsymbol{\xi}_A, \boldsymbol{\xi}_B) p_{\boldsymbol{\xi}_A, \boldsymbol{\xi}_B}(\boldsymbol{\xi}_A, \boldsymbol{\xi}_B) d^{\tilde{N}_o} \boldsymbol{\xi}_A d^{\tilde{N}_o} \boldsymbol{\xi}_B \quad (\text{C.1.3})$$

$$\begin{aligned} &= \int \dots \int \left[\delta(N_A - \tilde{\xi}_{A,1}, N_B - \tilde{\xi}_{B,1}) * \delta(N_A - \tilde{\xi}_{A,2}, N_B - \tilde{\xi}_{B,2}) * \dots \right. \\ &\quad \left. \dots * \delta(N_A - \tilde{\xi}_{A, \tilde{N}_o}, N_B - \tilde{\xi}_{B, \tilde{N}_o}) \right] p_{\boldsymbol{\xi}_A, \boldsymbol{\xi}_B}(\boldsymbol{\xi}_A, \boldsymbol{\xi}_B) d^{\tilde{N}_o} \boldsymbol{\xi}_A d^{\tilde{N}_o} \boldsymbol{\xi}_B \quad (\text{C.1.4}) \end{aligned}$$

where $p_{\boldsymbol{\xi}_A, \boldsymbol{\xi}_B}(\boldsymbol{\xi}_A, \boldsymbol{\xi}_B) = p_{\xi_{A,1}, \dots, \xi_{A, \tilde{N}_o}, \xi_{B,1}, \dots, \xi_{B, \tilde{N}_o}}(\xi_{A,1}, \dots, \xi_{A, \tilde{N}_o}, \xi_{B,1}, \dots, \xi_{B, \tilde{N}_o})$ represents the joint PDF of $\{\tilde{\xi}_{j,A}, \tilde{\xi}_{j,B}, j = 1..N_o\}$, and $\int d^{\tilde{N}_o} \boldsymbol{\xi}_A$ represents an \tilde{N}_o -dimensional integral with respect to $\boldsymbol{\xi}_A$ and similarly for $\int d^{\tilde{N}_o} \boldsymbol{\xi}_B$. Since each trial is independent of all others we have^[143]

$$p_{\boldsymbol{\xi}_A, \boldsymbol{\xi}_B}(\boldsymbol{\xi}_A, \boldsymbol{\xi}_B) = \prod_{j=1}^{\tilde{N}_o} p_{\xi_{A,j}, \xi_{B,j}}. \quad (\text{C.1.5})$$

Combining the previous two equations yields

$$\begin{aligned} p_{N_A, N_B}(N_A, N_B | \tilde{N}_o) &= \left[\int \delta(N_A - \tilde{\xi}_{A,1}, N_B - \tilde{\xi}_{B,1}) p_{\xi_{A,1}, \xi_{B,1}}(\xi_{A,1}, \xi_{B,1}) d\xi_{A,1} d\xi_{B,1} \right] * \dots \\ &\quad \dots * \left[\int \delta(N_A - \tilde{\xi}_{A, \tilde{N}_o}, N_B - \tilde{\xi}_{B, \tilde{N}_o}) p_{\xi_{A, \tilde{N}_o}, \xi_{B, \tilde{N}_o}}(\xi_{A, \tilde{N}_o}, \xi_{B, \tilde{N}_o}) d\xi_{A, \tilde{N}_o} d\xi_{B, \tilde{N}_o} \right] \quad (\text{C.1.6}) \end{aligned}$$

Using the sifting property of the δ function results in Eq. (4.2.14).

C.1.1.1 Joint PDF of parallel cascades

Figure 4.2.3 is an illustration of a parallel cascade of elementary processes. We let $\tilde{N}_{j,A,i}$ represent the number of quanta after the i th quantum process of path A for the j th input quantum and similarly for $\tilde{N}_{j,B,i}$. The total number of quanta from paths A and B, \tilde{N}_A and \tilde{N}_B , are therefore given by

$$\tilde{N}_A = \sum_{j=1}^{\tilde{N}_o} \tilde{N}_{j,A, n_A} \quad \text{and} \quad \tilde{N}_B = \sum_{j=1}^{\tilde{N}_o} \tilde{N}_{j,B, n_B} \quad (\text{C.1.7})$$

where n_A and n_B represent the number of elementary processes in paths A and B, respectively. For notational simplicity we let $\tilde{N}_{j,A} = \tilde{N}_{j,A, n_A}$ and $\tilde{N}_{j,B} = \tilde{N}_{j,B, n_B}$ represent the total number of quanta from paths A and B, respectively, corresponding to the j th input quantum. Assuming that each process in path A is independent of each process in path B, the joint PDF of $\tilde{N}_{j,A}$ and $\tilde{N}_{j,B}$ is

expressed as

$$p_{N_{j,A}, N_{j,B}} \left(N_{j,A}, N_{j,B} | \tilde{\xi}_{j,A}, \tilde{\xi}_{j,B} \right) = p_{N_{j,A}} \left(N_{j,A} | \tilde{\xi}_{j,A} \right) p_{N_{j,B}} \left(N_{j,B} | \tilde{\xi}_{j,B} \right). \quad (\text{C.1.8})$$

Since each trial is independent of the others we also have

$$\begin{aligned} p_{N_{1,A}, \dots, N_{\tilde{N}_o,A}, N_{1,B}, \dots, N_{\tilde{N}_o,B}} \left(N_{1,A}, \dots, N_{\tilde{N}_o,A}, N_{1,B}, \dots, N_{\tilde{N}_o,B} | \tilde{N}_o, \tilde{\xi}_A, \tilde{\xi}_B \right) \\ = \prod_{j=1}^{\tilde{N}_o} \prod_{j'=1}^{\tilde{N}_o} p_{N_{j,A}} \left(N_{j,A} | \tilde{\xi}_{j,A} \right) p_{N_{j',B}} \left(N_{j',B} | \tilde{\xi}_{j',B} \right). \end{aligned} \quad (\text{C.1.9})$$

Therefore, the joint PDF of \tilde{N}_A and \tilde{N}_B is given by

$$p_{N_A, N_B} \left(N_A, N_B | \tilde{N}_o, \tilde{\xi}_A, \tilde{\xi}_B \right) = p_{N_A} \left(N_A | \tilde{N}_o, \tilde{\xi}_A \right) p_{N_B} \left(N_B | \tilde{N}_o, \tilde{\xi}_B \right) \quad (\text{C.1.10})$$

where

$$p_{N_A} \left(N_A | \tilde{N}_o, \tilde{\xi}_A \right) = p_{N_{1,A}} \left(N_A | \tilde{\xi}_{1,A} \right) * p_{N_{2,A}} \left(N_A | \tilde{\xi}_{2,A} \right) * \dots * p_{N_{\tilde{N}_o,A}} \left(N_A | \tilde{\xi}_{\tilde{N}_o,A} \right) \quad (\text{C.1.11})$$

where a similar expression exists for $p_{N_B}(N_B | \tilde{N}_o, \tilde{\xi}_B)$. Combining the previous two equations yields

$$\begin{aligned} p_{N_A, N_B} \left(N_A, N_B | \tilde{N}_o, \tilde{\xi}_A, \tilde{\xi}_B \right) &= \left[p_{N_{1,A}} \left(N_A | \tilde{\xi}_{1,A} \right) p_{N_{1,B}} \left(N_B | \tilde{\xi}_{1,B} \right) \right] \\ &* \left[p_{N_{2,A}} \left(N_A | \tilde{\xi}_{2,A} \right) p_{N_{2,B}} \left(N_B | \tilde{\xi}_{2,B} \right) \right] \\ &\dots * \left[p_{N_{\tilde{N}_o,A}} \left(N_A | \tilde{\xi}_{\tilde{N}_o,A} \right) p_{N_{\tilde{N}_o,B}} \left(N_B | \tilde{\xi}_{\tilde{N}_o,B} \right) \right]. \end{aligned} \quad (\text{C.1.12})$$

Since $\{\tilde{N}_{j,A}, j = 1.. \tilde{N}_o\}$ are identically distributed RVs, the above expression reduces to

$$\begin{aligned} p_{N_A, N_B} \left(N_A, N_B | \tilde{N}_o, \tilde{\xi}_A, \tilde{\xi}_B \right) &= \left[p_{N_A^1} \left(N_A | \tilde{\xi}_A \right) p_{N_B^1} \left(N_B | \tilde{\xi}_B \right) \right] \\ &*^{\tilde{N}_o-1} \left[p_{N_A^1} \left(N_A | \tilde{\xi}_A \right) p_{N_B^1} \left(N_B | \tilde{\xi}_B \right) \right] \end{aligned} \quad (\text{C.1.13})$$

where $p_{N_A^1}(N_A | \tilde{\xi}_A)$ and $p_{N_B^1}(N_B | \tilde{\xi}_B)$ represent the PDFs of \tilde{N}_A and \tilde{N}_B , respectively, for one quantum input to the parallel cascade, and $[p_{N_A^1}(N_A | \tilde{\xi}_A) p_{N_B^1}(N_B | \tilde{\xi}_B)] *^{\tilde{N}_o-1} [p_{N_A^1}(N_A | \tilde{\xi}_A) p_{N_B^1}(N_B | \tilde{\xi}_B)]$ represents a two-dimensional convolution of $p_{N_A^1}(N_A | \tilde{\xi}_A) p_{N_B^1}(N_B | \tilde{\xi}_B)$ with itself $\tilde{N}_o - 1$ times.

C.1.1.2 Joint PDF of quantum-labelled parallel cascades

In many situations, the parameters describing the individual process (eg. gain or selection) in Fig. 4.2.3 are themselves functions of some RV associated with each quantum input to that process. This idea was introduced by Van Metter and Rabbani^[125] who called these input-labelled random processes. We adopt this idea to describe the depth-dependent collection efficiency in the top shaded path of Fig. 4.2.5 where we let the interaction depth \tilde{z}_1 be a RV with the appropriate exponential PDF. However, in the lower shaded box of Fig. 4.2.5 all processes are functions of either depth \tilde{z}_1 and/or scatter angle $\tilde{\theta}$. In addition, these processes are coupled because they are dependent on the same \tilde{z}_1 and $\tilde{\theta}$ for each individual interacting photon. We generalize the previous derivation to include the description of these input-labelled parallel processes.

We let $\tilde{\mathbf{b}}_j = [\tilde{b}_{j,1} \tilde{b}_{j,1} \dots \tilde{b}_{j,m}]$ be a $1 \times m$ random vector with components representing input parameters associated with the j th input quantum. We let $p_{\mathbf{b}}(\mathbf{b}_j) = p_{\mathbf{b}}(b_{j,1}, b_{j,2}, \dots, b_{j,m})$ represent the joint PDF of $\tilde{b}_{j,1} \tilde{b}_{j,1} \dots \tilde{b}_{j,m}$. The number of input parameters m is determined from the physical situation being described. For example, in the case of photoelectric interactions, the characteristic reabsorption probability depends on both the angle of characteristic emission $\tilde{\theta}$ and the depth of interaction \tilde{z}_1 , the number of collected secondaries also depends on the depth of interaction, and therefore $m = 2$. The set of input parameters for one quantum is independent of those for another quantum and, therefore, similar to the derivation above, the PDF of \tilde{N}_A and \tilde{N}_B given \tilde{N}_o , $\tilde{\xi}_A$, $\tilde{\xi}_B$, and $\{\tilde{\mathbf{b}}_j, j = 1.. \tilde{N}_o\}$ is given by

$$p_{N_A, N_B} \left(N_A, N_B | \tilde{N}_o, \tilde{\xi}_A, \tilde{\xi}_B, \{\tilde{\mathbf{b}}_j, j = 1.. \tilde{N}_o\} \right) = p_{N_A} \left(N_A | \tilde{N}_o, \tilde{\xi}_A, \tilde{\xi}_B, \{\tilde{\mathbf{b}}_j, j = 1.. \tilde{N}_o\} \right) \\ \times p_{N_B} \left(N_B | \tilde{N}_o, \tilde{\xi}_A, \tilde{\xi}_B, \{\tilde{\mathbf{b}}_j, j = 1.. \tilde{N}_o\} \right) \quad (\text{C.1.14})$$

where

$$p_{N_A} \left(N_A | \tilde{N}_o, \tilde{\xi}_A, \tilde{\xi}_B, \{\tilde{\mathbf{b}}_j, j = 1.. \tilde{N}_o\} \right) = p_{N_{1,A}} \left(N_A | \tilde{\xi}_{1,A}, \tilde{\mathbf{b}}_1 \right) * p_{N_{2,A}} \left(N_A | \tilde{\xi}_{2,A}, \tilde{\mathbf{b}}_2 \right) * \dots \\ \dots * p_{N_{\tilde{N}_o,A}} \left(N_A | \tilde{\xi}_{\tilde{N}_o,A}, \tilde{\mathbf{b}}_{\tilde{N}_o} \right). \quad (\text{C.1.15})$$

Combining with $p_{N_A}(N_A | \tilde{N}_o, \tilde{\xi}_A, \tilde{\xi}_B, \{\tilde{\mathbf{b}}_j, j = 1.. \tilde{N}_o\})$ and averaging over all possible values of $\tilde{\xi}_A$,

$\tilde{\xi}_B$, and $\{\tilde{\mathbf{b}}_j, j = 1..N_o\}$ yields

$$p_{N_A, N_B}(N_A, N_B | \tilde{N}_o) = \left\langle \left\langle p_{N_A^1}(N_A | \xi_A, \mathbf{b}) p_{N_B^1}(N_B | \xi_B, \mathbf{b}) \right\rangle_{\mathbf{b}} \right\rangle_{\xi_A, \xi_B} \\ *^{N_o-1} \left\langle \left\langle p_{N_A^1}(N_A | \xi_A, \mathbf{b}) p_{N_B^1}(N_B | \xi_B, \mathbf{b}) \right\rangle_{\mathbf{b}} \right\rangle_{\xi_A, \xi_B} \quad (\text{C.1.16})$$

where $p_{N_A^1}(N_A | \xi_A, \mathbf{b})$ and $p_{N_B^1}(N_B | \xi_B, \mathbf{b})$ represent the PDFs of \tilde{N}_A and \tilde{N}_B given $\xi_{j,A}$, $\xi_{j,B}$, and \mathbf{b}_j , for one quantum input to the parallel cascade, and

$$\left\langle p_{N_A^1}(N_A | \xi_A, \mathbf{b}) p_{N_B^1}(N_B | \xi_B, \mathbf{b}) \right\rangle_{\mathbf{b}} = \int p_{N_A^1}(N_A | \xi_A, \mathbf{b}) p_{N_B^1}(N_B | \xi_B, \mathbf{b}) p_{\mathbf{b}}(\mathbf{b}) d^m \mathbf{b} \quad (\text{C.1.17})$$

where $p_{\mathbf{b}}(\mathbf{b}_j) = p_{\mathbf{b}}(\mathbf{b})$ is independent of j . Averaging over all possible values of \tilde{N}_o yields

$$p_{N_A, N_B}(N_A, N_B) = \int \left[\left\langle \left\langle p_{N_A^1}(N_A | \xi_A, \mathbf{b}) p_{N_B^1}(N_B | \xi_B, \mathbf{b}) \right\rangle_{\mathbf{b}} \right\rangle_{\xi_A, \xi_B} \right. \\ \left. *^{N_o-1} \left\langle \left\langle p_{N_A^1}(N_A | \xi_A, \mathbf{b}) p_{N_B^1}(N_B | \xi_B, \mathbf{b}) \right\rangle_{\mathbf{b}} \right\rangle_{\xi_A, \xi_B} \right] p_o(N_o) dN_o. \quad (\text{C.1.18})$$

The above equation is a generic expression for the joint PDF of quanta from two parallel paths when elementary processes in each path depend on a number of input parameters $\tilde{\mathbf{b}}$.

C.2 PDF of number of quanta for a generalized interaction model

In this section we calculate the PDF of the total number of quanta for the generalized interaction model illustrated in Fig. 4.2.5. This model is used to describe energy deposition, conversion to secondary quanta, and collection of secondary quanta for both photoelectric and incoherent interactions. We let \tilde{N}_A , \tilde{N}_B , and \tilde{N}_C represent the number of quanta for top, middle, and bottom paths of Fig. 4.2.5, respectively, $\tilde{N}_{B+C} = \tilde{N}_B + \tilde{N}_C$, and $\tilde{N}_t = \tilde{N}_A + \tilde{N}_{B+C}$ represent the total number of quanta for interaction type t . We calculate $p_{N_t}(N_t)$ for one incident quantum, that is $p_{N_o}(N_o) = \delta(N_o - 1)$.

The first branching point in Fig. 4.2.5 represents separation of interacting photons that produce a fluorescent/scatter photon (paths B and C) from those that do not (path A). This process represents

a Bernoulli branch, and, therefore, the PDF of \tilde{N}_t can be calculated using Eq. (4.2.22):

$$p_{N_t}(N_t) = (1 - S_t) p_{N_A}(N_t | \tilde{S}_t = 0) + S_t p_{N_{B+C}}(N_t | \tilde{S}_t = 1) \quad (\text{C.2.1})$$

where $S_t = \tilde{S}_t$ represents the probability that a scatter/emission photon is generated, $p_{N_A}(N_A | \tilde{S}_t = 0)$ represents the PDF of \tilde{N}_A given no scatter/emission photon, and $p_{N_{B+C}}(N_{B+C} | \tilde{S}_t = 1)$ represents the PDF of \tilde{N}_{B+C} given a scatter/emission photon. Since the collection efficiency in path A is a function of interaction depth, and each process in paths B and C may be functions of interaction depth and fluorescent/scatter emission angle, calculation of $p_{N_A}(N_A | \tilde{S}_t = 0)$ and $p_{N_{B+C}}(N_{B+C} | \tilde{S}_t = 1)$ requires use of the joint PDF for quantum-labelled parallel processes derived above.

C.2.1 PDF of \tilde{N}_A

Path A describes the case where no scatter/emission photon is produced and all the energy of an interacting photon is deposited at the primary interaction site. In this case, $p_{N_A}(N_A | \tilde{S}_t = 0)$ can be obtained using Eq. (4.2.18):

$$p_{N_A}(N_A | \tilde{S}_t = 0) = \int p_{N_{A,0}}(N_{A,0} | \tilde{S}_t = 0) \int p_{N_{A,1}}(N_{A,1} | N_{A,0}) p_{N_{A,2}}(N_A | N_{A,1}) dN_{A,0} dN_{A,1} \quad (\text{C.2.2})$$

where $p_{N_{A,0}}(N_{A,0} | \tilde{S}_t = 0) = \delta(N_{A,0} - 1)$ and therefore

$$p_{N_A}(N_A | \tilde{S}_t = 0) = \int p_{N_{A,1}}(N_{A,1} | N_{A,0} = 1) p_{N_{A,2}}(N_A | N_{A,1}) dN_{A,1}. \quad (\text{C.2.3})$$

C.2.1.1 Conversion to secondary quanta

The first process after the Bernoulli branch in path A represents conversion to secondary quanta at the primary interaction site. This is described using the PDF transfer relationship for a quantum gain stage. Therefore

$$p_{N_A}(N_A | \tilde{S} = 0) = \int p_{g_A}(N_{A,1}) p_{N_{A,2}}(N_A | N_{A,1}) dN_{A,1} \quad (\text{C.2.4})$$

where $p_{g_A}(N_{A,1}) = p_{g_A}(g_A)|_{g_A=N_{A,1}}$ where $p_{g_A}(g_A)$ represents the PDF describing all possible gain values \tilde{g}_A and is given by Eqs. (4.2.8), (4.2.9), and (4.2.10) for Poisson, Gaussian, and deterministic

gain, respectively. In this work we assume that \tilde{g}_A is Poisson-distributed with mean $\bar{g} = E/w$ where E is the incident photon energy and w is the energy required to liberate one electron-hole pair.

C.2.1.2 Depth-dependent collection of secondary quanta

The second process in path A represents depth-dependent collection of secondary quanta and is characterized by a Bernoulli selection variable that takes on values of either zero or one with probabilities that depend on the depth of primary photon interaction \tilde{z}_1 . Transfer of the PDF through depth-dependent collection processes has recently been described,^[194] giving

$$p_{N_{A,2}}(N_A | N_{A,1}) = \int \mathcal{B}(N_A; N_{A,1}, \beta(z_1)) p_{z_1}(z_1) dz_1 \quad (\text{C.2.5})$$

where $\mathcal{B}(N_A; N_{A,1}, \beta(z_1))$ represents the binomial distribution with number of trials $N_{A,1}$ and probability of success $\beta(z_1)$ equal to the collection efficiency, and $p_{z_1}(z_1)$ represents the PDF of \tilde{z}_1 . Combining the previous two equations yields

$$p_{N_A}(N_A | \tilde{S} = 0) = \int p_{g_A}(N_{A,1}) \int \mathcal{B}(N_A; N_{A,1}, \beta(z_1)) p_{z_1}(z_1) dz_1 dN_{A,1}. \quad (\text{C.2.6})$$

C.2.2 PDF of $\tilde{N}_B + \tilde{N}_C$

In the case that a characteristic/scatter photon is generated, energy may be deposited at primary (path B) and secondary (path C) absorption sites as illustrated Fig. 4.2.5. The branch point separating paths B and C represents a cascade fork. All subsequent processes may be functions of interaction depth or emission/scatter angle or both, and therefore, from Eqs. (4.2.25) and (C.1.18), $p_{N_{B+C}}(N_{B+C} | \tilde{S}_t = 1)$ is given by

$$p_{N_{B+C}}(N_{B+C} | \tilde{S}_t = 1) = \left\langle p_{N_B}(N_{B+C} | \tilde{S}_t = 1, \mathbf{b}) * p_{N_C}(N_{B+C} | \tilde{S}_t = 1, \mathbf{b}) \right\rangle_{\mathbf{b}} \quad (\text{C.2.7})$$

where $\tilde{\mathbf{b}} = [\tilde{z}_1, \tilde{\theta}]$. In the following sections we calculate $p_{N_B}(N_B | \tilde{S}_t = 1, \mathbf{b})$ and $p_{N_C}(N_C | \tilde{S}_t = 1, \mathbf{b})$ for fixed $\tilde{\mathbf{b}} = [\tilde{z}_1, \tilde{\theta}]$ and then average over all possible values of $\tilde{\mathbf{b}} = [\tilde{z}_1, \tilde{\theta}]$ to get $p_{N_{B+C}}(N_{B+C} | \tilde{S}_t = 1)$. Averaging over all possible values of $[\tilde{z}_1, \tilde{\theta}]$ requires the joint PDF of \tilde{z}_1 and $\tilde{\theta}$, $p_{z_1, \theta}(z_1, \theta)$.

C.2.2.1 PDF of \tilde{N}_B for fixed \tilde{z}_1 and $\tilde{\theta}$

There are two processes following the cascade fork in Path B of Fig. 4.2.3. The first process represents conversion to secondary quanta at the primary interaction site and the second process represents depth-dependent collection of secondary quanta. In the case of incoherent interactions, the energy deposited at the primary interaction site is a function of the random scatter angle $\tilde{\theta}$. Therefore, from Eq. (4.2.18), $p_{N_B}(N_B|\tilde{S}_t = 1, \tilde{z}_1, \tilde{\theta})$ is given by

$$p_{N_B}(N_B|\tilde{S}_t = 1, \tilde{z}_1, \tilde{\theta}) = \int p_{N_{B,0}}(N_{B,0}|\tilde{S}_t = 1) \quad (\text{C.2.8})$$

$$\times \int p_{N_{B,1}}(N_{B,1}|N_{B,0}, \tilde{\theta}) p_{N_{B,2}}(N_B|N_{B,1}, \tilde{z}_1) dN_{B,1} dN_{B,0} \quad (\text{C.2.9})$$

where $p_{N_{B,0}}(N_{B,0}|\tilde{S} = 1) = \delta(N_{B,0} - 1)$:

$$p_{N_B}(N_B|\tilde{S}_t = 1, \tilde{z}_1, \tilde{\theta}) = \int p_{N_{B,1}}(N_{B,1}|N_{B,0} = 1, \tilde{\theta}) p_{N_{B,2}}(N_B|N_{B,1}, \tilde{z}_1) dN_{B,1} \quad (\text{C.2.10})$$

Conversion to secondary quanta at primary interaction site The first process following the cascade fork in path B represents conversion to secondary quanta at the primary interaction site. Therefore, similar to Eq. (C.2.4):

$$p_{N_B}(N_B|\tilde{S}_t = 1, \tilde{z}_1, \tilde{\theta}) = \int p_{g_B}(N_{B,1}; \tilde{\theta}) p_{N_{B,2}}(N_B|N_{B,1}, \tilde{z}_1) dN_{B,1} \quad (\text{C.2.11})$$

where $p_{g_B}(g_B; \tilde{\theta})$ represents the PDF of \tilde{g}_B for scatter/emission photon angle $\tilde{\theta}$. Similar to \tilde{g}_A , we assume \tilde{g}_B is Poisson-distributed with mean value $\bar{g}_B = (E - E'(\theta))/w$ where $E'(\theta)$ is the fluorescent/scatter photon energy for emission angle θ . Note that in the case of photoelectric interactions the fluorescent photon energy is independent of scatter angle.

Depth-dependent collection of secondary quanta For fixed \tilde{z}_1 , $p_{N_{B,2}}(N_B|N_{B,1}, \tilde{z}_1)$ is given by the binomial distribution^[193-195]

$$p_{N_{B,2}}(N_B|N_{B,1}, \tilde{z}_1) = \mathcal{B}(N_B; N_{B,1}, \beta(\tilde{z}_1)). \quad (\text{C.2.12})$$

Combining the previous two equations yields

$$p_{N_B} \left(N_B | \tilde{S}_t = 1, \tilde{z}_1, \tilde{\theta} \right) = \int p_{g_B} \left(N_{B,1}; \tilde{\theta} \right) \mathcal{B} \left(N_B; N_{B,1}, \beta \left(\tilde{z}_1 \right) \right) dN_{B,1}. \quad (\text{C.2.13})$$

C.2.2.2 PDF of \tilde{N}_C for fixed \tilde{z}_1 and $\tilde{\theta}$

There are three processes following the cascade fork in Path C of Fig. 4.2.3. Therefore, from Eq. (4.2.18), $p_{N_C}(N_C | \tilde{S}_t = 1, \tilde{z}_1, \tilde{\theta})$ is given by

$$\begin{aligned} p_{N_C} \left(N_C | \tilde{S}_t = 1, \tilde{z}_1, \tilde{\theta} \right) &= \int p_{N_{C,0}} \left(N_{C,0} | \tilde{S}_t = 1 \right) \int p_{N_{C,1}} \left(N_{C,1} | N_{C,0}, \tilde{\theta}, \tilde{z}_1 \right) \\ &\quad \times \int p_{N_{C,2}} \left(N_{C,2} | N_{C,1}, \tilde{\theta} \right) p_{N_{C,3}} \left(N_C | N_{C,2}, \tilde{z}_1 \right) dN_{C,2} dN_{C,1} dN_{C,0} \end{aligned} \quad (\text{C.2.14})$$

where $p_{N_{C,0}} \left(N_{C,0} | \tilde{S}_t = 1 \right) = \delta(N_{C,0} - 1)$. Therefore

$$\begin{aligned} p_{N_C} \left(N_C | \tilde{S}_t = 1, \tilde{z}_1, \tilde{\theta} \right) &= \int p_{N_{C,1}} \left(N_{C,1} | N_{C,0} = 1, \tilde{\theta}, \tilde{z}_1 \right) \\ &\quad \times \int p_{N_{C,2}} \left(N_{C,2} | N_{C,1}, \tilde{\theta} \right) p_{N_{C,3}} \left(N_C | N_{C,2}, \tilde{z}_1, \tilde{\theta} \right) dN_{C,2} dN_{C,1}. \end{aligned} \quad (\text{C.2.15})$$

Reabsorption of fluorescent/scatter photon The first process following the cascade fork in Path C of Fig. (4.2.5) represents selection of fluorescent/scatter photons that are reabsorbed in the x-ray convertor material. Therefore $p_{N_{C,1}}(N_{C,1} | N_{C,0} = 1, \tilde{\theta}, \tilde{z}_1)$ is equal to the Binomial distribution with 1 trial and probability of success equal to the reabsorption probability $f_t(\tilde{\theta}, \tilde{z}_1)$. Therefore^[195]

$$p_{N_{C,1}} \left(N_{C,1} | N_{C,0} = 1, \tilde{\theta}, \tilde{z}_1 \right) = \left[1 - f_t \left(\tilde{\theta}, \tilde{z}_1 \right) \right] \delta \left(N_{C,1} \right) + f_t \left(\tilde{\theta}, \tilde{z}_1 \right) \delta \left(N_{C,1} - 1 \right) \quad (\text{C.2.16})$$

Combining the previous two equations yields

$$\begin{aligned} p_{N_C} \left(N_C | \tilde{S}_t = 1, \tilde{z}_1, \tilde{\theta} \right) &= \left[1 - f_t \left(\tilde{\theta}, \tilde{z}_1 \right) \right] \int p_{N_{C,2}} \left(N_{C,2} | N_{C,1} = 0, \tilde{\theta} \right) p_{N_{C,3}} \left(N_C | N_{C,2}, \tilde{z}_1 \right) dN_{C,2} \\ &\quad + f_t \left(\tilde{\theta}, \tilde{z}_1 \right) \int p_{N_{C,2}} \left(N_{C,2} | N_{C,1} = 1, \tilde{\theta} \right) p_{N_{C,3}} \left(N_C | N_{C,2}, \tilde{z}_1, \tilde{\theta} \right) dN_{C,2} \end{aligned} \quad (\text{C.2.17})$$

where $\int p_{N_{C,2}}(N_{C,2}|N_{C,1} = 0)p_{N_{C,3}}(N_C|N_{C,2})dN_{C,2} = \delta(N_C)$. Therefore

$$p_{N_C} \left(N_C | \tilde{S}_t = 1, \tilde{z}_1, \tilde{\theta} \right) = \left[1 - f_t \left(\tilde{\theta}, \tilde{z}_1 \right) \right] \delta(N_C) + f_t \left(\tilde{\theta}, \tilde{z}_1 \right) \int p_{N_{C,2}} \left(N_{C,2} | N_{C,1} = 1, \tilde{\theta} \right) p_{N_{C,3}} \left(N_C | N_{C,2}, \tilde{z}_1, \tilde{\theta} \right) dN_{C,2}. \quad (\text{C.2.18})$$

Conversion to secondary quanta at reabsorption site The second process following the cascade fork in path C represents conversion to secondary quanta at the reabsorption site. Therefore, similar to Eqs. (C.2.4) and (C.2.11),

$$p_{N_C} \left(N_C | \tilde{S}_t = 1, \tilde{z}_1, \tilde{\theta} \right) = \left[1 - f_t \left(\tilde{\theta}, \tilde{z}_1 \right) \right] \delta(N_C) + f_t \left(\tilde{\theta}, \tilde{z}_1 \right) \int p_{g_C} \left(N_{C,2}; \tilde{\theta} \right) p_{N_{C,3}} \left(N_C | N_{C,2}, \tilde{z}_1, \tilde{\theta} \right) dN_{C,2} \quad (\text{C.2.19})$$

where $p_{g_C}(g_C; \tilde{\theta})$ represents the PDF of \tilde{g}_C for fluorescent/scatter angle $\tilde{\theta}$ where $\tilde{g}_C = E'(\theta)/w$. Similar to \tilde{g}_A and \tilde{g}_B , we assume that \tilde{g}_C is Poisson-distributed.

Depth-dependent collection of secondary quanta at reabsorption site The third process following the cascade fork in Path C represents depth-dependent collection of secondary quanta. We let $p_{z_2}(z_2|\tilde{z}_1, \theta)$ represent the PDF of reabsorption depth \tilde{z}_2 given primary interaction depth \tilde{z}_1 and emission angle $\tilde{\theta}$. Using the PDF transfer relationship for depth-dependent collection efficiency,^[194] $p_{N_{C,3}}(N_C|N_{C,2}, \tilde{z}_1, \tilde{\theta})$ is given by

$$p_{N_{C,3}} \left(N_C | N_{C,2}, \tilde{z}_1, \tilde{\theta} \right) = \int \mathcal{B}(N_C; g_C, \beta(z_2)) p_{z_2} \left(z_2 | \tilde{z}_1, \tilde{\theta} \right) dz_2. \quad (\text{C.2.20})$$

Therefore

$$p_{N_C} \left(N_C | \tilde{S}_t = 1, \tilde{z}_1, \tilde{\theta} \right) = \left[1 - f_t \left(\tilde{\theta}, \tilde{z}_1 \right) \right] \delta(N_C) + f_t \left(\tilde{\theta}, \tilde{z}_1 \right) \left[\int p_{g_C} \left(N_{C,2}; \tilde{\theta} \right) \times \int \mathcal{B}(N_C; g_C, \beta(z_2)) p_{z_2} \left(z_2 | \tilde{z}_1, \tilde{\theta} \right) dz_2 dN_{C,2} \right] \quad (\text{C.2.21})$$

C.2.2.3 PDF of $\tilde{N}_B + \tilde{N}_C$

Combining Eqs. (C.2.7), (C.2.13), and (C.2.21) yields

$$p_{B+C} \left(N_{B+C} | \tilde{S} = 1 \right) = \langle (1-f) \mathcal{B}_B(N_{B+C}; \beta) \rangle_{z_1, \theta} + \langle f \mathcal{B}_B(N_{B+C}; \beta) * \langle \mathcal{B}_C(N_{B+C}; \beta) \rangle_{z_2} \rangle_{z_1, \theta} \quad (\text{C.2.22})$$

where $\mathcal{B}_B(N_B; \beta)$ and $\mathcal{B}_C(N_C; \beta)$ are given by Eqs. (4.2.35) and (4.2.36), respectively.

C.2.3 PDF of $\tilde{N}_t = \tilde{N}_A + \tilde{N}_B + \tilde{N}_C$

Combining Eqs. (C.2.1), (C.2.6), and (C.2.22) yields the PDF of the total number of quanta for the generic x-ray interaction model illustrated in Fig. (4.2.5)

$$p_t(N_t) = (1-S) \langle \mathcal{B}_A(N_t; \beta) \rangle_{z_1} + S \langle (1-f) \mathcal{B}_B(N_t; \beta) \rangle_{z_1, \theta} + S \langle f \mathcal{B}_B(N_t; \beta) * \langle \mathcal{B}_C(N_t; \beta) \rangle_{z_2} \rangle_{z_1, \theta}. \quad (\text{C.2.23})$$

C.3 PDF of reabsorption depth \tilde{z}_2

Calculation of the total number of quanta for the generic interaction model (Eq. (C.2.23)) requires the PDF of reabsorption depth \tilde{z}_2 given primary interaction depth \tilde{z}_1 and scatter angle $\tilde{\theta}$. Using a cylindrical coordinate system with origin at \tilde{z}_1 , $p_{z_2}(z_2 | z_1, \theta)$ is given by

$$p_{z_2} \left(z_2 | \tilde{z}_1, \tilde{\theta} \right) = \iint p_{z_2} \left(z_2, r, \phi | \tilde{z}_1, \tilde{\theta} \right) r dr d\phi \quad (\text{C.3.1})$$

where $p_{z_2}(z_2, r, \phi | z_1, \theta)$ represents the joint PDF of \tilde{z}_2 , \tilde{r} , and azimuthal angle $\tilde{\phi}$ (Fig.4.2.5) given \tilde{z}_1 and $\tilde{\theta}$ and is given by

$$p_{z_2} \left(z_2, r, \phi | \tilde{z}_1, \tilde{\theta} \right) = C \left(\tilde{z}_1, \tilde{\theta} \right) \mu(E_s) e^{-\mu(E_s) \sqrt{r^2 + (\tilde{z}_1 - z_2)^2}} \quad (\text{C.3.2})$$

where $C(\tilde{z}_1, \tilde{\theta})$ is a normalization constant that is a function of both \tilde{z}_1 and scatter angle $\tilde{\theta}$. Assuming the scatter photon is reabsorbed, $C(\tilde{z}_1, \tilde{\theta})$ is determined by requiring the integral of $p_{z_2}(z_2, r, \phi | \tilde{z}_1, \tilde{\theta})$

over a semi-infinite slab of thickness L to be unity for all \tilde{z}_1 and $\tilde{\theta}$:

$$C(\tilde{z}_1, \tilde{\theta})^{-1} = 2\pi \begin{cases} \int_{\tilde{z}_1}^L \int_0^{(L-\tilde{z}_1)|\tan\theta|} \mu(E_s) e^{-\mu(E_s)\sqrt{r^2+(\tilde{z}_1-z_2)^2}} r dr dz_2 & 0 \leq \theta < \pi/2 \\ \int_0^{\tilde{z}_1} \int_0^{\tilde{z}_1|\tan\theta|} \mu(E_s) e^{-\mu(E_s)\sqrt{r^2+(\tilde{z}_1-z_2)^2}} r dr dz_2 & \pi/2 \leq \theta < \pi \end{cases}. \quad (\text{C.3.3})$$

Appendix D

Supplemental material for Chapter 5

In the following sections the mean number of counts and covariance of counts detected in energy bins of EPC x-ray detectors is derived. The derivation presented below is similar to that recently derived for photon-counting detectors that implement a single threshold to distinguish x-ray interactions from electronic noise.

D.1 Energy-binned image signal for energy-resolving photon-counting x-ray detectors

Energy-resolved photon counting imaging is achieved by applying two thresholds to assign interacting photon energy to one of n energy bins for each fast readout of the detector. Ideally, each readout interval is short such that the probability of multiple photon interactions in the same element is small (i.e. $a_t \ll 1/\bar{q}_0 a$). Pile-up occurs when this condition is not satisfied, resulting in spectral distortion and a reduced detected count rate.^[100,217] In either case, for the j th readout of the detector, the number of photons detected in energy bin ν is a Bernoulli RV $\tilde{s}_{\nu,nm}^j$ having sample values of 1 or 0 where

$$\tilde{s}_{\nu,nm}^j = \begin{cases} 1 & \text{for } t_\nu \leq \tilde{d}_{nm}^j \leq t_{\nu+1} \\ 0 & \text{otherwise} \end{cases} \quad (\text{D.1.1})$$

where t_ν and $t_{\nu+1}$ represent lower and upper thresholds for bin ν . We assume a lag-free detector such that $\tilde{s}_{\nu,nm}^j$ and $\tilde{s}_{\nu,nm}^i$ are independent RVs for $i \neq j$ and define $\tilde{s}_\nu^{\dagger j}(\mathbf{r})$ [mm^{-2}] as the sampled

and thresholded image signal:

$$\tilde{s}_\nu^{\dagger j}(\mathbf{r}) = \tilde{s}_\nu^j(\mathbf{r}) \sum_{n=-\infty}^{\infty} \sum_{m=-\infty}^{\infty} \delta(\mathbf{r} - \mathbf{r}_{nm}) \quad (\text{D.1.2})$$

where $\tilde{s}_\nu^j(\mathbf{r})$ is a continuous presampling representation of $\tilde{s}_{\nu,nm}^j$. An SPC image is produced after M readouts using $\tilde{s}_{\nu,nm}^j$ to increment a counter for each element, resulting in image $\tilde{c}_\nu^\dagger(\mathbf{r})$:

$$\tilde{c}_\nu^\dagger(\mathbf{r}) = \sum_{j=1}^M \tilde{s}_\nu^{\dagger j}(\mathbf{r}) \quad (\text{D.1.3})$$

represented as a sequence of scaled δ -functions.

D.2 Mean energy-binned signals

The mean iamge signal from energy bin ν is given by

$$\text{E}\{\tilde{c}_\nu^\dagger(\mathbf{r})\} = \sum_{n=-\infty}^{\infty} \sum_{m=-\infty}^{\infty} \text{E}\{\tilde{c}_\nu(\mathbf{r})\} \delta(\mathbf{r} - \mathbf{r}_{nm}). \quad (\text{D.2.1})$$

Following the notation of Papoulis^[143] and Tanguay *et al.*,^[192] we let $p_{c_\nu}(c_\nu; \mathbf{r})$ represent the PDF of $\tilde{c}_\nu(\mathbf{r})$. Since \tilde{c} is equal to the summation of M Bernoulli RVs, the binomial distribution gives^[143,192]

$$\text{E}(\tilde{c}_\nu(\mathbf{r})) = M \text{P}(t_\nu \leq \tilde{d}(\mathbf{r}) \leq t_{\nu+1}) \quad (\text{D.2.2})$$

where $\text{P}()$ represents the probability of observing the specified event. Similar to the derivation presented by Tanguay *et al.*,^[192] the above equation is expressed as

$$\text{E}(\tilde{c}_\nu(\mathbf{r})) = \bar{c}_\nu = M \int_{t_\nu}^{t_{\nu+1}} p_d(d) dd. \quad (\text{D.2.3})$$

The above equation shows the expected result that the mean signal from an energy bin is shift invariant and, more importantly, can be determined from the PDF of \tilde{d} .

D.3 Covariance between EPC energy bins

The covariance between energy bins ν and ρ is generally expressed as

$$\text{Cov}(\tilde{c}_\nu(\mathbf{r}), \tilde{c}_\rho(\mathbf{r})) = \mathbb{E}(\tilde{c}_\nu(\mathbf{r})\tilde{c}_\rho(\mathbf{r})) - \mathbb{E}(\tilde{c}_\nu(\mathbf{r}))\mathbb{E}(\tilde{c}_\rho(\mathbf{r})) \quad (\text{D.3.1})$$

$$= \mathbb{E}(\tilde{c}_\nu(\mathbf{r})\tilde{c}_\rho(\mathbf{r})) - \bar{c}_\nu\bar{c}_\rho \quad (\text{D.3.2})$$

where \bar{c}_ν and \bar{c}_ρ are given by Eq. (D.2.3). The first term in the above equation is given by:

$$\mathbb{E}(\tilde{c}_\nu(\mathbf{r})\tilde{c}_\rho(\mathbf{r})) = \mathbb{E}\left(\sum_{i=1}^M \sum_{j=1}^M \tilde{s}_\nu^i(\mathbf{r}) \tilde{s}_\rho^j(\mathbf{r})\right) \quad (\text{D.3.3})$$

$$= \sum_{j=1}^M \mathbb{E}(\tilde{s}_\nu^j(\mathbf{r}) \tilde{s}_\rho^j(\mathbf{r})) + \sum_{i=1}^M \sum_{\substack{j=1 \\ j \neq i}}^M \mathbb{E}(\tilde{s}_\nu^i(\mathbf{r}) \tilde{s}_\rho^j(\mathbf{r})) \quad (\text{D.3.4})$$

where we have separated the double summation into terms for which $i = j$ and $i \neq j$, $\mathbb{E}\{\tilde{s}_\nu^i(\mathbf{r}) \tilde{s}_\rho^j(\mathbf{r})\} = \bar{s}_\nu\bar{s}_\rho$ and, since \tilde{d} is WSS,

$$\mathbb{E}(\tilde{s}_\nu^j(\mathbf{r}) \tilde{s}_\rho^j(\mathbf{r})) = \int_{-\infty}^{+\infty} \int_{-\infty}^{+\infty} s_\nu^j s_\rho^j p_s(s_\nu^j, s_\rho^j) ds_\nu^j ds_\rho^j \quad (\text{D.3.5})$$

where $p_s(s_\nu^j, s_\rho^j)$ represents the joint PDF^[143] for $s_\nu^j(\mathbf{r})$ and $s_\rho^j(\mathbf{r})$ and is the same for all j and independent of \mathbf{r} :

$$p_s(s_\nu^j, s_\rho^j) = \sum_{i=0}^1 \sum_{l=0}^1 \zeta_{il} \delta(s_\nu^j - i) \delta(s_\rho^j - l) \quad (\text{D.3.6})$$

where ζ_{il} represents the probability that $\tilde{s}_\nu^j(\mathbf{r})$ equals i and $\tilde{s}_\rho^j(\mathbf{r})$ equals l . Since a photon can only be counted in bin ν or bin ρ , $\mathbb{E}(\tilde{s}_\nu^j(\mathbf{r}) \tilde{s}_\rho^j(\mathbf{r}))$ is always equal to 0 $\nu \neq \rho$. For $\nu = \rho$, $\mathbb{E}(\tilde{s}_\nu^j(\mathbf{r}) \tilde{s}_\rho^j(\mathbf{r}))|_{\nu=\rho} = \mathbb{E}(\tilde{s}_\nu^j(\mathbf{r})) = \bar{s}_\nu$. Therefore

$$\mathbb{E}(\tilde{s}_\nu^j(\mathbf{r}) \tilde{s}_\rho^j(\mathbf{r})) = \begin{cases} 0 & \text{for } \nu \neq \rho \\ \bar{s}_\nu & \text{for } \nu = \rho \end{cases} . \quad (\text{D.3.7})$$

Combining this result with Eqs. (D.3.2) and (D.3.4), and assuming $M \gg 1$ yields

$$\text{Cov}(\tilde{c}_\nu, \tilde{c}_\rho) = \begin{cases} -M\bar{s}_\nu\bar{s}_\rho & \text{for } \nu \neq \rho \\ M\bar{s}_\nu & \text{for } \nu = \rho \end{cases} \quad (\text{D.3.8})$$

$$= \begin{cases} -\bar{c}_\nu\bar{c}_\rho \times \frac{1}{M} & \text{for } \nu \neq \rho \\ \bar{c}_\nu & \text{for } \nu = \rho \end{cases} \quad (\text{D.3.9})$$

where $\bar{s}_\nu = \int_{t_\nu}^{t_{\nu+1}} p_d(d) dd$.

Appendix E

Monte Carlo simulation of fundamental energy-resolution limits in energy-resolving photon-counting x-ray detectors

This chapter is adapted from a manuscript entitled “The role of x-ray Swank factor in energy-resolving photon-counting imaging” by Jesse Tanguay, Ho Kyung Kim, and Ian A. Cunningham, published in *Medical Physics* 2010; 37: 6205-6211.

E.1 Introduction

The prospect of single-photon counting (SPC) detectors for x-ray image acquisition has identified a number of benefits over the usual approach in which the detector signal is proportional to total energy deposited during an image-acquisition interval. [18,29,111,129,171,172,174,187,216] One exciting aspect is the potential for energy-resolved x-ray imaging where the energy of each interacting x-ray photon is estimated with the goal of determining the spectrum of interacting photons for each image pixel. Studies have shown that the use of energy-resolving photon-counting (EPC) detectors can increase the contrast-to-noise ratio of calcifications and iodine by 35% or more compared with energy integrating technologies while maintaining the same patient dose. [166,174] An important reason for this increase is the use of task-specific weighting factors that are applied to the detection of

each photon based on absorbed energy.^[166,167,196] In addition, these detectors allow for rejection of electronic noise through the use of thresholding techniques.

Energy-resolving detectors may also enable new advanced material-specific imaging such as angiography without requiring subtraction of a mask image.^[29,61,152,165,202] These methods exploit the K-edge discontinuity in the attenuation coefficient to enhance visualization of bone or administered contrast agents such as iodine and gadolinium, and their success will depend on how accurately photon energy can be determined.^[167,202,203] Even if energy measurements are separated into only two energy bins (one below and one above the K-edge energy for example), high-quality energy resolution is necessary for sharp energy-bin separation.^[152,202]

There are a number of challenges that must be overcome before the full benefits of EPC imaging can be achieved. For example, current prototype detectors cannot achieve the high count rates required for radiography. Also, variability in deposited photon energy due to random escape of Compton scatter and characteristic emissions will degrade the precision of energy measurements, and reabsorption will result in cross-talk between elements. Unlike isotope imaging where a photo-peak is often isolated to determine photon energy, use of a broad spectrum of x-ray energies makes it impossible to determine a photo-peak and the full energy of an interacting photon can only be determined by summing signals from all detector elements in which energy is deposited. This will require the use of fast coincidence detection algorithms, such as that implemented in the Medipix-3 prototype detector,^[18] so that scattered photons can be distinguished from independent low-energy photons. We imagine an “adaptive” binning approach in which the signal from a number of elements surrounding each interaction is summed. This would result in the benefits of large elements for energy measurements, without the corresponding loss of spatial resolution, although scatter escape from front or rear surfaces will continue to be a problem. Even without energy discrimination, coincident events must be recognized to avoid counting both an initial interaction and absorption of scatter to prevent double counting which would result in increased image noise and noise correlations between elements.^[4,126]

The importance of variations in deposited energy was first identified by Swank.^[184,185] He showed that the detective quantum efficiency (DQE) of a detector (termed “noise-equivalent absorption” by Swank) is degraded both by variations in the energy of incident x-ray quanta (the x-ray energy distribution, XED) and the fraction of that energy deposited in the detector. These two contributions are sometimes separated giving rise to an energy-dependent Swank factor^[184,185] $I(E)$ (also used by Tapiovaara and Wagner,^[196] Jaffray *et al.*,^[?]] Blevis *et al.*,^[25] and others) and a broad-spectrum

Swank factor^[184] I . In this article we use the energy-dependent form:

$$\text{DQE}(E) = \eta(E) I(E) \quad (\text{E.1.1})$$

where $\eta(E)$ is the energy-dependent detector quantum efficiency. Swank originally expressed $I(E)$ as a product of two factors, one associated with the absorbed-energy distribution I_{AED} ,^[77,78] now known as the x-ray Swank factor, and the other associated with the distribution of optical-pulse heights from a phosphor, I_{OPD} .^[57] In this article we consider only variations in deposited x-ray energy due to single photon interactions, and thus concern ourselves with only the energy-dependent x-ray Swank factor and its impact on EPC detectors. By ignoring I_{OPD} we are in effect assuming that the number of charges collected by the detector from each primary interaction is sufficiently large that statistical variations in this number (due to Poisson statistics for example) can be ignored, and that depth-dependent variation in the charge collection efficiency is small. This assumption will fail, and results presented here will understate imprecision in energy measurements, if the number of charges collected is small, corresponding to a large effective ionization energy of the converter material (W value), and at low x-ray energies. We are essentially assuming a small Fano factor value (used in the description of radiation detectors^[?]) and no “secondary quantum sink” problem^[53] caused by low conversion gain.

The energy-dependent x-ray Swank factor is given by:^[184,196?]

$$I(E) = \frac{M_1^2(E)}{M_0(E) M_2(E)} \quad (\text{E.1.2})$$

where M_n is the n -th moment of the absorbed energy distribution (AED), which describes the average distribution of deposited energies for an incident photon of energy E .^[?] We show here that the ability of an EPC detector to determine the energy of an interacting x-ray photon is determined largely by the x-ray Swank factor.

E.2 Theory: Energy imprecision of EPC x-ray detectors

X rays interact in the converter material of a detector with photoelectric interactions dominating in high- Z materials such as HgI_2 , and Compton scatter being important in low- Z materials such as Si. The deposited energy will be distributed over one or more near-by detector elements due to production and reabsorption of Compton scatter and characteristic emissions (electron path lengths

are normally very short compared to detector element sizes for diagnostic energies). As discussed in the introduction, it is assumed that some form of ideal adaptive binning is used such that the binned detector signal d is proportional to all energy deposited from one interaction.

It is convenient to describe the energy response of a detector in terms of its response function, $R(\varepsilon, E)$, similar to recent works.^[48,165,172,203] The response function gives the probability density (per keV) of depositing energy ε given an interacting photon with energy E . The n -th energy moment of $R(\varepsilon, E)$ is given by

$$\mathfrak{R}_n(E) = \int_0^\infty \varepsilon^n R(\varepsilon, E) d\varepsilon. \quad (\text{E.2.1})$$

The mean and variance in an energy measurement are therefore

$$\bar{\varepsilon} = \mathfrak{R}_1(E) \quad (\text{E.2.2})$$

and

$$\sigma_\varepsilon^2 = \mathfrak{R}_2(E) - \mathfrak{R}_1^2(E), \quad (\text{E.2.3})$$

respectively. The relative root-mean-square (RMS) measurement imprecision is given by the coefficient of variation, σ_{rel} :

$$\sigma_{rel} = \frac{\sigma_E}{\bar{E}} = \sqrt{\frac{\mathfrak{R}_2(E)}{\mathfrak{R}_1^2(E)} - 1}. \quad (\text{E.2.4})$$

The AED $A(\varepsilon, E)$ describes the probability that an incident photon having energy E interacts in the detector and deposits energy ε :

$$A(\varepsilon, E) = \eta(E) R(\varepsilon, E). \quad (\text{E.2.5})$$

The n -th energy moment of $A(\varepsilon, E)$ is therefore

$$M_n(E) = \int_0^\infty \varepsilon^n \eta(E) R(\varepsilon, E) d\varepsilon = \eta(E) \mathfrak{R}_n(E) \quad (\text{E.2.6})$$

and substituting Eq. (E.2.6) into Eq. (E.1.2) gives

$$I(E) = \frac{M_1^2(E)}{M_0(E) M_2(E)} = \frac{\mathfrak{R}_1^2(E)}{\mathfrak{R}_2(E)}. \quad (\text{E.2.7})$$

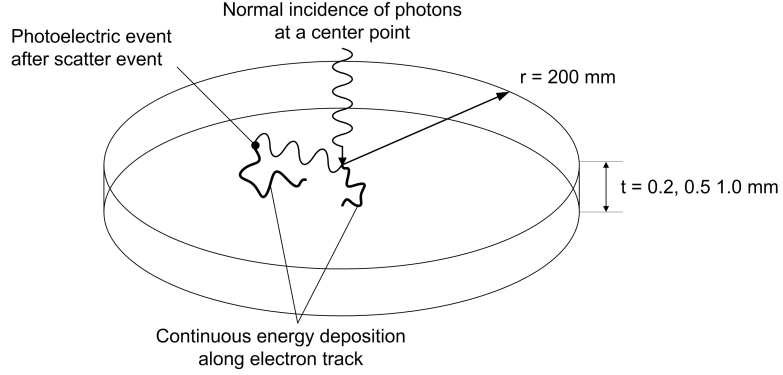


Figure E.3.1: Detector geometry modeled in the Monte Carlo calculations. The geometry simulates the large-area limit of a detector element. In this case, variability in deposited energy is a result of Compton scatter and characteristic x rays that escape through the top and bottom surfaces.

The second equality in the previous equation follows because the detector response function is normalized to unity ($\mathfrak{R}_0(E) = 1$). Combining Eqs. (E.2.4) and (E.2.7) yields

$$\sigma_{rel} = \sqrt{\frac{1}{I(E)} - 1}. \quad (\text{E.2.8})$$

This simple result is important because it shows that high-quality EPC imaging will require a high detector Swank factor, much like a high Swank factor is a requirement for obtaining a high DQE with conventional energy-integrating detectors. Eq. (E.2.8) is similar to a result described by Blevis *et al.*^[25] but from the perspective of energy measurements using EPC detectors.

E.3 Application to Common Detector Materials

The potential of common detector converter materials for precise energy measurements was determined by virtual pulse-height spectroscopy using Monte Carlo N-Particle transport simulations (MCNP Version 5, the Radiation Safety Information Computational Center or RSICC, Oak Ridge, TN, USA) to simulate the coupled photon-electron transport within *a*-Se, Si, CdZnTe, and HgI₂ detector converter materials (see Table E.1) for mono-energetic photon incidence. A single (large) detector element was modeled as a cylindrical slab with radius 20 cm as illustrated in Fig. E.3.1. A photon beam was incident normal to the detector at the center point of the top surface. This geometry prevents lateral escape of Compton scatter and characteristic emissions, allowing for escape in forward and reverse directions only, corresponding to the large-area limit of a detector element with the beam incident at the center. We considered interacting photon energies in the range 10 – 100 keV with 10⁷ photons per simulation.

Material	Atomic Number Z	Density (g/cm ³)	K-edge energy (keV)
<i>a</i> -Se	34	4.3	12.66
Si	14	2.3	1.84
Cd _{0.95} Zn _{0.05} Te	30(Zn), 48(Cd), 52(Te)	5.8	9.66(Zn), 26.71(Cd), 31.81(Te)
HgI ₂	80(Hg), 53(I)	6.3	83.10(Hg), 33.17(I)

Table E.1: Material properties used for the Monte Carlo calculations.

We applied a pulse-height tally, recording energy-absorption events due to every incident-photon interaction within the detector material. For incident photons of energy E , the Monte Carlo code provides the AED from which the energy moments can be determined. The Swank factor and relative imprecision are then calculated using Eq. (E.1.2) and (E.2.8).

The signal from EPC detectors will be proportional to energy deposited in the detector, $d = k\varepsilon$, where k is a constant that will be determined from a calibration (for example using the known photo-peak energies of one or two calibration sources similar to methods used in nuclear medicine and x-ray spectroscopy), and the relative accuracy of energy measurements is expressed as

$$\frac{\bar{d}}{d_0} = \frac{\bar{\varepsilon}}{E} = \frac{\mathfrak{R}_1(E)}{E} \quad (\text{E.3.1})$$

where d_0 is the photo-peak signal corresponding to an interacting photon with energy E . Relative imprecision in energy measurements, defined as the coefficient of variation in d , is given by

$$\frac{\sigma_d}{\bar{d}} = \frac{\sigma_\varepsilon}{\bar{\varepsilon}} = \sigma_{rel} \quad (\text{E.3.2})$$

where σ_{rel} is defined in Eq. (E.2.4) and (E.2.8).

E.4 Results

The response functions for a 100-keV photon incident on the center of 0.5-mm thick *a*-Se, Si, CdZnTe, and HgI₂ converter materials are shown in Fig. E.4.1. The key features are the photo-peak at $E = 100$ keV, K-escape peaks at $E - E_K$ and $E - 2E_K$, and a Compton edge at $2\alpha E / (1 + 2\alpha) = 28$ keV where $\alpha = E/m_o c^2$.^[17] The CdZnTe and HgI₂ results show additional escape peaks.

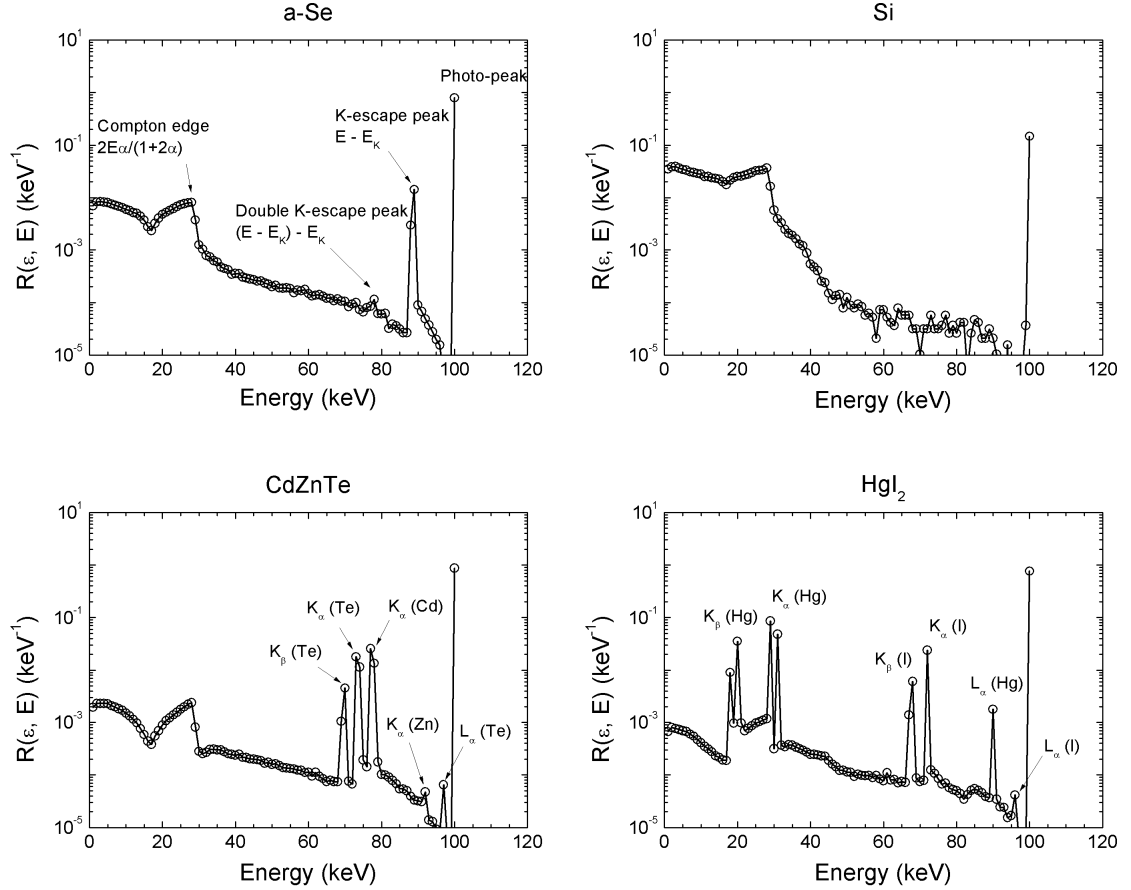


Figure E.4.1: The response functions $R(\varepsilon, E)$ for 0.5-mm thick *a*-Se, Si, CdZnTe, and HgI₂ detectors for 100-keV photons incident on the detector center as determined by Monte Carlo show the photo-peak at energy E , escape peaks and a Compton edge ($\alpha = E/m_0c^2$). A non-zero Fano factor would result in broadening of peaks in the response functions.

E.4.1 Relative energy accuracy

Results of the Monte Carlo calculation are shown in Fig. E.4.2. The left-most column shows relative energy accuracy based on Eq. (E.3.1) as a function of incident photon energy for each converter material with thicknesses of 0.2, 0.5, and 1.0 mm. These thicknesses and energies reflect those currently in use in many clinical systems and energy-resolving photon-counting systems under development.^[18,157] They do not, however, describe some novel designs such as strip-detectors using 1-3 cm of Si.^[16,29,31]

For the case of Si, relative accuracy shows a decrease as energy increases (and therefore the probability of Compton interactions and Compton-scatter escape), although the overall dependence of accuracy on converter thickness is modest as shown in Fig. E.4.2.

For the case of the high-Z materials (CdZnTe and HgI₂), relative accuracy is generally close to

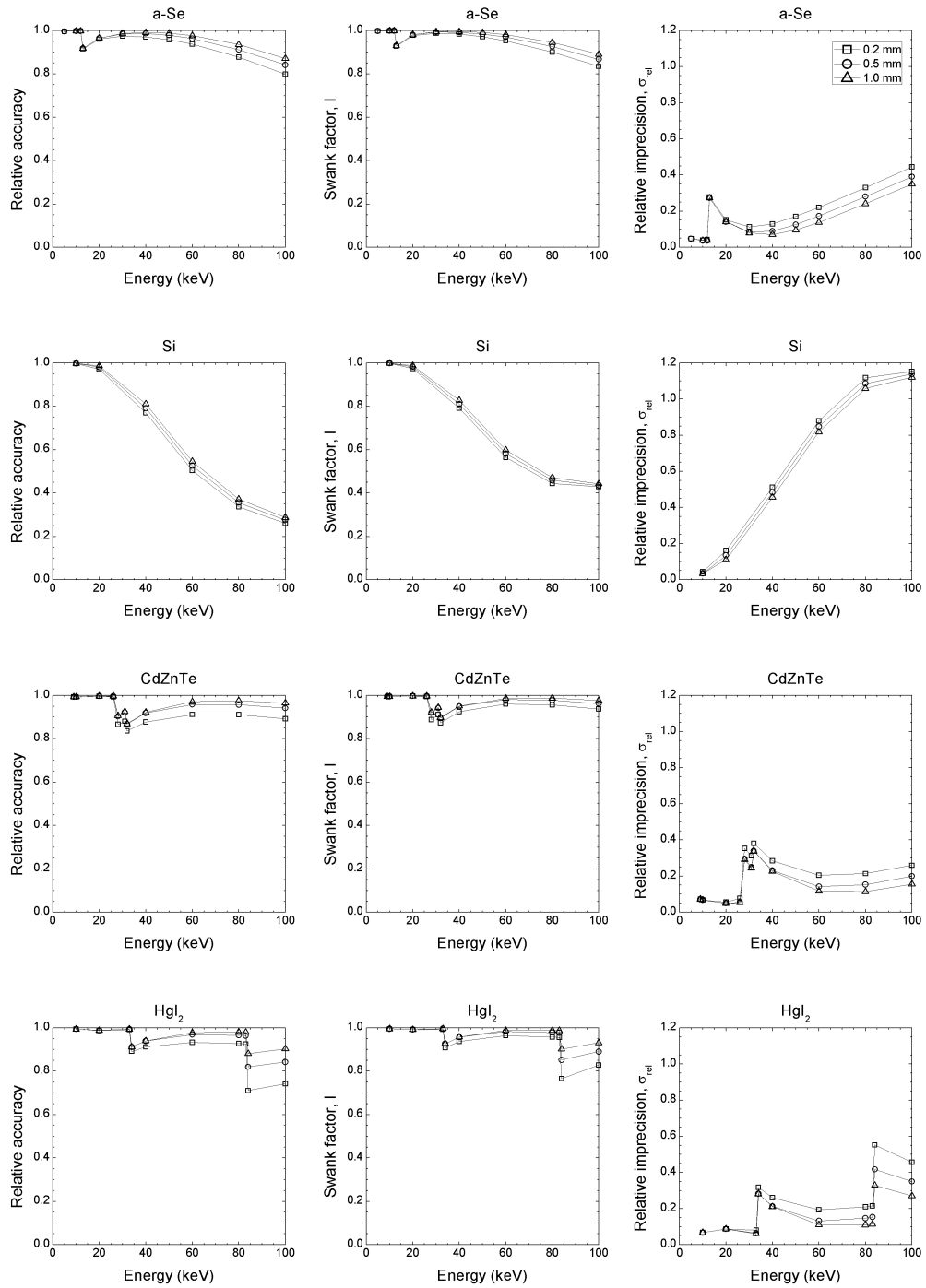


Figure E.4.2: Results of the Monte Carlo simulation. In the left, center and right columns are plots of the accuracy, Swank factor, and relative imprecision, respectively, as a function of incident photon energy for each detector material and thicknesses of 0.2 mm, 0.5 mm, and 1.0 mm.

unity below the K-edge energy for each material, although HgI₂ shows both K and L-edge effects. Above each edge, the potential for escape of characteristic emissions results in a drop in relative accuracy depending on escape probability. Above the K-edge energies, CdZnTe and HgI₂ show a greater dependence on thickness than Si.

The results for *a*-Se show trends similar to both Si and the high-Z materials. There is a sudden drop in relative accuracy at the K-edge energy and a continuous decrease in relative accuracy as the probability of Compton interactions increases.

E.4.2 Swank factor and relative energy imprecision

The Swank factor is shown in the center column of Fig. E.4.2. Below the K-edge energy for each material, the Swank factor is close to unity resulting in low relative imprecision. At energies above the K edge, the Swank factor decreases due to random escape of characteristic emissions and Compton scatter, with a corresponding increase in relative energy imprecision. While imprecision worsens with increasing energy, Compton scatter becomes important in *a*-Se and Si, resulting in a substantial increase in imprecision at the higher energies in Fig. E.4.2. For Si and *a*-Se the influence of converter thickness on relative energy imprecision is generally modest. For the high-Z materials the influence of converter thickness has a larger influence on relative imprecision. This is due to higher reabsorption probability for both characteristic and Compton x rays in the high-Z materials. In practice, a non-zero Fano factor would result in a broadening of peaks in the response functions (Fig. (E.4.1)) not shown here, and possibly an increase in imprecision.

E.5 Discussion

We have shown that while it is often (correctly) claimed that photon-counting detectors are insensitive to Swank noise, precision in energy measurements using EPC detectors *is* strongly linked to the energy-dependent x-ray Swank factor. Converter materials having a Swank factor close to unity (and low Fano factor) will tend to be the best materials for EPC detectors. However, this can be difficult to achieve. Even minor decreases in the Swank factor (eg. 5 - 15%) result in large increases in relative imprecision (30-40%). This relationship is shown explicitly in Fig. E.5.1 and underlies the critical need for a large Swank factor. If a specific imaging task requires a maximum relative imprecision σ_{max} , then Eq. (E.2.8) gives:

$$I \geq \frac{1}{\sigma_{max}^2 + 1}. \quad (\text{E.5.1})$$

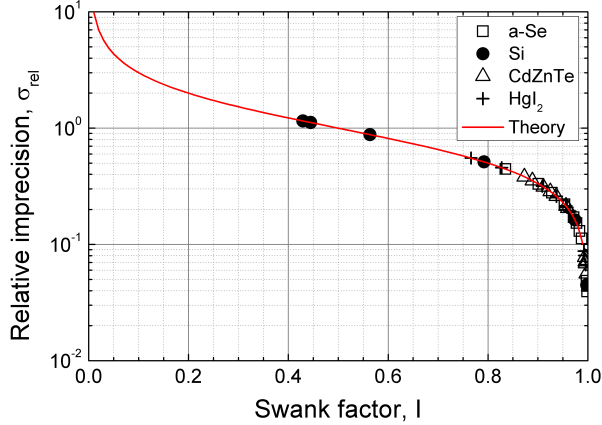


Figure E.5.1: A plot of the relationship between relative imprecision and the Swank factor given by Eq. (E.2.8) and compared with Monte Carlo results for 0.2-mm detector thickness. The multiple data points for each material correspond to the energies evaluated.

While the electrical properties of converter materials ignored in the Monte Carlo simulation (charge liberation and collection) will cause a broadening of peaks in the response function, ^[21,68,167] this will likely have minimal impact on the overall shape of the response and hence on the Swank factor. Regardless, it must be emphasized that unlike isotope imaging where a photo-peak can be isolated from a background of lower-energy events, photo-peak width is not as important as the Swank factor as a metric of performance for broad-spectrum imaging.

The Swank factor results presented here differ to some published values ^[25,45,46,57,77,78] due to our assumption of a large “binned” detector element with x rays incident at the center only. This reduces the effect of cross-talk between elements, corresponding to a true “zero-frequency” Swank factor, and will only be realized if some form of adaptive binned is implemented. The Medipix-3 prototype implements an early form of this binning. ^[18,126]

At mammographic energies (15 - 25 keV), relative energy RMS imprecision is 15-20% for *a*-Se, making it difficult to measure photon energy with imprecision less than 15%. A Si-based detector is only slightly better. Both CdZnTe and HgI₂-based detectors will have energy imprecision of 5-8%. For general radiography (near 60 keV), energy imprecision is 70-90% for Si, which may prohibit its use in energy-resolved imaging tasks at these energies. All of *a*-Se, CdZnTe, and HgI₂ have energy imprecision of 12-25% at 60 keV. It will therefore be very difficult to measure photon energy with imprecision less than 12% at general radiographic conditions. Similar observations can be made for energies typically used in chest radiography (80 keV), although HgI₂ will give 10 - 20% below 83 keV.

These results indicate that at most energies, it will be difficult to make accurate and precise measures of individual incident-photon energy. However, if only two energy bins are required for

an imaging task,^[202] then energy precision is only important near the boundary between bins. For example, *a*-Se has relatively good precision near 33 keV (iodine K-edge energy) and may be well suited for iodine-specific imaging. In general, spectral tailing caused by escape of scattered x rays causes the incident photon spectrum to be shifted towards lower energies and deconvolution methods, such as those implemented by the Medipix collaborators and others,^[29,128,145,165] may be an important part of accurate energy measurements.

E.6 Conclusions

Precision in photon-energy measurements by energy-resolving photon-counting (EPC) detectors is shown to depend directly on the energy-dependent x-ray Swank factor. A Swank factor value close to unity is known to be necessary to achieve a DQE value close to unity and it will continue to play a key role in EPC detectors. Even with the use of adaptive-binning algorithms to sum energy deposited in detector elements surrounding a primary interaction to estimate total deposited energy, it is shown that a modest decrease in the Swank factor (5 - 10%) due to characteristic emission and Compton scatter escape causes a large increase in relative energy imprecision (30 - 40%). The energy dependence of the x-ray Swank factor will therefore be an important consideration in determining the best detector material for a particular application. For example, CdZnTe and HgI₂ will result in better energy precision at mammographic energies than *a*-Se or Si-based detectors, while *a*-Se may be optimal for iodine-specific imaging (angiography) when good energy precision is required for minimizing cross-talk between energy bins near the iodine K-edge energy (34 keV).

Appendix F

Bibliography

- [1] Medical imaging - The assessment of image quality. ICRU 54, International Commission of Radiation Units and Measurements, 1995.
- [2] *Dorlands Illustrated Medical Dictionary 32nd Edition*. Saunders, 2011.
- [3] Herbert L. Abrams. History of cardiac radiology. *Am. J. Roentgenol.*, 167:431–438, 1996.
- [4] Raymond J Acciavatti and Andrew D. A. Maidment. An analytical model of NPS and DQE comparing photon counting and energy integrating detectors. *Proc. of SPIE*, 7622:76220I, 2010.
- [5] Raymond J. Acciavatti and D. A. Maidment. A comparative analysis of OTF, NPS, and DQE in energy integrating and photon counting digital x-ray detectors. *Med. Phys.*, 37:6480–6495, 2010.
- [6] Reza Akbarpour, Saul N Friedman, Jeffrey H Siewerdsen, John D Neary, and Ian A Cunningham. Signal and noise transfer in spatiotemporal quantum-based imaging systems. *J. Opt. Soc. Am. A Opt. Image Sci. Vis.*, 24(12):B151–B164, Dec 2007.
- [7] Adam M Alessio and Lawrence R MacDonald. Quantitative material characterization

- from multi-energy photon counting CT. *Med. Phys.*, 40(3):031108, Mar 2013. doi: 10.1118/1.4790692.
- [8] David A Alter, Peter Austin, and Jack V. Tu. *Institute for Clinical Evaluative Sciences Cardiovascular Atlas: Cardiovascular health and services in Ontario*, chapter 8: Use of coronary angiography, angioplasty, and bypass surgery after acute myocardial infarction in Ontario, pages 141–164. 1999.
- [9] Robert E Alvarez. Near optimal energy selective x-ray imaging system performance with simple detectors. *Med. Phys.*, 37(2):822–841, Feb 2010.
- [10] Robert E Alvarez. Estimator for photon counting energy selective x-ray imaging with multibin pulse height analysis. *Med. Phys.*, 38(5):2324–2334, May 2011.
- [11] Robert E. Alvarez and Albert Macovski. Energy-selective reconstructions in x-ray computerized tomography. *Phys. Med. Biol.*, 21:733–744, 1976.
- [12] S.R. Amendolia, E. Bertolucci, M.G. Bisogni, U. Bottigli, A. Ceccopieri, M.A. Ciocci, M. Conti, P. Delogu, M.E. Fantacci, P. Maestro, V. Marzulli, E. Pernigotti, N. Romeo, V. Rosso, P. Rosso, A. Stefanini, and S. Stumbo. Medipix: a vlsi chip for a gaas pixel detector for digital radiology. *Nucl. Inst. Meth. A*, 422:201–205, 1999.
- [13] Jeffrey L Anderson, Cynthia D Adams, Elliott M Antman, Charles R Bridges, Robert M Califf, Donald E Casey, William E Chavey, Francis M Fesmire, Judith S Hochman, Thomas N Levin, A. Michael Lincoff, Eric D Peterson, Pierre Theroux, Nanette Kass Wenger, R. Scott Wright, Sidney C Smith, Alice K Jacobs, Cynthia D Adams, Jeffrey L Anderson, Elliott M Antman, Jonathan L Halperin, Sharon A Hunt, Harlan M Krumholz, Frederick G Kushner, Bruce W Lytle, Rick Nishimura, Joseph P Ornato, Richard L Page, Barbara Riegel, American College of Cardiology, American Heart Association Task Force on Practice Guidelines (Writing Committee to Revise the 2002 Guidelines for the Management of Patients With Unstable Angina/Non-ST-Elevation Myocardial Infarction), American College of Emergency Physicians, Society for Cardiovascular Angiography, Interventions, Society of Thoracic Surgeons, American Association of Cardiovascular, Pulmonary Rehabilitation, and Society for Academic Emergency Medicine. Acc/aha 2007 guidelines for the management of patients with unstable angina/non-st-elevation myocardial infarction: a report of the american college of cardiology/american heart association task force on practice guidelines (writing committee to revise

the 2002 guidelines for the management of patients with unstable angina/non-st-elevation myocardial infarction) developed in collaboration with the american college of emergency physicians, the society for cardiovascular angiography and interventions, and the society of thoracic surgeons endorsed by the american association of cardiovascular and pulmonary rehabilitation and the society for academic emergency medicine. *J Am Coll Cardiol*, 50(7):e1–e157, Aug 2007.

- [14] Andreas Wielgosz *et al*, editor. *Changing Face of Heart Disease and Stroke in Canada 2000*. Heart and Stroke Foundation of Canada, 1999.
- [15] M. Aslund, E. Fredenberg, M. Telman, and M. Danielsson. Detectors for the future of x-ray imaging. *Radiat. Prot. Dosimetry*, 139(1-3):327–333, 2010. doi: 10.1093/rpd/ncq074.
- [16] Magnus Aslund, Björn Cederström, Mats Lundqvist, and Mats Danielsson. Physical characterization of a scanning photon counting digital mammography system based on Si-strip detectors. *Med. Phys.*, 34(6):1918–1925, Jun 2007.
- [17] Frank H. Attix. *Introduction to Radiological Physics and Radiation Dosimetry*. Wiley-Interscience, 1986.
- [18] R. Ballabriga, M. Campbell, E.H.M Heijne, X. Llopart, and L. Tlustos. The Medipix3 prototype, a pixel readout chip working in single photon counting mode with improved spectrometric performance. *IEEE Trans. Nucl. Sci.*, 54:1824–1829, 2007.
- [19] H. H. Barrett. Objective assessment of image quality: Effects of quantum noise and object variability. *J. Opt. Soc. Am. A.*, 7(7):1266–1278, Jul 1990.
- [20] H. H. Barrett and Kyle J. Myers. *Image Science: Mathematical and Statistical Foundations*. Wiley, 2001.
- [21] H. H. Barrett, J. D. Eskin, and H. B. Barber. Charge transport in arrays of semiconductor gamma-ray detectors. *Phys. Rev. Lett.*, 75(1):156–159, Jul 1995.
- [22] H. H. Barrett, R. F. Wagner, and K. J. Myers. Correlated point processes in radiological imaging. *Proc. of SPIE*, 3032:110–125, 1997.
- [23] Y. Bentoutou, N. Taleb, M. Chikr El Mezouar, M. Taleb, and L. Jetto. A results recapitulation of image registration techniques in digital subtraction angiography. In *IEEE Nuclear Science Symposium Conference Record*, 2008.

- [24] A. Bergamaschi, R. Dinapoli, B. Henrich, I. Johnson, A. Mozzanica, X. Shi, and B. Schmitt. Beyond single photon counting x-ray detectors. *Nucl. Inst. Meth. A*, 2010.
- [25] I. M. Blevis, D. C. Hunt, and J. A. Rowlands. X-ray imaging using amorphous selenium: Determination of swank factor by pulse height spectroscopy. *Med. Phys.*, 25(5):638–641, May 1998.
- [26] F. O. Bochud, J. F. Valley, F. R. Verdun, C. Hessler, and P. Schnyder. Estimation of the noisy component of anatomical backgrounds. *Med. Phys.*, 26(7):1365–1370, Jul 1999.
- [27] F. O. Bochud, C. K. Abbey, and M. P. Eckstein. Visual signal detection in structured backgrounds. III. Calculation of figures of merit for model observers in statistically nonstationary backgrounds. *J Opt Soc Am A Opt Image Sci Vis*, 17(2):193–205, Feb 2000.
- [28] Hans Bornefalk. Task-based weights for photon counting spectral x-ray imaging. *Med. Phys.*, 38(11):6065, Nov 2011. doi: 10.1118/1.3653195.
- [29] Hans Bornefalk and Mats Danielsson. Photon-counting spectral computed tomography using silicon strip detectors: A feasibility study. *Phys. Med. Biol.*, 55(7):1999–2022, Apr 2010. doi: 10.1088/0031-9155/55/7/014.
- [30] Hans Bornefalk, John M Lewin, Mats Danielsson, and Mats Lundqvist. Single-shot dual-energy subtraction mammography with electronic spectrum splitting: Feasibility. *Eur. J. Radiol.*, 60(2):275–278, Nov 2006. doi: 10.1016/j.ejrad.2006.08.004.
- [31] Hans Bornefalk, Cheng Xu, Christer Svensson, and Mats Danielsson. Design considerations to overcome cross talk in a photon counting silicon strip detector for computed tomography. *Nucl. Instrum. Meth. A*, 621:371–378, 2010.
- [32] L. M. Boxt. Intravenous digital subtraction angiography of the thoracic and abdominal aorta. *Cardiovasc Intervent Radiol*, 6(4-6):205–213, 1983.
- [33] Ronald Bracewell. *The Fourier transform and its applications*. McGraw-Hill Science, 3 edition, 1999.
- [34] W. R. Brody. Radiology-important advances in clinical medicine: Digital subtraction angiography. *West. J. Med.*, 139(1):89–90, Jul 1983.

- [35] W. R. Brody, A. Macovski, L. Lehmann, F. A. DiBianca, D. Volz, and L. S. Edelheit. Intravenous angiography using scanned projection radiography: Preliminary investigation of a new method. *Invest. Radiol.*, 15(3):220–223, 1980.
- [36] W. R. Brody, G. Butt, A. Hall, and A. Macovski. A method for selective tissue and bone visualization using dual energy scanned projection radiography. *Med. Phys.*, 8(3):353–357, 1981.
- [37] W. R. Brody, D. R. Enzmann, L. S. Deutsch, A. Hall, and N. Pelc. Intravenous carotid arteriography using line-scanned digital radiography. *Radiology*, 139(2):297–300, May 1981.
- [38] W. R. Brody, D. R. Enzmann, D. C. Miller, D. F. Guthaner, N. J. Pelc, G. S. Keyes, and S. J. Riederer. Intravenous arteriography using digital subtraction techniques. *JAMA*, 248(6):671–674, Aug 1982.
- [39] William R. Brody. Digital subtraction angiography. *IEEE Trans. Nucl. Sci.*, NS-29:1176–1180, 1982.
- [40] Albert V. G. Brusckke, William C. Sheldon, Earl K. Shirey, and William L. Proudfit. A half century of selective coronary arteriography. *J. Am. Coll. Cardiol.*, 54(23):2139–2144, Dec 2009. doi: 10.1016/j.jacc.2009.06.051.
- [41] A. P. H. Butler, N. G. Anderson, R. Tipples, N. Cook, R. Watts, and J. Meyer. Bio-medical x-ray imaging with spectroscopic pixel detectors. *Nucl. Inst. Meth. A*, 591:141–146, 2008.
- [42] R. M. Califf, P. W. Armstrong, J. R. Carver, R. B. D’Agostino, and W. E. Strauss. 27th Bethesda conference: Matching the intensity of risk factor management with the hazard for coronary disease events. Task Force 5. Stratification of patients into high, medium and low risk subgroups for purposes of risk factor management. *J. Am. Coll. Cardiol.*, 27(5):1007–1019, Apr 1996.
- [43] H. N. Cardinal and A. Fenster. Analytic approximation of the log-signal and log-variance functions of x-ray imaging systems, with application to dual-energy imaging. *Med. Phys.*, 18(5):867–879, 1991.
- [44] C. Carpentieri, M. G. Bisogni, A. Del Guerra, P. Delogu, M. E. Fantacci, J. Fogli, A. Marchi, V. Marzulli, V. Rosso, A. Stefanini, and A. Tofani. A pixel detector-based single photon-counting system as fast spectrometer for diagnostic x-ray beams. *Radiat Prot Dosimetry*, 129(1-3):119–122, 2008. doi: 10.1093/rpd/ncn147.

- [45] H. P. Chan and K. Doi. Energy and angular dependence of x-ray absorption and its effect on radiographic response in screen–film systems. *Phys. Med. Biol.*, 28(5):565–579, May 1983.
- [46] H. P. Chan and K. Doi. Studies of x-ray energy absorption and quantum noise properties of x-ray screens by use of monte carlo simulation. *Med. Phys.*, 11(1):37–46, 1984.
- [47] W. A. Chilcote, M. T. Modic, W. A. Pavlicek, J. R. Little, A. J. Furian, P. M. Duchesneau, and M. A. Weinstein. Digital subtraction angiography of the carotid arteries: A comparative study in 100 patients. *Radiology*, 139:287–295, 1981.
- [48] G. Cho, H. K. Kim, H. Woo, G. Oh, and D. K. Ha. Electronic dose conversion technique using a NaI(Tl) detector for assessment of exposure dose rate from environmental radiation. *IEEE Trans. Nucl. Sci.*, 45:981–985, 1998.
- [49] G. Cowan. *Statistical Data Analysis*. Oxford University Press, 1998.
- [50] A. B. Crummy, C. M. Strother, J. F. Sackett, D. L. Ergun, C. G. Shaw, R. A. Kruger, C. A. Mistretta, W. D. Turnipseed, R. P. Lieberman, P. D. Myerowitz, and F. F. Ruzicka. Computerized fluoroscopy: Digital subtraction for intravenous angiocardiology and arteriography. *AJR Am. J. Roentgenol.*, 135(6):1131–1140, Dec 1980. doi: 10.2214/ajr.135.6.1131.
- [51] A. B. Crummy, C. M. Strother, R. P. Lieberman, M. F. Stieghorst, J. F. Sackett, M. M. Wojtowycz, R. A. Kruger, W. D. Turnipseed, D. L. Ergun, C. G. Shaw, C. A. Mistretta, and F. F. Ruzicka. Digital video subtraction angiography for evaluation of peripheral vascular disease. *Radiology*, 141(1):33–37, Oct 1981.
- [52] I. A. Cunningham. *Handbook of Medical Imaging*, chapter 2, pages 79–160. SPIE Press, 2000.
- [53] I. A. Cunningham, M. S. Westmore, and A. Fenster. A spatial-frequency dependent quantum accounting diagram and detective quantum efficiency model of signal and noise propagation in cascaded imaging systems. *Med. Phys.*, 21(3):417–427, Mar 1994.
- [54] Ian A. Cunningham and Rodney Shaw. Signal-to-noise optimization of medical imaging systems. *J. Opt. Soc. Am. A*, 16:621–632, 1999.
- [55] J. T. Cusma, M. R. Bell, M. A. Wondrow, J. P. Taubel, and D. R. Holmes. Real-time measurement of radiation exposure to patients during diagnostic coronary angiography and percutaneous interventional procedures. *J. Am. Coll. Cardiol.*, 33(2):427–435, Feb 1999.

- [56] P. Dawson. Digital subtraction angiography: A critical analysis. *Clin. Radiol.*, 39(5):474–477, Sep 1988.
- [57] M. Drangova and J. A. Rowlands. Optical factors affecting the detective quantum efficiency of radiographic screens. *Med. Phys.*, 13(2):150–157, 1986.
- [58] Justin L Ducote, Tong Xu, and Sabeel Molloy. Dual-energy cardiac imaging: An image quality and dose comparison for a flat-panel detector and x-ray image intensifier. *Phys. Med. Biol.*, 52(1):183–196, Jan 2007. doi: 10.1088/0031-9155/52/1/012.
- [59] H. Elleaume, A. M. Charvet, S. Corde, F. Estève, and J. F. Le Bas. Performance of computed tomography for contrast agent concentration measurements with monochromatic x-ray beams: Comparison of k-edge versus temporal subtraction. *Phys. Med. Biol.*, 47(18):3369–3385, Sep 2002.
- [60] R. Fahrig, J. A. Rowlands, and M. J. Yaffe. X-ray imaging with amorphous selenium: Detective quantum efficiency of photoconductive receptors for digital mammography. *Med. Phys.*, 22(2):153–160, Feb 1995.
- [61] Sebastian Feuerlein, Ewald Roessl, Roland Proksa, Gerhard Martens, Oliver Klass, Martin Jeltsch, Volker Rasche, Hans-Juergen Brambs, Martin H K Hoffmann, and Jens-Peter Schlomka. Multienergy photon-counting K-edge imaging: Potential for improved luminal depiction in vascular imaging. *Radiology*, 249(3):1010–1016, Dec 2008. doi: 10.1148/radiol.2492080560.
- [62] Alope V Finn, Masataka Nakano, Jagat Narula, Frank D Kolodgie, and Renu Virmani. Concept of vulnerable/unstable plaque. *Arterioscler. Thromb. Vasc. Biol.*, 30(7):1282–1292, Jul 2010. doi: 10.1161/ATVBAHA.108.179739.
- [63] H. W. Fischer and K. R. Thomson. Contrast media in coronary angiography: A review. *Invest. Radiol.*, 13:450–459, 1978.
- [64] Werner Forssmann. Die sondierung des rechten herzens [probing of the right heart]. *Klin Wochenschr*, 8:2085–2087, 1929.
- [65] British Nutrition Foundation. *Cardiovascular Disease: Diet, Nutrition, and Emerging Risk Factors*. Blackwell, 2005.

- [66] Kim Fox, Maria Angeles Alonso Garcia, Diego Ardissino, Pawel Buszman, Paolo G Camici, Filippo Crea, Caroline Daly, Guy De Backer, Paul Hjemdahl, José Lopez-Sendon, Jean Marco, João Morais, John Pepper, Udo Sechtem, Maarten Simoons, Kristian Thygesen, Silvia G Priori, Jean-Jacques Blanc, Andrzej Budaj, John Camm, Veronica Dean, Jaap Deckers, Kenneth Dickstein, John Lekakis, Keith McGregor, Marco Metra, João Morais, Ady Osterspey, Juan Tamargo, José L Zamorano, Task Force on the Management of Stable Angina Pectoris of the European Society of Cardiology, and E. S. C. Committee for Practice Guidelines (CPG). Guidelines on the management of stable angina pectoris: executive summary: The task force on the management of stable angina pectoris of the european society of cardiology. *Eur. Heart J.*, 27(11):1341–1381, Jun 2006. doi: 10.1093/eurheartj/ehl001.
- [67] Erik Fredenberg, Magnus Hemmendorff, Björn Cederström, Magnus Aslund, and Mats Danielsson. Contrast-enhanced spectral mammography with a photon-counting detector. *Med Phys*, 37(5):2017–2029, May 2010.
- [68] Erik Fredenberg, Mats Lundqvist, Bjorn Cederström, Magnus Aslund, and Mats Danielsson. Energy resolution of a photon-counting silicon strip detector. *Nucl. Inst. Meth. A*, 613:156–162, 2010.
- [69] Hiroshi Fujita, Du-Yih Tsai, Takumi Itoh, Kunio Doi, Junji Morishita, Katsuhiko Ueda, and Akiyoshi Ohtsuka. A simple method for determining the modulation transfer function in digital radiography. *IEEE Trans. Med. Imaging.*, 11:34–39, 1992.
- [70] R. Van Gastel, I. Sikharulidze, S. Schramm, J. P. Abrahams, B. Poelsema, R. M. Tromp, and S. J. van der Molen. Medipix 2 detector applied to low energy electron microscopy. *Ultramicroscopy*, 110(1):33–35, Dec 2009. doi: 10.1016/j.ultramic.2009.09.002.
- [71] R. J. Gibbons, K. Chatterjee, J. Daley, J. S. Douglas, S. D. Fihn, J. M. Gardin, M. A. Grunwald, D. Levy, B. W. Lytle, R. A. O’Rourke, W. P. Schafer, and S. V. Williams. ACC/AHA/ACP-ASIM guidelines for the management of patients with chronic stable angina: Executive summary and recommendations. A report of the American College of Cardiology/American Heart Association Task Force on practice guidelines (committee on management of patients with chronic stable angina). *Circulation*, 99(21):2829–2848, Jun 1999.
- [72] Nikolaos A Gkanatsios, Walter Huda, and Keith R Peters. Effect of radiographic techniques (kVp and mAs) on image quality and patient doses in digital subtraction angiography. *Med. Phys.*, 29(8):1643–1650, Aug 2002.

- [73] K. L. Gould and K. Lipscomb. Effects of coronary stenoses on coronary flow reserve and resistance. *Am. J. Cardiol.*, 34(1):48–55, Jul 1974.
- [74] K. L. Gould, R. L. Kirkeeide, and M. Buchi. Coronary flow reserve as a physiologic measure of stenosis severity. *J. Am. Coll. Cardiol.*, 15(2):459–474, Feb 1990.
- [75] D. F. Guthaner, W. R. Brody, B. D. Lewis, G. S. Keyes, and B. F. Belanger. Clinical application of hybrid subtraction digital angiography: Preliminary results. *Cardiovasc. Intervent. Radiol.*, 6(4-6):290–294, 1983.
- [76] D. F. Guthaner, L. Wexler, D. R. Enzmann, S. J. Riederer, G. S. Keyes, W. F. Collins, and W. R. Brody. Evaluation of peripheral vascular disease using digital subtraction angiography. *Radiology*, 147:393–398, 1983.
- [77] G. Hajdok, J. Yao, J. J. Battista, and I. A. Cunningham. Signal and noise transfer properties of photoelectric interactions in diagnostic x-ray imaging detectors. *Med. Phys.*, 33(10):3601–3620, Oct 2006.
- [78] G. Hajdok, J. J. Battista, and I. A. Cunningham. Fundamental x-ray interaction limits in diagnostic imaging detectors: Frequency-dependent Swank noise. *Med. Phys.*, 35(7):3194–3204, Jul 2008.
- [79] G. Hajdok, J. J. Battista, and I. A. Cunningham. Fundamental x-ray interaction limits in diagnostic imaging detectors: spatial resolution. *Med Phys*, 35(7):3180–3193, Jul 2008.
- [80] E. Haschek and O. T. Lindenthal. A contribution to the practical use of photography according to Roentgen. *Wien Klin Wochenschr*, 9:63, 1896.
- [81] Peng He, Hengyong Yu, Patrick Thayer, Xin Jin, Qiong Xu, James Bennett, Rachael Tappenden, Biao Wei, Aaron Goldstein, Peter Renaud, Anthony Butler, Phillip Butler, and Ge Wang. Preliminary experimental results from a MARS Micro-CT system. *J. Xray Sci. Technol.*, 20(2):199–211, 2012. doi: 10.3233/XST-2012-0329.
- [82] William Heberden. Some account of a disorder of the breast. *Med. Transact. R. Coll. Phys. Lond.*, 2:59, 1772.
- [83] K Hecht. Zum mechanismus des lichtelektrischen primarstromes in isolierenden kristallen. *Z. Phys.*, 77:235–245, 1932.

- [84] C. B. Higgins. Effects of contrast materials on left ventricular function. *Invest. Radiol.*, 15: S220–S231, 1980.
- [85] C. B. Higgins, K. H. Gerber, R. F. Mattrey, and R. A. Slutsky. Evaluation of the hemodynamic effects of intravenous administration of ionic and nonionic contrast materials. Implications for deriving physiologic measurements from computed tomography and digital cardiovascular imaging. *Radiology*, 142(3):681–686, Mar 1982.
- [86] W. Hillen, W. Eckenbach, P. Quadflieg, and T. Zaengel. Signal-to-noise performance in cesium iodide x-ray fluorescent screens. *SPIE Medical Imaging V: Imaging Physics*, 1443:121–131, 1991.
- [87] Alan T. Hirsch, Ziv J. Haskal, Norman R. Hertzner, Curtis W. Bakal, Mark A. Creager, Jonathan L. Halperin, Loren F. Hiratzka, William R C. Murphy, Jeffrey W. Olin, Jules B. Puschett, Kenneth A. Rosenfield, David Sacks, James C. Stanley, Lloyd M Taylor, Jr, Christopher J. White, John White, Rodney A. White, Elliott M. Antman, Sidney C Smith, Jr, Cynthia D. Adams, Jeffrey L. Anderson, David P. Faxon, Valentin Fuster, Raymond J. Gibbons, Jonathan L. Halperin, Loren F. Hiratzka, Sharon A. Hunt, Alice K. Jacobs, Rick Nishimura, Joseph P. Ornato, Richard L. Page, Barbara Riegel, American Association for Vascular Surgery, Society for Vascular Surgery, Society for Cardiovascular Angiography and Interventions, Society for Vascular Medicine and Biology, Society of Interventional Radiology, A. C. C/A. H. A Task Force on Practice Guidelines, American Association of Cardiovascular and Pulmonary Rehabilitation, Lung, National Heart, Blood Institute, Society for Vascular Nursing, TransAtlantic Inter-Society Consensus, and Vascular Disease Foundation. Acc/aha 2005 guidelines for the management of patients with peripheral arterial disease (lower extremity, renal, mesenteric, and abdominal aortic): executive summary a collaborative report from the american association for vascular surgery/society for vascular surgery, society for cardiovascular angiography and interventions, society for vascular medicine and biology, society of interventional radiology, and the acc/aha task force on practice guidelines (writing committee to develop guidelines for the management of patients with peripheral arterial disease) endorsed by the american association of cardiovascular and pulmonary rehabilitation; national heart, lung, and blood institute; society for vascular nursing; transatlantic inter-society consensus; and vascular disease foundation. *J Am Coll Cardiol*, 47(6):1239–1312, Mar 2006.
- [88] T. L. Houk, R. A. Kruger, C. A. Mistretta, S. J. Riederer, C. G. Shaw, J. C. Lancaster,

- and D. C. Flemming. Real-time digital k-edge subtraction fluoroscopy. *Invest. Radiol.*, 14(4): 270–278, 1979.
- [89] Michael Anthony Hurrell, Anthony Philip Howard Butler, Nicholas James Cook, Philip Howard Butler, J. Paul Ronaldson, and Rafidah Zainon. Spectral hounsfield units: a new radiological concept. *Eur. Radiol.*, Dec 2011. doi: 10.1007/s00330-011-2348-3.
- [90] Q. Le Huy, Justin L Ducote, and Sabee Molloi. Radiation dose reduction using a cdznte-based computed tomography system: comparison to flat-panel detectors. *Med. Phys.*, 37(3): 1225–1236, Mar 2010.
- [91] Jan S Iwanczyk, Einar Nygård, Oded Meirav, Jerry Arenson, William C Barber, Neal E Hart-sough, Nail Malakhov, and Jan C Wessel. Photon counting energy dispersive detector arrays for x-ray imaging. *IEEE. Trans. Nucl. Sci.*, 56(3):535–542, 2009. doi: 10.1109/TNS.2009.2013709.
- [92] B. Jacobson. Dichromatic absorption radiography. *Acta. radiol.*, 39(6):437–452, Jun 1953.
- [93] C. M. Johnson, P. F. Sheedy, F. Earnest, and A. W. Stanson. Digital subtraction angiography. *Surg. Clin. North. Am.*, 64(1):151–171, Feb 1984.
- [94] S. O. Kasap. X-ray sensitivity of photoconductors: Applications to stabilized a-Se. *J. Phys. D: Appl. Phys.*, 33:2853–2865, 2000.
- [95] Demosthenes Katritsis and Michael M. Webb-Peploe. The role of digital subtraction angiogra-phy in the quantitation of coronary stenosis. *International Journal of Cardiology*, 29:277–283, 1990.
- [96] B. T. Katzen. Current status of digital angiography in vascular imaging. *Radiol. Clin. North. Am.*, 33(1):1–14, Jan 1995.
- [97] F. Kelcz. Absorption-edge fluoroscopy using a three-spectrum technique. *Med. Phys.*, 3(3): 159–168, 1976.
- [98] F. Kelcz, C. A. Mistretta, and S. J. Riederer. Spectral considerations for absorption-edge fluoroscopy. *Med. Phys.*, 4(1):26–35, 1977.
- [99] F. Kelcz, P. M. Joseph, and S. K. Hilal. Noise considerations in dual energy CT scanning. *Med. Phys.*, 6(5):418–425, 1979.
- [100] G.F Knoll. *Radiation Detection and Measurement*. Wiley, New York, 2000.

- [101] Thomas Koenig, Andreas Zwerger, Marcus Zuber, Patrick Schuenke, Simeon Nill, Ewald Guni, Alex Fauler, Michael Fiederle, and Uwe Oelfke. On the energy response function of a cdte medipix2 hexa detector. *Nucl. Inst. Meth. A*, 648:S265–S268, 2011.
- [102] Thomas Koenig, Julia Schulze, Marcus Zuber, Kristian Rink, Jochen Butzer, Elias Hamann, Angelica Cecilia, Andreas Zwerger, Alex Fauler, Michael Fiederle, and Uwe Oelfke. Imaging properties of small-pixel spectroscopic x-ray detectors based on cadmium telluride sensors. *Phys. Med. Biol.*, 57(21):6743–6759, Nov 2012. doi: 10.1088/0031-9155/57/21/6743.
- [103] Alexander Korn, Markus Firsching, Gisela Anton, Martin Hoheisel, and Thilo Michel. Investigation of charge carrier transport and charge sharing in x-ray semiconductor pixel detectors such as Medipix2. *Nucl. Inst. Meth. A*, 576:239–242, 2007.
- [104] L. Norgren *et al.* Inter-society consensus for the management of peripheral arterial disease (TASC II). *Eur. J. Vasc. Endovasc. Surg.*, 33(Suppl 1):S1–75, 2007.
- [105] Huy Q. Le and Sabee Molloy. Least squares parameter estimation methods for material decomposition with energy discriminating detectors. *Med. Phys.*, 38:245–255, 2011.
- [106] Robert J LeClair, Yinkun Wang, Peiyong Zhao, Michel Boileau, Lilie Wang, and Fabrice Fleurot. An analytic model for the response of a czt detector in diagnostic energy dispersive x-ray spectroscopy. *Med Phys*, 33(5):1329–1337, May 2006.
- [107] L. A. Lehmann, R. E. Alvarez, A. Macovski, W. R. Brody, N. J. Pelc, S. J. Riederer, and A. L. Hall. Generalized image combinations in dual kVp digital radiography. *Med. Phys.*, 8: 659–667, 1981.
- [108] Michael R Lemacks, S. Cheenu Kappadath, Chris C Shaw, Xinming Liu, and Gary J Whitman. A dual-energy subtraction technique for microcalcification imaging in digital mammography—A signal-to-noise analysis. *Med. Phys.*, 29(8):1739–1751, Aug 2002.
- [109] Shuai Leng, Lifeng Yu, Jia Wang, Joel G Fletcher, Charles A Mistretta, and Cynthia H McCollough. Noise reduction in spectral CT: Reducing dose and breaking the trade-off between image noise and energy bin selection. *Med. Phys.*, 38(9):4946–4957, Sep 2011. doi: 10.1118/1.3609097.
- [110] X. Llopart, M. Campbell, D San Segundo, E. Pernigotti, and R. Dinapoli. Medipix2, a 64k pixel read out chip with 55 μm square elements working in single photon counting mode. In *Nuclear Science Symposium Conference Record, 2001 IEEE*, 2001.

- [111] Mario Locker, Peter Fisher, Sven Krimmel, Hans Kruger, Markus Lindner, Kazuhiro Nakazawa, Tadayuki Takahashi, and Norbert Wermes. Single photon counting x-ray imaging with Si and CdTe single chip pixel detectors and multichip pixel modules. *IEEE Trans. Nucl. Sci.*, 51:1717–1723, 2004.
- [112] M. S. Van Lysel. Limitations of the lead oxide vidicon for dual-energy digital subtraction angiography. *IEEE Trans Med Imaging*, 10:530–537, 1991.
- [113] M. S. Van Lysel. Optimization of beam parameters for dual-energy digital subtraction angiography. *Med. Phys.*, 21(2):219–226, Feb 1994.
- [114] M. S. Van Lysel, JT Dobbins, 3rd, W. W. Pepler, B. H. Hasegawa, C. S. Lee, C. A. Mistretta, W. C. Zarnstorff, A. B. Crummy, W. Kubal, B. Bergsjordet, C. M. Strother, and J. F. Sackett. Work in progress: hybrid temporal-energy subtraction in digital fluoroscopy. *Radiology*, 147(3):869–874, Jun 1983.
- [115] M. S. Van Lysel, W. P. Miller, D. G. Senior, V. K. Gupta, D. J. Ende, and D. J. Albright. Left ventricular dual-energy digital subtraction angiography: a motion immune digital subtraction technique. *Int. J. Card. Imaging.*, 7(1):55–65, 1991.
- [116] M. S. Van Lysel, W. P. Miller, T. P. Fuerst, and D. J. Albright. Improved densitometric measurement of left ventricular ejection fraction using dual-energy digital subtraction angiography. *Int. J. Card. Imaging.*, 10(2):113–121, Jun 1994.
- [117] J Mackay and G Mensah. *The atlas of heart disease and stroke*. World Health Organization, 2004.
- [118] P. Maj, P. Grybos, R. Szczygiel, M. Zoladz, T. Sakamura, and Y. Tsuji. 18k channels single photon counting readout circuit for hybrid pixel detector. *Nucl. Inst. Meth. A*, 697:32–39, 2013.
- [119] G. B. Mancini and C. B. Higgins. Digital subtraction angiography: A review of cardiac applications. *Prog Cardiovasc Dis*, 28(2):111–141, 1985.
- [120] G. B. Mancini, J. N. Bloomquist, V. Bhargava, J. B. Stein, W. Lew, R. A. Slutsky, R. Shabetai, and C. B. Higgins. Hemodynamic and electrocardiographic effects in man of a new nonionic contrast agent (iohexol): Advantages over standard ionic agents. *Am. J. Cardiol.*, 51(7):1218–1222, Apr 1983.

- [121] C. H. McCollough, M. S. Van Lysel, W. W. Peppler, and C. A. Mistretta. A correlated noise reduction algorithm for dual-energy digital subtraction angiography. *Med. Phys.*, 16(6): 873–880, 1989.
- [122] E. H. Meijering, W. J. Niesssen, and M. A. Viergever. Retrospective motion correction in digital subtraction angiography: A review. *IEEE Trans. Med. Imaging*, 18(1):2–21, Jan 1999. doi: 10.1109/42.750248.
- [123] E. H. Meijering, W. J. Niessen, J. Bakker, A. J. van Der Molen, G. A. de Kort, R. T. Lo, W. P. Mali, and M. A. Viergever. Reduction of patient motion artifacts in digital subtraction angiography: evaluation of a fast and fully automatic technique. *Radiology*, 219(1):288–293, Apr 2001.
- [124] T. R. Melzer, N. J. Cook, A. P. Butler, R. Watts, N. Anderson, R. Tipples, and P. H. Butler. Spectroscopic biomedical imaging with the medipix2 detector. *Australas Phys. Eng. Sci. Med.*, 31(4):300–306, Dec 2008.
- [125] R. Van Metter and M. Rabbani. An application of multivariate moment-generating functions to the analysis of signal and noise propagation in radiographic screen-film systems. *Med. Phys.*, 17(1):65–71, 1990.
- [126] T. Michel, G. Anton, M. Bohnel, J. Durst, M. Firsching, A. Korn, B. Kreisler, A. Loehr, F. Nachtrab, D. Niederlohner, F. Sukowski, and P. Takoukam Talla. A fundamental method to determine the signal-to-noise ratio (SNR) and detective quantum efficiency (DQE) for a photon counting pixel detector. *Nucl. Instrum. Meth. A*, 568:799–802, 2006.
- [127] Thilo Michel, Gisela Anton, Jurgen Durst, Peter Bartl, Michael Bohnel, Markus Firsching, Bjorn Kreisler, Alexander Korn, Anja Loehr, Frank Nachtrab, Daniel Niederlohner, Frank Sukowski, and Patrick Takoukam-Talla. Investigating the dqe of the medipix detector using the multiplicity concept. *IEEE Nuclear Symposium Conference Record*, M06-169:1955–1959, 2006.
- [128] Thilo Michel, Patrick Takoukam Talla, Markus Firsching, Jurgen Durst, Michael Bohnel, and Gisela Anton. Reconstruction of x ray spectra with the energy sensitive photon counting detector Medipix2. *Nucl. Instrum. Meth. A*, 598:510–514, 2009.
- [129] B. Mikulec. Development of segmented semiconductor arrays for quantum imaging. *Nucl. Instrum. Meth. A*, 510:1–23, 2003.

- [130] C. A. Mistretta, M. G. Ort, F. Kelcz, J. R. Cameron, M. P. Siedband, and A. B. Crummy. Absorption edge fluoroscopy using quasi-monoenergetic x-ray beams. *Invest. Radiol.*, 8(6):402–412, 1973.
- [131] C. A. Mistretta, F. Kelcz, M. G. Ort, M. P. Siedband, J. R. Cameron, A. B. Crummy, and R. E. Polcyn. Absorption edge fluoroscopy. *IEEE Trans. Nucl. Sci.*, 21:645–651, 1974.
- [132] C. A. Mistretta, W. W. Pepler, M. Van Lysel, J. Dobbins, B. Hasegawa, P. D. Myerowitz, D. Swanson, C. S. Lee, N. Shaik, and W. Zarnstorff. Recent advances in digital radiography. *Ann Radiol (Paris)*, 26(7):537–542, Nov 1983.
- [133] Charles A. Mistretta, Andrew B. Crummy, and Charles M. Strother. Digital angiography: A perspective. *Radiology*, 139:273–276, 1981.
- [134] S. Molloi, A. Ersahin, and Y. J. Qian. Ccd camera for dual-energy digital subtraction angiography. *IEEE Trans Med Imaging*, 14(4):747–752, 1995. doi: 10.1109/42.476115.
- [135] S. Y. Molloi and C. A. Mistretta. Quantification techniques for dual-energy cardiac imaging. *Med Phys*, 16(2):209–217, 1989.
- [136] S. Y. Molloi, D. M. Weber, W. W. Pepler, J. D. Folts, and C. A. Mistretta. Quantitative dual-energy coronary arteriography. *Invest. Radiol.*, 25(8):908–914, Aug 1990.
- [137] K. J. Myers, J. P. Rolland, H. H. Barrett, and R. F. Wagner. Aperture optimization for emission imaging: Effect of a spatially varying background. *J. Opt. Soc. Am.*, 7:1279–1293, 1990.
- [138] S. J. Nik, J. Meyer, and R. Watts. Optimal material discrimination using spectral x-ray imaging. *Phys. Med. Biol.*, 56(18):5969–5983, Sep 2011. doi: 10.1088/0031-9155/56/18/012.
- [139] H.E. Nilsson, B. Norlin, C. Frojdh, and L. Tlustos. Charge sharing suppression using pixel-to-pixel communication in photon counting x-ray imaging systems. *Nucl. Inst. Meth. A*, pages 243–247, 2007.
- [140] Public Health Agency of Canada, Canadian Institute for Health Information, Canadian Stroke Network, Heart, Stroke Foundation of Canada, and Statistics Canada, editors. *Tracking Heart Disease and Stroke in Canada*. 2009.

- [141] K. Ohara, K. Doi, C. E. Metz, and M. L. Giger. Investigation of basic imaging properties in digital radiography. 13. Effect of simple structured noise on the detectability of simulated stenotic lesions. *Med. Phys.*, 16(1):14–21, 1989.
- [142] A. R. Owen and G. H. Roditi. Peripheral arterial disease: The evolving role of non-invasive imaging. *Postgrad. Med. J.*, 87(1025):189–198, Mar 2011. doi: 10.1136/pgmj.2009.082040.
- [143] Athanasios Papoulis. *Probability, Random Variables, and Stochastic Processes*. McGraw-Hill, Inc., 3 edition, 1991.
- [144] Frank Pomposelli. Arterial imaging in patients with lower extremity ischemia and diabetes mellitus. *J. Vasc. Surg.*, 52(3 Suppl):81S–91S, Sep 2010. doi: 10.1016/j.jvs.2010.06.013.
- [145] Cyril Ponchut. Correction of the charge sharing in photon-counting pixel detector data. *Nucl. Inst. Meth. A*, 591:311–313, 2008.
- [146] M. Rabbani, R. Shaw, and R. Van Metter. Detective quantum efficiency of imaging systems with amplifying and scattering mechanisms. *J. Opt. Soc. Am. A*, 4(5):895–901, May 1987.
- [147] G. Revesz, H. L. Kundel, and M. A. Graber. The influence of structured noise on the detection of radiologic abnormalities. *Invest. Radiol.*, 9(6):479–486, 1974.
- [148] S. Richard, J. H. Siewerdsen, D. A. Jaffray, D. J. Moseley, and B. Bakhtiar. Generalized DQE analysis of radiographic and dual-energy imaging using flat-panel detectors. *Med. Phys.*, 32(5):1397–1413, May 2005.
- [149] S. J. Riederer and R. A. Kruger. Intravenous digital subtraction: A summary of recent developments. *Radiology*, 147:633–638, 1983.
- [150] Robert S. McKelvie *et al.* The 2012 canadian cardiovascular society heart failure management guidelines update: Focus on acute and chronic heart failure. *Can. J. Cardiol.*, 29:168–181, 2013.
- [151] W. C. Roentgen. On a new kind of rays. *Science*, 3:227–231, 1896.
- [152] E. Roessl and C. Herrmann. Cramér-Rao lower bound of basis image noise in multiple-energy x-ray imaging. *Phys. Med. Biol.*, 54(5):1307–1318, Mar 2009. doi: 10.1088/0031-9155/54/5/014.
- [153] E. Roessl and R. Proksa. K-edge imaging in x-ray computed tomography using multi-bin photon counting detectors. *Phys. Med. Biol.*, 52(15):4679–4696, Aug 2007. doi: 10.1088/0031-9155/52/15/020.

- [154] Ewald Roessl, Andy Ziegler, and Roland Proksa. On the influence of noise correlations in measurement data on basis image noise in dual-energylike x-ray imaging. *Med. Phys.*, 34(3): 959–966, Mar 2007.
- [155] Ewald Roessl, Heiner Daerra, Klaus Jiirgen Engel, Axel Thran, Carsten Schirra, and Roland Proksa. Combined effects of pulse pile-up and energy response in energy-resolved, photon-counting computed tomography. In *IEEE Nuclear Science Symposium Conference Record*, pages 2309–2313, 2011.
- [156] J. P. Rolland and H. H. Barrett. Effect of random background inhomogeneity on observer detection performance. *J Opt Soc Am A*, 9(5):649–658, May 1992.
- [157] John A. Rowlands and John Yorkston. *Handbook of Medical Imaging*, chapter 4, pages 223–329. SPIE Press, 2000.
- [158] A. Ruzin and Y. Nemirowsky. Methodology for evaluations of mobility-lifetime product by spectroscopy measurements using CdZnTe spectrometers. *J. Appl. Phys.*, 82:4166–4171, 1997.
- [159] S. C. Smith *et al.* ACC/AHA guidelines for percutaneous coronary intervention (revision of the 1993 PTCA guidelines)-executive summary: A report of the American College of Cardiology/American Heart Association task force on practice guidelines (Committee to revise the 1993 guidelines for percutaneous transluminal coronary angioplasty) endorsed by the Society for Cardiac Angiography and Interventions. *Circulation*, 103(24):3019–3041, Jun 2001.
- [160] Hajime Sakuma. Coronary CT versus MR angiography: The role of MR angiography. *Radiology*, 258(2):340–349, Feb 2011. doi: 10.1148/radiol.10100116.
- [161] E. Samei, M. J. Flynn, and D. A. Reimann. A method for measuring the presampled MTF of digital radiographic systems using an edge test device. *Med. Phys.*, 25(1):102–113, Jan 1998.
- [162] E. Samei, M. J. Flynn, and W. R. Eyler. Detection of subtle lung nodules: Relative influence of quantum and anatomic noise on chest radiographs. *Radiology*, 213(3):727–734, 1999.
- [163] Ehsan Samei, Michael J Flynn, Edward Peterson, and William R Eyler. Subtle lung nodules: Influence of local anatomic variations on detection. *Radiology*, 228(1):76–84, 2003. doi: 10.1148/radiol.2273020509.
- [164] Mike Sattarivand and I. A. Cunningham. Computational engine for development of complex cascaded models of signal and noise in x-ray imaging systems. *IEEE Trans Med Imaging*, 24(2):211–222, 2005. doi: 10.1109/TMI.2004.839680.

- [165] J. P. Schlomka, E. Roessl, R. Dorscheid, S. Dill, G. Martens, T. Istel, C. Bäumer, C. Herrmann, R. Steadman, G. Zeitler, A. Livne, and R. Proksa. Experimental feasibility of multi-energy photon-counting K-edge imaging in pre-clinical computed tomography. *Phys. Med. Biol.*, 53(15):4031–4047, Aug 2008. doi: 10.1088/0031-9155/53/15/002.
- [166] Taly Gilat Schmidt. Optimal "image-based" weighting for energy-resolved CT. *Med. Phys.*, 36(7):3018–3027, Jul 2009.
- [167] Taly Gilat Schmidt. CT energy weighting in the presence of scatter and limited energy resolution. *Med. Phys.*, 37(3):1056–1067, Mar 2010.
- [168] Florian F Schmitzberger, Eva Maria Fallenberg, Rüdiger Lawaczeck, Magnus Hemmendorff, Elin Moa, Mats Danielsson, Ulrich Bick, Susanne Diekmann, Alexander Pöllinger, Florian J Engelken, and Felix Diekmann. Development of low-dose photon-counting contrast-enhanced tomosynthesis with spectral imaging. *Radiology*, 259(2):558–564, May 2011. doi: 10.1148/radiol.11101682.
- [169] C. G. Shaw and D. B. Plewes. Effects of scattered radiation and veiling glare in dual-energy tissue-bone imaging: A theoretical analysis. *Med. Phys.*, 14(6):956–967, 1987.
- [170] R. Shaw. The equivalent quantum efficiency of the photographic process. *J. Photogr. Sci.*, 11:199–204, 1963.
- [171] Polad M Shikhaliev. Tilted angle CZT detector for photon counting/energy weighting x-ray and CT imaging. *Phys. Med. Biol.*, 51(17):4267–4287, Sep 2006. doi: 10.1088/0031-9155/51/17/010.
- [172] Polad M Shikhaliev. Computed tomography with energy-resolved detection: A feasibility study. *Phys. Med. Biol.*, 53(5):1475–1495, Mar 2008. doi: 10.1088/0031-9155/53/5/020.
- [173] Polad M Shikhaliev. Energy-resolved computed tomography: First experimental results. *Phys. Med. Biol.*, 53(20):5595–5613, Oct 2008. doi: 10.1088/0031-9155/53/20/002.
- [174] Polad M Shikhaliev. Projection x-ray imaging with photon energy weighting: Experimental evaluation with a prototype detector. *Phys. Med. Biol.*, 54(16):4971–4992, Aug 2009. doi: 10.1088/0031-9155/54/16/009.
- [175] Polad M. Shikhaliev. Photon counting spectral CT: Improved material decomposition with k-edge-filtered x-rays. *Phys. Med. Biol.*, 57(6):1595–1615, Mar 2012. doi: 10.1088/0031-9155/57/6/1595.

- [176] Polad M Shikhaliev and Shannon G Fritz. Photon counting spectral CT versus conventional CT: Comparative evaluation for breast imaging application. *Phys. Med. Biol.*, 56(7):1905–1930, Apr 2011. doi: 10.1088/0031-9155/56/7/001.
- [177] Polad M Shikhaliev, Tong Xu, and Sabee Molloy. Photon counting computed tomography: Concept and initial results. *Med. Phys.*, 32(2):427–436, Feb 2005.
- [178] Polad M Shikhaliev, Shannon G Fritz, and John W Chapman. Photon counting multienergy x-ray imaging: Effect of the characteristic x rays on detector performance. *Med. Phys.*, 36(11):5107–5119, Nov 2009.
- [179] J.A. Sicard and G. Forestier. Injections intravasculaires d’huile iodée sous contrôle radiologique. *CR Soc. Biol (Paris)*, 88:1200, 1923.
- [180] J. H. Siewerdsen, L. E. Antonuk, Y. el Mohri, J. Yorkston, W. Huang, J. M. Boudry, and I. A. Cunningham. Empirical and theoretical investigation of the noise performance of indirect detection, active matrix flat-panel imagers (AMFPIs) for diagnostic radiology. *Med. Phys.*, 24(1):71–89, Jan 1997.
- [181] Justin D Silkwood, Kenneth L Matthews, and Polad M Shikhaliev. Photon counting spectral breast CT: Effect of adaptive filtration on CT numbers, noise, and contrast to noise ratio. *Med. Phys.*, 40(5):051905, May 2013. doi: 10.1118/1.4800504.
- [182] Matthias Simon, Klaus Jürgen Engel, Bernd Menser, Xavier Badel, and Jan Linnros. X-ray imaging performance of scintillator-filled silicon pore arrays. *Med. Phys.*, 35(3):968–981, Mar 2008.
- [183] F. M. Sones and E. K. Shirey. Cine coronary arteriography. *Med. Concepts Cardiovasc. Dis.*, 31:735–738, 1962.
- [184] R. K. Swank. Absorption and noise in x-ray phosphors. *J. Appl. Phys.*, 44:4199–4203, 1973.
- [185] R. K. Swank. Measurement of absorption and noise in an x-ray image intensifier. *J. Appl. Phys.*, 45:3673–3678, 1974.
- [186] Katsuyuki Taguchi, Eric C Frey, Xiaolan Wang, Jan S Iwanczyk, and William C Barber. An analytical model of the effects of pulse pileup on the energy spectrum recorded by energy resolved photon counting x-ray detectors. *Med. Phys.*, 37(8):3957–3969, Aug 2010.

- [187] Hiroyasu Tajima, Tatsuya Nakamoto, Takaaki Tanaka, Shingo Uno, Tekefumi Mitani, Eduardo do Couto e Silva, Tuneyoshi Kamae Yasushi Fukazawa, Grzegorz Madejski, Daniel Marlow, Kazuhiro Nakazawa, Masaharu Nomachi, Yu Okada, and Tadayuki Takahashi. Performance of a low noise front-end ASIC for Si/CdTe detectors in Compton gamma-ray telescope. *IEEE Trans. Nucl. Sci.*, 51:842–847, 2004.
- [188] M. Takahashi, Y. Koga, H. Bussaka, and M. Miyawaki. The value of digital subtraction angiography in peripheral vascular diseases. *Br. J. Radiology*, 57:123–132, 1984.
- [189] Gale L Tang, Jason Chin, and Melina R Kibbe. Advances in diagnostic imaging for peripheral arterial disease. *Expert. Rev. Cardiovasc. Ther.*, 8(10):1447–1455, Oct 2010. doi: 10.1586/erc.10.134.
- [190] T. Y. Tang, J. M. U-King-Im, S. R. Walsh, V. E. Young, U. Sadat, Z. Y. Li, A. J. Patterson, K. Varty, and J. H. Gillard. Invasive and non-invasive modalities of imaging carotid stenosis. *J. Cardiovasc. Surg. (Torino)*, 50(6):715–725, Dec 2009.
- [191] Jesse Tanguay, Ho Kyung Kim, and Ian A. Cunningham. The role of x-ray swank factor in energy-resolving photon-counting imaging. *Med. Phys.*, 37:6205–6211, 2010.
- [192] Jesse Tanguay, Ho Kyung Kim, and Ian A Cunningham. A theoretical comparison of x-ray angiographic image quality using energy-dependent and conventional subtraction methods. *Med. Phys.*, 39(1):132, Jan 2012. doi: 10.1118/1.3658728.
- [193] Jesse Tanguay, Ho Kyung Kim, and Ian A. Cunningham. Extension of cascaded systems analysis to single-photon-counting x-ray detectors. *Proc. of SPIE*, 8313 (10):1–13, 2012.
- [194] Jesse Tanguay, Seungman Yun, Ho Kyung Kim, and Ian A Cunningham. Cascaded systems analyses of photon-counting x-ray detectors. *Proc. of SPIE*, 8668:0S1–0S14, 2013.
- [195] Jesse Tanguay, Seungman Yun, Ho Kyung Kim, and Ian A. Cunningham. The detective quantum efficiency of photon-counting x-ray detectors using cascaded systems analyses. *Med. Phys.*, 40:041913, 2013.
- [196] Markku J Tapiovaara and Robert F Wagner. SNR and DQE analysis of broad spectrum x-ray imaging. *Phys. Med. Biol.*, 30:519–529, 1985.
- [197] N. Teranishi. Required conditions for photon-counting image sensors. *IEEE Transactions on Electrical Devices*, 59:2199–2205, 2012.

- [198] L. Tlustos. Spectroscopic x-ray imaging with photon counting pixel detectors. *Nucl. Inst. Meth. A*, 623:823–828, 2010.
- [199] D. M. Tucker, G. T. Barnes, and D. P. Chakraborty. Semiempirical model for generating tungsten target x-ray spectra. *Med Phys*, 18(2):211–218, 1991.
- [200] P. A. Turski, W. J. Zwiebel, C. M. Strother, A. B. Crummy, G. G. Celesia, and J. F. Sackett. Limitations of intravenous digital subtraction angiography. *Am. J. Neuroradiol.*, 4(3):271–273, 1983.
- [201] A. S. Wang and N. J. Pelc. Sufficient statistics as a generalization of binning in spectral x-ray imaging. *IEEE Trans. Med. Imaging*, 30:84–93, Aug 2011. doi: 10.1109/TMI.2010.2061862.
- [202] Adam S. Wang and Norbert J. Pelc. Optimal energy thresholds and weights for separating materials using photon counting x-ray detectors with energy discriminating capabilities. *Proc. of SPIE*, 7258:725821, 2009.
- [203] Adam S. Wang and Norbert J Pelc. Impact of photon counting detector spectral response on dual energy techniques. *Proc. of SPIE*, 7622:76223L, 2010.
- [204] Adam S. Wang, Daniel Harrison, Vladimir Lobastov, and J Eric Tkaczyk. Pulse pileup statistics for energy discriminating photon counting x-ray detectors. *Med Phys*, 38(7):4265–4275, Jul 2011.
- [205] X. Wang, D. Meier, S. Mikkelsen, G. E. Maehlum, D. J. Wagenaar, B. M W Tsui, B. E. Patt, and E. C. Frey. MicroCT with energy-resolved photon-counting detectors. *Phys. Med. Biol.*, 56(9):2791–2816, May 2011. doi: 10.1088/0031-9155/56/9/011.
- [206] J. Watt, D.W. Davidson, C. Johnston, C. Smith, L. Tlustos, B. Mikulec K.M. Smith, and M. Rahman. Dose reductions in dental x-ray imaging using medipix. *Nucl. Inst. Meth. A*, 513: 65–69, 2003.
- [207] S. V. Williams, S. D. Fihn, R. J. Gibbons, American College of Cardiology, American Heart Association, and American College of Physicians-American Society of Internal Medicine. Guidelines for the management of patients with chronic stable angina: diagnosis and risk stratification. *Ann. Intern. Med.*, 135(7):530–547, Oct 2001.
- [208] Jeffrey F. Williamson, Sicong Li, Slobodan Devic, Bruce R. Whiting, and Fritz A. Lerma. On two-parameter models of photon cross sections: Application to dual-energy CT imaging. *Med. Phys.*, 33(11):4115–4129, Nov 2006.

- [209] G. A. Wright, K. W. Taylor, and J. A. Rowlands. Noise in stenosis measurement using digital subtraction angiography. *Med. Phys.*, 12(6):705–712, 1985.
- [210] C Xu, M Danielsson, S Karlsson, C Svensson, and H Bornefalk. Performance characterization of a silicon strip detector for spectral computed tomography utilizing a laser testing system. *Proc. of SPIE*, 7961:79610S, 2011.
- [211] C Xu, M Yveborg, H Chen, M Danielsson, S Karlsson, C Svensson, and H Bornefalk. Evaluation of an ultra-fast photon-counting energy-resolved ASIC for spectral CT. *Proc. of SPIE*, 8313:831334, 2012.
- [212] Cheng Xu, Mats Danielsson, and Hans Bornefalk. Evaluation of energy loss and charge sharing in cadmium telluride detectors for photon-counting computed tomography. *IEEE Transactions on Nuclear Science*, 58:614–625, 2011.
- [213] Tong Xu, Justin L Ducote, Jerry T Wong, and Sabee Molloi. Feasibility of real time dual-energy imaging based on a flat panel detector for coronary artery calcium quantification. *Med. Phys.*, 33(6):1612–1622, Jun 2006.
- [214] J. Yao and I. A. Cunningham. Parallel cascades: New ways to describe noise transfer in medical imaging systems. *Med. Phys.*, 28(10):2020–2038, Oct 2001.
- [215] Mohammad Y. Yazdandoost, Kyung W. Shin, Nader Safavian, Farhad Taghibakhsh, and Karim S. Karim. Photon counting pixel and array in amorphous silicon technology for large area digital medical imaging applications. *Proc. of SPIE*, 7622:76221A1–76221A10, 2010.
- [216] John Yorkston. Recent developments in digital radiography detectors. *Nucl. Instrum. Meth. A*, 580:974–985, 2007.
- [217] D. F. Yu and J. A. Fessler. Mean and variance of single photon counting with deadtime. *Phys. Med. Biol.*, 45(7):2043–2056, Jul 2000.
- [218] S Yun, J Tanguay, H K Kim, and I A Cunningham. Cascaded-systems analysis and the detective quantum efficiency of single-Z x-ray detectors include photoelectric, coherent and incoherent interactions. *Medical Physics*, 40:0419161–04191616, 2013.
- [219] Seungman Yun, Ho Kyung Kim, H. Youn, Jesse Tanguay, and Ian A Cunningham. Analytic model of energy-absorption response functions in compound x-ray detector materials. *IEEE Trans. Med. Imaging [Epub ahead of print]*, 2013.

- [220] Moa Yveborg, Mats Danielsson, and Hans Bornefalk. Performance evaluation of a sub-millimetre spectrally resolved ct system on high- and low-frequency imaging tasks: A simulation. *Phys. Med. Biol.*, 57(8):2373–2391, Apr 2012. doi: 10.1088/0031-9155/57/8/2373.
- [221] Wei Zhao, Goran Ristic, and J. A. Rowlands. X-ray imaging performance of structured cesium iodide scintillators. *Med. Phys.*, 31(9):2594–2605, Sep 2004.
- [222] Z. Zhong, D. Chapman, R. Menk, J. Richardson, S. Theophanis, and W. Thomlinson. Monochromatic energy-subtraction radiography using a rotating anode source and a bent laue monochromator. *Phys. Med. Biol.*, 42(9):1751–1762, Sep 1997.

Appendix G

Permission to reproduce copyrighted
material

G.1 Permission to reproduce figures 1.3, 1.4, 1.5b, 1.6, 1.7, and 1.8

The following pages include permissions to reproduce figures 1.3, 1.4, 1.5b, 1.6, 1.7, 1.8, and 1.9 in the order that they appear in this thesis.

**ELSEVIER LICENSE
TERMS AND CONDITIONS**

Jul 08, 2013

This is a License Agreement between JESSE TANGUAY ("You") and Elsevier ("Elsevier") provided by Copyright Clearance Center ("CCC"). The license consists of your order details, the terms and conditions provided by Elsevier, and the payment terms and conditions.

All payments must be made in full to CCC. For payment instructions, please see information listed at the bottom of this form.

Supplier	Elsevier Limited [REDACTED]
Registered Company Number	1982084
Customer name	JESSE TANGUAY
Customer address	ROBARTS RESEACH INSTITUTE [REDACTED]
License number	3184351242860
License date	Jul 08, 2013
Licensed content publisher	Elsevier
Licensed content publication	Journal of the American College of Cardiology
Licensed content title	A Half Century of Selective Coronary Arteriography
Licensed content author	Albert V.G. Brusckke,William C. Sheldon,Earl K. Shirey,William L. Proudfit
Licensed content date	1 December 2009
Licensed content volume number	54
Licensed content issue number	23
Number of pages	6
Start Page	2139
End Page	2144
Type of Use	reuse in a thesis/dissertation
Portion	figures/tables/illustrations
Number of figures/tables/illustrations	1
Format	both print and electronic
Are you the author of this Elsevier article?	Yes

Will you be translating?	No
Order reference number	
Title of your thesis/dissertation	Image quality in energy-resolved x-ray angiography
Expected completion date	Sep 2013
Estimated size (number of pages)	200
Elsevier VAT number	GB 494 6272 12
Permissions price	0.00 USD
VAT/Local Sales Tax	0.00 USD / 0.00 GBP
Total	0.00 USD
Terms and Conditions	

INTRODUCTION

1. The publisher for this copyrighted material is Elsevier. By clicking "accept" in connection with completing this licensing transaction, you agree that the following terms and conditions apply to this transaction (along with the Billing and Payment terms and conditions established by Copyright Clearance Center, Inc. ("CCC"), at the time that you opened your Rightslink account and that are available at any time at <http://myaccount.copyright.com>).

GENERAL TERMS

2. Elsevier hereby grants you permission to reproduce the aforementioned material subject to the terms and conditions indicated.

3. Acknowledgement: If any part of the material to be used (for example, figures) has appeared in our publication with credit or acknowledgement to another source, permission must also be sought from that source. If such permission is not obtained then that material may not be included in your publication/copies. Suitable acknowledgement to the source must be made, either as a footnote or in a reference list at the end of your publication, as follows:

“Reprinted from Publication title, Vol /edition number, Author(s), Title of article / title of chapter, Pages No., Copyright (Year), with permission from Elsevier [OR APPLICABLE SOCIETY COPYRIGHT OWNER].” Also Lancet special credit - “Reprinted from The Lancet, Vol. number, Author(s), Title of article, Pages No., Copyright (Year), with permission from Elsevier.”

4. Reproduction of this material is confined to the purpose and/or media for which permission is hereby given.

5. Altering/Modifying Material: Not Permitted. However figures and illustrations may be altered/adapted minimally to serve your work. Any other abbreviations, additions, deletions and/or any other alterations shall be made only with prior written authorization of Elsevier Ltd. (Please contact Elsevier at permissions@elsevier.com)

6. If the permission fee for the requested use of our material is waived in this instance, please be advised that your future requests for Elsevier materials may attract a fee.

7. **Reservation of Rights:** Publisher reserves all rights not specifically granted in the combination of (i) the license details provided by you and accepted in the course of this licensing transaction, (ii) these terms and conditions and (iii) CCC's Billing and Payment terms and conditions.
8. **License Contingent Upon Payment:** While you may exercise the rights licensed immediately upon issuance of the license at the end of the licensing process for the transaction, provided that you have disclosed complete and accurate details of your proposed use, no license is finally effective unless and until full payment is received from you (either by publisher or by CCC) as provided in CCC's Billing and Payment terms and conditions. If full payment is not received on a timely basis, then any license preliminarily granted shall be deemed automatically revoked and shall be void as if never granted. Further, in the event that you breach any of these terms and conditions or any of CCC's Billing and Payment terms and conditions, the license is automatically revoked and shall be void as if never granted. Use of materials as described in a revoked license, as well as any use of the materials beyond the scope of an unrevoked license, may constitute copyright infringement and publisher reserves the right to take any and all action to protect its copyright in the materials.
9. **Warranties:** Publisher makes no representations or warranties with respect to the licensed material.
10. **Indemnity:** You hereby indemnify and agree to hold harmless publisher and CCC, and their respective officers, directors, employees and agents, from and against any and all claims arising out of your use of the licensed material other than as specifically authorized pursuant to this license.
11. **No Transfer of License:** This license is personal to you and may not be sublicensed, assigned, or transferred by you to any other person without publisher's written permission.
12. **No Amendment Except in Writing:** This license may not be amended except in a writing signed by both parties (or, in the case of publisher, by CCC on publisher's behalf).
13. **Objection to Contrary Terms:** Publisher hereby objects to any terms contained in any purchase order, acknowledgment, check endorsement or other writing prepared by you, which terms are inconsistent with these terms and conditions or CCC's Billing and Payment terms and conditions. These terms and conditions, together with CCC's Billing and Payment terms and conditions (which are incorporated herein), comprise the entire agreement between you and publisher (and CCC) concerning this licensing transaction. In the event of any conflict between your obligations established by these terms and conditions and those established by CCC's Billing and Payment terms and conditions, these terms and conditions shall control.
14. **Revocation:** Elsevier or Copyright Clearance Center may deny the permissions described in this License at their sole discretion, for any reason or no reason, with a full refund payable to you. Notice of such denial will be made using the contact information provided by you. Failure to receive such notice will not alter or invalidate the denial. In no event will Elsevier or Copyright Clearance Center be responsible or liable for any costs, expenses or damage incurred by you as a result of a denial of your permission request, other than a refund of the amount(s) paid by you to Elsevier and/or Copyright Clearance Center for denied permissions.

LIMITED LICENSE

The following terms and conditions apply only to specific license types:

15. **Translation:** This permission is granted for non-exclusive world **English** rights only unless your license was granted for translation rights. If you licensed translation rights you may only translate this content into the languages you requested. A professional translator must perform all translations and reproduce the content word for word preserving the integrity of the article. If this license is to re-use 1 or 2 figures then permission is granted for non-exclusive world rights in all languages.

16. **Website:** The following terms and conditions apply to electronic reserve and author websites:
Electronic reserve: If licensed material is to be posted to website, the web site is to be password-protected and made available only to bona fide students registered on a relevant course if

This license was made in connection with a course,

This permission is granted for 1 year only. You may obtain a license for future website posting,

All content posted to the web site must maintain the copyright information line on the bottom of each image,

A hyper-text must be included to the Homepage of the journal from which you are licensing at <http://www.sciencedirect.com/science/journal/xxxxx> or the Elsevier homepage for books at <http://www.elsevier.com> , and

Central Storage: This license does not include permission for a scanned version of the material to be stored in a central repository such as that provided by Heron/XanEdu.

17. **Author website** for journals with the following additional clauses:

All content posted to the web site must maintain the copyright information line on the bottom of each image, and the permission granted is limited to the personal version of your paper. You are not allowed to download and post the published electronic version of your article (whether PDF or HTML, proof or final version), nor may you scan the printed edition to create an electronic version. A hyper-text must be included to the Homepage of the journal from which you are licensing at <http://www.sciencedirect.com/science/journal/xxxxx> . As part of our normal production process, you will receive an e-mail notice when your article appears on Elsevier's online service ScienceDirect (www.sciencedirect.com). That e-mail will include the article's Digital Object Identifier (DOI). This number provides the electronic link to the published article and should be included in the posting of your personal version. We ask that you wait until you receive this e-mail and have the DOI to do any posting.

Central Storage: This license does not include permission for a scanned version of the material to be stored in a central repository such as that provided by Heron/XanEdu.

18. **Author website** for books with the following additional clauses:

Authors are permitted to place a brief summary of their work online only.

A hyper-text must be included to the Elsevier homepage at <http://www.elsevier.com> . All content posted to the web site must maintain the copyright information line on the bottom of each image.

You are not allowed to download and post the published electronic version of your chapter, nor may you scan the printed edition to create an electronic version.

Central Storage: This license does not include permission for a scanned version of the material to be stored in a central repository such as that provided by Heron/XanEdu.

19. **Website** (regular and for author): A hyper-text must be included to the Homepage of the journal from which you are licensing at <http://www.sciencedirect.com/science/journal/xxxxx>. or for books to the Elsevier homepage at <http://www.elsevier.com>

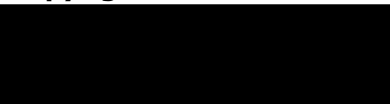
20. **Thesis/Dissertation**: If your license is for use in a thesis/dissertation your thesis may be submitted to your institution in either print or electronic form. Should your thesis be published commercially, please reapply for permission. These requirements include permission for the Library and Archives of Canada to supply single copies, on demand, of the complete thesis and include permission for UMI to supply single copies, on demand, of the complete thesis. Should your thesis be published commercially, please reapply for permission.

21. **Other Conditions**:

v1.6

If you would like to pay for this license now, please remit this license along with your payment made payable to "COPYRIGHT CLEARANCE CENTER" otherwise you will be invoiced within 48 hours of the license date. Payment should be in the form of a check or money order referencing your account number and this invoice number RLNK501060948. Once you receive your invoice for this order, you may pay your invoice by credit card. Please follow instructions provided at that time.


**Make Payment To:
Copyright Clearance Center**



For suggestions or comments regarding this order, contact RightsLink Customer Support: customercare@copyright.com or +1-877-622-5543 (toll free in the US) or +1-978-646-2777.

Gratis licenses (referencing \$0 in the Total field) are free. Please retain this printable license for your reference. No payment is required.


July 9, 2013

Jesse Tanguay


Dear Jesse Tanguay:

The Radiological Society of North America (RSNA[®]) is pleased to grant you permission to reproduce the following figure in print and electronic format for educational use in your thesis "Image Quality in Energy-Resolved X-ray Angiography," provided you obtain author permission* and give full credit to the authors and the original publication.

Figure 1c
Sakuma H. Coronary CT versus MR angiography: the role of MR angiography.
Radiology 2011;258:340-349.


*Author e-mail: 

This permission is a one-time, non-exclusive grant for English language use and is exclusively limited to the usage stated and underlined above. The requestor guarantees to reproduce the material as originally published. Permission is granted under the condition that a full credit line is prominently placed (i.e. author name(s), journal name, copyright year, volume #, inclusive pages and copyright holder).

This permission becomes effective upon receipt of this signed contract. Please sign a copy of this agreement and return a signed copy to me and retain a copy for your files. Thank you for your interest in our publication.

[Print Name]: Jesse Tanguay

SIGNATURE:  Date: July 17, 2013

Sincerely,


Ashley E. Daly
Senior Manager, Journal Rights & Communications
Publications



ELSEVIER LICENSE TERMS AND CONDITIONS

Jul 08, 2013

This is a License Agreement between JESSE TANGUAY ("You") and Elsevier ("Elsevier") provided by Copyright Clearance Center ("CCC"). The license consists of your order details, the terms and conditions provided by Elsevier, and the payment terms and conditions.

All payments must be made in full to CCC. For payment instructions, please see information listed at the bottom of this form.

Supplier	Elsevier Limited [REDACTED]
Registered Company Number	1982084
Customer name	JESSE TANGUAY
Customer address	ROBARTS RESEACH INSTITUTE [REDACTED]
License number	3184360794883
License date	Jul 08, 2013
Licensed content publisher	Elsevier
Licensed content publication	Computerized Medical Imaging and Graphics
Licensed content title	A 3D space-time motion evaluation for image registration in digital subtraction angiography
Licensed content author	N. Taleb,Y. Bentoutou,O. Deforges,M. Taleb
Licensed content date	6 May 2001
Licensed content volume number	25
Licensed content issue number	3
Number of pages	11
Start Page	223
End Page	233
Type of Use	reuse in a thesis/dissertation
Intended publisher of new work	other
Portion	figures/tables/illustrations
Number of figures/tables/illustrations	1
Format	both print and electronic

Are you the author of this Elsevier article? No

Will you be translating? No

Order reference number

Title of your thesis/dissertation Image quality in energy-resolved x-ray angiography

Expected completion date Sep 2013

Estimated size (number of pages) 200

Elsevier VAT number GB 494 6272 12

Permissions price 0.00 USD

VAT/Local Sales Tax 0.00 USD / 0.00 GBP

Total 0.00 USD

Terms and Conditions

INTRODUCTION

1. The publisher for this copyrighted material is Elsevier. By clicking "accept" in connection with completing this licensing transaction, you agree that the following terms and conditions apply to this transaction (along with the Billing and Payment terms and conditions established by Copyright Clearance Center, Inc. ("CCC"), at the time that you opened your Rightslink account and that are available at any time at <http://myaccount.copyright.com>).

GENERAL TERMS

2. Elsevier hereby grants you permission to reproduce the aforementioned material subject to the terms and conditions indicated.

3. Acknowledgement: If any part of the material to be used (for example, figures) has appeared in our publication with credit or acknowledgement to another source, permission must also be sought from that source. If such permission is not obtained then that material may not be included in your publication/copies. Suitable acknowledgement to the source must be made, either as a footnote or in a reference list at the end of your publication, as follows:

“Reprinted from Publication title, Vol /edition number, Author(s), Title of article / title of chapter, Pages No., Copyright (Year), with permission from Elsevier [OR APPLICABLE SOCIETY COPYRIGHT OWNER].” Also Lancet special credit - “Reprinted from The Lancet, Vol. number, Author(s), Title of article, Pages No., Copyright (Year), with permission from Elsevier.”

4. Reproduction of this material is confined to the purpose and/or media for which permission is hereby given.

5. Altering/Modifying Material: Not Permitted. However figures and illustrations may be altered/adapted minimally to serve your work. Any other abbreviations, additions, deletions and/or any other alterations shall be made only with prior written authorization of Elsevier Ltd. (Please contact Elsevier at permissions@elsevier.com)

6. If the permission fee for the requested use of our material is waived in this instance, please be advised that your future requests for Elsevier materials may attract a fee.
7. Reservation of Rights: Publisher reserves all rights not specifically granted in the combination of (i) the license details provided by you and accepted in the course of this licensing transaction, (ii) these terms and conditions and (iii) CCC's Billing and Payment terms and conditions.
8. License Contingent Upon Payment: While you may exercise the rights licensed immediately upon issuance of the license at the end of the licensing process for the transaction, provided that you have disclosed complete and accurate details of your proposed use, no license is finally effective unless and until full payment is received from you (either by publisher or by CCC) as provided in CCC's Billing and Payment terms and conditions. If full payment is not received on a timely basis, then any license preliminarily granted shall be deemed automatically revoked and shall be void as if never granted. Further, in the event that you breach any of these terms and conditions or any of CCC's Billing and Payment terms and conditions, the license is automatically revoked and shall be void as if never granted. Use of materials as described in a revoked license, as well as any use of the materials beyond the scope of an unrevoked license, may constitute copyright infringement and publisher reserves the right to take any and all action to protect its copyright in the materials.
9. Warranties: Publisher makes no representations or warranties with respect to the licensed material.
10. Indemnity: You hereby indemnify and agree to hold harmless publisher and CCC, and their respective officers, directors, employees and agents, from and against any and all claims arising out of your use of the licensed material other than as specifically authorized pursuant to this license.
11. No Transfer of License: This license is personal to you and may not be sublicensed, assigned, or transferred by you to any other person without publisher's written permission.
12. No Amendment Except in Writing: This license may not be amended except in a writing signed by both parties (or, in the case of publisher, by CCC on publisher's behalf).
13. Objection to Contrary Terms: Publisher hereby objects to any terms contained in any purchase order, acknowledgment, check endorsement or other writing prepared by you, which terms are inconsistent with these terms and conditions or CCC's Billing and Payment terms and conditions. These terms and conditions, together with CCC's Billing and Payment terms and conditions (which are incorporated herein), comprise the entire agreement between you and publisher (and CCC) concerning this licensing transaction. In the event of any conflict between your obligations established by these terms and conditions and those established by CCC's Billing and Payment terms and conditions, these terms and conditions shall control.
14. Revocation: Elsevier or Copyright Clearance Center may deny the permissions described in this License at their sole discretion, for any reason or no reason, with a full refund payable to you. Notice of such denial will be made using the contact information provided by you. Failure to receive such notice will not alter or invalidate the denial. In no event will Elsevier or Copyright Clearance Center be responsible or liable for any costs, expenses or damage incurred by you as a result of a denial of your permission request, other than a refund of the amount(s) paid by you to

Elsevier and/or Copyright Clearance Center for denied permissions.

LIMITED LICENSE

The following terms and conditions apply only to specific license types:

15. **Translation:** This permission is granted for non-exclusive world **English** rights only unless your license was granted for translation rights. If you licensed translation rights you may only translate this content into the languages you requested. A professional translator must perform all translations and reproduce the content word for word preserving the integrity of the article. If this license is to re-use 1 or 2 figures then permission is granted for non-exclusive world rights in all languages.

16. **Website:** The following terms and conditions apply to electronic reserve and author websites:
Electronic reserve: If licensed material is to be posted to website, the web site is to be password-protected and made available only to bona fide students registered on a relevant course if:

This license was made in connection with a course,

This permission is granted for 1 year only. You may obtain a license for future website posting,

All content posted to the web site must maintain the copyright information line on the bottom of each image,

A hyper-text must be included to the Homepage of the journal from which you are licensing at

<http://www.sciencedirect.com/science/journal/xxxxx> or the Elsevier homepage for books at

<http://www.elsevier.com> , and

Central Storage: This license does not include permission for a scanned version of the material to be stored in a central repository such as that provided by Heron/XanEdu.

17. **Author website** for journals with the following additional clauses:

All content posted to the web site must maintain the copyright information line on the bottom of each image, and the permission granted is limited to the personal version of your paper. You are not allowed to download and post the published electronic version of your article (whether PDF or HTML, proof or final version), nor may you scan the printed edition to create an electronic version.

A hyper-text must be included to the Homepage of the journal from which you are licensing at

<http://www.sciencedirect.com/science/journal/xxxxx> . As part of our normal production process,

you will receive an e-mail notice when your article appears on Elsevier's online service

ScienceDirect (www.sciencedirect.com). That e-mail will include the article's Digital Object

Identifier (DOI). This number provides the electronic link to the published article and should be

included in the posting of your personal version. We ask that you wait until you receive this e-mail and have the DOI to do any posting.

Central Storage: This license does not include permission for a scanned version of the material to be stored in a central repository such as that provided by Heron/XanEdu.

18. **Author website** for books with the following additional clauses:

Authors are permitted to place a brief summary of their work online only.

A hyper-text must be included to the Elsevier homepage at <http://www.elsevier.com> . All content

posted to the web site must maintain the copyright information line on the bottom of each image. You are not allowed to download and post the published electronic version of your chapter, nor may you scan the printed edition to create an electronic version.

Central Storage: This license does not include permission for a scanned version of the material to be stored in a central repository such as that provided by Heron/XanEdu.

19. **Website** (regular and for author): A hyper-text must be included to the Homepage of the journal from which you are licensing at <http://www.sciencedirect.com/science/journal/xxxxx>. or for books to the Elsevier homepage at <http://www.elsevier.com>

20. **Thesis/Dissertation**: If your license is for use in a thesis/dissertation your thesis may be submitted to your institution in either print or electronic form. Should your thesis be published commercially, please reapply for permission. These requirements include permission for the Library and Archives of Canada to supply single copies, on demand, of the complete thesis and include permission for UMI to supply single copies, on demand, of the complete thesis. Should your thesis be published commercially, please reapply for permission.

21. **Other Conditions**:

v1.6

If you would like to pay for this license now, please remit this license along with your payment made payable to "COPYRIGHT CLEARANCE CENTER" otherwise you will be invoiced within 48 hours of the license date. Payment should be in the form of a check or money order referencing your account number and this invoice number RLNK501060965. Once you receive your invoice for this order, you may pay your invoice by credit card. Please follow instructions provided at that time.

**Make Payment To:
Copyright Clearance Center**



For suggestions or comments regarding this order, contact RightsLink Customer Support: customercare@copyright.com or +1-877-622-5543 (toll free in the US) or +1-978-646-2777.

Gratis licenses (referencing \$0 in the Total field) are free. Please retain this printable license for your reference. No payment is required.

ELSEVIER LICENSE TERMS AND CONDITIONS

Jul 08, 2013

This is a License Agreement between JESSE TANGUAY ("You") and Elsevier ("Elsevier") provided by Copyright Clearance Center ("CCC"). The license consists of your order details, the terms and conditions provided by Elsevier, and the payment terms and conditions.

All payments must be made in full to CCC. For payment instructions, please see information listed at the bottom of this form.

Supplier	Elsevier Limited [REDACTED]
Registered Company Number	1982084
Customer name	JESSE TANGUAY
Customer address	ROBARTS RESEACH INSTITUTE [REDACTED]
License number	3184361467323
License date	Jul 08, 2013
Licensed content publisher	Elsevier
Licensed content publication	Pattern Recognition
Licensed content title	An invariant approach for image registration in digital subtraction angiography
Licensed content author	Y. Bentoutou,N. Taleb,M. Chikr El Mezouar,M. Taleb,L. Jetto
Licensed content date	December 2002
Licensed content volume number	35
Licensed content issue number	12
Number of pages	13
Start Page	2853
End Page	2865
Type of Use	reuse in a thesis/dissertation
Intended publisher of new work	other
Portion	figures/tables/illustrations
Number of figures/tables/illustrations	2
Format	both print and electronic

Are you the author of this Elsevier article? No

Will you be translating? No

Order reference number

Title of your thesis/dissertation Image quality in energy-resolved x-ray angiography

Expected completion date Sep 2013

Estimated size (number of pages) 200

Elsevier VAT number GB 494 6272 12

Permissions price 0.00 USD

VAT/Local Sales Tax 0.00 USD / 0.00 GBP

Total 0.00 USD

Terms and Conditions

INTRODUCTION

1. The publisher for this copyrighted material is Elsevier. By clicking "accept" in connection with completing this licensing transaction, you agree that the following terms and conditions apply to this transaction (along with the Billing and Payment terms and conditions established by Copyright Clearance Center, Inc. ("CCC"), at the time that you opened your Rightslink account and that are available at any time at <http://myaccount.copyright.com>).

GENERAL TERMS

2. Elsevier hereby grants you permission to reproduce the aforementioned material subject to the terms and conditions indicated.

3. Acknowledgement: If any part of the material to be used (for example, figures) has appeared in our publication with credit or acknowledgement to another source, permission must also be sought from that source. If such permission is not obtained then that material may not be included in your publication/copies. Suitable acknowledgement to the source must be made, either as a footnote or in a reference list at the end of your publication, as follows:

“Reprinted from Publication title, Vol /edition number, Author(s), Title of article / title of chapter, Pages No., Copyright (Year), with permission from Elsevier [OR APPLICABLE SOCIETY COPYRIGHT OWNER].” Also Lancet special credit - “Reprinted from The Lancet, Vol. number, Author(s), Title of article, Pages No., Copyright (Year), with permission from Elsevier.”

4. Reproduction of this material is confined to the purpose and/or media for which permission is hereby given.

5. Altering/Modifying Material: Not Permitted. However figures and illustrations may be altered/adapted minimally to serve your work. Any other abbreviations, additions, deletions and/or any other alterations shall be made only with prior written authorization of Elsevier Ltd. (Please contact Elsevier at permissions@elsevier.com)

6. If the permission fee for the requested use of our material is waived in this instance, please be advised that your future requests for Elsevier materials may attract a fee.
7. Reservation of Rights: Publisher reserves all rights not specifically granted in the combination of (i) the license details provided by you and accepted in the course of this licensing transaction, (ii) these terms and conditions and (iii) CCC's Billing and Payment terms and conditions.
8. License Contingent Upon Payment: While you may exercise the rights licensed immediately upon issuance of the license at the end of the licensing process for the transaction, provided that you have disclosed complete and accurate details of your proposed use, no license is finally effective unless and until full payment is received from you (either by publisher or by CCC) as provided in CCC's Billing and Payment terms and conditions. If full payment is not received on a timely basis, then any license preliminarily granted shall be deemed automatically revoked and shall be void as if never granted. Further, in the event that you breach any of these terms and conditions or any of CCC's Billing and Payment terms and conditions, the license is automatically revoked and shall be void as if never granted. Use of materials as described in a revoked license, as well as any use of the materials beyond the scope of an unrevoked license, may constitute copyright infringement and publisher reserves the right to take any and all action to protect its copyright in the materials.
9. Warranties: Publisher makes no representations or warranties with respect to the licensed material.
10. Indemnity: You hereby indemnify and agree to hold harmless publisher and CCC, and their respective officers, directors, employees and agents, from and against any and all claims arising out of your use of the licensed material other than as specifically authorized pursuant to this license.
11. No Transfer of License: This license is personal to you and may not be sublicensed, assigned, or transferred by you to any other person without publisher's written permission.
12. No Amendment Except in Writing: This license may not be amended except in a writing signed by both parties (or, in the case of publisher, by CCC on publisher's behalf).
13. Objection to Contrary Terms: Publisher hereby objects to any terms contained in any purchase order, acknowledgment, check endorsement or other writing prepared by you, which terms are inconsistent with these terms and conditions or CCC's Billing and Payment terms and conditions. These terms and conditions, together with CCC's Billing and Payment terms and conditions (which are incorporated herein), comprise the entire agreement between you and publisher (and CCC) concerning this licensing transaction. In the event of any conflict between your obligations established by these terms and conditions and those established by CCC's Billing and Payment terms and conditions, these terms and conditions shall control.
14. Revocation: Elsevier or Copyright Clearance Center may deny the permissions described in this License at their sole discretion, for any reason or no reason, with a full refund payable to you. Notice of such denial will be made using the contact information provided by you. Failure to receive such notice will not alter or invalidate the denial. In no event will Elsevier or Copyright Clearance Center be responsible or liable for any costs, expenses or damage incurred by you as a result of a denial of your permission request, other than a refund of the amount(s) paid by you to

Elsevier and/or Copyright Clearance Center for denied permissions.

LIMITED LICENSE

The following terms and conditions apply only to specific license types:

15. **Translation:** This permission is granted for non-exclusive world **English** rights only unless your license was granted for translation rights. If you licensed translation rights you may only translate this content into the languages you requested. A professional translator must perform all translations and reproduce the content word for word preserving the integrity of the article. If this license is to re-use 1 or 2 figures then permission is granted for non-exclusive world rights in all languages.

16. **Website:** The following terms and conditions apply to electronic reserve and author websites:
Electronic reserve: If licensed material is to be posted to website, the web site is to be password-protected and made available only to bona fide students registered on a relevant course if:

This license was made in connection with a course,

This permission is granted for 1 year only. You may obtain a license for future website posting,

All content posted to the web site must maintain the copyright information line on the bottom of each image,

A hyper-text must be included to the Homepage of the journal from which you are licensing at

<http://www.sciencedirect.com/science/journal/xxxxx> or the Elsevier homepage for books at

<http://www.elsevier.com> , and

Central Storage: This license does not include permission for a scanned version of the material to be stored in a central repository such as that provided by Heron/XanEdu.

17. **Author website** for journals with the following additional clauses:

All content posted to the web site must maintain the copyright information line on the bottom of each image, and the permission granted is limited to the personal version of your paper. You are not allowed to download and post the published electronic version of your article (whether PDF or HTML, proof or final version), nor may you scan the printed edition to create an electronic version.

A hyper-text must be included to the Homepage of the journal from which you are licensing at

<http://www.sciencedirect.com/science/journal/xxxxx> . As part of our normal production process,

you will receive an e-mail notice when your article appears on Elsevier's online service

ScienceDirect (www.sciencedirect.com). That e-mail will include the article's Digital Object

Identifier (DOI). This number provides the electronic link to the published article and should be

included in the posting of your personal version. We ask that you wait until you receive this e-mail and have the DOI to do any posting.

Central Storage: This license does not include permission for a scanned version of the material to be stored in a central repository such as that provided by Heron/XanEdu.

18. **Author website** for books with the following additional clauses:

Authors are permitted to place a brief summary of their work online only.

A hyper-text must be included to the Elsevier homepage at <http://www.elsevier.com> . All content

posted to the web site must maintain the copyright information line on the bottom of each image. You are not allowed to download and post the published electronic version of your chapter, nor may you scan the printed edition to create an electronic version.

Central Storage: This license does not include permission for a scanned version of the material to be stored in a central repository such as that provided by Heron/XanEdu.

19. **Website** (regular and for author): A hyper-text must be included to the Homepage of the journal from which you are licensing at <http://www.sciencedirect.com/science/journal/xxxxx>. or for books to the Elsevier homepage at <http://www.elsevier.com>

20. **Thesis/Dissertation**: If your license is for use in a thesis/dissertation your thesis may be submitted to your institution in either print or electronic form. Should your thesis be published commercially, please reapply for permission. These requirements include permission for the Library and Archives of Canada to supply single copies, on demand, of the complete thesis and include permission for UMI to supply single copies, on demand, of the complete thesis. Should your thesis be published commercially, please reapply for permission.

21. **Other Conditions**:

v1.6

If you would like to pay for this license now, please remit this license along with your payment made payable to "COPYRIGHT CLEARANCE CENTER" otherwise you will be invoiced within 48 hours of the license date. Payment should be in the form of a check or money order referencing your account number and this invoice number RLNK501060979. Once you receive your invoice for this order, you may pay your invoice by credit card. Please follow instructions provided at that time.

**Make Payment To:
Copyright Clearance Center**



For suggestions or comments regarding this order, contact RightsLink Customer Support: customercare@copyright.com or +1-877-622-5543 (toll free in the US) or +1-978-646-2777.

Gratis licenses (referencing \$0 in the Total field) are free. Please retain this printable license for your reference. No payment is required.

G.2 Permission to reproduce Chapters 2, 3, and Appendix E



American Association of Physicists in Medicine

One Physics Ellipse
College Park, MD 20740-3846
(301) 209-3350
Fax (301) 209-0862
<http://www.aapm.org>

Office of the Executive Director

Angela R. Keyser
Phone: [REDACTED]
E-mail: [REDACTED]

DATE OF REQUEST: July 17, 2013

FROM:

Jesse Tanguay
[REDACTED]

EMAIL ADDRESS: [REDACTED]

1. Permission is granted to:

Jesse Tanguay
PhD candidate in the department of Medical Biophysics at the University of Western Ontario

2. Permission is requested to use the following material:

1. Jesse Tanguay, Ho Kyung Kim, and Ian. A. Cunningham, "The role of x-ray Swank factor in energy-resolving photon-counting imaging," *Med. Phys.* 37(12):6205-6211, 2010.

2. Jesse Tanguay, Ho Kyung Kim, and Ian. A. Cunningham, "A theoretical comparison of x-ray angiographic image quality using energy-dependent and conventional subtraction methods," *Med. Phys.* 39(1):132-142, 2012.

3. Jesse Tanguay, Seungman Yun, Ho Kyung Kim, and Ian. A. Cunningham, "The detective quantum efficiency of photon-counting x-ray detectors using cascaded-systems analyses," *Med. Phys.* 40(4):0419131-04191315, 2013.

3. For what purpose:

The articles will comprise the body chapters of my PhD thesis entitled "Image quality in energy-resolved approaches for x-ray angiography."

Authors seeking permission must also notify the first author of the article from which permission is being sought.

Permission is hereby granted:

[REDACTED]

Signature

July 18, 2013

Date

Curriculum Vitae

Name: Jesse Tanguay

Year of birth: 1985

Education and Training

09/09-present Ph.D. Candidate
Department of Medical Biophysics
Western University
London, Ontario, Canada
Thesis: Image quality of energy-dependent approaches for x-ray angiography
Supervisor: Dr. Ian Cunningham

09/05-05/09 B.Sc. (Hon.) Honors Specialization in Physics with a Major in Applied
Mathematics
Western University
London, Ontario, Canada
Thesis: Applications of the Lambert W function to statistical physics

Academic Awards, Scholarships, and Distinctions

- 05/11-05/14 Natural Sciences and Engineering Council of Canada Alexander Graham Bell
Canada Graduate Scholarship (NSERC CGS-D)
National
\$35,000 per year for 3 consecutive years
- 09/11-09/12 Ontario Graduate Scholarship (OGS)
Awarded to students enrolled in graduate studies at the master's and doctoral
levels.
Provincial
\$5,000 per term for 2 consecutive terms
- 09/10-09/11 Ontario Graduate Scholarship in Science and Technology (OGSST)
Awarded to students enrolled in graduate studies at the master's and doctoral
levels.
Provincial
\$5,000 per term for 2 consecutive terms
- 09/10-09/11 Schulich Graduate Scholarship
Awarded to graduate students who enroll with an average of 80% or above.
Institutional
The University of Western Ontario,
London, Ontario, Canada
\$6,670 per year for one year

- 09/09-09/11 Canadian Institutes of Health Research Strategic Training Program in Vascular Research
 The program is awarded to selected applicants enrolled in a Masters or Doctoral program in an area of vascular research.
 Institutional
 The University of Western Ontario,
 London, Ontario, Canada
\$10,000 per year for two consecutive years
- 09/09-09/10 Ontario Graduate Scholarship in Science and Technology (OGSST)
 Awarded to students enrolled in graduate studies at the master's and doctoral levels.
 Provincial
\$5,000 per term for 2 consecutive terms.
- 09/09-09/10 Schulich Graduate Scholarship
 Awarded to graduate students who enroll with an average of 80% or above.
 Institutional
 The University of Western Ontario,
 London, Ontario, Canada
\$6,670 per year for one year
- 09/09-09/10 Natural Sciences and Engineering Research Council Undergraduate Student Research Awards (NSERC USRA)
 The awards are meant to stimulate interest in research in the natural sciences and engineering and are awarded to students with a minimum average of 80%.
 National
\$4, 500

- 05/09 Graduation with Distinction
Conferred upon students in degree programs who have achieved an overall average of 80% and no grade lower than 70% on the entire program with no failed courses.
- 05/09 Dean's Honor List
Awarded to a full time student who has maintained an average of 80% or more.
Institutional
The University of Western Ontario,
London, Ontario, Canada
- 05/08-09/08 Natural Sciences and Engineering Research Council Undergraduate Student
Research Awards (NSERC USRA)
The awards are meant to stimulate interest in research in the natural sciences and engineering and are awarded to students with a minimum average of 80%.
National
\$4, 500
- 05/08 Dean's Honor List
Awarded to a full time student who has maintained an average of 80% or more.
Institutional
The University of Western Ontario,
London, Ontario, Canada
- 05/07 Dean's Honor List
Awarded to a full time student who has maintained an average of 80% or more.
Institutional
The University of Western Ontario,
London, Ontario, Canada

05/06

Dean's Honor List

Awarded to a full time student who has maintained an average of 80% or more.

Institutional

The University of Western Ontario,

London, Ontario, Canada

Publications and Presentations

Peer-reviewed journal manuscripts (10 published)

Jesse Tanguay, Seungman Yun, Ho Kyung Kim, and Ian A. Cunningham. The detective quantum efficiency of photon-counting x-ray detectors using cascaded-systems analyses. *Med. Phys.* 40 (4), 2013.

Seungman Yun, Ho Kyung Kim, H. Youn, **Jesse Tanguay**, and Ian A. Cunningham. Analytic energy-absorption response functions in compound semiconductor x-ray detectors. *IEEE Trans. Med. Imaging [Epub ahead of print]*, 2013.

Seungman Yun, **Jesse Tanguay**, Ho Kyung Kim, and Ian A. Cunningham. Cascaded-systems analysis and the detective quantum efficiency of single-Z x-ray detectors including photoelectric, coherent, and incoherent interactions. *Med. Phys.* 40 (4), 2013.

Ho Kyung Kim, Chang Hwy Lim, **Jesse Tanguay**, Seungman Yun, and Ian A. Cunningham. (2012) Spectral analysis of fundamental signal and noise performances in photoconductors for mammography. *Med. Phys.* 39 (5), 2012.

Jesse Tanguay, Ho Kyung Kim, and Ian A. Cunningham. A theoretical comparison of x-ray angiographic image quality using energy-dependent and conventional subtraction methods. *Med. Phys.* 39 (1), 2012.

Seungman Yun, Ho Kyung Kim, H. Youn, O. Joe, S. Kim, J. Park, D. G. Kang, Y. H. Sung, J. Marchal, **Jesse Tanguay**, and Ian A. Cunningham. Detective quantum efficiency of a silicon microstrip photon-counting detector having edge-on geometry under mammography imaging condition. *J. Instrum.*, 6(12), 2011.

Hanbean Youn, Jong Chul Han, Min Kook Cho, Sun Young Jang, Ho Kyung Kim, Jong Hyo Kim, **Jesse Tanguay**, and Ian A. Cunningham. Numerical generation of digital mammograms considering imaging characteristics of an imager. *Nucl. Instru. Methods A*, 652 (1), 810-814, 2011.

Seungman Yun, Chang Hwy Lim, Ho Kyung Kim, **Jesse Tanguay**, and Ian A. Cunningham. Finding the best photoconductor for digital mammography detectors. *Nucl. Instru. Methods A*, 652 (1), 829-833, 2011.

Jesse Tanguay, Ho Kyung Kim, and Ian A. Cunningham. The role of Swank noise in energy-resolving photon-counting x-ray imaging detectors. *Med. Phys.* 37, 2010.

Jesse Tanguay, Manuel Gil, David Jeffrey, and Sree R Valluri. D-dimensional Bose gases and the Lambert W function. *J. Math. Phys.* 51 (12), 2010.

Peer-reviewed published conference proceedings (6)

Jesse Tanguay, Seungman Yun, Ho Kyung Kim, and Ian A. Cunningham. Cascaded systems analyses of photon-counting x-ray detectors. Proceedings of the Society of Photographic Instrumentation Engineers, 2013.

Seungman Yun, **Jesse Tanguay**, Ho Kyung Kim, and Ian A. Cunningham. Cascaded-systems analyses of the DQE of double-Z x-ray detectors including photoelectric, coherent and incoherent interactions. Proceedings of the Society of Photographic Instrumentation Engineers, 2013.

Seungman Yun, Ho Kyung Kim, Hanbean Youn, **Jesse Tanguay**, and Ian A. Cunningham. Analytic Response Functions in Compound Semiconductor Detectors. IEEE Nuclear Science Symposium and Medical Imaging Conference Record, 2012.

Jesse Tanguay, Ho Kyung Kim, and Ian A. Cunningham. Extension of cascaded systems analysis to single-photon-counting x-ray detectors. Proceedings of the Society of Photographic Instrumentation Engineers, 2012.

Jesse Tanguay, Ho Kyung Kim, and Ian A. Cunningham. The case for single-exposure angiography using energy-resolving photon-counting detectors: A theoretical comparison of signal and noise with conventional subtraction angiography. Proceedings of the Society of Photographic Instrumentation Engineers, 2011

Jesse Tanguay, Ho Kyung Kim, and Ian A. Cunningham. Noise in energy-discriminating photon-counting x-ray detectors. Proceedings of the Society of Photographic Instrumentation Engineers, 2010.

Peer-reviewed oral presentations (6)

Jesse Tanguay, Ho Kyung Kim, and Ian A. Cunningham. Cascaded systems analysis of photon-counting x-ray detectors. Society of Photographic Instrumentation Engineers, Orlando, Florida, USA, 2013.

Jesse Tanguay, Ho Kyung Kim, and Ian A. Cunningham. Extension of cascaded systems analysis to single-photon-counting x-ray detectors. Society of Photographic Instrumentation Engineers, San Diego, California, USA, 2012 .

Jesse Tanguay and Ian A. Cunningham. Next-generation angiography: A theoretical comparison of energy-resolved and multi-energy approaches. American Association of Physicists in Medicine and Canadian Organization of Medical Physicists joint meeting, Vancouver, BC, Canada, 2011.

Jesse Tanguay and Ian A. Cunningham. Will energy-dependent x-ray imaging approaches eliminate motion artifacts in angiography? London Imaging Discovery Day, London, ON, Canada, 2011.

Jesse Tanguay, Ho Kyung Kim, and Ian A. Cunningham. The case for single-exposure angiography using energy-resolving photon-counting detectors: A theoretical comparison of signal and noise with conventional subtraction angiography. Society of Photographic Instrumentation Engineers, Orlando, Florida, USA, 2011.

Jesse Tanguay, Ho Kyung Kim, and Ian A. Cunningham. (2010) Noise in energy-discriminating photon-counting x-ray detectors. Society of Photographic Instrumentation Engineers, San Diego, California, USA, 2011.

Peer-reviewed poster presentations (6)

Jesse Tanguay Seungman Yun, Ho Kyung Kim, and Ian A. Cunningham. Will photon-counting detectors improve x-ray image quality? Imaging Network of Ontario Symposium, Toronto, ON, Canada, 2013.

Jesse Tanguay Seungman Yun, Ho Kyung Kim, and Ian A. Cunningham. Phantom comparison of energy-subtraction angiography with conventional non-subtraction cardiac angiography. Imaging Network of Ontario Symposium, Toronto, ON, Canada, 2013.

Seungman Yun, **Jesse Tanguay**, Ho Kyung Kim, and Ian A. Cunningham. Cascaded-systems analyses of the DQE of double-Z x-ray detectors including photoelectric, coherent and incoherent interactions. Proceedings of the Society of Photographic Instrumentation Engineers, 2013.

Jesse Tanguay, Ho Kyung Kim, and Ian A. Cunningham. Should we invest in energy-dependent cardiac angiography? London Imaging Discovery Day, London, ON, Canada, 2012.

Jesse Tanguay and Ian A. Cunningham. Will energy-dependent x-ray imaging approaches eliminate motion artifacts in angiography? London Imaging Discovery Day, London, ON, Canada, 2011.

Jesse Tanguay, Ho Kyung Kim, and Ian A. Cunningham. Will energy-resolving photon-counting detectors enable advanced spectroscopic procedures? London Imaging Discovery Day, London, Ontario, Canada, 2010.

Relevant Graduate Courses

09/10-04/11	PHYSICS 9655	Radiological Physics - 82 %
09/09-04/10	BIOPHYS 9516	Advanced Imaging Principles - 90 %
	BIOPHYS 9513	Scientific Communication - 90 %
	BIOPHYS 9509	Digital Image Processing - 94%
	VASCPROG 9560	Vascular Imaging
09/08-04/09	PHYSICS 9005	Mathematical Methods of Physics - 87 %

Research Experience

05/09-09/09	Summer Research Student Physics and Astronomy The University of Western Ontario, London, Ontario, Canada Project: A feasibility study on the use of CT scanners for small animal irradiation <ul style="list-style-type: none">• Designed and developed a spot densitometer for film dosimetry
-------------	------------------------------------------------------------------------------------------------------------------------------------------------------------------------------------------------------------------------------------------------------------------------------------------------------------------------------------